SAPIENZA
UNIVERSITÀ DI ROMA

Improvements to the nitrogen dioxide observations by means of the MKIV Brewer spectrophotometer

By
Henri Diémoz

Supervisor
Prof. Anna Maria Siani

A thesis submitted in partial fulfilment
of the requirements for the degree of

Doctor of Philosophy
in
Remote Sensing

Cycle XXVI

Department of Information Engineering,
Electronics and Telecommunications

Academic Year 2013/2014

Abstract

Nitrogen dioxide (NO_2) is a key component of the Earth's atmosphere, being involved in the ozone destruction and production and influencing the radiative balance of our planet. Furthermore, it impacts on human health and contributes to the tropospheric pollution. Techniques to measure atmospheric nitrogen dioxide from both the space and the ground have noticeably advanced in the last decades and provide valuable information, while also presenting some serious limitations.

In 1985, an automated Brewer ozone spectrophotometer was modified to add capability to measure solar visible radiation and retrieve atmospheric nitrogen dioxide besides total ozone and sulfur dioxide. Since then, more than 60 MKIV Brewer spectrophotometers have been put in operation in a worldwide network and long-term nitrogen dioxide records have been collected at several sites. However, the original algorithm, developed in the 1980's, has never been officially updated and, although notable efforts have been done in the last years to improve the retrieval by the Brewer, high-quality estimates of nitrogen dioxide by this instrument are still difficult to acquire.

This work introduces substantial innovation in measuring nitrogen dioxide with MKIV Brewers. For the first time, an instrument of this type was thoroughly characterised in its operating spectral range. A novel mathematical framework supporting observations was then developed to update the Brewer processing algorithm, to better understand its potentials and limitations and to optimise the measurement technique. The spectroscopic data sets used within the algorithm were completely updated using the most recently published absorption cross sections. Model calculations were performed with top-level radiative transfer codes to test the new algorithm, which not only allows more accurate estimates of nitrogen dioxide, but also introduces new capabilities in Brewer measurements, such as the retrieval of the oxygen dimer (O_2–O_2) and the degree of the linear polarisation of skylight.

To test the new method, four field campaigns were organised. The limitations in the traditional calibration techniques due to the daily evolution of nitrogen dioxide were overcome by employing an innovative method and one Brewer (#066) was successfully calibrated and compared to an instrument belonging to the Network for the Detection of Atmospheric Composition Change. The two different observation techniques in which the Brewer operates, namely by looking directly to the sun or vertically to the zenith, were proven to be equivalent within the stated uncertainty. The latter was thoroughly evaluated by means of a Monte Carlo based method.

The new algorithm was effectively applied to reprocess the long-term series recorded in the European Brewer stations of Saint-Christophe and Rome (Italy), Athens (Greece), Hradec Králové (Czech Republic). To this purpose, two empirical methods to calibrate the Brewer instruments through statistical analyses were validated. The results were compared with satellite total column data retrieved from the SCIAMACHY, GOME-2 and OMI instruments and with in-situ measurements of tropospheric concentrations to assess the impact of anthropogenic emissions.

ABSTRACT

Acknowledgements

"No man is an island", said a poet once[1], and the same applies to this thesis, which has been a magnificent and collective adventure with several travel companions.

First must come my supervisor, Anna Maria Siani, who introduced me to the fabulous world of Brewer spectrophotometers (and users) many years ago and more recently has proposed me to start my Ph.D. She greatly supported me, with scientific rigour and human warmth, and inspected this manuscript in detail. In addition, my work would have remained an unattainable dream had it not been for the Brewer users community and, most of all: Vladimir Savastiouk (IOS) for the patient and indefatigable email correspondence, his unrivalled expertise and especially his miraculous Canadian Maple syrup; Alberto Redondas (AEMET) and his team (Virgilio, Juan José and Marta) for their scientific skill, their "Canarian acquaintance" and for hosting me in Izaña, one of the most astonishing destinations in all my life; Tom McElroy (York University) and Ken Lamb (IOS) for the enriching (and challenging) exchanges of views.

A broad acknowledgement must go to the colleagues around Europe who provided the measurement series analysed in the last chapter of my thesis: Giuseppe Casale (Sapienza – University of Rome), Konstantinos Eleftheratos (University of Athens), Mihalis Vrekoussis (EEWRC) and Martin Stanek (ČHMÚ). Their friendly help was not limited to some data, but they shared much with me, each in his own way: long discussions and correspondence, meticulous field campaigns and "leisure time" after our meetings (beer and Brewers have always been a perfect pair). Along with them, it is with gratitude that I acknowledge John P. Burrows, Andreas Richter and Andreas Hilboll (University of Bremen) for kindly providing the satellite data and Alexei Rozanov, from the same university, for his guidance about the SCIATRAN model. I also owe my gratitude to the Ph.D. committee for financially supporting the Izaña campaign and my attendance to several meetings. Particular mention should additionally go to the Italian Air Force for hosting the Plateau Rosa campaign.

This thesis would not have been possible unless the approval and the endorsement by the Environmental Protection Agency (ARPA) of the Aosta Valley. I am indebted to the ARPA directorate: Giovanni Agnesod, Marco Cappio Borlino and Corrado Cantele; my colleagues Eric Impérial and Leo Cerise, who shared the "hard work" with me (carrying the Brewer to 3500 m a.s.l., waking up early in the morning to drop me off at the airport, etc.); my dining companions Valeria Bottura and Marco, again, for spending together the everyday lunch breaks in a familiar spirit; the colleagues in charge for the regional air quality network for providing the in-situ measurements. I consider it an honour to work together with such enthusiastic people.

Finally, I wish to thank all my friends and people I spent much time with during the last three years: Enrica, Demian, Massimo, Stefania, Sara, Giuseppe, Leonardo, Alessandra, Elena, Pietro, Silvia, Valentina, Carlo, Albino, Nicola, Ciccio, Alessandro, Antonio, Agim, Uddin and their respective families.

Above all, my deepest thanks must go to my family (my mother Adriana and my father Giorgio, Paul, André and Enrica) and my gramps, for all their support and affection.

[1] John Donne, *Meditation XVII*, 1623.

Glossary

AEMET	Agencia Estatal de Meteorologia.
AMF	Air Mass Factor.
BE	Bootstrap Estimation.
BLB law	Bouguer-Lambert-Beer law.
DOAS	Differential Optical Absorption Spectroscopy.
ds	direct sun.
DU	Dobson Units.
ESA	European Space Agency.
FTIR	Fourier Transform Infrared Spectroscopy.
FWHM	Full Width at Half Maximum.
GAW	Global Atmospheric Watch.
GOME-2	Global Ozone Monitoring Experiment 2.
GUM	Guide to the expression of uncertainty in measurements.
IOS	International Ozone Services.
IQR	Inter-Quartile Range.
MAX-DOAS	Multi AXis Differential Optical Absorption Spectroscopy.
MCM	Monte Carlo Method.
MLE	Minimum-Amount Langley Extrapolation.
NDACC	Network for the Detection of Atmospheric Composition Change.
NO_2	nitrogen dioxide.
NO_x	active odd nitrogen.
OMI	Ozone Monitoring Instrument.
PBL	Planetary Boundary Layer.

PDF	Probability Density Function.
PMOD/WRC	Physikalisch-Meteorologisches Observatorium Davos/World Radiation Centre.
PMT	PhotoMultiplier Tube.
RMSD	Root Mean Square Deviation.
SAOZ	Système d'Analyse par Observation Zénithale.
SCD	Slant Column Density.
SCIAMACHY	SCanning Imaging Absorption spectroMeter for Atmospheric CHartographY.
SNR	Signal-to-Noise Ratio.
UV	ultraviolet.
VCD	Vertical Column Density.
WHO	World Health Organisation.
WMO	World Meteorological Organisation.
WOUDC	World Ozone and Ultraviolet Data Center.
zs	zenith sky.

Contents

CHAPTER 1

Introduction

1.1 Rationale

1.1.1 General background

Since its discovery by Priestley (1775), nitrogen dioxide (NO_2) has been recognised as a key component of the atmosphere. Despite its very low concentration, it drives several chemical and physical processes. In the upper atmosphere, it participates to the catalytic cycles that govern the ozone chemistry. In the troposphere, it controls the oxidative capacity of the atmosphere, favours the photochemical smog in urban areas as well as acid rains and, in high concentrations, can have adverse effects on human health. Moreover, the radiative effects on climate by nitrogen dioxide were found to be significant. Finally, NO_2 can remarkably impact on the accuracy of the measurement of different atmospheric compounds.

Although measurement techniques have noticeably advanced in the last decades, the retrieval of atmospheric nitrogen dioxide from both the space and the ground still presents some challenging issues. Among other ground-based instruments, the MKIV Brewer spectrophotometers have the capability to measure NO_2 and the advantage of being connected in a worldwide network.

1.1.2 Current state of knowledge

In recent years, striking progress has been made in understanding the role of nitrogen dioxide in the atmosphere and in determining its concentration:

chemical processes. Nitrogen oxides chemistry is extremely complex, but well understood (Seinfeld, 1986; Monks, 2005). Models were developed that explain a large fraction of the ozone removal in the stratosphere by gas-phase reactions involving nitrogen oxides (Crutzen, 1970; Garcia and Solomon, 1994). Besides, scientists have also found the importance of nitrogen dioxide in limiting the "ozone hole" at the higher latitudes (Goutail et al., 1994; Chartrand et al., 1999; Feng et al., 2011; Aquila et al., 2013). In the troposphere, nighttime chemistry, involving reservoir species, and daytime photochemistry are correctly described by theory and confirmed by measurements (Haagen-Smit, 1952; Leighton, 1961; Suda et al., 2011; Mendolia et al., 2013);

sources of nitrogen dioxide. Long-lived nitrous oxide (N_2O) originating from microbial activity in soil as well as from anthropogenic sources has been recognised as a major source of nitrogen dioxide in the stratosphere (Bates and Hays, 1967; Lee, 1994; Martin et al., 2006). Several

biogenic processes at the origin of tropospheric NO_2, namely biomass burning, soil emission and lightnings, were identified (Lee et al., 1997; Lerdau, 2000; Schumann and Huntrieser, 2007). Anthropogenic sources such as fossil fuel combustion and fertilisers were discovered to be of primary importance as well (Houghton et al., 2001; Beirle et al., 2004; Eyring et al., 2005; Olivier et al., 2005; Kim et al., 2006);

vertical and spatial distribution. It is ascertained that the concentration of nitrogen dioxide peaks in two distinct atmospheric layers, in the stratosphere and at the surface (Brewer and McElroy, 1973; Kerr et al., 1977). It is also known that the total stratospheric column is dominant in remote environments, while the tropospheric column may considerably exceed the former in polluted sites (Elokhov and Gruzdev, 1995; Lelieveld et al., 2002; Martin et al., 2004; Cede et al., 2006a). Furthermore, it was discovered that the spatial distribution follows from the coupled action of photochemistry and transport, resulting in a latitudinal gradient and "hot spots" regions (Noxon, 1979; Velders et al., 2001; Wenig et al., 2003; Sussmann et al., 2005; Hayn et al., 2009). As instance, the atmosphere in the Po Valley has been identified to be one of the most polluted in the world (Petritoli et al., 2004; Ordónez et al., 2006). Global maps of nitrogen dioxide concentrations are available in the scientific literature, from both ground-based and satellite estimates (Hayn et al., 2009; Dirksen et al., 2011);

temporal variability. Daily, weekly and seasonal variability of nitrogen dioxide concentration has been frequently found, resulting from both photochemical processes and anthropogenic emissions (McKenzie et al., 1991; Beirle et al., 2004; Gil et al., 2008; Hayn et al., 2009; Ma et al., 2013). On a larger time scale, long-term data sets collected around the world represent a valuable source of information about the nitrogen dioxide stratospheric trends (Liley et al., 2000; McLinden et al., 2001b; Rinsland et al., 2003; Struthers et al., 2004; Vaughan et al., 2006; Gruzdev and Elokhov, 2009; Cook and Roscoe, 2009; Hendrick et al.; Werner et al., 2013). Additionally, an overall decrease of the tropospheric NO_2 concentrations has been discovered as an effect of environmental policies and even of the global economic recession (Lövblad et al., 2004; Richter et al., 2005; Alvarez et al., 2007; van der A et al., 2008; Castellanos and Boersma, 2012; Schneider and van der A, 2012; Russell et al., 2012; Liu et al., 2013; Hilboll et al., 2013);

effects. Several articles are published that have assessed various effects of nitrogen dioxide. The contribution of NO_2 to the radiative balance is very large in polluted areas and can even exceed the effect of the most important greenhouse gas, CO_2 (Solomon et al., 1999; Houghton et al., 2001). From a biological point of view, recent research has proved that NO_2 can adversely affect human health both directly, being a powerful oxidant, and indirectly, through formation of other dangerous compounds (Finzi et al., 2001; Brunekreef and Holgate, 2002; WHO, 2006; Samoli, 2006; Latza et al., 2009; Chiusolo et al., 2011). Effects on vegetation, ecosystems and materials, also through acid rain deposition, have been reported (Smith, 1872; Odén, 1968; Krug and Frink, 1983; Bell and Treshow, 2002; Ferm et al., 2005; Sutton and Bleeker, 2013). Finally, it is recognised that nitrogen dioxide interferes in the determination of the aerosol optical properties and should be taken into account in such measurements (Shaw, 1976; Schroeder and Davies, 1987; Arola and Koskela, 2004; Krotkov et al., 2005; Gianelli, 2005);

measurement techniques. Nitrogen oxides concentrations in the boundary layer has been being measured for several years using in situ chemiluminescence detectors, e.g. operated by the Environmental Protection Agencies. Moreover, total concentrations on the vertical column can be effectively retrieved by means of absorption spectroscopy techniques, by analysing the intensity of the sunlight or skylight at several wavelengths and taking advantage of the peculiar spectral attenuation of the solar light by different compounds in the atmosphere (Brewer and McElroy, 1973; Noxon, 1975; McKenzie and Johnston, 1982; Pommereau and Goutail, 1988; Hönninger et al., 2004; Schofield et al., 2004; Platt and Stutz, 2008; Vlemmix et al., 2011). Such techniques can be applied on both ground-based and spaceborne instruments;

Brewer spectrophotometry. The Brewer spectrophotometer (Kerr et al., 1983, 1985) is the reference instrument for ozone measurements. The MKIV model, developed in the 1980's, adds the capability to measure also nitrogen dioxide by gathering the light intensity from the sun or from the zenith sky (Kerr, 1989). About 60 stations belonging to the Brewer network all over the world record series that can be processed to provide NO_2 estimates. Attempts were recently made to update the traditional technique and algorithm (Pinheiro, 2003; Francesconi et al., 2004; Cede et al., 2006a; Barton, 2007);

radiative transfer models. The radiative transfer theory was started more than two centuries ago (Bouguer, 1729; Langley, 1880; Rayleigh, 1899; Schuster, 1905; Chandrasekhar, 1960; Solomon et al., 1987). However, radiative models underwent an exponential expansion in the latest years thanks to the increasing computer speed. Several open source codes are available to the scientific community. Given the correct inputs describing the state of the atmosphere and some boundary conditions, they are able to reproduce the radiation field with great accuracy (Mayer et al., 2012; Rozanov et al., 2014).

1.1.3 Gaps in the current knowledge

trends. While consistent results are found for tropospheric trends, recent studies about the stratospheric NO_2 climatological trends come to contrasting conclusions. More and accurate series are required to reach a better understanding of the overall behaviour of nitrogen dioxide. Additionally, NO_2 trends published in the current scientific literature do not generally agree with the rate of increase of nitrous oxide, the main precursor in the stratosphere (Liley et al., 2000; WMO, 2007). The discordance could be even an indication of changes in the general atmospheric circulation (Fish et al., 2000);

sources. NO_2 measurements in more countries would be of help in improving the inventories used by chemical transport models, which are known to underestimate actual emissions (Miyazaki et al., 2012; Tang et al., 2013). Moreover, atmospheric and biological studies have yielded seriously incompatible results regarding the role of the vegetation as a sink or source of nitrogen oxides (Lerdau, 2000);

in-situ measurements are inherently limited. While measurements of in-situ nitrogen oxides concentrations are common in air quality networks, few estimates of the vertical distribution of pollutants in the urban boundary layer are reported. It has also been found that local concentrations are not necessarily representative of the total vertical column density and may be strongly influenced by fluctuations of the mixing layer height (Schafer et al., 2008; Dieudonné et al., 2013; Mendolia et al., 2013). Furthermore, conventional techniques do not allow separation between NO and NO_2 and the standard equipment based on chemiluminescence could be inappropriate for low concentrations of nitrogen oxides and may be affected by poorly-quantified biases (Ordónez et al., 2006; Alvarez et al., 2007; Steinbacher et al., 2007);

spaceborne instrumentation. Although studies based on satellite radiometers are increasing, care should be taken when relying only on spaceborne instruments. Indeed, large uncertainties may arise, especially over polluted areas and regions with complex orography or snow-covered surfaces, due to the not well known path of the solar beam in the lower atmospheric layers (Boersma, 2004; Leitao et al., 2010). Moreover, the frequency of polar satellites measurements is insufficient to capture the NO_2 diurnal cycle. The low spatial resolution (large dimensions of the pixels) do not allow to resolve the variability typical of NO_2 and may lead to inconsistencies when comparing different instruments (Hilboll et al., 2013). Therefore, validation of spaceborne estimates through ground-based instruments needs to continue;

Brewer spectrophotometers. While the Brewer is considered a reference for ozone retrievals, accurate measurements of NO_2 are still an issue with this instrument. Large deviations in the Brewer estimates compared to reference instruments, both systematic overestimations (40-200%) and random variations (10-30%), were observed during intercomparison exercises

(McElroy et al., 1994; Cappellani and Bielli, 1995; Hofmann et al., 1995; Pinheiro, 2003). Poor agreement was also found when comparing the Brewer to satellite data, with overestimations of up to 50% by the former and low to medium correlation indexes (Francesconi et al., 2004; Wenig et al., 2008; Celarier et al., 2008). Although some updates have been suggested in recent works (Cede et al., 2006a; Barton, 2007), the Brewer algorithm employed at present to process the recorded solar light intensity and retrieve the nitrogen dioxide vertical column still makes use of obsolete spectroscopic data sets (e.g., cross sections of absorbing gases). Moreover, many authors have reported interferences by other atmospheric species and high noise in measurements. Besides, no world travelling Brewer reference currently exist to calibrate the global network for NO_2 measurements, as opposed to ozone retrievals. Finally, no work has been made, yet, to compare nitrogen dioxide estimates in the two different Brewer observation geometries (direct sun and zenith sky).

1.1.4 Reasons for the research

From previous research, it is clear that the Brewer algorithm and technique to retrieve nitrogen dioxide need to be substantially improved. Until then, Brewer NO_2 estimations within the existing worldwide network will be unreliable and useless. A backward-compatible implementation of the potential improvements must be developed to allow extraction of accurate nitrogen dioxide densities from historical data sets (about 60 all over the world, most of them never analysed in detail), some of which spanning up to two decades. This could lead to a better understanding of current trends and future scenarios of atmospheric composition and dynamics. High-quality measurements from ground-based stations could finally contribute to further validation of satellite data.

1.2 Hypotheses

The present work is expected to confirm, or reject, the following hypotheses. They will additionally serve as a leading thread for summarising the conclusions at the end of the book.

a better instrumental characterisation allows to improve the Brewer performances. An innovative feature of my work is the fine characterisation of a Brewer instrument, which was never attempted in the visible range used to retrieve nitrogen dioxide. Based on similar findings about ozone measurements (Savastiouk, 2005), I expect that a better characterisation will considerably contribute to increase the NO_2 estimates accuracy by the Brewer;

the observed overestimations by the Brewer can be reduced by employing more recent spectroscopic data. Currently, the Brewer algorithm developed by Kerr (1989) is based on obsolete laboratory data (Vigroux, 1952; Johnston and Graham, 1976). Additionally, the coefficients for the Rayleigh scattering in the ultraviolet, which have already been proven to be unsuitable, are improperly used also in the visible. A preliminary and mainly theoretical study by Barton (2007) has given promising results which are to be tested with real measurements;

better techniques are available to reduce the measurement noise and increase the information content of the retrieval. Some articles are published that describe alternative techniques making use of a larger set of wavelengths than the standard method, for both ozone (Kerr, 2002; Kerr and Davis, 2007) and nitrogen dioxide retrievals (Cede et al., 2006a) in the ultraviolet range. I expect that these methods can work as well in the visible range where the MKIV Brewers operate;

direct sun and zenith sky estimates by the Brewer are consistent within their respective uncertainties. A comparison of the results with both observation geometries has never been published. Although measurements along the zenith should be more sensitive to the stratospheric concentration and the direct sun technique should be equally sensitive to both the stratospheric and tropospheric columns, I suppose, if the path of the solar beam is

correctly characterised, that no relevant differences should be found. Moreover, the study could provide useful information about the vertical distribution of nitrogen dioxide;

reliable information about the NO_2 trends can be derived by reprocessing existing long-term data sets. Until now, few Brewer NO_2 series were employed in the scientific literature. Yet, I am convinced that the analysis can provide further knowledge about the climatological tendency of nitrogen dioxide. Also, I believe that some recently developed algorithms to calibrate an instrument with statistical techniques (Herman et al., 2009) can be successfully used also for the Brewer;

satellite total column estimates and in-situ concentration measurements are not always representative of the nitrogen dioxide density in the atmosphere. While satellites are more and more employed in the scientific research and the environmental agencies have been relying for several years on in-situ detectors, both techniques have serious limitations that could lead to erroneous conclusions. I strongly believe that ground-based instrumentation is still the reference and that remarkable, though well explicable, deviations will be found when comparing different methods.

1.3 Objectives

1.3.1 Purpose

The purpose of my thesis is to present a new and improved algorithm to retrieve the atmospheric nitrogen dioxide by means of MKIV Brewer solar spectrophotometry.

1.3.2 Specific aims

The main purpose can be further divided into several and gradual steps:

1. to thoroughly characterise a MKIV Brewer in the visible range;
2. to develop a mathematical framework feasible to update the Brewer processing algorithm and to optimise the measurement technique;
3. to update the spectroscopic data sets used by the Brewer algorithm;
4. to explain the observed inconsistencies in the present Brewer estimates and to relate them to the influence of unaccounted factors on Brewer measurements;
5. to introduce new capabilities in Brewer measurements (e.g., retrieval of the oxygen dimer and water vapour, measurement of the linear polarisation degree of the skylight);
6. to test in the field the newly developed methods, to solve the limitations in traditional calibration techniques (e.g., Langley plot with variable absorber amounts) and to validate the results through comparison with reference instruments;
7. to prove the equivalence of direct sun and zenith sky geometries and to explain the remaining observed differences;
8. to thoroughly evaluate, by means of the Monte Carlo method, the combined uncertainty of the NO_2 Brewer estimates;
9. to describe a method to transfer the calibration from a reference Brewer to different spectrophotometers and to reprocess long-term NO_2 series;
10. to validate some statistical methods to calibrate the Brewer instruments and to reprocess the series recorded in several European Brewer stations;
11. to evaluate the accuracy of satellite estimates compared to ground-based spectrophotometry and to assess the impact of anthropogenic activities on NO_2.

1.4 Dissertation outline

The present study is presented in six different chapters.

1. Chapter 2 is devoted to illustrating the scientific context and introducing the origin and the role of nitrogen oxides in the Earth's atmosphere. Moreover, the main benefits of measuring the columnar density of nitrogen dioxide in the atmosphere will be explained in detail;

2. Chapter 3 depicts the MKIV Brewer spectrophotometer, used in this work, and illustrates its operating principles and algorithm along with its capabilities and limitations;

3. the first original results of my work are reported in Chap. 4, starting from the efforts I made to carefully characterise one Brewer (#066). Furthermore, I will show my contribution to the improvements of the Brewer retrieval algorithm for nitrogen dioxide and, to the purpose, I will introduce an innovative and robust mathematical framework;

4. measurements from four campaigns will be shown in Chap. 5. The updates proposed in the previous chapters are now applied to real data collected in the field. A novel approach to account for the daily variation of nitrogen dioxide during the calibration is proposed. Additionally, the uncertainty of measurement is thoroughly addressed by applying the Monte Carlo technique for the first time on a Brewer;

5. finally, in Chap. 6, some empirical methods to calibrate a Brewer without performing a Langley plot are introduced and validated. Long-term series from four European stations are reprocessed and analysed to provide an example of the possible applications of the new algorithm. Additionally, correlations with satellite data and in-situ concentrations are investigated;

6. conclusions are reported in Chap. 7 along with some original ideas for further research on the subject.

Every chapter ends with a "highlights" box, which summarises the main concepts presented in the preceding text. A list of published and submitted papers and conference talks given during my Ph.D. is provided in Appendix B.

CHAPTER 2

Nitrogen dioxide in the Earth's atmosphere

In the 1770's, the philosopher and chemist Joseph Priestley discovered, by means of his experiments using a glass ampule, a gas composed by the two main constituents in the Earth's atmosphere: nitrogen and oxygen (Priestley, 1775). This reddish-brown gas, nitrogen dioxide (NO_2), has nowadays been recognised as one of the fundamental ingredients in the upper and lower atmosphere, although its concentration is rather low, for its role in several chemical and physical processes. In the upper atmosphere, NO_2 participates to the catalytic cycles that contribute in destroying one of the most delicate and fundamental gases for life on our planet: ozone (O_3). Nitrogen dioxide is likewise present in the lower atmospheric layers, where it controls of the oxidative capacity of the atmosphere. Here, it favours the photochemical smog in urban areas, being a key precursor of a range of secondary pollutants, and raises, both directly and indirectly, health problems to humans and damage to the ecosystems.

This chapter is devoted to illustrating the scientific context and introducing the origin and the role of nitrogen oxides in the Earth's atmosphere. First, the composition and vertical structure of the atmosphere will be depicted. Hence, the reader will be helped to correctly understand the behaviour of NO_2 at the various altitudes as well as the main findings of the present work, concerning both the upper and lower layers of the atmosphere. Then, some principles of the stratospheric and tropospheric chemistry of the nitrogen oxides will be illustrated to justify the spatial distribution and the short- and long-term variability of NO_2. Finally, the main benefits of measuring the columnar density of nitrogen dioxide in the atmosphere will be explained in detail.

2.1 Composition and structure of the Earth's atmosphere

The planetary atmosphere, the relatively thin layer of air extending up to some hundred kilometres above the Earth's surface, is primarily composed of about 78% nitrogen (N_2), 21% oxygen (O_2), 1% argon (Ar) and 0.04% carbon dioxide (CO_2). Other constituents, while fundamental for the thermal and chemical balance of the atmosphere, are present in lower mixing ratios. The bulk of the air mass, about 80–90%, stands in the few tenths kilometres closest to the surface and about half is located even in the lowest 5 kilometres.

The thermal structure of the atmosphere (e.g. Visconti, 2001) allows to easily identify many regions with very different properties (Fig. 2.1): some regions have nearly constant temperature profile (tropopause, stratopause and mesopause), others have distinct thermal gradients (e.g. troposphere, stratosphere, mesosphere, thermosphere).

The most interesting layers for the purposes of the present work are:

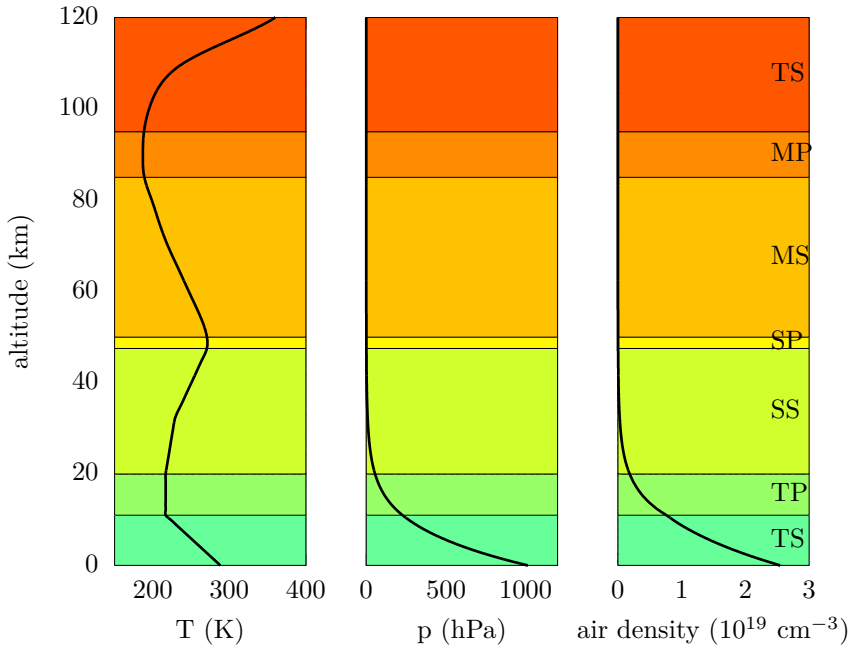

Figure 2.1: Vertical profiles of temperature, pressure and air density of the standard US atmosphere as defined by NASA and USAF (1976) and used in several radiative transfer models. The names of different atmospheric regions, from the troposphere to the thermosphere, are reported as two-letters codes.

the troposphere, extending from the surface up to 7–20 km altitude depending on latitude with minimum thickness at the poles and maximum at the equator. The temperature of the troposphere generally decreases with altitude, as a result of the decreasing pressure and heating of the ground. This is the region where life develops and the common meteorological phenomena occur. The lowest part of the troposphere (some hundred metres to few km), where friction with the Earth's surface influences the air flow, is called the Planetary Boundary Layer (PBL). Pollutants originate, spread over and chemically react in the PBL and may occasionally be transported to higher altitudes. The highest layers in the troposphere, just beneath the tropopause, host the jetstream currents, namely the violent and narrow winds originating from the horizontal thermal gradient of the planet.

The stratosphere, extending up to about 50 km altitude. Even though the air density is far lower than the troposphere, many chemical, dynamical and energetic processes happen in this region. Notably, the ozone "layer", which protects the Earth's surface against the most harmful UV radiation, achieves its maximum concentration in the stratosphere, where it triggers a characteristic temperature profile by converting solar energy into heat. The stratosphere is thus stratified in temperature, with warmer layers higher up and cooler layers farther down. While different from the usual troposphere meteorology, many dynamic processes occur even in the stratosphere.

The boundary between the troposphere and the stratosphere, where an abrupt change in lapse rate usually occurs, is called **the tropopause**. The thermal profile of the tropopause acts as a lid, which generally prevents the exchanges between the two neighbouring layers, unless under the influence of peculiar events, such as folds and intrusions linked with synoptic weather systems.

2.2 Nitrogen dioxide in the atmosphere

Nitrogen dioxide belongs to the wider group of nitrogen oxides (NO_x, box below). Since interconversion ceaselessly occurs among the various species of nitrogen compounds, especially in the gaseous phase, e.g. between nitric oxide (NO) and nitrogen dioxide - which greatly complicates the treatise of single nitrogen compounds - some general families were defined which may be considered as nearly "static" species:

Active odd nitrogen (NO_x). It is a generic term to designate (mono-)nitrogen oxides, i.e. NO and NO_2. The definition is commonly used in the context of the ozone science (NO_x actively participate to the ozone destruction) and air quality measurements and forecasts (NO_x contribute to the ozone formation in the polluted troposphere).

Reservoir species (NO_z). The term refers to all fixed nitrogen oxides, such as HNO_3, PAN, HONO, NO_3, N_2O_5, organic nitrates (RNO_3), particulate nitrates, etc.

Total odd nitrogen (NO_y). This group includes all oxides of nitrogen in which the oxidation state of the N atom is +2 or greater, except the very stable N_2O, namely the sum of NO_x and NO_z.

The concentration of nitrogen dioxide peaks in the stratosphere and at the surface (Fig. 2.2), as first discovered by Brewer and McElroy (1973), whose measurements led to the conclusion that two layers with different properties (near the ground and in the upper atmosphere) should exist. Some years later, Kerr et al. (1977) retrieved a real NO_2 vertical profile using the tangential ray technique, confirming previous results.

Nowadays, it is known that the total stratospheric column is dominant in remote environments, having a columnar density of about 0.05–0.25 Dobson units (DU, see below), while the tropospheric column may considerably exceed the former in polluted locations, with concentrations up to 2 DU (Elokhov and Gruzdev, 1995; Cede et al., 2006a) confined in the lowest 800–1000 metres near the surface on average (Ordónez et al., 2006; Hayn et al., 2009) or slightly higher altitudes, up to 1500 m, in the summer season (Martin et al., 2004).

Dobson unit (DU). The concentration of a trace gas in the entire atmosphere can be expressed as the total number of molecules hovering over a unit area, usually molec cm^{-2}, by imaging a column of air extending from the surface to the "top" of the atmosphere. The Dobson unit, after the name of Gordon Miller Bourne Dobson, the British physicist and meteorologist who pioneered the ozone science, is an alternative unit of measurement of the columnar density of a trace gas. It refers to the thickness of a layer of gas, expressed in 10^{-2} mm, under standard temperature and pressure.

The two units of measurements are linked together by the Loschmidt constant:

$$n_0 \equiv \frac{p_0}{k_B T_0} = 2.6867774(47) \cdot 10^{25} \mathrm{m}^{-3} \tag{2.1}$$

where k_B is the Boltzmann constant. Since it is ordinary in the ozone community - and thus, among the Brewer spectrophotometer users - to express column concentrations in DU, this unit will also be preferred throughout the text.

As both the sources and the behaviour of nitrogen dioxide are different in either layers, stratospheric and tropospheric NO_2 will be separately discussed further below.

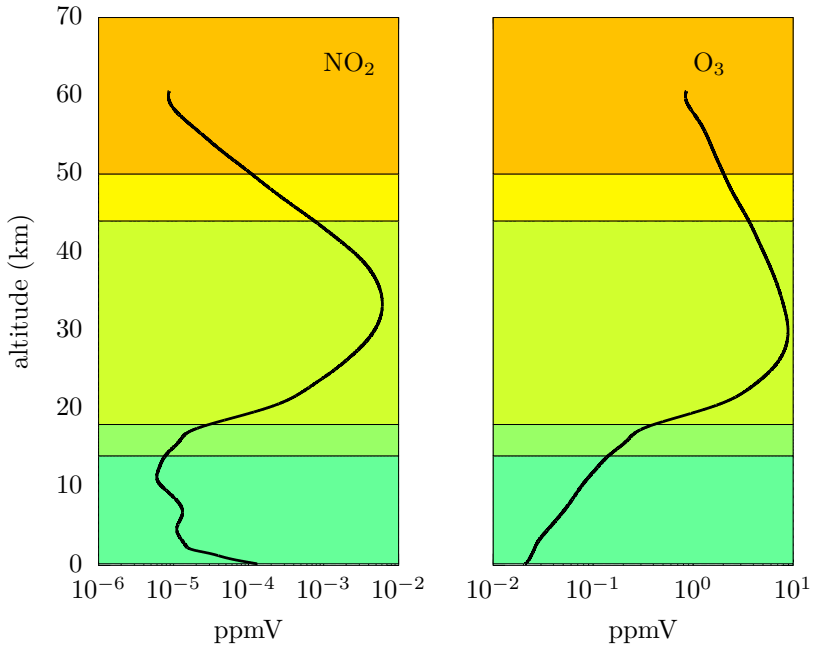

Figure 2.2: Vertical profiles of nitrogen dioxide (left) and ozone (right) at latitude 25°N (corresponding, e.g., to the Izaña station) from a climatological data base obtained using a 2D chemo-dynamical model developed at MPI Mainz (Brühl and Crutzen, 1993), as employed in the radiative transfer model SCIATRAN. The same profiles will be used in the next chapters.

2.3 Sources and spatial distribution in the stratosphere

Long-lived nitrous oxide (N_2O), originating from microbiological activity in soil (Bates and Hays, 1967) and water, as well as from anthropogenic sources, is transported upwards from the troposphere to the stratosphere. Here, it is converted to nitric oxide and nitrogen dioxide (Sect. 2.5). N_2O accounts for a NO_2 production of about 0.1–1 Tg year^{-1} (Lee et al., 1997; Martin et al., 2006).

The NO_2 spatial distribution in the stratosphere results from the coupled action of photochemistry and transport. Noxon (1979), who pioneered the technique of visible spectroscopy for the measurement of stratospheric trace gases, first discovered that NO_2 concentration at the equator is approximately half than at midlatitudes (Fig. 2.3). However, since the production of nitrogen oxides at the equator is higher than at the poles, he realised that an upward and poleward flow introduced by atmospheric heating should exist. Furthermore, he discovered a sharp decrease of the NO_2 column at higher latitudes during wintertime. The decrease, with implications for later ozone depletion studies and which is today known as the "Noxon cliff", is a consequence of the conversion of NO_2 into long-term nitrogen reservoirs inside the polar vortex (Sect. 2.8). An updated map of the stratospheric NO_2 distribution is shown in Fig. 2.4.

2.4 Sources and spatial distribution in the troposphere

Nitrogen oxides are mainly emitted as nitric oxide (NO) in the troposphere (Fig. 2.5), where it reacts rapidly (within minutes) with ozone, the hydroperoxyl and peroxyl radicals (HO_2, RO_2) to form NO_2 (Mendolia et al., 2013), as we will see below in the text. Biogenic processes are involved in the production of NO_2 (Lee et al., 1997; Schumann and Huntrieser, 2007; Herman et al., 2009):

biomass burning contributes by about 20% of NO2 globally, with 4–24 Tg year^{-1};

soil microbial production accounts for 4–16 Tg year^{-1};

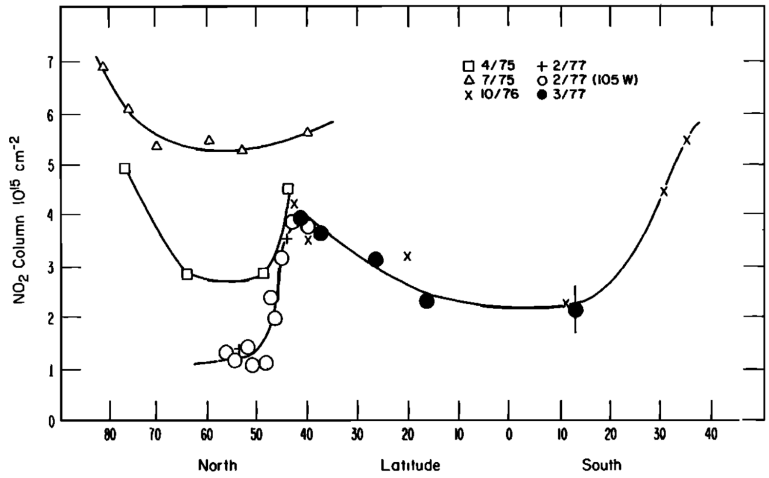

Figure 2.3: Groups of measurements of total column abundance of stratospheric NO_2 (Noxon, 1979).

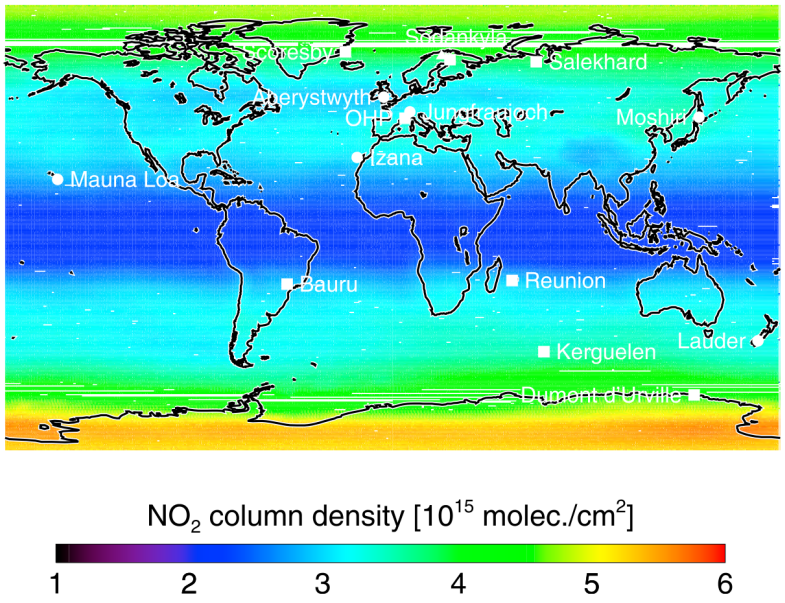

Figure 2.4: The coloured map represents the annual mean of stratospheric NO_2 for 2005 (Dirksen et al., 2011) together with 14 ground-based measurement sites used in the same study.

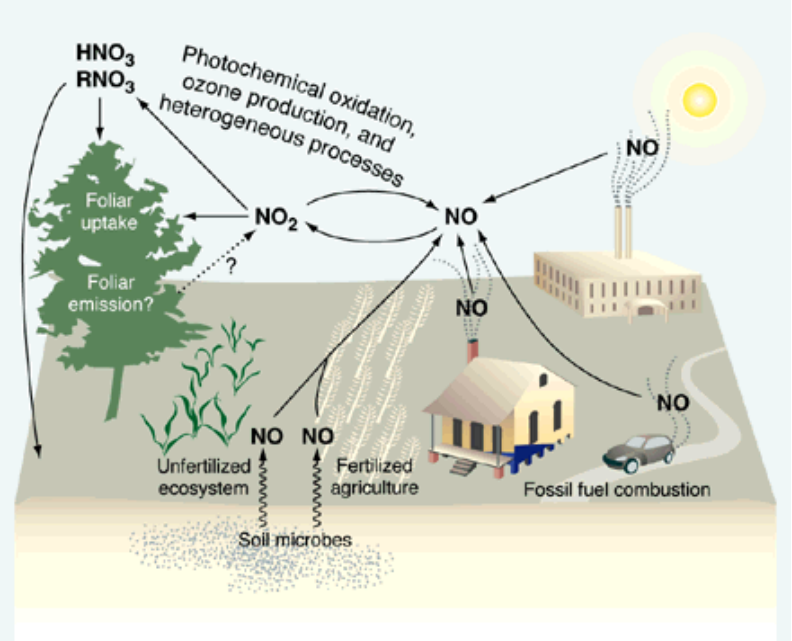

Figure 2.5: Diagram of the main sources of nitrogen oxides in the troposphere (Lerdau, 2000).

lightnings production, e.g. in equatorial tropopause or from the top of thunderstorm clouds to the ionosphere (Brewer, 1999), followed by transport, is estimated from previous studies to be about 5 Tg year^{-1}, with very large uncertainties;

as well as anthropogenic sources (Houghton et al., 2001; Beirle et al., 2004; Eyring et al., 2005; Olivier et al., 2005; Kim et al., 2006):

fossil fuel combustion from traffic, power plants, industry and even ships and aircrafts accounts for 28–32 Tg year^{-1}, making NO_2 a good indicator of high temperature combustion processes;

soil emissions include the use of fertiliser and subsequent oxidation of ammonia.

A global map of the main tropospheric sources of nitrogen oxides is presented in Fig. 2.6. It is apparent from Fig. 2.7 that most of the tropospheric nitrogen emissions occur at Northern midlatitudes.

The tropospheric spatial distribution of nitrogen dioxide is strongly related to the NO_2 lifetime. The latter depends on several factors as the OH concentration, the photolysis rate and air temperature. NO_2 can exist for about 6–27 hours in the polluted boundary layer, depending on season, and up to 4–5 days at higher tropospheric altitudes (Leue et al., 2001; Beirle et al., 2003). While sufficiently large to make the role of horizontal transport relevant (Noxon et al., 1979; Sussmann et al., 2005; Hayn et al., 2009), especially in some regions such as the Monsoon area, South Africa, North Sea and the English Channel, the NO_2 lifetime is at the same time short enough to allow clear identification of main pollution sources in the troposphere from spaceborne instruments, as in Fig. 2.8. Indeed, the so-called "hot spots", i.e. relatively small air masses transporting high concentrations of NO_2 even in remote environments, are easily detectable from satellite radiometers (Velders et al., 2001; Wenig et al., 2003).

As visible from the maps, the Po Valley (Northern Italy) is one of the most polluted sites in the world, due to its orographic characteristics - a basin delimited by the Alps to the North and by the Apennines to the South - which favour the buildup of pollutants and the stagnation of air masses, together with high levels of NO_x emission from both natural and anthropogenic sources (industry, traffic, use of fertilisers in the rural areas). It has been shown to be both a source and

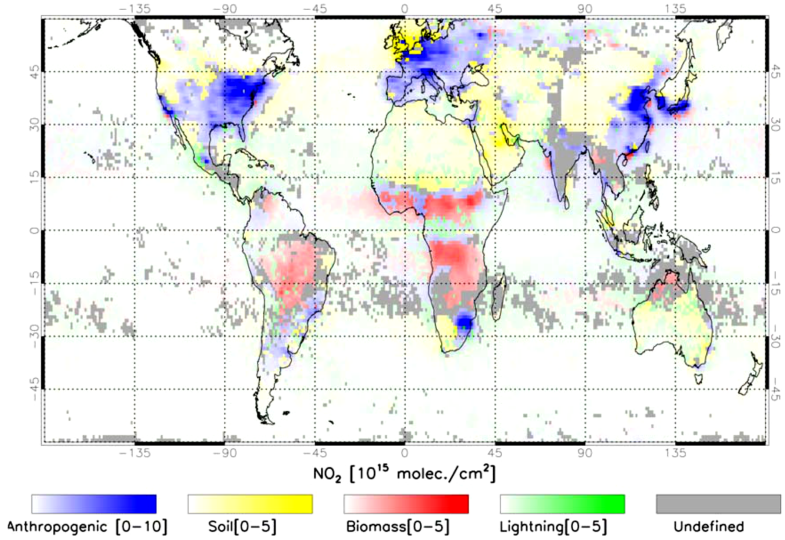

Figure 2.6: Dominant NO_x source identification from satellite observations (van der A et al., 2008).

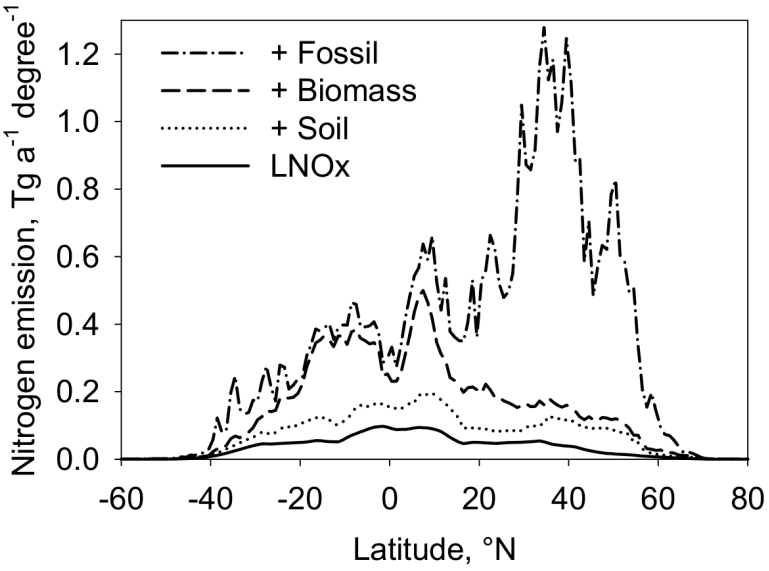

Figure 2.7: Atmospheric annual nitrogen mass emission rate versus latitude for the year 2000. LNOx stands for lightning emissions relative to the year 2000 (Schumann and Huntrieser, 2007).

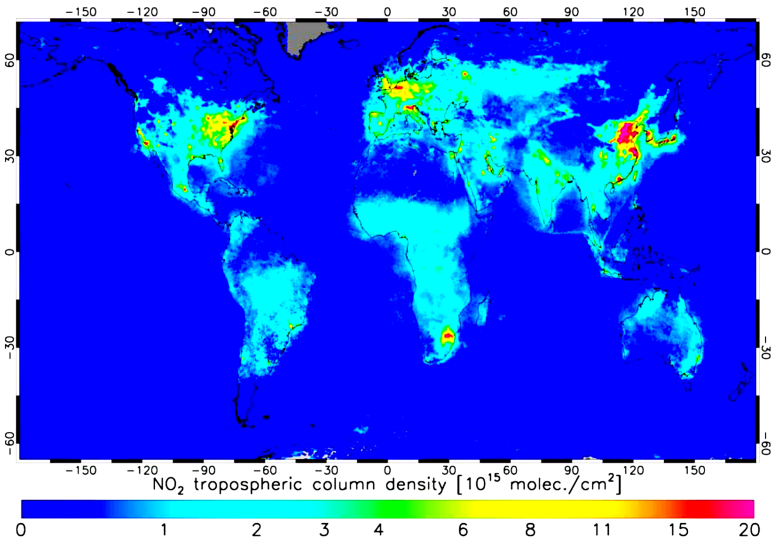

Figure 2.8: The mean tropospheric NO_2 column for the year 2004 derived from the SCIAMACHY radiometer onboard the ENVISAT station (van der A et al., 2008).

a sink of NO_x pollution with respect to central Europe (Petritoli et al., 2004). Even the Aosta Valley, a relatively remote region where most part of the measurements of the present work was done, is likely to be influenced by transport episodes from the neighbouring Po Valley.

Generally speaking, the whole Mediterranean area has proven to be a sort of crossroads for pollution from other continents. Polluted air masses have even been observed to reach the tropopause (Lelieveld et al., 2002).

2.5 Stratospheric chemistry of nitrogen oxides

From the chemical point of view, stratospheric nitrogen oxides and ozone are strongly connected in many ways, among which:

1. the ozone photolysis, along with the presence of N_2O, is the primary source of active nitrogen in the stratosphere and the reason why the NO_2 vertical profile peaks at about 30–40 km altitude;
2. between 25–40 km altitude, NO_2 is involved in the catalytic cycles that accounts for almost half of the ozone removal by gas-phase reactions (Garcia and Solomon, 1994);
3. below 25 km, NO_2 moderates the ozone loss caused by active chlorine (ClO_x), bromine (BrO_x) and hydrogen (HO_x) by converting them into their inactive reservoir forms.

To understand the basis of the O_3-NO_x chemistry, it is usual to start from the elementary reactions discovered by Chapman (1930):

$$O_2 + h\nu \longrightarrow O + O \quad (\lambda < 242\text{nm}) \tag{2.2}$$
$$O + O_2 + M \longrightarrow O_3 + M \tag{2.3}$$
$$O_3 + h\nu \longrightarrow O_2 + O \quad (240\text{nm} < \lambda < 320\text{nm}) \tag{2.4}$$
$$O_3 + O \longrightarrow 2\,O_2 \tag{2.5}$$

where M is a generic molecule involved in the reaction and acquiring the excess energy, which is finally transformed into heat. The above equations represent a chemical null cycle, with two important effects:

the oxygen and ozone molecules shield the lower layers of the atmosphere from the most harmful UV radiation, so that no radiation with wavelength lower than about 290 nm reaches the Earth's surface;

the solar radiation is transformed into thermal energy. As a fundamental consequence, the above equations control the thermodynamic equilibrium of the atmosphere.

The Chapman cycle, which involves reactions between oxygen-only compounds, accounts however for about merely 20% of the observed total natural destruction rate for stratospheric ozone. While an additional 10% can be ascribed to catalytic cycles involving H, OH and HO_2, the most part - about 70% - of total ozone destruction has to be attributed to catalytic reactions involving nitrogen oxides, as discovered by the Nobel prize winning chemist Paul Jozef Crutzen (Crutzen, 1970).

First, active nitrogen species are produced from nitrous oxide, transported from the lower layers to the stratosphere, and the excited oxygen atoms from the ozone photolysis (Eq. 2.4):

$$\mathrm{N_2O + O(^1D) \longrightarrow 2\,NO} \tag{2.6}$$

Then, the following reactions occur:

$$\mathrm{NO_2} + h\nu \longrightarrow \mathrm{NO + O(^3P)} \quad (\lambda < 420\mathrm{nm}) \tag{2.7}$$

$$\mathrm{NO + O_3 \longrightarrow NO_2 + O_2} \tag{2.8}$$

$$\mathrm{NO_2 + O \longrightarrow NO + O_2} \tag{2.9}$$

The NO_2 photolysis (Eq. 2.7) takes place during daylight hours, when UV-visible light is easily found in the atmosphere. Therefore, the abundance of nitrogen dioxide is lower in the daytime than at night, as clearly detectable by measurements (Kerr et al., 1977).

The resulting mixture of nitrogen oxides has approximately equal concentrations of NO and NO_2, depending on the intensity of light and ozone concentration, as expressed in Eq. 2.8. Notably (Gil et al., 2008):

$$\frac{[\mathrm{NO}]}{[\mathrm{NO_2}]} \approx \frac{J_{2.7} + k_{2.9}[\mathrm{O}]}{k_{2.8}[\mathrm{O_3}]} \tag{2.10}$$

At nighttime most NO is converted to NO_2 via the reaction with ozone (2.8), which is temperature - and thus, altitude - dependent (Seinfeld, 1986):

$$k_{2.8} = 2.2 \cdot 10^{-12} \exp\left(-1430\, T^{-1}\right) \tag{2.11}$$

For the ozone concentration and temperature present in the stratosphere, the time constants of the conversion are of the order of a few minutes. Hence, variations at twilight occur very rapidly.

The result of the previous processes is the net destruction of ozone without consuming nitrogen oxides, making NO_x a key species in the ozone depletion issue on a global scale:

$$\mathrm{Net:\ O_3 + O \longrightarrow 2\,O_2} \tag{2.12}$$

A summary of stratospheric NO_x chemistry is shown in Fig. 2.9.

Denitrification. In the polar regions where the "ozone hole" phenomenon occur, NO_x contribute to protect the ozone layer. Indeed, nitrogen oxides control the amount of chlorofluorocarbon (CFC) compounds, deactivating the dangerous chlorine radicals that destroy ozone (Goutail et al., 1994). As an example (Chartrand et al., 1999):

$$\mathrm{ClO + NO_2 + M \longrightarrow ClONO_2 + M} \tag{2.13}$$

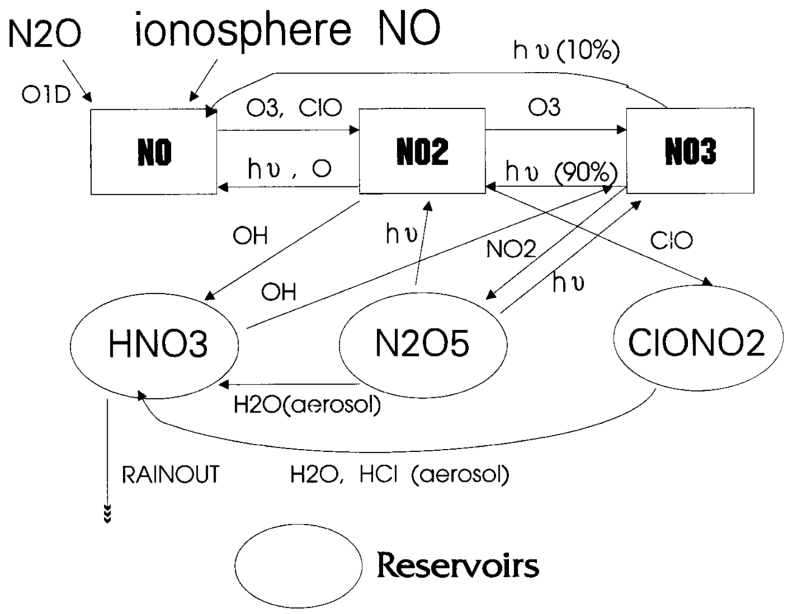

Figure 2.9: Nicolet diagram for the NO_x family (Chartrand et al., 1999).

The resulting chlorine nitrate ($ClONO_2$) is a reservoir species, which does not readily attack ozone, unless after photolysis:

$$ClONO_2 + h\nu \longrightarrow Cl + NO_3 \tag{2.14}$$

Similar processes control the concentration of other ozone-destroying compounds, as bromine and hydrogen species.

Consequently, any process that depletes the stratosphere of nitrogen oxides enhances ozone depletion even up to 30% (Feng et al., 2011). The effect, which is called *denitrification*, may be due to heterogeneous chemistry taking place on polar stratospheric clouds or on volcanic aerosols (Aquila et al., 2013).

2.6 Tropospheric chemistry of nitrogen oxides

Nitrogen oxides partly control the oxidising capacity of the troposphere, as well as the abundance of lower tropospheric ozone, since O_3 is formed as a result of the photolysis of NO_2:

$$NO_2 + h\nu \longrightarrow NO + O \quad (\lambda < 420\text{nm}) \tag{2.7}$$
$$O + O_2 + M \longrightarrow O_3 + M \tag{2.3}$$

Reaction 2.3 is temperature dependent, with constant:

$$k_{2.3} = 6.0 \cdot 10^{-34}(T/300)^{-2.3} \tag{2.15}$$

The previous reactions are the only known routes of producing ozone in the troposphere (Monks, 2005). Tropospheric ozone can then be destroyed by the same NO_x participating to its production:

$$NO + O_3 \longrightarrow NO_2 + O_2 \tag{2.8}$$

Reactions 2.7–2.8 occur very rapidly, leading to a steady state. If no other chemical species were present, the ozone concentration from the photostationary equilibrium would be determined according to the Leighton relationship (Leighton, 1961; Suda et al., 2011):

$$[O_3] = \frac{J_{2.7}[NO_2]}{k_{2.8}[NO]} \tag{2.16}$$

which clearly shows that ozone production is proportional to the solar flux reaching the surface, the concentration of NO_2 and inversely proportional to the concentration of NO.

Although the Leighton relationship works for remote regions unaffected by pollution, it greatly underestimates the ozone concentration in urban areas. Indeed, odd nitrogen can also participate in other chemical processes and myriads of other reactions have an effect on O_3 levels, as will be described in the next section.

2.7 The photochemical smog

The name "photochemical smog" was coined from the contraction of the two terms "smoke" and "fog" after the discovery by Haagen-Smit (1952) of the importance of the photolysis of NO_2 in air pollution chemistry. It is now the common designation given to the particular mixture of reactants and products that exist when volatile organic compounds (VOCs, e.g. hydrocarbons and aldehydes) and oxides of nitrogen occur together - mainly as a result of motor vehicle emissions - in the troposphere in the presence of sunlight. The photochemical smog originates with the following steps:

1. the oxidation of VOCs by OH in urban air produces peroxy radicals, which are central to ozone production in the troposphere and in the lower stratosphere;
2. in case of large NO_x concentrations, e.g. above 50 ppt (Suda et al., 2011), peroxyl radicals are effective catalysts in converting NO - which scavenges O3 - to NO_2 without destroying ozone;
3. analogous reactions with aldehydes form acyl and acylperoxyl radicals, ending up with similar effects;
4. NO_2 supplies the oxygen atom necessary to form O_3 owing to the reactions listed in Sect. 2.6.

Example 1. The simplest peroxyl radical is HO_2, one of the species capable of oxidising NO to NO_2:

$$HO_2 + NO \longrightarrow OH + NO_2 \tag{2.17}$$

with a reaction rate which depends on temperature, according to:

$$k_{2.17} = 3.7 \cdot 10^{-12} \exp(240/T) \tag{2.18}$$

The OH radical may regenerate HO_2 with a time scale of seconds:

$$OH + CO + O_2 \longrightarrow HO_2 + CO_2 \tag{2.19}$$

The net result of the processes involving NO_2 photolysis in urban conditions (Eqs. 2.7–2.3) is thus:

$$CO + 2\,O_2 + h\nu \longrightarrow CO_2 + O_3 \tag{2.20}$$

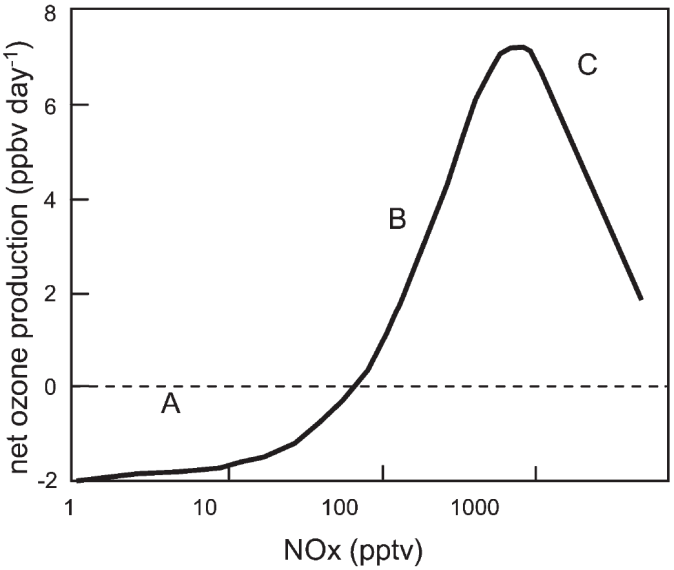

Figure 2.10: Representation of the dependence of the net ozone production (or destruction) on the concentration of NO_x (Monks, 2005).

As a consequence, the ozone concentration depends also on the ratio $\frac{[NO_x]}{[HO2]}$ (Mendolia et al., 2013). Conversely, in the remote atmosphere when little NO_x is present the following reaction dominates, leading to the catalytic destruction of ozone:

$$HO_2 + O_3 \longrightarrow OH + 2\,O_2 \tag{2.21}$$

A schematic representation is given in Fig. 2.10.

Example 2. Considering a simple hydrocarbon, CH_4:

$$OH + CH_4 \longrightarrow H_2O + CH_3 \tag{2.22}$$
$$CH_3 + O_2 + M \longrightarrow CH_3O_2 + M \tag{2.23}$$
$$CH_3O_2 + NO \longrightarrow CH_3O + NO_2 \tag{2.24}$$

NO_2 is again produced without consuming ozone.

More generally:

$$OH + RH \longrightarrow H_2O + R \tag{2.25}$$
$$R + O_2 \longrightarrow RO_2 \tag{2.26}$$
$$RO_2 + NO \longrightarrow RO + NO_2 \tag{2.27}$$

where RO_2 is a species oxidising NO to NO_2.
Similar reactions occur with aldehydes:

Example 3. The simplest and most abundant aldehyde in the atmosphere, belonging to the huge family of oxygenated volatile organic compounds (OVOCs), is formaldehyde (HCHO). It is produced during photochemical degradation of methane and non-methane hydrocarbons (NMHC).

$$\begin{aligned} \mathrm{HCHO} + h\nu &\longrightarrow 2\,\mathrm{HO_2} + \mathrm{CO} \quad (\lambda < 334\mathrm{nm}) && (2.28)\\ &\longrightarrow \mathrm{H_2} + \mathrm{CO} && (2.29)\\ \mathrm{HCHO} + \mathrm{OH} &\longrightarrow \mathrm{HO_2} + \mathrm{CO} + \mathrm{H_2O} && (2.30)\\ \mathrm{HO_2} + \mathrm{NO} &\longrightarrow \mathrm{OH} + \mathrm{NO_2} && (2.17) \end{aligned}$$

In the formaldehyde-NO_x-air system, photolysis of HCHO (and other aldehydes, formed from initial hydrocarbons) is the dominant initial source of free radicals.

More generally, aldehydes (RCHO) form acyl (RCO) and acylperoxy ($RC(O)O_2$) radicals. Then,

$$\mathrm{RC(O)O_2} + \mathrm{NO} \longrightarrow \mathrm{RC(O)O} + \mathrm{NO_2} \qquad (2.31)$$

Free radicals can be converted back to the original peroxy radicals. Hence, once a free radical is formed, it participates in several propagation steps before extinction:

$$\begin{aligned} \mathrm{RO} + \mathrm{O_2} &\longrightarrow \mathrm{R^{'}CHO} + \mathrm{HO_2} && (2.32)\\ \mathrm{HO_2} + \mathrm{NO} &\longrightarrow \mathrm{OH} + \mathrm{NO_2} && (2.17)\\ \mathrm{RC(O)O} &\longrightarrow \mathrm{R} + \mathrm{CO_2} && (2.33)\\ \mathrm{R} + \mathrm{O_2} &\longrightarrow \mathrm{RO_2} && (2.26) \end{aligned}$$

Figure 2.11 gives an overview of the complex chemistry in a VOC-NO_x polluted system. In case of low NO_x concentrations, e.g. <10 ppt (Suda et al., 2011), peroxy radicals are removed by

$$\mathrm{RO_2} + \mathrm{R^{'}O_2} \longrightarrow \mathrm{ROOR^{'}} + \mathrm{O_2} \qquad (2.34)$$

Ozone production is thus proportional to NO_x concentration and independent of VOCs. Conversely, in case of large NO_x concentrations, NO_2 competes with VOCs for the OH radical:

$$\mathrm{NO_2} + \mathrm{OH} + \mathrm{M} \longrightarrow \mathrm{HNO_3} + \mathrm{M} \qquad (2.35)$$

and limits the production of peroxy radicals. The termination of the chain reactions, described in the above equation and in the next section, leads to nitric acid and organic nitrates.

2.8 Nitrogen reservoir species

Other nitrogen compounds, such as NO_3, N_2O_5 and HNO_3, play a central role in the tropospheric chemistry and are worth being mentioned.

The nitrate radical (NO_3) may be formed by the reaction of NO_2 with O or, more effectively, O_3. During daylight hours, NO_3 may photolyse to regenerate NO_2. Alternatively, the NO_3 radical may react with NO:

$$\begin{aligned} \mathrm{NO} + \mathrm{NO_3} &\longrightarrow 2\,\mathrm{NO_2} && (2.36)\\ \mathrm{NO_2} + \mathrm{O_3} &\longrightarrow \mathrm{NO_3} + \mathrm{O_2} && (2.37) \end{aligned}$$

or with an additional NO_2:

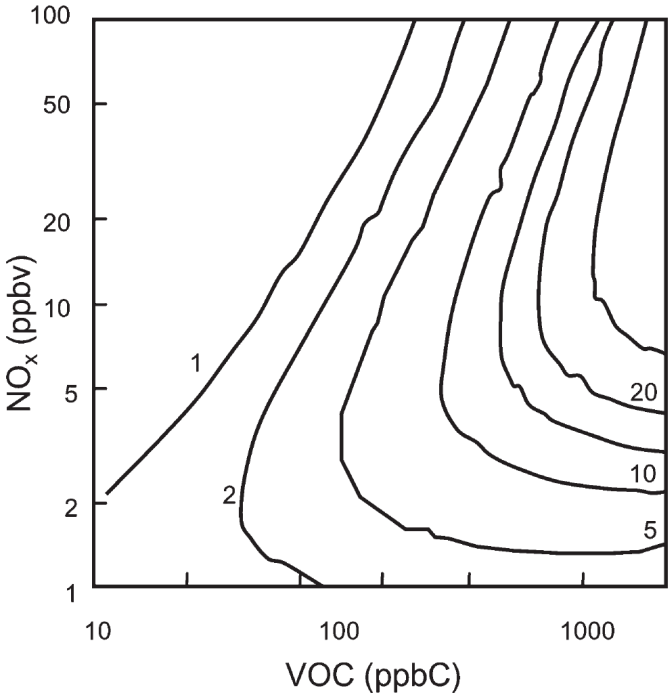

Figure 2.11: Isopleths giving net rate of ozone production (ppb h^{-1}) as a function of VOC and NO_x (Monks, 2005).

$$NO_3 + NO_2 + M \longleftrightarrow N_2O_5 + M \tag{2.38}$$

The majority of NO_3 exists as dinitrogen pentoxide (N_2O_5), formed in reaction 2.38. N_2O_5 acts as a reservoir for the nitrate radical limiting its concentration, with an equilibrium very sensitive on temperature. The buildup of N_2O_5 during the night is followed by a slow decrease during the day through photolysis:

$$N_2O_5 + h\nu \longrightarrow 2\,NO_2 + O \quad (\lambda < 400\text{nm}) \tag{2.39}$$

Those processes give rise to the well-known diurnal cycle of nitrogen oxides in the stratosphere. As an example, Fig. 2.12 illustrates one of the first studies about the daily variations of NO_x using photochemical models. At lower altitudes, while some N_2O_5 may thermally decompose, a fraction reacts heterogeneously with aerosol and water and produces nitrate-bound particles. This mechanism serves as a major nighttime NO_x sink (Fig. 2.13).

Nitric acid (HNO_3) is the main nitrogen reservoir species in the troposphere. It may be formed through reactions with the OH radical, which is, together with photolysis, a major sink of NO_2, accounting for about 50% of the removal (Monks, 2005):

$$NO_2 + OH + M \longrightarrow HNO_3 + M \tag{2.35}$$

The above process is fundamental, for example, in the NO_x-saturated regime, where the ozone production decreases with increasing NO_x concentration since HO_x cycling is inhibited by the chain-terminating reaction of OH with NO_2.

Nitric acid also represents an important form of nitrogen transport: it is the main route of stratosphere-troposphere exchange for reactive nitrogen and it can sediment to the surface through tropospheric rainout, originating dangerous acid rains, or through dry deposition.

HNO_3 may be photolysed by solar radiation (Noxon, 1979):

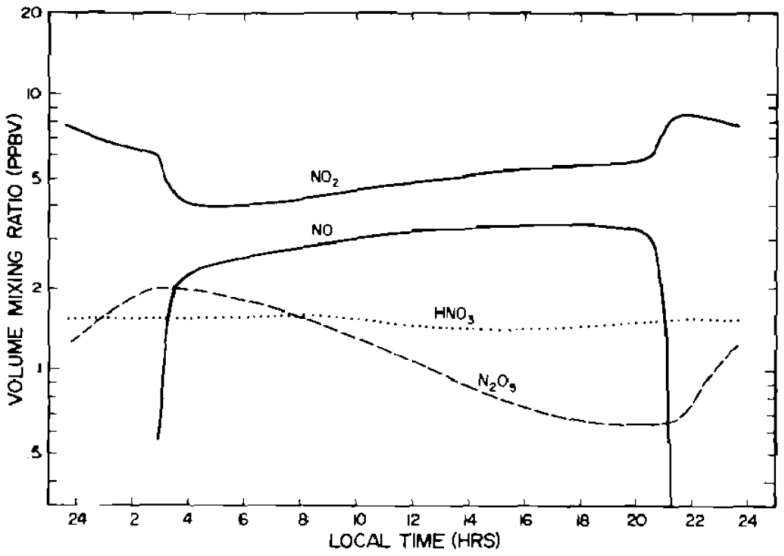

Figure 2.12: Calculated diurnal variations of NO, NO_2, N_2O_5 and HNO_3 at 30 km altitude (Evans et al., 1976).

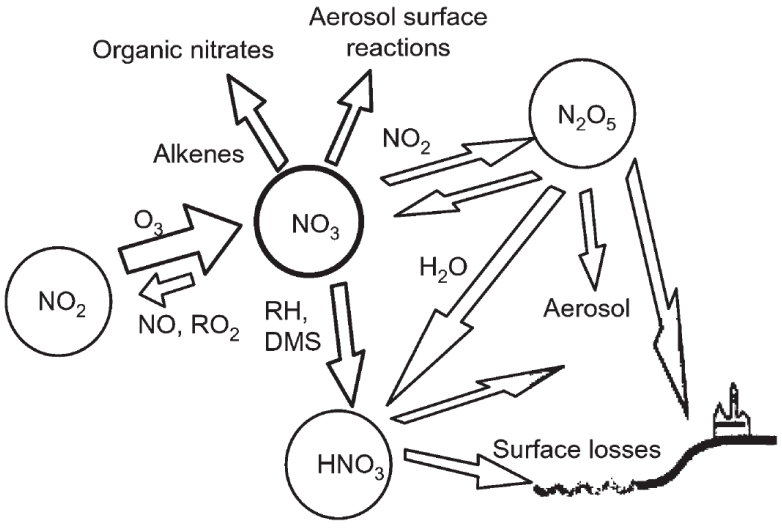

Figure 2.13: A simplified reaction scheme for night-time chemistry involving the nitrate radical (Monks, 2005).

$$HNO_3 + h\nu \longrightarrow NO_2 + OH \quad (\lambda < 550\text{nm}) \tag{2.40}$$

As already noted, the concentration of reservoir species is a key parameter in the polar ozone depletion issues. During autumn and winter, NO_2 is converted to the long-term reservoir forms HNO_3 and $ClNO_3$ either through gas-phase reactions or hydrolysis of N_2O_5 on aerosol particles. A minimum occur in the polar vortex by rapid conversion of N_2O_5 to HNO_3 on polar stratospheric clouds. Afterwards, in spring and summer the reservoir species are photolysed or destroyed by OH, regenerating NO_2 which therefore reaches a maximum around mid-summer.

A further, notorious nitrogen reservoir compound is peroxyacetyl nitrate (PAN), ubiquitous throughout the troposphere. It is formed from the peroxyacetyl radical, produced in the photooxidation of many different kinds of hydrocarbons, and nitrogen dioxide:

$$CH_3C(O)O_2 + NO_2 \longleftrightarrow CH_3C(O)O_2NO_2 \tag{2.41}$$

PAN thermally decomposes in the warmer boundary layer, but is relatively stable in the middle and upper troposphere and acts as a transport species.

2.9 Temporal variability

Natural and human-induced NO_2 temporal variability, both in the stratosphere and in the troposphere, will be analysed in this section, proceeding from higher to lower frequencies.

Daily variability. Although high frequency waves, e.g. of about 15 minutes (Gil et al., 2003), have been reported in the scientific literature, the most distinguishable rapid NO_2 pattern commonly recognised is the diurnal cycle. This oscillation is due, in the stratosphere, to the transformation of reactive nitrogen species in reservoir species, as already mentioned (Fig. 2.12). A daily cycle in the troposphere is also often measured due to vehicular traffic, domestic heating and industrial emissions.

Weekly cycle. At slightly lower frequencies, the weekly cycle in the tropospheric NO_2 density has been measured by several authors. Beirle et al. (2003) discovered a significant decrease, up to 25–50%, in industrialised regions on Sundays using the GOME radiometer onboard the ERS-2 satellite. Hayn et al. (2009) noticed that the cleanest days of the week corresponds to non-working days in different cultures (Friday, Saturday and Sunday) using the same radiometer, while negligible (Hayn et al., 2009) or small (Ma et al., 2013) weekly effect was found in China using satellite and ground-based measurements.

Seasonal variability. A significant seasonal cycle in the stratospheric NO_2 content can be measured over remote locations. The cycle is characterised by a maximum in the warm season (summer in the Northern hemisphere) and a minimum in the cold season (winter) and is due to the combined effects of photochemistry and atmospheric transport (Noxon, 1979; McKenzie et al., 1991). The amplitude of the pattern is minimum near the equator, about 2 at midlatitudes and 6 at higher latitudes. An example of the seasonal waves is provided in Fig. 2.14 for the Izaña station.

A seasonal cycle is as well measurable in the tropospheric column, although of opposite phase (maximum in the cold season and minimum in the warm season). At least three key factors contribute to the wave:

1. NO_2 photolysis is larger in the warm season, decreasing tropospheric NO_2 levels (while increasing tropospheric ozone concentrations);
2. the photolysis of OH precursors (e.g. O_3, HONO, aldehydes) favours reaction 2.35 (Mendolia et al., 2013);
3. domestic heating is lower in summer compared to winter. As an example, differences between domestic heating in winter and summer are about 14% in Lombardy (Ordónez et al., 2006).

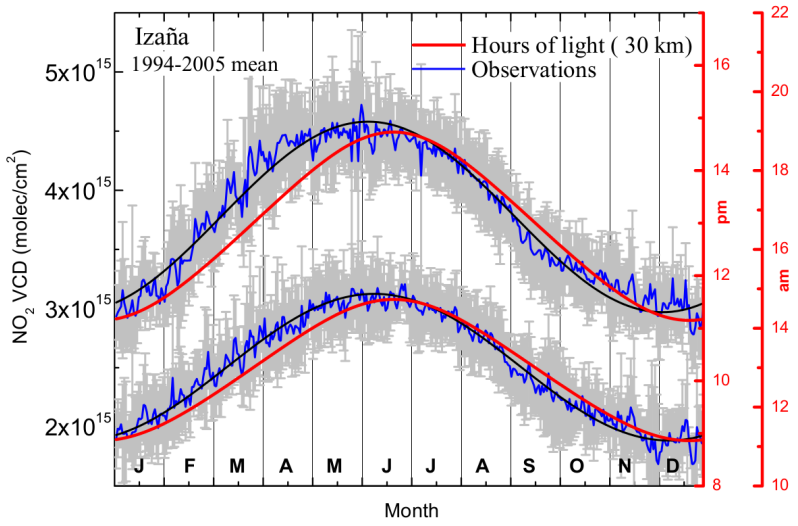

Figure 2.14: Climatological seasonal waves for morning (a.m.) and afternoon (p.m.) data (blue lines) at the Izaña station. Gray error bars represent one standard deviation (Gil et al., 2008).

2.10 Recent trends in stratospheric nitrogen dioxide

Long-term stratospheric NO_2 observations over the last decades display contrasting trends, which are different for the various stations. Generally, those trends do not agree with the rate of increase of nitrous oxide, the NO_2 precursor in the stratosphere (Sect. 2.3), which ranges from 2.2 to 3% (Liley et al., 2000; WMO, 2007). The discordance could be an indication of changes in the overall atmospheric circulation (Fish et al., 2000). Long-term series are therefore of paramount importance to understand current trends and assess future scenarios of atmospheric composition and dynamics. Some of the most interesting findings are presented in the followings in chronological order.

Lauder (New Zealand) owns the longest available visible spectroscopy dataset. Liley et al. (2000) found an increase of NO_2 stratospheric column of approximately 5%±1% decade^{-1} for the period 1980–1999. Dirksen et al. (2011) further confirmed a 5% decade^{-1} trend for the period 1980–2011 at the same location. The Lauder trend can be understood if the increase in N_2O is combined with the decrease in ozone and the change in odd nitrogen partitioning due to increased chlorine concentrations, together with variations in volcanic aerosols due to the Mount Pinatubo eruption (McLinden et al., 2001b).

Kitt Peak (Arizona). Rinsland et al. (2003) measured a positive 5.2%±3.2% decade^{-1} using a Fourier Transform Infrared Spectroscopy (FTIR) spectrometer.

Arrival Heights (Antarctica). Struthers et al. (2004) compared measured data with a three-dimensional coupled chemistry-climate model (CCM) and again found a greater rate of increase of NO_2 compared to N_2O both in the measurements and the model.

Aberystwyth (Wales). Vaughan et al. (2006) found a trend of 4–6% decade^{-1} since 1998, preceded by with a sharp relative reduction in late 1991, caused by the eruption of Mount Pinatubo. Most of the reduction was due to a real change in the NO_2 column, except a small component (few percents) due to changes in aerosol scattering from high altitudes.

Izaña (Canary Islands). No significant long-term trend in the 1993–2006 data record was found by Gil et al. (2008).

23 worldwide sites being part to the Network for the Detection of Atmospheric Composition Change (NDACC) were analysed by Gruzdev and Elokhov (2009) for the years 1983–2007,

using different period for each station. The detected NO_2 trend is predominantly positive at mid-latitudes in the Southern hemisphere, while negative trends are observed at most Northern hemisphere mid-latitude sites. No significant trend was found, except few stations, using multiple regression models (Werner et al., 2013).

Antarctica. Cook and Roscoe (2009) analysed the period 1990–2007, discovering that the measured trend strongly depends on the selected interval. It is about +10% decade^{-1} for the years 1990–2000 and -20% decade^{-1} for the years 2000–2007. No significant trend was found for the full time period.

Jungfraujoch (Switzerland). The series was analysed by Hendrick et al.. A trend of $-3.7\% \pm 1.1\%$ decade^{-1} was found using Système d'Analyse par Observation Zénithale (SAOZ) and FTIR instruments for the period 1990–2009 and of $-2.4\% \pm 1.1\%$ decade^{-1}, $-4.3\% \pm 1.4\%$ decade^{-1} and $-3.6\% \pm 2.2\%$ decade^{-1} using SAOZ, FTIR and satellite instruments, respectively. Since those trends are opposite in sign to the globally observed trend in N_2O, the authors presumed that factors other than the nitrous oxide are driving the evolution of stratospheric NO_2 at Northern midlatitudes. Among them, the stratospheric cooling, a decrease in stratospheric chlorine content and the strengthening of Dobson-Brewer circulation are convincing hypotheses.

2.11 Recent trends in tropospheric nitrogen dioxide

Since pre-industrial times, tropospheric NO_2 has increased six times in industrialised areas (Werner et al., 2013). In the last decades, several protocols were adopted to control the emissions of nitrogen oxides or their transboundary fluxes and thus to abate acidification, eutrophication and ground-level ozone. Remarkable success was obtained in Europe and Eastern U.S. (Fig. 2.15). The scientific literature reports reduction in those regions of -30% between 1990–2000 (Lövblad et al., 2004), -7% year^{-1} (van der A et al., 2008), -12% year^{-1} (Hayn et al., 2009), -20% between 2005–2008 (Castellanos and Boersma, 2012), -3% to -4.5% year^{-1} (Schneider and van der A, 2012), -6% year^{-1} (Hilboll et al., 2013).

The global economic recession may have played a role in the last years. In 2009, concentrations lower by 20–40% than 2005 in European industrialised regions due to the economic recession were reported by Castellanos and Boersma (2012). Reductions of -32%±7% in 7 years, with the steepest decrease, about -8% year^{-1}, during the recession were also found in the U.S. (Russell et al., 2012). Concurrently, the same authors report a new, increasing trend in non-urban, background tropospheric NO_2 by 10–20%, probably due to changes in agricultural emissions.

While NO_x levels have generally fallen in industrialised countries, emissions by diesel vehicles may have had an adverse effect. Indeed, the fraction of NO_2 on NO_x is increasing in Europe (Alvarez et al., 2007). The NO_2/NO_x emission fraction by diesel vehicles with catalytic converters and particle filter systems that employ NO_2 to oxidise trapped soot can even reach 70%.

On the other hand, increasing trends are found in the North Sea region and in Eastern Europe, about +15% between 2005–2008 (Castellanos and Boersma, 2012), but most of all in Asia, Middle East, Russia and Western U.S. Richter et al. (2005) found increases of about +50% between 1996–2004 in China, a much larger trend than the forecasts from bottom-up inventories. Other authors report various, but always positive, trends for the same region: +29% year^{-1} (van der A et al., 2008), +15% year^{-1} (Hayn et al., 2009), +19% year^{-1} (Schneider and van der A, 2012), +20% year^{-1} (Hilboll et al., 2013). Increased emissions are likely responsible for the observed enhanced nitrogen depositions at the surface of up to 60% since 1980 (Liu et al., 2013). Finally, Hayn et al. (2009) found a trend of +11% year^{-1} for the Western U.S. and the Middle East region.

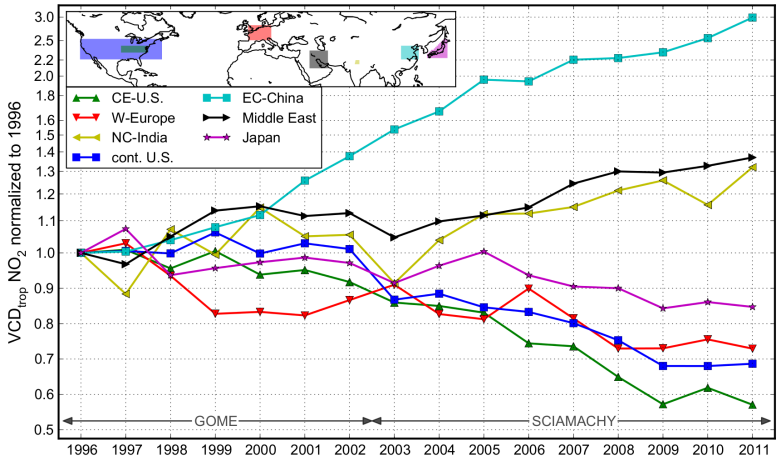

Figure 2.15: Mean annual vertical column density normalised to 1996 from satellite radiometers (Hilboll et al., 2013).

2.12 Effects of nitrogen dioxide

Besides the above mentioned contribution of nitrogen dioxide to the atmospheric chemistry, NO_2 has many other effects on the atmosphere and the biosphere. Among them,

Radiative effects. It is well known that nitrogen dioxide absorbs solar radiation, with maximum power in the visible (blue) wavelength range. For that reason, at high NO_2 concentrations, polluted air and exhaust plumes assume a typical brownish color. The absorption of light by NO_2 gives rise to visibility issues in megacities as well as significant radiative effects: the incoming solar radiation can be reduced at the ground by about 5-12% (Solomon et al., 1999). This is estimated to produce a radiative forcing of 2–10 W m^{-2}, which is remarkable compared, for example, to the effect of the most important greenhouse gas, CO_2, estimated at 1.4 W m^{-2} (Houghton et al., 2001). Therefore, nitrogen dioxide may potentially play a direct role in global climate change.

Effects on human health. Nitrogen dioxide can adversely affect human health both directly, as a powerful oxidant, and indirectly, through formation of other dangerous compounds. The only relevant route of exposure to humans is inhalation: 70–90% of nitrogen dioxide can be absorbed from the respiratory tract (WHO, 2006) and the maximum exposure is reached in the terminal bronchioles (Samoli, 2006).

Animal and human experimenal toxicology indicates that nitrogen dioxide is, in very high concentrations, a toxic gas with significant airway effects, including host defence against microbiological agents and enhanced bronchial hyperresponsiveness in asthmatics to allergen and irritant stimuli (Brunekreef and Holgate, 2002). In high concentrations, NO_2 can also cause irritation to mucous membrane of eyes and nose (Finzi et al., 2001).

Epidemiological studies from outdoor air reveal significant association with increased total natural, cardiovascular and respiratory mortality, e.g. (Chiusolo et al., 2011), even in the medium term, i.e. 2–6 days (Samoli, 2006). Furthermore, some studies give indication of possible correlations between NO_2 exposure and hospital admissions or emergency department visits for respiratory and cardiovascular diseases and asthma aggravation, with particular regard to children (WHO, 2006). However, those studies are often unable to separate the effects of nitrogen dioxide from those of other pullutans, especially fine particles. Indeed, NO_2 is strongly correlated to the various products of traffic-related emissions and in many cases the results become non-significant after adjusting for particles (Latza et al., 2009).

Secondary health effects due to formation of ozone, particulate matter, PAN and nitrosamines are also undeniable (Platt and Stutz, 2008).

Effects on vegetation. Vegetation gives a fundamental contribution to the concentration of nitrogen oxides in the atmosphere, as NO_x is removed directly from the air through the uptake of NO_2 by foliage (Lerdau, 2000). This process also removes soil-derived NO_x from the air before it can be exported to the atmosphere. However, high concentration of NO_2 may cause leaf necrosis and reduction of crop production (Bell and Treshow, 2002). Moreover, acid rains, caused by emissions of sulfur dioxide and nitrogen oxide, which react with water molecules in the atmosphere, can have harmful effects on plants due to their low pH.

Effects on ecosystems and biological diversity. Nitric acid and nitrates, removed by rain and dry deposition from the atmosphere, contribute to excess nutrients in sensitive ecosystems. This is known to contribute, e.g., to the formation of algae in water (Sutton and Bleeker, 2013).

Effects on materials. The acidification of the nitrogen compounds in the atmosphere and subsequent formation of nitric acid can lead to fading of coloured tissues, loss of resistance in fibres of tissues, corrosion in alloys with nickel and brass. It may also damage the cultural heritage (Ferm et al., 2005).

2.13 Further benefits from ground-based NO_2 measurements

Measuring the NO_2 columnar content in the atmosphere, e.g. by means of a Brewer spectrophotometer as will be described in the next chapters, may be of great help in supporting other techniques using different operating principles, for a number of reasons.

Conventional *in-situ* techniques to measure nitrogen oxides, for example, as used worldwide in air quality networks, are inherently limited, for many reasons:

1. the measured *local* concentration is not necessarily representative of the *total* column density integrated on a vertical profile, especially in the urban atmospheric boundary layer (Dieudonné et al., 2013). Also, surface concentrations may be strongly affected by the height of the mixing layer (Schafer et al., 2008). Measurements of the NO_2 columnar content besides to *in-situ* concentrations can thus supply useful information about the vertical distribution of NO_2;

2. there are no standard analysers for NO_2 only. Conventional bag sampling techniques do not allow separation between NO and NO_2, since the former is converted to the latter within minutes (Alvarez et al., 2007). In addition, it should be noted that the NO_x concentration as defined by regulations has the molar mass of NO_2. Distinct measurements of NO and NO_2 may be needed, for example, when studying the effects of diesel emissions;

3. standard equipment to estimate NO_x is based on chemiluminescence. As recently reported, this technique is inappropriate for very low concentrations of nitrogen oxides and may be affected by poorly-quantified biases, so that NO_z are measured in addition to NO_x (Ordónez et al., 2006; Steinbacher et al., 2007).

Ground-based columnar measurements are also useful to validate spaceborne radiometers (Vaughan et al., 2006), which are increasingly employed in different fields, as air quality, atmospheric photolysis and chemistry (Herman et al., 2009). The larger uncertainty in satellite estimates is connected to the evaluation of the air mass factors (AMFs) (Boersma, 2004; Leitao et al., 2010), especially in highly polluted areas and in regions with complex orography or snow-covered surfaces (e.g. the Aosta Valley).

Furthermore, NO_2 measurements are of help in improving the inventories used by chemical transport models, which are known to underestimate actual emissions (Miyazaki et al., 2012).

Finally, independent nitrogen dioxide estimates are essential to perform high quality measurements of the aerosol optical properties, since both species absorb in the visible range and may interfere. Notably, Shaw (1976) suggested that significant errors in aerosol optical depth estimates can arise if absorption by nitrogen dioxide is neglected. Schroeder and Davies (1987) showed that the measured aerosol optical depth can decrease by up to 47% after including NO_2, columnar number density by 51–95%, columnar number mass by 13–26% and that the aerosol size distribution gets narrower. Similarly, Gianelli (2005) found that the determination of the fine-mode effective radius and the accuracy of the aerosol size distribution from shadowband spectroradiometers are strongly sensitive to NO_2. Again, Arola and Koskela (2004) and Krotkov et al. (2005) reported that the NO_2 absorption represents a significant source of error in aerosol absorption optical thickness and spectral dependence measurements in the UV, especially in fall-winter months with typically dry conditions and low aerosol loadings.

Chapter highlights

- nitrogen dioxide (NO_2) is involved in the catalytical cycles connected to ozone destruction and production and has fundamental effects on Earth's radiative balance and human health;
- NO_2 density peaks in two different atmospheric layers in the stratosphere and in the tropospheric boundary layer;
- both natural and anthropogenic factors contribute to the NO_2 abundance and variability in the atmosphere;
- recent studies about the stratospheric NO_2 climatological trends come to contrasting conclusions, while consistent results are found for tropospheric trends;
- ground-based measurements of columnar NO_2 represent a valuable source of knowledge for the atmospheric science.

CHAPTER 3

Measuring nitrogen dioxide by Brewer spectrophotometry

Few physical laws had the same lucky fate as the simple principle discovered throughout the course of two centuries (1729–1852) by three scientists: Pierre Bouguer, Johann Heinrich Lambert and August Beer. The Bouguer-Lambert-Beer law (BLB law), describing the way in which radiation and matter interact, prepared the ground for the modern spectroscopy and is now employed, among many other things, with most instruments for the remote sensing of the atmosphere, including satellites, and radiative transfer models. Indeed, every atmospheric compound leaves a distinct "signature" in the spectrum of the solar radiation passing through the Earth's atmosphere, thus allowing to measure its abundance in the distance, for instance at ground.

The Brewer spectrophotometer, after the name of the Canadian-English physicist and climatologist Alan Brewer (1915–2007), is one of the most useful, and used, ground-based instruments to retrieve the amount of ozone. Since the Brewer spectrophotometer, or simply "the Brewer" - as is familiarly called in the scientific community -, is also the key instrument employed in my Ph.D., an entire chapter is devoted to its description, operating principles, algorithm, together with its capabilities and limitations. In addition, the most important studies about the the Brewer spectrophotometer, since the year it was adapted to the measurement of nitrogen dioxide in 1985, will be briefly summarised to introduce the reader to the goals and the main findings of my thesis.

3.1 Radiative transfer in the Earth's atmosphere

Everyday experience shows that matter attenuates light. From a scientific point of view, when electromagnetic (e.g. solar) radiation and matter (e.g. the atmosphere) interact, two different kind of phenomena may occur:

absorption. A photon is absorbed by an atom, a molecule or a more complex chemical compound. The particle reacts by splitting into two (or more) components, for instance molecules or atoms (photolysis) or even subatomic particles (photoionisation), or, if the photon energy is lower, by increasing its internal energy (rotational, translational, vibrational or electronic, in ascending order of magnitude), which is finally transformed into heat. The strength of the absorption depends on the characteristics of the interacting particle and the wavelength of the incoming light (Sect. 3.2 and Fig. 3.6), as will be explained later after introducing the "cross section" concept;

scattering. The absorbed radiation is remitted by the particle, the net result being redirection of light at a different angle from the incident beam. The scattering regime and its strength,

as will be described later, strongly depend on the wavelength of incident radiation (λ) and the size of the particle of radius r or, more easily, by their ratio (*size parameter*):

$$\chi \equiv \frac{2\pi r}{\lambda} \tag{3.1}$$

The remitted photon may be of the same wavelength as the incident radiation (*elastic scattering*) or characterised by a - slightly - different wavelength (*inelastic scattering*). The latter, often neglected since its effect is insignificant on an absolute scale, will be thoroughly analysed later due to its effects on NO_2 measurements using the Brewer spectrophotometer.

Extinction is the result of both absorption and scattering. Extinction defines, for instance, the intensity at the Earth's surface of the direct component of sunlight traversing the atmosphere, accounting for every physical process occurring along the photon path.

3.1.1 Bouguer-Lambert-Beer law

The BLB law quantitatively describes the progressive weakening of a parallel monochromatic beam of light traversing a thin layer of absorptive medium (Fig. 3.1). It states that the extinction is directly proportional to the thickness of the sample, as discovered by Bouguer before 1729 - but often attributed to Lambert, who cited the *Essai d'optique sur la gradation de la lumière* by Bouguer (1729) and treated the subject in detail -, and to the concentration of the sample, as formalised by Beer in 1852. When neither a source term nor the multiple scattering contribution is considered, the law can be written, in its differential form, as

$$\mathrm{d}I(\lambda) = -I(\lambda)\sigma(\lambda)n\,\mathrm{d}s \tag{3.2}$$

where $I(\lambda)$ is the spectral intensity, $\mathrm{d}I(\lambda)$ its variation after traversing a layer of thickness $\mathrm{d}s$ and n the number density of the medium, expressed as number of molecules per unit volume. $\sigma(\lambda)$ is a constant which depends on the nature and state of the substance and on the wavelength of the radiation passing through it, has the dimensions of a surface per molecule ($\mathrm{cm^2\,molec^{-1}}$) and is called *cross section*. $\sigma(\lambda)$ of several substances may be accurately measured in well-equipped laboratories.

The same law may be also expressed as a function of the mass concentration ρ ($\mathrm{g\,cm^{-3}}$) by introducing the molar mass and the Avogadro constant in Eq. 3.2.

Radiometric quantities

Radiance. The power per unit area per unit wavelength per unit solid angle of the incident light ($\mathrm{W\,m^{-2}\,nm^{-1}\,rad^{-1}}$). It is a convenient physical quantity, since it does not depend on the geometrical effects linked to the distance of the receiver from the source. Indeed, both the power and the solid angle decrease in a similar manner with increasing distance, thus cancelling out their respective effects.

Irradiance. The power per unit area per unit wavelength ($\mathrm{W\,m^{-2}\,nm^{-1}}$) incident on a flat surface, weighted by the cosine of the relative angle between the normal to the place and the direction of the beam (zenith angle). The irradiance can be calculated by integrating the radiance over a hemisphere (2π radiants) and applying the cosine law.

After integration over the full path in the medium, the BLB law can be written as

$$I(\lambda) = I_0(\lambda)\,\mathrm{e}^{-\int \sigma(\lambda)n\,\mathrm{d}s} \tag{3.3}$$

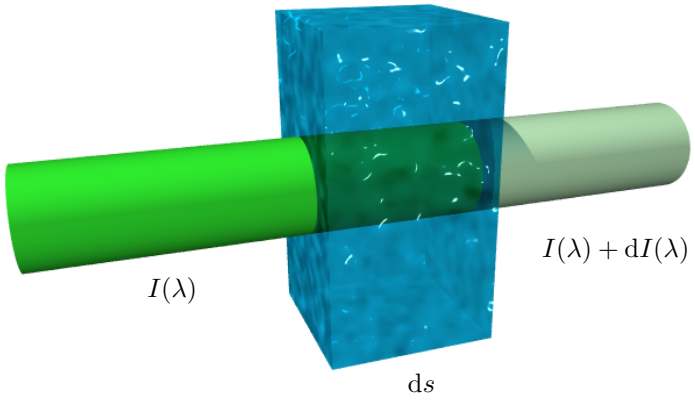

Figure 3.1: A parallel monochromatic beam of light traversing - from the left to the right - a thin layer of absorptive medium, thus decreasing its intensity. The medium is characterised by a cross section $\sigma(\lambda)$, number density n and total thickness $\mathrm{d}s$.

where $I_0(\lambda)$ is the initial intensity of light before any extinction process occurs. The quantity in the exponent is called *optical depth*

$$\tau(\lambda) \equiv \int \sigma(\lambda) n \, \mathrm{d}s \tag{3.4}$$

The integral formulation clearly shows that, if $I_0(\lambda)$ and the path are known and once the cross section of the substance has been determined (e.g. by laboratory experiments), the density of the medium can be easily determined by measuring the resulting intensity at the exit interface of the medium. The BLB law will be used in the text to retrieve the nitrogen dioxide (NO_2) amount from the direct sun (ds) measurements, namely when the Brewer spectrophotometer is directly pointing to the sun.

An alternative formulation makes use of the Slant Column Density (SCD), S, instead of the number density, n. By dividing and multiplying by the Loschmidt constant, n_0, introduced in Eq. 2.1,

$$\frac{\mathrm{d}I(\lambda)}{I(\lambda)} = -\sigma(\lambda) n_0 \frac{n \, \mathrm{d}s}{n_0} \tag{3.5}$$

$$= -\alpha(\lambda) \, \mathrm{d}S \tag{3.6}$$

$\alpha(\lambda)$ has the dimensions of an inverse length (L^{-1}) and is defined as the *extinction* (*absorption* or *scattering*) *coefficient*. A 10^5 factor may be introduced both in the coefficient and in the SCD to express the slant column density in Dobson Units (DU) instead of metres.

Explanation of the BLB law. Even though some theoretical demonstrations exist, based for instance on the Boltzmann equation (Mayer et al., 2012) or on Maxwell's equations (Wendisch and Yang, 2012), an intuitive and mostly phenomenological explanation of the BLB law can be given with reference to Fig. 3.1. The medium may be conceived to be composed by single independently-absorbing particles, whose power in extinguishing the radiation can be mathematically

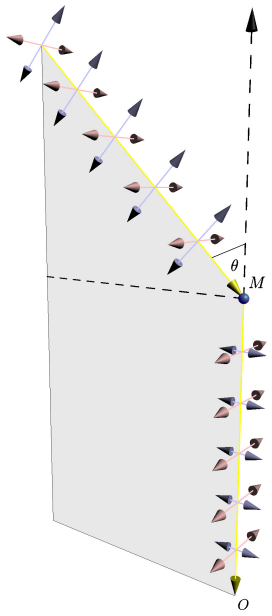

Figure 3.2: An unpolarised ray of light impinging from a zenith angle θ on a scattering molecule M and heading towards an observer O. The pink and blue arrows represents the components of the electric field of the electromagnetic wave in the plane perpendicular to the propagating direction. It is worth noting that the component of the emerging beam parallel to the scattering plane, grey-coloured in the figure, depends on the scattering angle and is generally lower than the perpendicular component.

described using an effective surface σ (cross section). The probability that a photon bumps into a particle is defined by the ratio between the total number of particles in the medium, $\mathrm{d}N$, times their cross section (resulting in the total effective extinction surface of the medium) and the area hit by the light beam, Σ. This is also equal to the (negative) relative variation of the beam intensity, $\frac{\mathrm{d}I(\lambda)}{I(\lambda)}$, i.e.

$$-\frac{\mathrm{d}I(\lambda)}{I(\lambda)} = \frac{\sigma(\lambda)\,\mathrm{d}N}{\Sigma} \tag{3.7}$$

Now, the total particle number is the product of volume ($\mathrm{d}V = \Sigma\,\mathrm{d}s$, where $\mathrm{d}s$ is the thickness of the absorbing layer) and number density. Thus,

$$-\frac{\mathrm{d}I(\lambda)}{I(\lambda)} = \frac{\sigma(\lambda)n\Sigma\,\mathrm{d}s}{\Sigma} \tag{3.8}$$

After simplifying, Eq. 3.2 is obtained. ■

3.1.2 Scattering regimes

The size parameter, defined in Eq. 3.1, identifies different scattering regimes with distinct properties (Wendisch and Yang, 2012):

$\chi \lesssim 0.1$ When the wavelength of the incident radiation is much larger than the size of the interfering particle, e.g. in the case of visible light and air molecules, the scattering behaviour is well described using the theory first developed by the Nobel prize Lord Rayleigh (1899). Modern calculations of the Rayleigh scattering cross section report (Penndorf, 1957; Bodhaine et al., 1999)

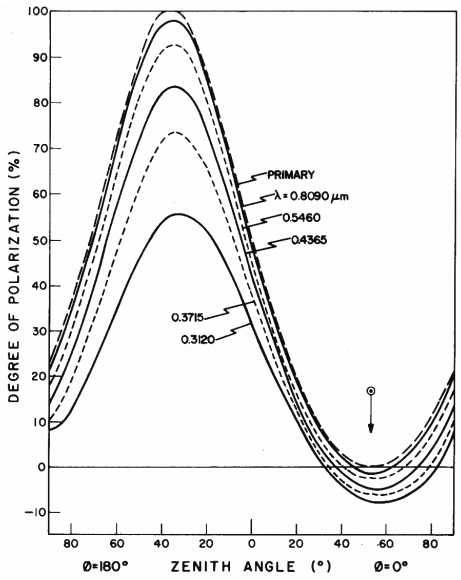

Figure 3.3: Degree of polarisation as a function of angle in the plane of the sun's vertical for a plane-parallel Rayleigh atmosphere at five different wavelengths (expressed in μm) for a solar zenith angle of 53.1° (Coulson, 1988).

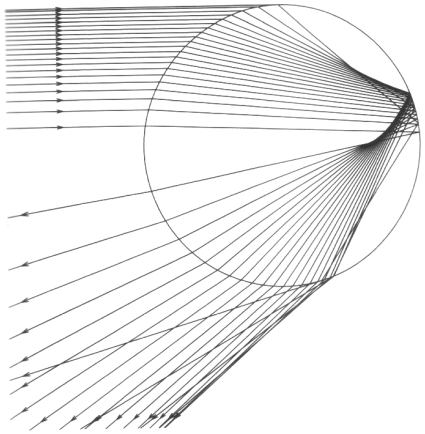

Figure 3.4: Illustration of the mechanism of the primary (first-order) rainbow, using simple geometric optics (Wendisch and Yang, 2012).

$$\sigma(\lambda) = \frac{24\pi^3(\widetilde{n}_a^2 - 1)^2}{\lambda^4 M^2(\widetilde{n}_a^2 + 2)^2} \left(\frac{6 + 3\rho^\star}{6 - 7\rho^\star}\right) \tag{3.9}$$

where $\widetilde{n}_a$ is the refractive index of air, M the molecular density and $\rho^\star$ the depolarisation factor, which describes the effect of molecular anisotropy. The most prominent feature is the dependency of the cross section on λ^{-4}, which enhances scattering at very low wavelengths and explains, for example, the blue colour of the sky and, at twilight, the reddening of the sun.

An additional interesting property of the Rayleigh scattering is the polarisation of light. Figure 3.2 shows an unpolarised ray impinging on a scattering particle. The emerging light is partially polarised, according to the Rayleigh theory, since the observer is only able to "see" a projection of the varying electric/magnetic field of the scattered radiation, which in turn cannot lie in the direction of the incident beam. Thus, the component parallel to the scattering plane (i.e. the plane including the source, the scattering particle and the observer) depends on the scattering angle and is generally lower than the perpendicular component. This is the case of zenith sky (zs) measurements at twilight: the sun is at about 90° to the zenith, while the Brewer spectrophotometer is looking upwards, and the perpendicular component is far larger than the parallel one. The dependency of the degree of polarisation on the scattering angle is represented in Fig. 3.3 for a pure Rayleigh atmosphere. Aerosol and clouds may introduce some depolarisation in the zenith radiation, which allows us to infer their properties by measuring the polarisation of the sky (Chap. 5);

$\chi \gtrsim 50$ When the size of the particle is much larger than the wavelength of the incident radiation, e.g. when visible light impinges on a raindrop (Fig. 3.4), the problem can be solved with the basic principles of geometric optics in terms of Snel's law, the Fresnel formulas and the Fraunhofer diffraction theory. Rainbows and halos, some of the most spectacular optical phenomena in the atmosphere, can be successfully explained in the geometric-optics regime;

$0.1 \lesssim \chi \lesssim 50$ The intermediate case, regarding for instance transmission of light in clouds and aerosol, is the most complex, since the complete electromagnetic theory is required to describe the scattering regime. The Lorenz-Mie-Debye formulation solves the Maxwell's equations for spherical particles, providing complex results which are treated elsewhere (van de Hulst, 1957). The Mie theory predicts much sharper scattering peaks in the forward direction and a less pronounced spectral dependency compared to the Rayleigh regime. Notably, the Ångström parameterisation approximates with a sufficient accuracy the aerosol optical depth (Ångström, 1929):

$$\tau_{aer}(\lambda) = \beta \cdot \lambda^{-\alpha} \tag{3.10}$$

where β is proportional to the amount of aerosol in the atmosphere, while the α exponent is linked to the aerosol size and is usually about 1.3 ± 0.5 (Iqbal, 1983). This relationship will be extensively used in the Brewer algorithm, setting $\alpha = 1$, which is an intermediate value representative of most natural atmospheres.

It is worth noting that both the Rayleigh and the geometrical regimes are included as borderline cases in the more general Mie theory when spherical particles are considered.

3.1.3 Rotational Raman scattering

Whereas the previously described scattering regimes are elastic process, since frequency - and thus energy - of the scattered photons is not changed, rotational Raman scattering is inelastic and the energy of scattered photons is slightly different from the energy of the incident photons. Indeed, the molecules can absorb (or remit) energy, resulting in a (anti-)Stoke line on the longer (shorter) wavelength side of the spectrum relative to the initial wavelength. In the atmosphere and in the

visible and UV region, Raman scattering is caused by interactions with diatomic molecules, such as N_2 and O_2, and rotational energy transitions.

The Raman effect is frequently associated to another interesting feature: the Ring effect (Grainger and Ring, 1962). Indeed, the solar spectrum is highly structured due to absorption lines by several elements in the solar atmosphere, called Fraunhofer lines. Rotational Raman scattering is a major contributor to the broadening and weakening, also known as "filling-in", of the Fraunhofer lines in the sky spectra relative to the direct sunlight (Brinkmann, 1968), especially at large solar zenith angles.

Furthermore, the Raman effect can also act on the highly structured absorption spectra of atmospheric molecules, such as NO_2. This phenomenon is frequently called "molecular Ring effect" to differentiate it from the solar Ring effect.

The magnitude of the Ring effect is negligible on an absolute scale, but since the filling-in slightly changes the shape of the solar spectrum measured at ground, it can interfere with retrievals of minor constituents, such as NO_2, and give largely erroneous molecular amounts.

3.1.4 The Radiative Transfer Equation (RTE) for the diffuse component

The BLB law efficiently describes the extinction of the direct component of the sunlight in the atmosphere, which can be practically measured by pointing a collimated instrument to the sun. However, scattering by gas molecules and aerosols in the atmosphere also contributes to the diffuse component, which makes the sky bright. The physical laws describing the radiative transfer of diffuse light are more complex compared to the BLB law, since both single and multiple scattering must be taken into account. Therefore, I'll show hereafter only the resulting equation, in the case of a plane-parallel atmosphere without taking polarisation into account and dropping the wavelength dependency for ease of presentation (Mayer et al., 2012):

$$\begin{aligned}\cos(\theta)\,\frac{\mathrm{d}I(z,\Omega)}{\mathrm{d}\tau} = &- I(z,\Omega) + \\ &+ \frac{\tilde{\omega}(z)}{4\pi}\{\pi I_0 \mathcal{P}(\Omega,\Omega_0)\,\mathrm{e}^{-\frac{\tau}{\cos\theta_0}} + \\ &+ \int_0^{2\pi}\mathrm{d}\phi' \int_{-1}^{+1}\mathrm{d}(\cos\theta')\;\mathcal{P}(\Omega;\Omega')\,I(z;\Omega')\}\end{aligned} \tag{3.11}$$

where θ and θ_0 are the zenith angles of the diffuse and direct component, respectively, I the diffuse radiance, I_0 the extraterrestrial component, z the vertical coordinate (altitude above the observation point), τ the optical depth as defined in Eq. 3.4, Ω and Ω_0 the directions of the diffuse and direct beam, $\tilde{\omega}$ the single scattering albedo (i.e. the ratio between the diffused energy and the total extinguished energy when light collides with a particle) and $\mathcal{P}$ the phase function, describing the redistribution of light in all directions after a scattering event. The cosine factor takes into account the tilt angle of the light rays in a parallel atmosphere, which will be clearer in the next section.

The first term on the right side represents a "BLB-like" law for the diffuse light which has already undergone scattering, the second term takes into account the single scattering and the last term describes the multiple scattering component.

Unfortunately, the above integro-differential equation cannot be analytically solved. Several algorithms based on numerical techniques were developed in the last century and are now implemented in state-of-the-art radiative models, which also include the numerical values of the physical quantities listed in Eq. 3.11 (for instance, density profiles of many atmospheric constituents and properties of a number of different kinds of atmospheres).

The above equation, slightly modified to account for the atmosphere sphericity and the polarisation of light, can be used to simulate the zs measurements, when the Brewer spectrophotometer points in the zenith direction and measures the diffuse radiance.

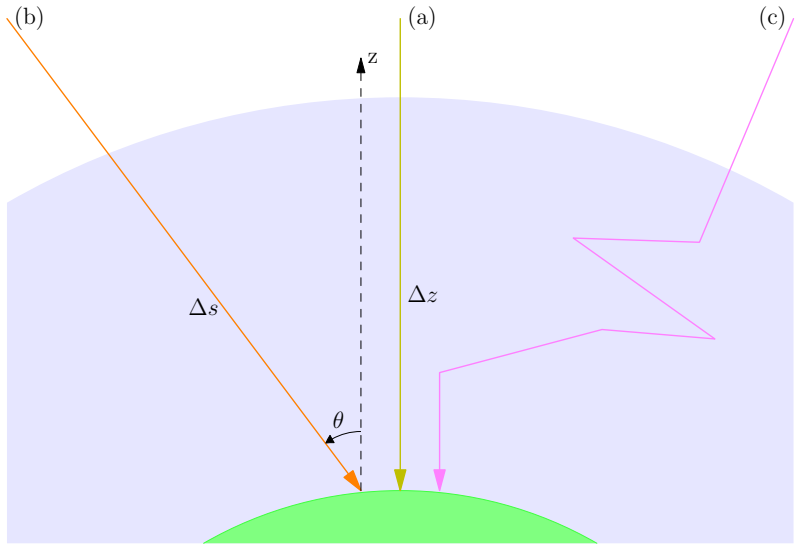

Figure 3.5: A sketch to represent the Air Mass Factor (AMF) concept. Ray (a) enters the atmosphere along the vertical, z, while the path of ray (b) is enhanced by a factor $\Delta s/\Delta z$, which depends on the zenith angle θ. This is the case of ds observations. Ray (c) undergoes scattering and finally reaches the ground along the zenith direction. The enhancement factor is now more complex to calculate and numerical radiative models may be of help. This case represents a zs observation.

3.1.5 Airmass factor and observation geometries

Until now, the BLB law, for example in Eq. 3.3, was expressed as a function of the path s. However, it is often more convenient to specify the dependency on the vertical coordinate z. This may be very useful, for instance, since the atmospheric properties essentially depend on altitude. Also, it is preferable to integrate the total concentration of a gas over the vertical, instead of the propagating direction (as is, for example, the SCD S in Eq. 3.6), thus making it independent of the observation geometry.

Therefore, it may be of great use to define the AMF as the derivative of the path with respect to altitude, namely

$$\mu(z) \equiv \frac{\mathrm{d}s}{\mathrm{d}z} \tag{3.12}$$

Generally, μ depends on altitude because a sun ray may change its direction before reaching the ground due, for example, to scattering or refraction. Also, the AMF depends on wavelength, as radiation of different wavelengths may undergo different radiative processes.

Recalling the definition of the SCD, S, in Eq. 3.6, we can find a link between the differential SCD and the differential Vertical Column Density (VCD), $\mathrm{d}X$:

$$\mathrm{d}S = \mu(z)\ \mathrm{d}X \tag{3.13}$$

An integral AMF can then be defined as the ratio of the SCD and the VCD

$$\mu \equiv \frac{S}{X} = \frac{\int n(s)\,\mathrm{d}s}{\int n(z)\,\mathrm{d}z} \tag{3.14}$$

which clearly shows that μ also depends on the concentration vertical profile of the given constituent.

For a plane-parallel atmosphere, the AMF for the direct component is simply the secant of the zenith angle:

$$\mu_{pp} = \frac{1}{\cos(\theta)} \tag{3.15}$$

as in Eq. 3.11.

The standard Brewer algorithm assumes that a certain absorber resides in a thin layer at altitude h in the atmosphere. For a spherical atmosphere, the AMF for the direct beam is thus approximated by the following formula

$$\mu = \sec\left[\arcsin\left(k \cdot \sin\theta\right)\right] \tag{3.16}$$

where

$$k = \frac{R_E}{R_E + h} \tag{3.17}$$

and R_E is the Earth's radius. The formula is used in the standard Brewer processing algorithm to calculate the AMF of the Rayleigh scattering (using $h = 5$ km), ozone and nitrogen dioxide ($h = 22$ km). A derivation of the formula may be found in Savastiouk (2005).

The larger is the zenith angle, the longer is the path of light in the atmosphere and the higher is the AMF, as in Fig. 3.5. As a consequence, measurements at large AMFs, although characterised by fewer photons reaching the ground (which produces higher instrumental noise), are more sensitive to the gas absorption along the path. Thus, a compromise between the intensity of the signal (instrumental noise) and the benefits of a larger AMF must be found.

Also, the path enhancement is the reason why zs measurements are done, even though they are far more problematic to analyse due to the complex path followed by the radiation: the path, especially at twilight, is greatly enhanced by the atmosphere's scattering and the radiation reaching the ground from the sky "carries more information" about the concentration of a specific constituent compared to a ds measurement.

Furthermore, a fundamental difference between ds and zs measurements relates to the various altitudes probed by each technique. While ds measurements are more sensitive to absorption in the troposphere, where the bulk of the air mass resides, the zs technique is more affected by absorption in the stratosphere since most of the path traced by the zenith scattered photons is located in the highest layers (Solomon et al., 1987). The difference may be even exploited to partition between the stratospheric and tropospheric column density of a trace gas (Schofield et al., 2004).

Some recent techniques, as the Multi AXis Differential Optical Absorption Spectroscopy (MAX-DOAS), take advantage of the sensitivity of the probed altitude to the observation geometry to retrieve the concentration profiles of specific constituents (Hönninger et al., 2004; Vlemmix et al., 2011).

3.2 Absorption spectroscopy

So many factors affect the intensity of solar radiation in the atmosphere that it would seem impossible to separate the various effects and efficiently retrieve the concentration of a specific constituent using whatever kind of remote sensing technique. Yet, every factor influences the spectra of light in a slightly different way, as seen in Sect. 3.1, revealing its own spectral "signature". If measurements of solar irradiance at several wavelengths are taken into account and the spectral behaviour of the involved processes is known, then absorption spectroscopy becomes a reality. The NO_2 cross section (Sect. 3.1.1) measured in a laboratory, and further used in the present work, is shown as an example in Fig. 3.6.

Pioneering works using the absorption spectroscopy were done during the last century. The first study using solar absorption spectroscopy to investigate the concentration of NO_2 in the atmosphere was performed by Brewer and McElroy (1973). As already stated in Sect. 2.2, the authors discovered that the concentration of nitrogen dioxide peaks in two distinct layers at different altitudes (the stratosphere and at the surface) and correctly ascribed to this feature the differences they found between zs and ds measurements (see Eq. 3.14).

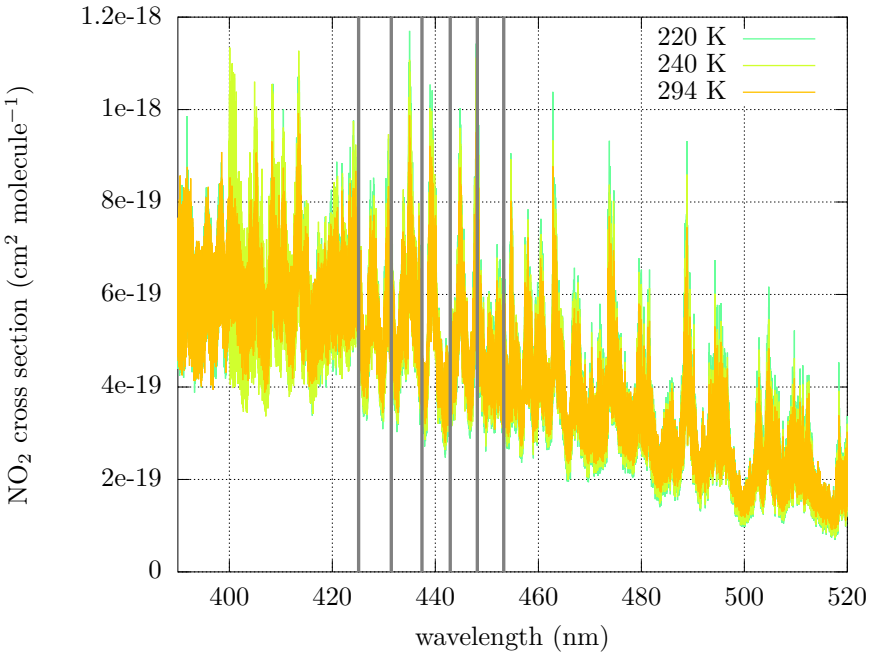

Figure 3.6: The NO_2 absorption cross section at different temperatures, as measured by Vandaele et al. (2002). The grey lines represents the wavelengths used by the Brewer spectrophotometer #066 to measure nitrogen dioxide in the atmosphere (default micrometer setting).

Noxon (1975) employed the zs technique using ground-based measurements at 3000 m a.s.l. The author proved that the maximum sensitivity of zs measurements is found at 15–30 km altitude. He also divided the recorded spectra by a common reference spectrum to remove the Fraunhofer structure, laying the groundwork to the modern Differential Optical Absorption Spectroscopy (DOAS). Furthermore, the author detected an absorption feature by water vapour at 442.5 nm.

Pommereau (1982) and Pommereau and Goutail (1988) used absorption spectroscopy with zs measurements by means of a SAOZ instrument. Agreement was found with chemical models assuming that the NO_2 layer is centered at about 30 km altitude.

Several other fundamental studies to infer the concentration of NO_2 in the atmosphere from the ground were accomplished based on the spectral features of this gas (McKenzie and Johnston, 1982; Solomon et al., 1987). A comprehensive review of the main works can be found in Platt and Stutz (2008).

Spaceborne instruments. Not only ground-based instruments, but also satellite radiometers use absorption spectroscopy. The latter ones measure the backscattered light of the sun from the Earth's atmosphere and ground or the light transmitted through the atmosphere.

These instruments - e.g. SCanning Imaging Absorption spectroMeter for Atmospheric CHartographY (SCIAMACHY), Ozone Monitoring Instrument (OMI) and Global Ozone Monitoring Experiment 2 (GOME-2) - offer innovative and extraordinary opportunities to study the chemical composition of the Earth's atmosphere. Among other merits, spatial coverage is the main asset: spaceborne instruments allow to probe the entire globe using only one instrument.

On the other hand, the frequency of the measurements, especially for polar satellites, is very poor and the lower spatial resolution does not allow to resolve the variability typical of NO_2 and may lead to inconsistencies when comparing

Figure 3.7: Brewer #066 on the terrace of the ARPA Valle d'Aosta building. The main components of the Brewer system may be seen: the spectrometer case (upper part), the tracker (middle) and the tripod.

different instruments (Hilboll et al., 2013). Also, the AMF calculation using radiative transfer models is a major source of uncertainty in satellite estimates, especially over polluted or cloudy areas and complex topography (Boersma, 2004; Leitao et al., 2010).

3.3 The Brewer spectrophotometer

My Ph. D. work focuses on the MKIV Brewer spectrophotometer instrument, represented in Fig. 3.7. A short history of the Brewer spectrophotometer and a detailed explanation of its working principles will be provided in the following sections.

3.3.1 History of the Brewer spectrophotometer

The Brewer spectrophotometer was invented as an automated Dobson spectrophotometer, the standard ground-based, manual instrument employed since 1927 - and still used today all over the world - to accurately measure the ozone column density in the atmosphere using the absorption spectroscopy of solar UV light. In the late 1960's, when the Dobson was no longer available commercially, Prof. Alan Brewer and Dr. David Wardle at the University of Toronto initiated the development of a new ozone spectrophotometer in the hope that it would prove to be a suitable replacement for the Dobson (Brewer, 1973). Through the seventies, scientists at the Atmospheric Environment Service of Environment Canada, Dr. Jim Kerr, Dr. Thomas McElroy along with Dr. Wardle continued the research and development and by early 1980's a fully automated Brewer Ozone Spectrophotometer (or "Brewer", for short) was developed (Kerr et al., 1983, 1985). Since the MKII (an acronym for "mark 2") model became commercially-available, over 200 Brewers have

been manufactured and are now measuring the ozone layer - as well as sulphur dioxide and UV radiation - worldwide (Kipp & Zonen, 2012). These Brewers are in operation in more than 40 countries, ranging from the Arctic via the equator to the Antarctic. For these reasons, the three inventors received the United Nations Environment Programme's Montreal Protocol Innovators Award during the 20th anniversary celebrations of the Montreal Protocol in 2007, recognising that "the award winners scientific breakthroughs had a significant impact on the way that Canada, and the world, understands the issue of ozone depletion".

The first MKIV Brewer was built in 1985 (Kerr, 1989) and since then measurements provided by more than 60 MKIV Brewers have been sent to the World Ozone and Ultraviolet Data Center (WOUDC) (WOUDC, 2013). MKIV's have the same measurement capabilities as the MKII instrument as well as the ability to measure column NO_2 in the visible range. They are sometimes referred to as "dual Brewers" because they have two separate modes of operation: an ozone measurement mode and an NO_2 measurement mode. MKII and MKIV are referred as "single Brewers" since they have a single monochromator. As a consequence, straylight inside the instrument can affect the measurement, especially when the sun is low on the horizon (Fioletov et al., 2000).

Therefore, some years later, in 1992, a novel model (MKIII) equipped with a double monochromator was introduced to allow very accurate measurements of the ozone density and UV even at very large SCD, up to 1500 DU (Environment Canada, 2008). Also, the new design removes the instrument temperature dependence typical of other Brewers. MKIII's make the same type of measurements as MKII's and are sometimes referred to as "double Brewers" because they have a double monochromator.

Finally, MKV Brewers, manufactured since 1991, are equipped with an order filter that allows for column ozone measurements to be made in the red portion of the visible spectrum (Chappuis ozone absorption band), which is the reason why they are sometimes referred to as "red Brewers". MKV's are suited to the polar regions where very large zenith angles prevail for much of the year, the UV radiation available for ozone measurements is decreased by the effect of Rayleigh scattering and measurements are degraded by straylight.

The Brewer spectrophotometer has proven to be an exceptionally flexible instrument, able to perform several kinds of measurements with different techniques and maintained by a very lively scientific community.

3.3.2 System description and diagnostic tests

The complete Brewer system (Fig. 3.7) is composed by a spectrometer, which is housed in a weatherproof enclosure and constitutes the fundamental component of the instrument, and a tracker, which allows the instrument to turn and point to the sun. Both parts are remotely controlled by a computer via a serial cable and installed on a tripod, fixable to the ground.

A schematic view of the spectrometer is given in Fig. 3.8. Sunlight can enter the instrument through a quartz dome and a teflon diffuser, used to perform global UV irradiance scans, or an inclined quartz window and a collimator, employed when direct sun or zenith sky measurements are required. A quartz-halogen lamp (standard lamp) and a mercury discharge lamp are installed beneath the input optics and provide well-regulated light sources used to check the stability and the wavelength alignment, respectively, of the instrument (Sect. 3.3.3). A right-angle prism, rotated by a microprocessor-controlled zenith stepper motor through a 270° rotation range, directs the incoming light from the sun, the sky or the lamps onto the optical axis of the instrument.

The light subsequently passes through the foreoptics, made up by a set of lenses to adequately focus the beam, an iris diaphragm and two filterwheels.

The iris diaphragm controls the field of view of the instrument. When it is closed, about three solar diameters of skylight around the sun pass through the aperture into the spectrometer. When the iris is open, about 10° of skylight enters the spectrometer.

Two filterwheels, each one with six 25.4 mm diameter holes, are mounted on bronze bearings. The first wheel contains six filters used by the different observation techniques: an open hole (e.g. for moon and UV measurements), a ground G1-quartz diffuser disk (e.g. for ozone ds measurements or lamp tests), a second ground quartz with a neutral density filter (used for NO_2 measurements),

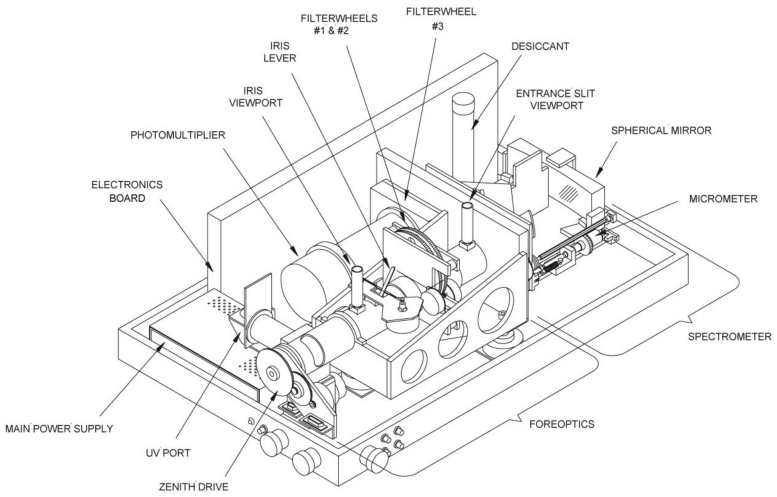

Figure 3.8: Schematic view of the spectrometer with cover removed (Kipp & Zonen, 2007).

a polariser film with axis perpendicular to the entrance slit (for zs and Umkehr measurements), a second film polariser (axis parallel to entrance slit), and an opaque blank for dark counting. The second filterwheel is employed to adjust the light intensity entering the system to guarantee that the detector is working in its linear regime. Neutral density filters with attenuations of 0, 0.5, 1, 1.5, 2, 2.5 decades are mounted on it.

Polarised skylight. Use of polarising filters when measuring zenith light has a twofold advantage. First, the Brewer spectrophotometer suffers from internal polarisation (Cede et al., 2006b), which makes it sensitive to the degree of polarisation of light entering the instrument. Moreover, zs measurements has been historically performed with reference to the polarisation parallel to the scattering plane (Brewer and McElroy, 1973). Indeed, that component is essentially due to the multiple scattering and all skies, both clear and cloudy, appear as thick clouds. The sensitivity to clouds is thus greatly reduced.

Light entering the monochromator through a vertical slit is reflected on a spherical mirror with radius 324 mm and aluminised reflecting surface, dispersed into a high-quality spectrum by a diffraction grating and reflected again. The system is a modified Ebert-type (Fastie, 1952) with focal length 16 cm and aperture ratio f/6. The holographic plane diffraction grating installed in MKIV Brewers has 1200 lines mm^{-1} and is used in the third order in the ultraviolet when measuring ozone ("`o3` mode") and in the second order in the visible when measuring nitrogen dioxide ("`n2` mode"). Polychromatic light emerging from the grating is scattered at different angles, following the grating equation:

$$d\,(\sin\theta_i + \sin\theta_m) = m\lambda \tag{3.18}$$

where d is the distance between the grating lines, θ_i is the incidence angle relative to the grating normal, θ_m is the diffraction angle of the maximum at the mth-order of diffraction and λ is the considered wavelength. It is easy to notice that the emerging wavelengths when the diffraction grating is used at the second order (NO_2 measurements) are scaled by $\frac{3}{2}$ relative to the third order wavelengths.

The grating is rotated by a high-precision stepper motor which drives a micrometer acting on a lever arm. One motor step corresponds to a change of 0.006 nm in the wavelength projected on the exit slit plane in the UV region and to 0.009 nm in the visible. The range of wavelengths

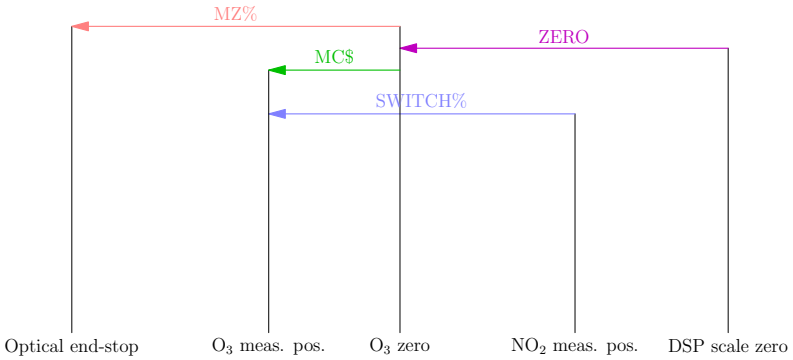

Figure 3.9: The most used positions of the micrometer and their respective `GWBASIC` names in the Brewer operating software. From left to right: the optical end-stop which limits the micrometer, the ozone measuring position (determined by the SC test), the zero of the ozone scale (adjusted with the HG test), the NO_2 measuring position (usually, a factory setting) and the zero of the UV and dispersion scale.

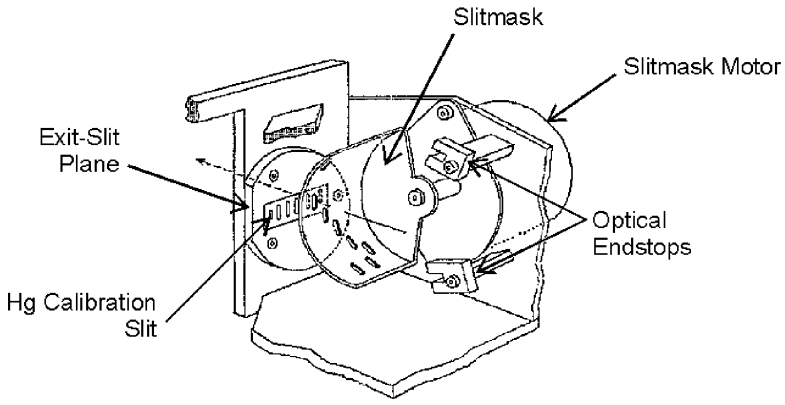

Figure 3.10: The slit mask assembly (Kipp & Zonen, 2007).

measurable with MKIV Brewers, without installing an additional extended arm (which would turn them in the so-called "MKIV-e" Brewers), is about 280–330 nm in the UV and 420–500 in the visible. A scheme of the relevant micrometer positions is given in Fig. 3.9.

A correction lens with convex-cylindrical and concave-spherical surfaces reduces the optical aberrations typical of a modified Ebert-type system (Johnston et al., 2000).

At the exit of the monochromator a slotted cylindrical mask (Fig. 3.10) exposes only one slit at a time. The mask is positioned by a stepped motor in one of eight positions. The first slit is normally used for the HG test, described in Sect. 3.3.3. The second position blocks light from all slits so that a dark count measurement can be made. Then, the next five positions are routinely used to measure the irradiance at different wavelengths at almost the same time. Finally, the eighth mask position exposes two of the exit slits so that the dead time of the photon counting system may be determined. In a ds or zs measurement, the slit mask is rotated many times (usually 20) since a large number of collected photons allows a better Signal-to-Noise Ratio (SNR).

On MKIV models, light emerging from the monochromator passes thought a third filter wheel, which contains a UG-11 and $NiSO_4$ filter combination to filter radiation above 325 nm (ozone mode) and a BG-12 filter which blocks UV radiation (nitrogen dioxide mode) to assure that light from other orders is rejected.

The light beam is finally transformed in an electric pulse by a low-noise PhotoMultiplier Tube (PMT). The photon pulses are amplified, discriminated and divided by 4, then transmitted to a

counter. The resulting photon count is registered in one of six wavelength channels.

Dead time. Every photon counting system exhibit a characteristic called deadtime (Daniel and Fessler, 2000). If two pulses overlap within the "dead time", one single distorted pulse is measured. Depending on the system, one or both arrivals will be lost. In a paralysable system, each photon arrival, whether recorded or not, produces a dead time of a certain length. In a non-paralysable system, only recorded photons produce a dead time.

Some mathematical models may be developed to correct for the dead time using Poisson statistics.

The spectrometer system also includes the electronics necessary to run the Brewer: a main power supply, the electronics boards, an I/O interface, a photon counter, a real-time clock and calendar, an analog-to-digital 10-bit converter for monitoring instruments voltages, currents, temperature and moisture, a pulse amplifier, a lamp control board and a high voltage control module.

The Brewer spectrophotometer contains its own 8051-based microprocessor, which controls all internal instrument operation. It is programmed to accept commands from an external computer, execute the commands and return results. The software was originally written in `GWBASIC` and, since the source code is available (`GWBASIC` is an interpreter), it is kept up to date by the community. It consists of a main program (`main.asc`) and several external routines, which can be called by typing a two- or three-letter code (e.g. `hg`, `sl`, `ds`, etc.) in the interface or in an automated schedule. Therefore, the software can be easily expanded by simply writing new routines, which I extensively did during my work.

Data are saved in two different kinds of files. "B-files" include the most complete set of data useful for the post-processing, while "D-files" are written in a human-readable form.

3.3.3 Diagnostic tests

Thanks to a series of diagnostic tests, which should be included in the schedule of the measurements, the Brewer can guarantee the highest accuracy and operate for long periods of time without the need of a specialised operator on site. Some tests will be listed and explained below.

A first series of tests is needed to assure the correct pointing of the Brewer to the sun and the characterisation of the instrumental field of view.

SR test. The SR test is invoked to calculate the number of steps required by the tracker motor to accomplish a complete revolution. It is necessary to assure that the tracker is working properly and the instrument is correctly pointing to the sun;

SI test. An ephemeris algorithm, implemented in the Brewer operating software, points the Brewer to the sun based on the given geographical coordinates (latitude and longitude) and the time of measurement. Additional offsets, both on the zenith and on the azimuth plane, may be introduced to correct slight misalignments. The sighting test checks whether the Brewer is correctly aligned and the sun is imaged in the center of the optical axis of the instrument. The test needs the presence of an operator, looking through a viewport and adjusting the offsets if necessary;

FV test. The field of view test, unlike the sighting test, does not require the presence of an operator to check the correct alignment of the instrument to the sun. Irradiance from the sun and the solar aureole - by slightly offsetting the zenith and azimuth Brewer pointing direction relative to the sun - is recorded and the user can check whether the maximum irradiance corresponds to the sun. Since it uses the sun as a source, the test needs to be performed when the sun is unobscured by clouds or, at least, clouds are far from the sun aureole.

Other tests take advantage of the two lamps installed inside the Brewer to check the radiometric and wavelength stability of the instrument.

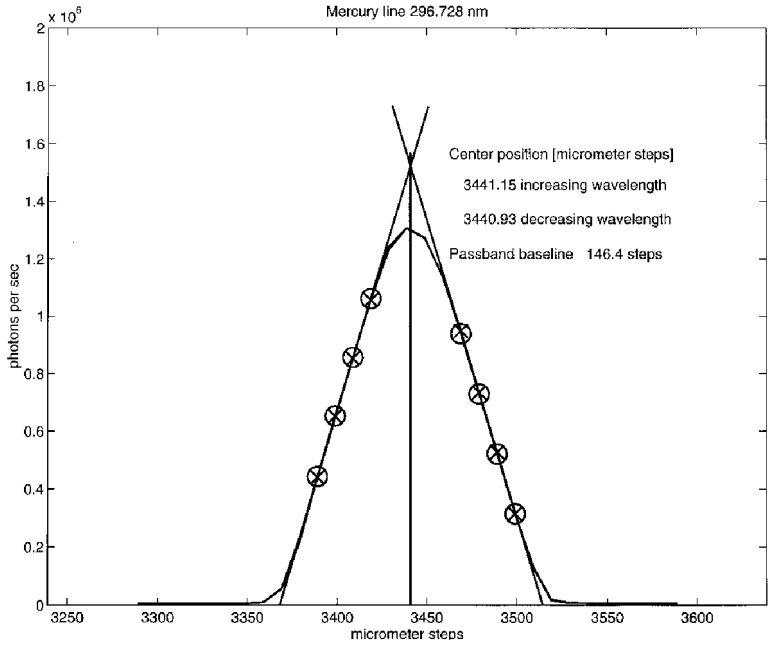

Figure 3.11: Example of a 296.73-nm mercury line scan as well as the calculated centre position (Gröbner et al., 1998).

SL test. When the standard lamp test is running, an internal quartz-halogen lamp (20 W and 1.5 A, stable to within 0.5%) is turned on. The zenith prism is rotated downward to the lamps and a complete set of ozone, sulphur dioxide or nitrogen dioxide measurements is performed using the internal light source instead of the sun. A value, corresponding to a fictitious column density and often called R_6, R_5 or F-ratio (depending on whether the ozone, sulphur dioxide or nitrogen dioxide processing algorithm is applied), is obtained after processing. Slow variations of the SL test results with time may be representative of a change in the relative spectral (but not absolute, because of the way the retrieval algorithm works) sensitivity of the Brewer and may be even used to correct the final value of the solar measurements;

HG test. The wavelength alignment of the Brewer is an essential requirement for accurate measurements. However, spectral shifts occur in the spectrometer as the instrument's temperature changes. To check whether the diffraction grating in the monochromator is correctly positioned, the mercury lamp is switched on and an emission line at a well-known wavelength (either 302.15 or 296.73 nm, depending on settings) is scanned and the nominal wavelength is compared to the position of the line peak (Fig. 3.11). Corrections to the micrometer position are made and, if the required adjustment is greater than 2 steps, then the scan is repeated.

The following tests are also used to characterise the wavelength scale and to chose the appropriate positioning of the micrometer.

DSP test. The dispersion test is essential to obtain the relation between the step number of the micrometer motor and the wavelength projected at each exit slit. Several emission lines produced by some discharge lamps with different gases (e.g. mercury, cadmium, zinc, indium, neon, etc.), are scanned through each slit and their peaks are found and regressed against the nominal wavelengths of the lines. A second-order polynomial is usually fitted and the (3×6) coefficients are saved as the "dispersion constants". Attempts have been made to improve the dispersion approximation by introducing a more complex, but physically-based, formula (Gröbner et al., 1998), which I used in my work as explained in the next chapter.

The dispersion test has an additional purpose: it can be used to determine the resolution of each slit (and its dependence on the micrometer step). This quantity must be known to calculate the "effective" absorption coefficients used by the algorithm, namely the convolution of the absorption coefficients measured in a laboratory and the instrumental slit functions;

SC test. After the dispersion coefficients are found, the "sun scan" test fine-tunes the position of the micrometer that minimises the sensitivity of ozone calculations to small changes in the angle of the grating. A series of ds measurements are taken at several micrometer steps and the total ozone column is calculated and plotted against the micrometer step number. The optimal position of the grating is the point where the derivative of the fitted polynomial is the lowest. Then, since the results of the test depend on the ozone SCD, the sun scan is repeated at different AMFs and an optimal position is found corresponding to the median ozone SCD during the year for the site (usually, 680 DU at midlatitudes).

Several commands are extremely useful to characterise some components of the instrument.

FI test. Nominally, all attenuation filters should be neutral, i.e. they should attenuate irradiance at different wavelengths by the same amount. However, it has been proven that this is not necessarily the case (Savastiouk, 2005) and that small variations with wavelength can introduce large errors in the derived column amounts. The FI test measures the attenuation of the neutral density filters at different wavelengths using the internal standard lamp and calculates the error induced by their non-linearity;

RS test. Since the slit mask normally cycles through all five operating wavelengths at high speed, approximately once per second, it is fundamental to compare the counts recorded in the dynamic ("run") mode with the static ("stop") mode to confirm that the slit mask motor is operating correctly. The "run-stop" test is usually executed once a day and calculates the ratio of irradiances in both modes, which should be as close as possible to unity;

DT test. During a dead time test, the standard lamp is switched on and readings are taken at four slit mask positions corresponding to the shutter, the second and fourth wavelengths separately and together (last slit mask position). Poisson statistics is assumed to describe the photon flux:

$$R = R_0 \, \mathrm{e}^{-R_0 \cdot \tau} \tag{3.19}$$

where R_0 and R are the true and observed count rates, respectively, and τ is the dead time. The dead time is then obtained by inverting the relation through an iterative approach. The test is repeated at both high and moderate light intensity levels by using two different neutral density filter settings to check the linearity of the instrument after the dead time correction;

Finally, the electronics and the overall state of the Brewer can be monitored by the following test.

AP test. The test writes to the standard interface all voltages from the sensors connected to the A/D converter. It is essential to check whether the Brewer is affected by electric problems or temperature/moisture issues.

3.4 Brewer retrieval algorithm for nitrogen dioxide

The retrieval of atmospheric column nitrogen dioxide is a complex task starting from the raw counts registered by the Brewer electronics. The standard algorithm, employed on all MKIV Brewers at present, will be accurately described in the following sections.

3.4.1 Data reduction

Raw photons counts registered by the Brewer electronics at different - normally 5 - slits must be processed following a data reduction scheme prior to being used in the retrieval algorithm. First, the contribution introduced by the system to the measured photocurrent (dark counts) must be subtracted to the signal and the resulting value is divided by the total slit sampling time (Kipp & Zonen, 2007):

$$R_i = 2\,\frac{C_i - C_{dark}}{CY \cdot IT} \tag{3.20}$$

where R_i is the count rate at slit i, C_i and C_{dark} are the raw counts measured at slit i and the dark counts, respectively, CY is the number of slit mask cycles (usually, 20) and IT is the interval-scaling factor, which incorporates slit sampling time and duty cycle. The factor 2 originates from the scaling factor 4 of the counting system (previous section) and the back-and-forth movement of the slit mask for every cycle.

The dead time correction is then applied following Eq. 3.19. The count rates are normalised by computing the base-ten logarithm, then multiplied by 10^4:

$$F_i \equiv 10^4\ \log_{10} R_i \tag{3.21}$$

and a compensation for the Brewer's sensitivity to its internal temperature - mainly due to the $NiSO_4$ filter (Cappellani and Kochler, 1999; Meltzer et al., 2000) and partly to the detector (Weatherhead et al., 2001) - may be applied, if needed, as in the case of ozone measurements. This will be explained in more detail in the next chapter.

The Brewer algorithm accounts for the attenuation value of the neutral density filters by adding a value AF_p, depending on the filter position p, to the logarithm:

$$F_i' = F_i + AF_p \tag{3.22}$$

This procedure is equivalent to multiplying the count rates by the attenuation of the used filter, due to the properties of the logarithm function. It should to be noted, however, that the standard Brewer algorithm only deals with ideal neutral density filters and that the above correction does not take into account the spectral variability of AF_p.

3.4.2 Bouguer-Lambert-Beer law for Brewers

The value obtained from the data reduction is proportional to the solar intensity $I(\lambda_i)$ governed by the BLB law. After integration of Eq. 3.6, we can thus write

$$F_i = F_{0i} - \alpha_i\, S \tag{3.23}$$

where the absorption coefficient should now be scaled by 10^4 and $\log_{10}(\mathrm{e})$ according to Eq. 3.21. In addition, the absorption coefficient must be calculated accounting for the instrument limited resolution. Usually, a simple convolution with the slit function $f_i(\lambda)$, determined during the dispersion test, is applied:

$$\alpha_i \equiv \frac{\int \alpha(\lambda)\, f_i(\lambda)\ \mathrm{d}\lambda}{\int f_i(\lambda)\ \mathrm{d}\lambda} \tag{3.24}$$

More details will be given about the limitations of this approach in the next chapter, when introducing the so-called "I_0 correction".

Many factors influence the solar irradiance at ground. The standard Brewer algorithm for nitrogen dioxide (Kerr, 1989) considers the contribution of five of them:

1. the Rayleigh scattering (Sect. 3.1.2);

2. the nitrogen dioxide absorption;

3. the ozone absorption;

4. the aerosol extinction (Sect. 3.1.2);

5. all spectrally-flat factors, such as the Earth-sun distance or, to a first approximation, the presence clouds.

As a consequence, the general BLB law (Eq. 3.23) can be splitted into several components:

$$\begin{aligned} F_i = & F_{0i} + \\ & - \mu_R \, \beta_{Ri} + \\ & - \mu_{NO_2} \, \alpha_{NO_2 i} \, X_{NO_2} + \\ & - \mu_{O_3} \, \alpha_{O_3 i} \, X_{O_3} + \\ & - \mu_A \, \delta_{Ai} + \\ & - const \end{aligned} \tag{3.25}$$

X represents the VCD of a given species in the atmosphere. The air mass factors, introduced in Eq. 3.14, are indicated with the letter μ followed by a subscript representing their respective species. Indeed, since different constituents may be located at different altitudes in the atmosphere and may have different vertical profiles, the corresponding AMFs can differ. For example, μ_R and μ_A are calculated for a layer of 5 km altitude (Eq. 3.16) in the standard Brewer algorithm, while μ_{NO_2} and μ_{O_3} are obtained assuming that the concentration of their respective absorbers peaks at 22 km altitude.

β_{Ri} is the Rayleigh scattering coefficient, which depends on wavelength, λ_i, and pressure, according to the following equation:

$$\beta_{Ri} = \beta_{R0i} \frac{p}{p_0} \tag{3.26}$$

where p is the atmospheric pressure at ground level and β_{R0i} is the Rayleigh coefficient at a standard pressure $p_0 = 1013$ hPa. The bulk of the Rayleigh scattering may be removed by correcting F_i by the same amount:

$$F_i' = F_i + \mu_R \beta_{R0i} \frac{p}{p_0} \tag{3.27}$$

using the average pressure in the measuring location in a year. The Rayleigh contribution will be then completely removed by the linear combination as explained further below. Moreover, the standard Brewer algorithm for the determination of nitrogen dioxide uses the same Rayleigh coefficients as for the ozone retrieval in the UV range, which in turn are recognised to be obsolete and to introduce an offset in the calculations (Gröbner, personal communication, 2011).

$\alpha_{NO_2 i}$ and $\alpha_{O_3 i}$ are the absorption coefficients for nitrogen dioxide and ozone, respectively. They were originally calculated based on the Johnston and Graham (1976) (NO_2) and the Vigroux (1952) (O_3) cross-sections smoothed to 0.85 nm resolution.

δ_{Ai} is the extinction coefficient for aerosol, obtained from the Ångström law (Eq. 3.10) assuming $\alpha = 1$.

It is worth noting that the above absorption coefficients were originally calculated by Kerr (1989) based on the wavelengths and the slit resolutions of a specific Brewer instrument, but they are used as-is in all Brewers at present.

3.4.3 Determination of nitrogen dioxide column

Not only the nitrogen dioxide column, but the amounts of all five influencing factors listed in the previous section and accounted for in the BLB law are generally unknown and act together on the same range of wavelengths. In order to disentangle their respective contributions, we take

Table 3.1: From left to right: slit numbers, Kerr's Full Width at Half Maximum (FWHM), nominal slit wavelengths, weightings as used in the standard algorithm and NO_2 cross sections (Barton, 2007).

i	FWHM$_i$ (nm)	λ_i (nm)	γ_i	NO_2 cross section (10^{-19} cm^2)
1	0.816	431.42	0.1	6.127
2	0.836	437.34	-0.59	4.749
3	0.868	442.82	0.11	4.260
4	0.858	448.10	1.2	6.610
5	0.848	453.22	-0.82	4.612

advantage of the principles of absorption spectroscopy (Sect. 3.2). Indeed, five measurements corresponding to the slit positions are taken at nearly the same time and five relations similar to Eq. 3.25, the i index running from 1 to 5, can be combined into a system:

$$\begin{cases} F_1 = F_{01} - \mu_R\beta_{R1} - \mu_{NO_2}\alpha_{NO_2 1}X_{NO_2} - \mu_{O_3}\alpha_{O_3 1}X_{O_3} - \mu_A\delta_{A1} - const \\ \vdots \\ F_5 = F_{05} - \mu_R\beta_{R5} - \mu_{NO_2}\alpha_{NO_2 5}X_{NO_2} - \mu_{O_3}\alpha_{O_3 5}X_{O_3} - \mu_A\delta_{A5} - const \end{cases} \tag{3.28}$$

Traditionally, the above system has been solved by linear combination, i.e. by multiplying each equation by a weighting, γ_i, and finally adding the obtained terms. If the weightings are appropriately chosen, all unknown factors except one may be cancelled out. For example, nitrogen dioxide is easily found when the weightings are chosen so that

$$\begin{cases} \sum_{i=1}^{5} \gamma_i \cdot \lambda_i^{-4} \equiv 0 \\ \sum_{i=1}^{5} \gamma_i \cdot \alpha_{O_3 i} \equiv 0 \\ \sum_{i=1}^{5} \gamma_i \cdot \lambda_i^{-1} \equiv 0 \\ \sum_{i=1}^{5} \gamma_i \equiv 0 \end{cases} \tag{3.29}$$

The above conditions remove the contribution of Rayleigh scattering (note the λ^{-4} dependency in Eq. 3.9), ozone absorption, aerosol extinction (Eq. 3.10 assuming $\alpha = 1$) and all factors independent of the wavelength ("*const*"), respectively. The null space of the system has dimension 1, which ensures that infinite solutions exist other than the null vector ($\gamma_1 = 0, \ldots, \gamma_5 = 0$) and allows us to freely normalise the weightings without altering the solution of Eqs. 3.28. A more profound meaning of Eqs. 3.29, making use of linear algebra and geometry, will be given in the next chapter.

The weightings used in the standard algorithm for nitrogen dioxide are listed in Table 3.1.

Therefore,

$$\sum_{i=1}^{5} \gamma_i \cdot F_i = \sum_{i=1}^{5} \gamma_i \cdot F_{0i} - \mu_{NO_2} X_{NO_2} \sum_{i=1}^{5} \gamma_i \cdot \alpha_{NO_2 i} \tag{3.30}$$

or, in a simpler form,

$$\mathscr{F} = \mathscr{F}_0 - \mu_{NO_2} X_{NO_2} \tag{3.31}$$

where

$$\mathscr{F} \equiv \frac{\sum_{i=1}^{5} \gamma_i F_i}{\Delta\alpha_{NO_2}} \tag{3.32}$$

$$\mathscr{F}_0 \equiv \frac{\sum_{i=1}^{5} \gamma_i F_{0i}}{\Delta\alpha_{NO_2}} \tag{3.33}$$

and $\Delta\alpha_{NO_2}$, the differential absorption coefficient, is

$$\Delta\alpha_{NO_2} \equiv \sum_{i=1}^{5} \gamma_i \, \alpha_{NO_2 i} \tag{3.34}$$

The total column of nitrogen dioxide can be calculated by inverting Eq. 3.31:

$$X_{NO_2} = \frac{\mathscr{F}_0 - \mathscr{F}}{\mu_{NO_2}} \tag{3.35}$$

Equation 3.31 – 3.35 clearly state that the value of column nitrogen dioxide (X_{NO_2}) can be simply obtained if:

1. the irradiances at five distinct wavelengths are measured to obtain their linear combination $\mathscr{F}$;
2. the weightings, γ_i, are properly calculated for the specified instrument and for a set of ozone cross sections, Rayleigh and aerosol coefficients;
3. the differential absorption coefficient, $\Delta\alpha_{NO_2}$, which depends in the instrumental characteristics and on the NO_2 cross sections employed in the algorithm, is known;
4. an extraterrestrial constant, $\mathscr{F}_0$, dependent on the instrument, is found through a *calibration* procedure;
5. the airmass, μ_{NO_2}, is determined for the used observation geometry.

For every ds or zs NO_2 observation, a set of 5 or 7 samples, for ds and zs respectively, is collected - each one including 20 slit cycles - and an average value and the standard deviation are calculated. The latter may be useful to remove bad data or measurements affected by fast-moving clouds.

3.4.4 Tracking possible variations in the Brewer spectral sensitivity

The internal SL diagnostic test is designed to accurately track any variation of the Brewer sensitivity. As explained in Sect. 3.3.2, the test returns a value equivalent to a slant column, but obtained using the lamp as a source, called F-ratio for measurements in `n2` mode. Any variation of the F-ratio corresponds to a change in the differential signal:

$$\mathscr{F}' - \mathscr{F} = F'_{ratio} - F_{ratio} \tag{3.36}$$

where $\mathscr{F}'$ and F'_{ratio} are the currently measured values and $\mathscr{F}$ and F_{ratio} are reference values, traceable, for instance, to the calibration conditions. Therefore, it is possible to obtain the corrected value $\mathscr{F}$ from $\mathscr{F}'$ and the results of the SL test. The correction is usually applied to $\mathscr{F}_0$ instead of $\mathscr{F}$, in Eq. 3.31.

Derivation. If the Brewer spectrophotometer slightly changes its spectral sensitivity after calibration, it will measure F'_i counts, relative to slit i, instead of the corrected ones, F_i:

$$F'_i = k_i \, F_i \tag{3.37}$$

where k_i is a scale factor, hopefully close to unity. When calculating the linear combination, thanks to the properties of the logarithm function,

$$\sum \gamma_i \log_{10} F_i' = \sum \gamma_i \log_{10}(k_i F_i) = \sum \gamma_i \log_{10} k_i + \sum \gamma_i \log_{10} F_i \qquad (3.38)$$

If we assume that the same variations, and k_i's, affect the lamp measurements, L_i, then

$$\sum \gamma_i \log_{10} F_i' - \sum \gamma_i \log_{10} F_i = \sum \gamma_i \log_{10} k_i = \sum \gamma_i \log_{10} L_i' - \sum \gamma_i \log_{10} L_i \qquad (3.39)$$

which is Eq. 3.36. ■

3.4.5 Current limitations of NO_2 measurements using MKIV Brewers

While the Brewer is considered as a reference for ozone measurements, with attainable accuracy better than 1%, accurate measurements of nitrogen dioxide were always - and are still - an issue (Cappellani and Bielli, 1995). Several intercomparison were performed between MKIV Brewers and other spectrophotometers, which often identified large deviations - usually a systematic overestimation - of the former relative to other instruments:

on behalf of the World Meteorological Organisation (WMO), Canada organised and hosted the Visible Light Nitrogen Dioxide Spectrophotometer Intercomparison in 1991. Four countries (Canada, Germany, Soviet Union and New Zealand) participated to the comparison, which took place on Mt. Kobau, Canada, the oldest dark sky preserve in the world. The high altitude site was chosen to avoid large contaminations of tropospheric NO_2. The MKIV Brewer systematically measured higher slant columns amounts, up to 40–100%, at 84° solar zenith angle each day compared to other instruments (McElroy et al., 1994);

in 1992, seven groups from seven countries (New Zealand, Italy, France, Belgium, Germany, Canada and U.S.) met in Lauder, New Zealand, to intercompare their remote sensing instruments for the measurement of atmospheric column NO_2 from the surface. The campaign was hosted by the Network for the Detection of Stratospheric Change (NDSC). The group as a whole was able to make measurements of the 90° solar zenith angle slant path column amount that agreed to about ±10% most of the time. However, the Brewer showed systemic and random deviations of 10—30% (Hofmann et al., 1995);

Pinheiro (2003) reports about a comparison between a MKIV Brewer installed in Cachoeira Paulista, Brazil, and a SAOZ located 200 km apart, in Bauru. Average deviations up to 20.42%±12.9% between the two series were found;

Vaughan et al. (2006) reports about comparing a MKIV Brewer spectrophotometer and a SAOZ instrument from December 2000 to August 2003 in Aberystwyth. The Brewer instrument measured NO_2 by direct solar observation, rather than zenith sky, and was therefore more sensitive to lower tropospheric pollution. During this period, the mean ratio SAOZ/Brewer for individual days was 1.01 with a standard deviation in the ratio of 0.05;

a balloon campaign, called Middle Atmosphere Nitrogen Trend Assessment (MANTRA), was held in 2004 at the Vanscoy Balloon Facility in Saskatchewan, Canada. During the course of the balloon campaign, an intercomparison of ground-based measurements of NO_2 was also carried out and included measurements from 6 instruments, among which a Brewer spectrophotometer. The Brewer zenith measurements using the standard algorithm were about 200% compared to measurements by a SAOZ instrument, which in turn agreed with profile concentration measurements by the balloons (Barton, 2007);

even comparisons between MKIV Brewers and satellites show poor agreement. As an example, Francesconi et al. (2004) found 50% overestimation of Brewer measurements relative to the GOME-2 satellite over Rome and a low (0.4) correlation coefficient between the two series.

Many factors contribute to the poor performances of current NO_2 measurements using MKIV Brewers, among which:

1. the MKIV Brewer processing algorithm has not been officially updated since 1985. This can trigger many consequences:
   (a) the laboratory NO_2 cross sections used in the standard algorithm (Johnston and Graham, 1976) are obsolete. For example, it has been recognised that they suffer from wavelengths misalignments and baseline errors (Orphal, 2003). An error in the differential absorption coefficient $\Delta\alpha_{NO_2}$ could thus be introduced, which in turn induces a scale factor in NO_2 measurements;
   (b) the laboratory cross sections used in the standard algorithm for species other than NO_2 are obsolete and may lead to wrong weighting coefficients, which in turn induce cross-talk between different species without completely removing their contributions to the differential signal. In other words, the linear combinations in Eqs. 3.29 could be different from zero;
   (c) the UV Rayleigh scattering coefficients, as already stated, are used as-is in the visible range. Additionally, it has been recognised that the Rayleigh correction in the Brewer standard algorithm is obsolete and should be replaced. This may introduce an offset in the retrieved NO_2;
2. the weightings and the differential NO_2 absorption coefficients were originally obtained for a specific Brewer, with a given set of wavelengths and resolutions. However, the same constants are used indiscriminately in all Brewer instruments. Indeed, it has been discovered that, at least for ozone determinations, small instrumental differences between Brewers may lead to large discrepancies if a standard set of constant is used (Savastiouk, 2005). An accurate characterisation of each single instrument is thus fundamental to fine-tune the processing algorithm;
3. no travelling standard MKIV Brewer is currently available in the world for NO_2 calibration, unlike ozone reference instruments (e.g. MKII Brewer #017). Therefore, Brewers running in many stations have never been recalibrated after purchase and initial setting. Thus, the extraterrestrial constants in many instrument are likely wrong, which can introduce deviations proportional to the inverse of the AMF;
4. other factors, as the rotational Raman scattering or some unaccounted trace gases in the atmosphere, could interfere in the NO_2 determination (WMO, 1992), as explained in the following section.

3.5 Recent works about the measurement of nitrogen dioxide using Brewer spectrophotometers

A short and subjective review of some interesting works is hereinafter provided, which constitute a promising basis for improving the measurements of NO_2 with MKIV Brewers.

Francesconi et al. (2004) analysed the NO_2 series recorded with MKIV Brewers at two Italian stations, Rome and Ispra (in the Po Valley), using the standard algorithm. The respective mean values of the series were found to be 1.63 DU for Rome and 1.60 DU for Ispra. A quasi-simultaneous comparison with a satellite radiometer (GOME-2), including efficient cloudscreening of Brewer data, was performed. A large disagreement, up to a factor 10 (the

Brewer results being larger than the satellite estimates), was initially found. After accounting for corrections in the extraterrestrial constant and SL test results, the difference decreased to 50%. The remaining discrepancies were attributed to unknown deficiencies in the instrument and in the algorithm as well as to the different spatial resolutions and air masses probed by the Brewer and GOME-2. The last point was partly confirmed by analysing few orbits of the SCIAMACHY satellite, which gave slightly better results thanks to its higher resolution;

Pinheiro (2003) used a MKIV Brewer to measure the total, tropospheric and stratospheric NO_2 columns in several stations in Brazil. The author also noticed that the influence of Rayleigh scattering is not completely removed by the standard weightings, which can result in errors up to 20%, and accounted for the resulting bias. Finally, the extraterrestrial constants were updated on the basis of the SL test results, although a complete recalibration was not attempted;

Cede et al. (2006a) designed a completely new algorithm for retrieving NO_2 columns amounts with MKIII Brewers in the UV-A spectral range, since this model is not able to measure in the visible. The observations were performed in the ds geometry to reduce the uncertainty due to the estimation of the AMF, to avoid the use of a priori profile needed for zs measurements and to neglect the Ring effect. Moreover, direct sun observations are equally sensitive to the contribution of NO_2 located in both the stratosphere and the troposphere, where it is assumed to accumulate due to the tropospheric pollution at the measurement station. On the other hand, the choice of the ds geometry, causing a lower NO_2 signal than in zs measurements, and the use of irradiances in the 349-363 nm wavelength range, which is not optimal for NO_2, caused large scatter in the observations and long-time averages were required.

Among many other improvements to the algorithm, irradiances at all six slits were used instead of only five as the standard algorithm. Indeed, although the first slit cannot collect enough light in the UV range, there is no reason for not using it in the visible. Also, three different micrometer positions were used, for a total of 18 wavelengths. Additional species absorbing in the UV-A with fixed amounts (SO_2, HCHO, BrO, O_4) were included in the algorithm as well as the influence of scattered light entering the field of view of the instrument, which is an issue especially for the lowest wavelengths.

A "bootstrap method", capable to select a subset of days with low tropospheric NO_2 content, was implemented and applied to a long series for calibrating the Brewer without doing any Langley campaign (see next chapters). Furthermore, an uncertainty assessment was made, resulting in 0.2–0.6 DU extended uncertainty. Concluding remarks by the authors included the suggestion to apply their improvements to MKIV Brewer, with the advantage of having larger cross sections, higher sensitivity and lower straylight than MKIII's, and accounting for the absorption by water vapour and the oxygen dimer (Greenblatt et al., 1990) at the wavelenths corresponding to some MKIV Brewer slits. Also, a Langley calibration in a clean, high altitude site was recommended as a more accurate calibration procedure compared to the bootstrap method.

Comparisons between cloud-free MKIII Brewer data using the new methods and satellite estimates were performed. The linear correlation coefficient between both series was not very large (0.48), but the seasonal cycles were similar and the average values quite close to each other (0.67 DU for the Brewer and 0.62 DU for SCIAMACHY). Two successive works (Wenig et al., 2008; Celarier et al., 2008) compared the measurements by the same MKIII Brewer to OMI satellite radiometer. Correlations between the respective monthly mean series were high (0.9) and the Brewer was 25–35% higher than OMI;

Barton (2007) made an interesting, though mainly theoretical, study about measurements by MKIV Brewers in the zs geometry. The author developed an algorithm using all the six Brewer slits and accounting for the absorption by the oxygen dimer. He performed a complete sensitivity analysis using a radiative transfer model taking into account the polarisation of the scattered radiation and calculated the effect of water vapour absorption and Ring effect.

The introduction of newer O_3 and NO_2 cross sections produced a significant improvement, by decreasing of about 20% the retrieved NO_2 column amounts.

Additionally, measurements with a new polarisation geometry were performed. The Brewer was positioned perpendicularly to the sun when taking zs measurements, thus increasing the number of collected photons (Fig. 3.2), improving the SNR - as already Brewer and McElroy (1973) supposed - and remarkably decreasing the Ring effect. Data in the new polarisation are believed to be 30% lower - and therefore, better - than in the old polarisation, but slightly more sensitive to thick clouds, with optical density larger than about 3.

Some inconsistencies, however, were found between model estimates and measurements and more experimental data are needed to understand some features, e.g. the magnitude of the Ring effect in both polarisations and the influence of water vapour and clouds.

In his final recommendations, the author suggested, for future studies, to identify a new placement for the micrometer so as to minimise the effects of water vapour, oxygen dimer and Ring effect, since the influence of these factors occurs in relatively small regions of the visible spectra. A program could be developed to slide the six slits across all the absorption spectra until an optimum location is found where the NO_2 absorption contribution is greatest and the absorption contribution from other species is the least. This is exactly the starting point of my Ph.D. work (Sect. 4.3).

Some more findings are worth being cited, although relating to only ozone measurements:

Kerr (2002) and Kerr and Davis (2007) developed a new methodology based on scanning a complete wavelength range by moving the Brewer grating rather than simply measuring the irradiances at five wavelengths at one micrometer position. Although this kind of measurements is slower, it leads to an over-constrained system of equations and allows to retrieve a larger number of unknowns (Sect. 4.2.7);

Savastiouk (2005) meticulously characterised a MKV Brewer for ozone measurements in the visible range and improved the retrieval algorithm by including, for instance, the effect of non-neutral density filters and recalculating the weighting coefficients for a specific instrument. New factors, such as the aerosol optical depth and the ozone effective temperature, were determined.

3.6 Goals of the present work

Once the theoretical and operating principles of a Brewer spectrophotometer have been explained and a review of the most influential scientific literature on the subject has been illustrated, the main goals of my thesis can be finally presented:

1. since the NO_2 absorption in the solar light is very weak and the algorithm variables strongly depend on the instrumental characteristics of a specific Brewer, a MKIV Brewer spectrophotometer must be accurately characterised in the visible range. Brewer #066 will be used to this purpose;

2. the standard NO_2 algorithm currently implemented in the Brewer operating software has clearly shown many limitations. It is necessary to update it, based on both the main findings in previous literature and some original ideas;

3. the measurement technique can be improved, based on some advanced principles of operation of the Brewer spectrophotometer, for example trying to move the micrometer in different positions to optimise the NO_2 signal while reducing other interferences;

4. a detailed comparison between data taken in direct sun and zenith sky (with both polarisations) geometries has never been attempted. This would definitely allow a better comprehension of the Brewer performances and of some theoretical principles and would probably throw some light on the partitioning between tropospheric and stratospheric column densities;

5. no travelling standard NO_2 Brewer exists nowadays. A key point would be to accurately calibrate Brewer #066, thus establishing a reference MKIV instrument for NO_2 in Europe;

6. several MKIV Brewer instruments have been collecting NO_2 data for many years (more than 20 years, at some stations), which are not processed due to current algorithm limitations. Therefore, the results of my work will be valuable not only to start new series of accurate measurements, but also to reprocess historical series of measurements from more than 70 stations all over the world (WOUDC, 2013).

Chapter highlights

- the electromagnetic radiation and the atmosphere can interact in many ways: light from the sun is both absorbed by atmospheric constituents and scattered. Numerical models have been recently developed which accurately simulate the radiative tranfer in the Earth's atmosphere based on physical laws;
- absorption spectroscopy takes advantage of the peculiar spectral influence on solar light by different compounds in the atmosphere and allows to retrieve their content by analysing the intensity of the sunlight or skylight at several wavelengths;
- the Brewer spectrophotometer is a widely used and flexible instrument to measure ozone as well as sulphur dioxide density columns, along with irradiance in the UV. Some Brewers (about 60 in the world), the so-called "Mark four" (MKIV) models, can additionally measure the column concentration of nitrogen dioxide in the atmosphere;
- notable efforts have been done in the last years to improve the retrieval of nitrogen dioxide by Brewers. However, much work is still required to update the algorithm, to refine the technique and to throw light on some poorly understood issues;
- the results of my work will be useful not only to start new series of accurate measurements, but also to reprocess several long-term NO_2 series recorded worldwide.

CHAPTER 4

Instrumental characterisation and algorithm update

The exciting side of experimental science is the intrinsic interconnection between theory and practice. Theory without measurements is just an interesting set of hypotheses, which can or cannot come true when put to the test of the real world. For the purpose, the experimental scientist must use his instruments at their best and know them to perfection, in order to discriminate between the real signal of the physical quantity to be measured and the disturbances introduced in the measurement by the instrument itself. However, practice without theory is not science, which gets through to the deep understanding of the fundamental processes and tries to describe them by the beautiful and elegant laws of mathematics.

This chapter is the first to report the main results of my work. I will start by describing the efforts I made to carefully characterise Brewer #066, namely determine its sensitivity and the main characteristics which may be relevant to the measurement. This first step is essential when dealing with a weak absorber as nitrogen dioxide, since the slightest disturbance may compromise the accuracy of the estimation. Then, in the second part of the chapter, I will show my contribution to the improvements of the Brewer retrieval algorithm for nitrogen dioxide. For this purpose, I will introduce an original and robust mathematical framework in order to understand thoroughly how the algorithm works and its limitations. Finally, practice and theory will be combined together, in order to optimally "tune" the algorithm on Brewer #066, and a first test of the algorithm will be performed with the help of a radiative transfer model.

4.1 Characterisation of Brewer #066

The first part of my Ph.D. work was devoted to accurately determine the instrumental characteristics of Brewer #066 in the `n2` operating mode: the dispersion of the monochromator, the attenuation of the internal filters, the deadtime of the photon counting system, the straylight and the sensitivity to the internal polarisation and temperature. The main results on this subject were presented at the Beijing Brewer Meeting (Diémoz, 2011). Every step of my work will be described in detail in the following sections.

4.1.1 Dispersion properties of the monochromator

One of the most essential properties to be assessed in a Brewer spectrophotometer is its ability to separate the solar light into different spectral components. The determination of the dispersion function, for instance, allows to connect the grating position to the operating wavelengths of each slit.

Figure 4.1: One of the lamps used for the dispersion test on Brewer #066. The lamp fits the upper dome normally employed for global UV measurements.

Traditionally, a dispersion test (`dsp` routine) is carried out in the UV range during every Brewer calibration. The operator has to own a set of lamps with different gases (Fig. 4.1), each one emitting a different spectrum made up with several well-known lines. The Brewer scans the spectral irradiance entering through the UV dome at the shorter and longer wavelengths about some selected emission lines. The scan is performed forward and backward and the results are averaged in order to compensate for any temporal linear drift. Afterwards, a dedicated software is employed to calculate the centre of the lines in term of the micrometer step and to fit their values to the known nominal emission wavelengths. The fitting function is usually a second degree polynomial, which results in three different coefficients for each slit.

Generally speaking, every measurement by a scanning device, e.g. a spectrometer, is the convolution, $I^{\star}(\lambda)$, of its instrumental slit function $f(\lambda)$, defining the resolution of the instrument, and the real input spectra $I(\lambda)$:

$$I^{\star}(\lambda) = \int_{-\infty}^{+\infty} I(\lambda')\, f(\lambda - \lambda')\, \mathrm{d}\lambda' \tag{4.1}$$

Since the shape of the narrow emission lines in a dispersion test can be approximated to a delta function, the results of the dispersion measurements are the (mirrored) slit functions of the Brewer. Thus, the dispersion test is also useful to determine the resolution of every slit in the monochromator and its shape. As will be described later, this allows to correctly convolve the cross sections of the absorbing gases at the instrumental resolution and to check that the instrument is correctly in focus.

Dispersion function in the visible range

Since Eq. 3.18 relates the wavelength emerging from the grating to the incidence and diffraction angles and the diffraction order, theoretically both the coefficients of the dispersion function and the resolution in the visible band could be estimated by simply multiplying the UV coefficients and resolution by $\frac{3}{2}$, namely the ratio of the two orders used for the UV and visible modes, respectively. Nevertheless, I preferred to determine the dispersion in the visible by means of independent experiments, in order to avoid the effects resulting from any possible optical aberration in the instrument causing the breakdown of the grating relation.

Table 4.1: New dispersion lines in the visible range of MKIV Brewers.

gas	emission wavelengths (nm)		
mercury		435.8335	
cadmium	467.8149	479.9912	508.5822
zinc	468.014	472.215	481.053

Nevertheless, this approach required to rewrite the `dsp` routine and to find new lines in the visible range of MKIV Brewers. Based on the emission wavelengths published on an atomic spectroscopic database (NIST), I selected several lines emitted by mercury, cadmium and zinc lamps (Table 4.1). Xenon was also tested, but the presence of a *continuum* prevented good measurements. I modified the `dsp` routine to include the new lines and to pick out the right neutral density filters. The updated `dsp` routine is now part of the official software released by International Ozone Services Inc. and is available to all users worldwide (International Ozone Services Inc., 2013).

Improved fitting function

Many authors had already found that the estimate of the NO_2 content by any instrument (Orphal, 2003), and specifically by Brewers (Cede et al., 2006a), is very sensitive to any small wavelength misalignment. I therefore decided to use the more accurate and physically-based fitting function described by Gröbner et al. (1998), although it is much more complex to handle in mathematical terms. The improved fitting function takes account of the Brewer geometry and projects measurements from all slits onto one reference slit (slit 4, in my case) using the nominal technical specifications given by the manufacturer. A single polynomial was fitted to the whole data set to obtain an expression relating the micrometer steps of the grating motor to the wavelength measured at (or projected onto) the reference slit. Wavelengths for the remaining slits could then be recalculated making use of the grating equation. Finally, the algorithm was iterated, allowing the model positions of slits 1, 2, 3, 5 and 6 to vary, which was needed to account for the effect by the coma-correcting lens, misalignments and slight deviations between the technical drawings and the real slit positions.

Algorithm implementation and results

In order to process the dispersion data, I developed a dedicated software, which is able to read the output of the `dsp` routine and retrieve the dispersion function.

The program processes the counts measured when scanning each line following the standard data reduction scheme (Sect. 3.4.1) and fits the points between 20% and 80% of the maximum of each line with an isosceles triangle as in Gröbner et al. (1998). The step at the vertex of the triangle is defined as the centre of the line (Fig. 4.2). The algorithm to retrieve the dispersion function is then iterated 200 times to reach convergence. The shape of the slit function, which will be used later for the convolution of the cross sections, is interpolated with a trapezoid with a height of 0.87 that of the triangle, as defined by Kerr and as assumed in a similar existing software (Savastiouk, personal communication, 2011).

Figure 4.3 shows the dispersion function (operating wavelengths against micrometer step) for each slit as obtained from the dispersion test on Brewer #066. Both the operating wavelength and the resolution of each slit at the default micrometer step (1000) are listed in Table 4.2. The variation of the resolution with reference to the micrometer step is assumed to be linear. As an example, the full width at half maximum of the third slit function is depicted in Fig. 4.4.

The residuals of the improved fit, i.e. the difference between the nominal wavelengths of the emission lines and the dispersion function at the measured step, are displayed in Fig. 4.5 and are uniformly distributed in the range ± 0.005 nm.

Table 4.2: Operational wavelength and resolution for each slit at step 1000 for Brewer #066.

slit	wavelength (nm)	fwhm (nm)
1	425.10	0.58
2	431.46	0.84
3	437.41	0.84
4	442.89	0.86
5	448.15	0.84
6	453.27	0.83

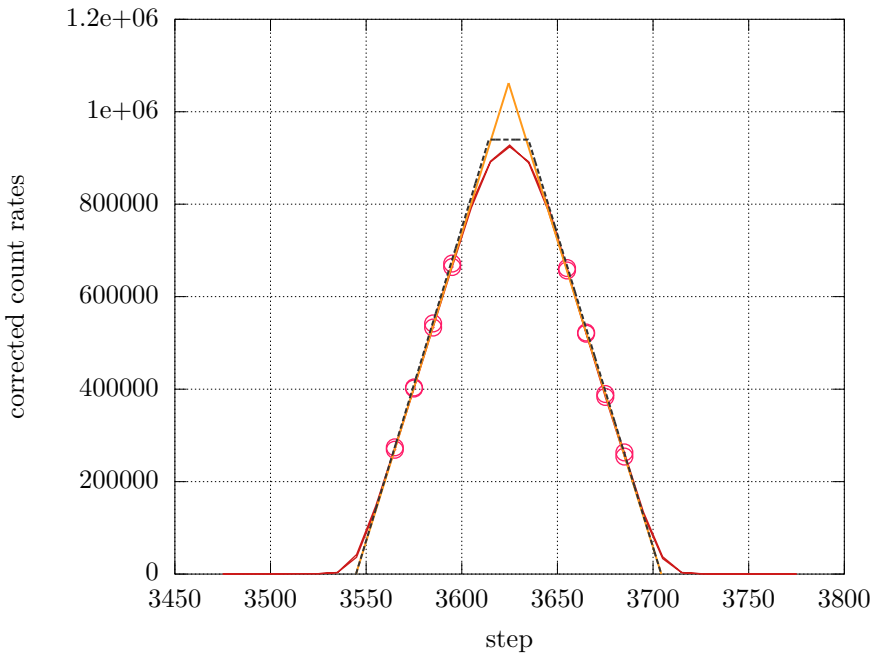

Figure 4.2: Scan of one of the lines used in the dispersion test (sixth slit, cadmium line at 479.9912 nm). The forward and backward scans (dark red lines) are indistinguishable. The orange lines identify the isosceles fit. Only the points in the range 20–80% of the maximum (pink circles) are taken into account for the fit. The black, dashed line represents the trapezoidal slit function used for the convolution of the cross sections.

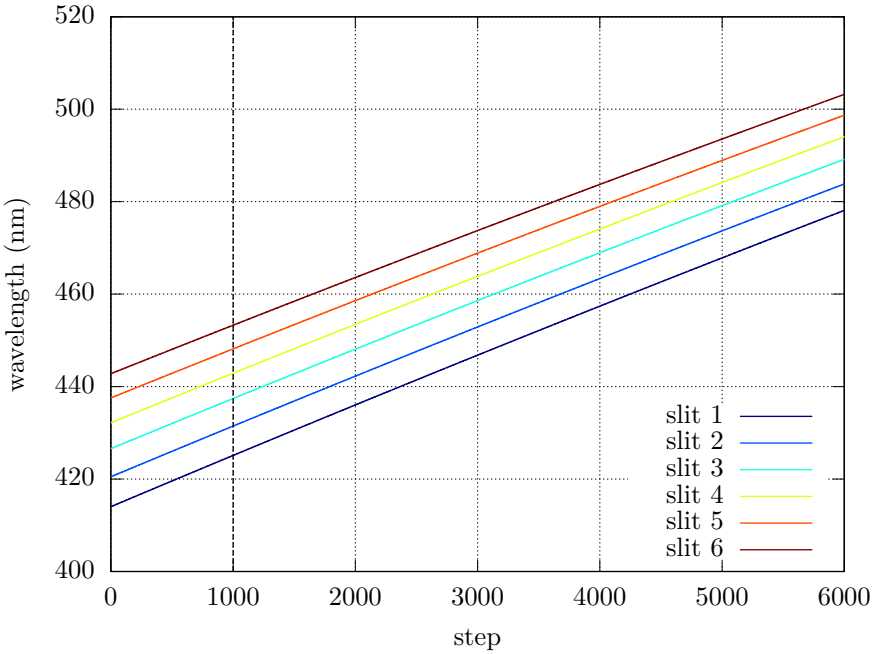

Figure 4.3: Dispersion functions for each slit for Brewer #066, as determined from the dispersion test. The standard operating step 1000 is shown as a vertical dashed line.

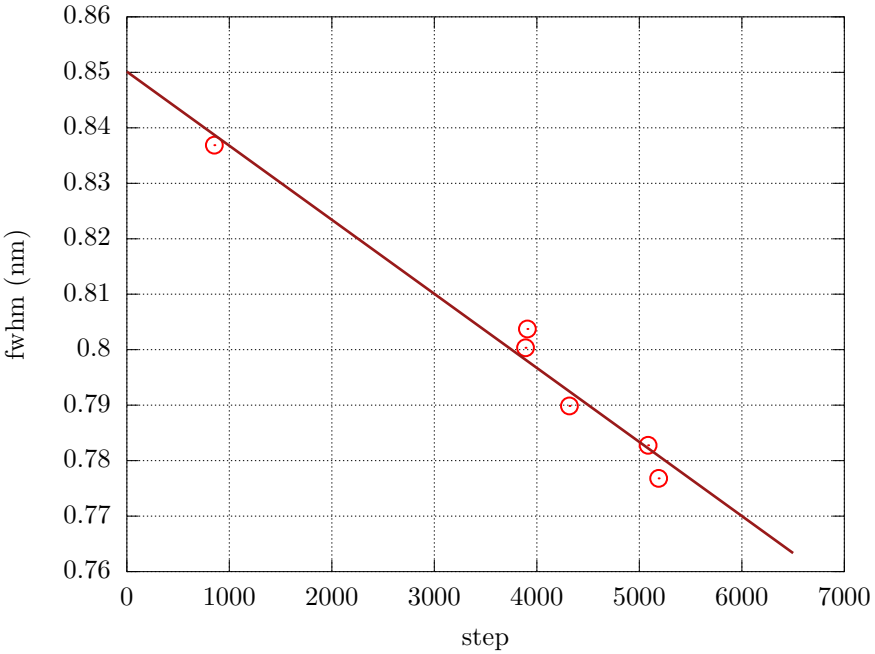

Figure 4.4: Resolution at the third slit function as measured during the dispersion test (circles) and estimated by a linear regression (line).

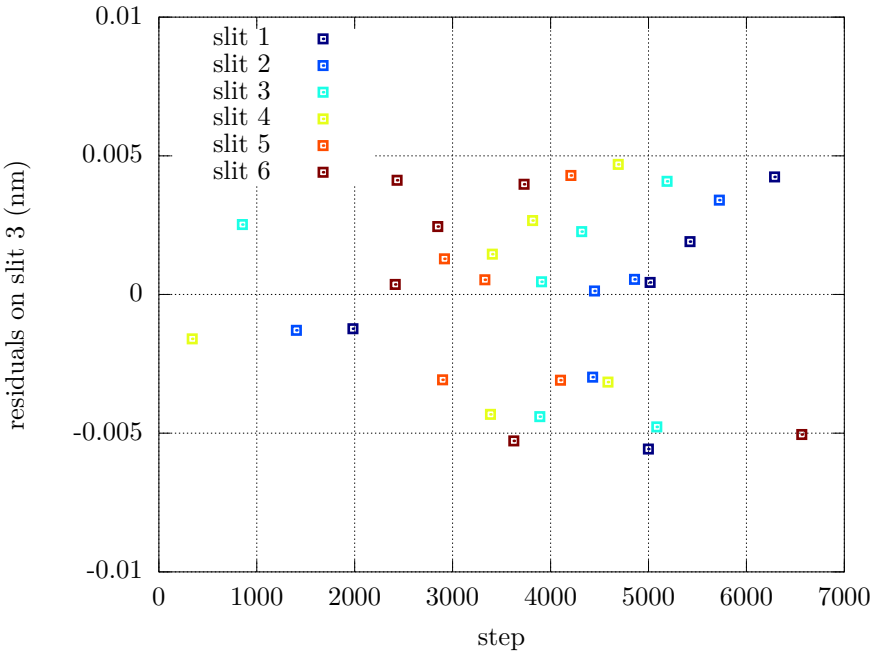

Figure 4.5: Residuals of the fit of the dispersion test.

Comparison between UV and visible dispersion functions

A comparison between the results of the new dispersion test in the visible and the values I would have obtained from the UV dispersion function may be useful to check whether the Brewer is correctly in focus and whether any unexpected optical aberration is taking place. As stated before, from the grating equation, both the wavelength and the resolution in the visible should be $\frac{3}{2}$ those in the UV for the same grating position.

The difference between the resolutions obtained with the UV and visible dispersion functions (both calculated with the improved fitting algorithm by Gröbner et al. (1998)) is depicted in Fig. 4.6. Compared to the resolution (e.g. Table 4.2), the difference is negligible and the Brewer #066 can be reasonably considered in focus.

However, I did not found the same agreement when comparing the wavelengths obtained with the UV and visible dispersion functions. Figure 4.7 represents the deviation of the wavelengths obtained with both dispersion functions. The difference between the wavelengths of the dispersion lines retrieved using the UV dispersion function (from the micrometer step of the line maxima) and the nominal wavelengths of the emission lines is superimposed in the same figure as circles. As a criterion for comparison, it should be kept in mind that the uncertainty of 1 micrometer step, resulting from the `hg` test, translates to 0.01 nm in the visible. The same test was repeated on other MKIV instruments: Brewer #067, operated in Rome (Fig. 4.8), and Brewer #098, operated in Hradec Králové - Czech Republic (Fig. 4.9), and even larger discrepancies were obtained. The magnitude of the difference is relevant and proves that the UV dispersion function cannot accurately reproduce the dispersion observed in the visible.

Correlation to Fraunhofer solar structures

In order to rule out any error in the previous method and any bug in the new `dsp` routine, which might cause the observed shifts, a completely different procedure was developed and confirmed the previous results. A new routine, `vi`, was written to scan the global spectrum in the visible range of the Brewer, just as the routine `uv` - which is already available in the Brewer operating software - records the global spectral irradiance in the UV. The irradiance scale of the Brewer in

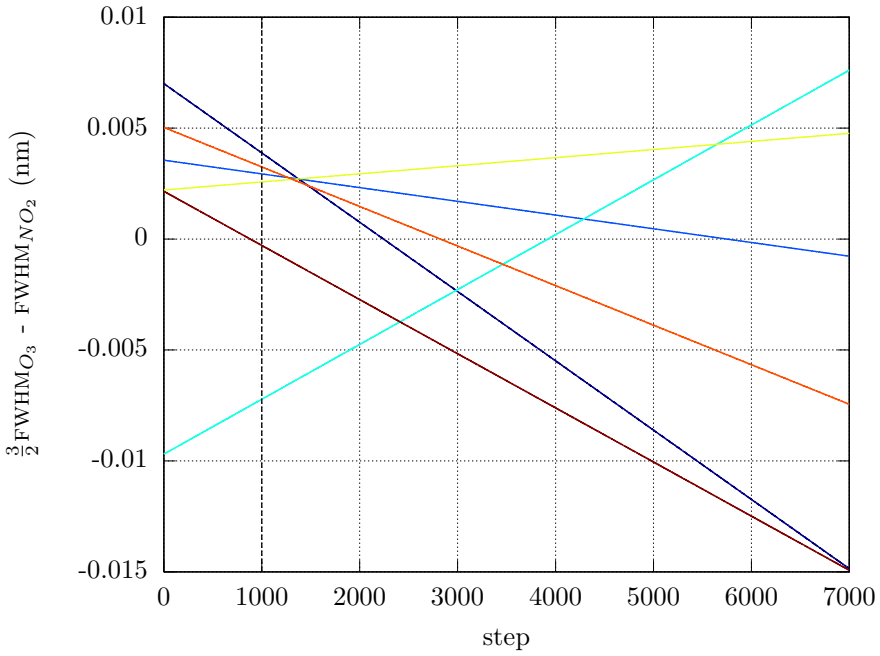

Figure 4.6: Difference between the resolution expected from the UV dispersion function, multiplied by $\frac{3}{2}$ to take into account the diffraction orders used in `o3` and `n2` modes, and the dispersion function obtained in the visible during the dispersion test for each slit as a function of the grating position (micrometer step). The colour convention is similar to the previous figures.

the visible range was calibrated by comparison against a well-tested spectroradiometer traceable to the world reference (Diémoz et al., 2011). Both routines use the traditional UV dispersion function defined as a second order polynomial. Then, the SHICrivm software (Slaper et al., 1995) was run on several spectra, measured in March 2012, to assess the wavelength alignment of the instrument compared to the Fraunhofer structure of the solar spectrum.

While the best correlation between the Fraunhofer lines and the spectra recorded in the UV is reached for shifts well below ±0.02 nm (not shown), which is the stated uncertainty of the SHICrivm algorithm, the results using the UV dispersion function in the visible range are considerably beyond that limit (Fig. 4.10). Furthermore, the results from the SHICrivm software agree with the data from the dispersion test.

Analysis of the discrepancies between the dispersion functions

As emerged from the previous paragraphs, the UV function is not well-suited to represent the wavelength dispersion in the visible. Indeed, wavelength misalignments of several steps (>4–5), which are much larger than the accuracy of the `hg` routine for the Brewer wavelength alignment, would be required to justify the experimental results to "save" the UV dispersion function.

The issue was investigated in detail, since even slight misalignment can trigger large errors on the retrieved nitrogen dioxide. I considered some reasons for the deviations:

coma. Residual coma aberrations in the Brewer spectrophotometer (Johnston et al., 2000) could be responsible for the observed behaviour. As a result, the measured dispersion lines should be slightly tilted (McElroy, personal communication, 2011). However, no asymmetry was observed in the dispersion lines;

spectral responsivity. The steep variation of the Brewer responsivity in the visible (Fig. 4.11) could distort the recorded dispersion lines and consequently contribute to the discrepancy.

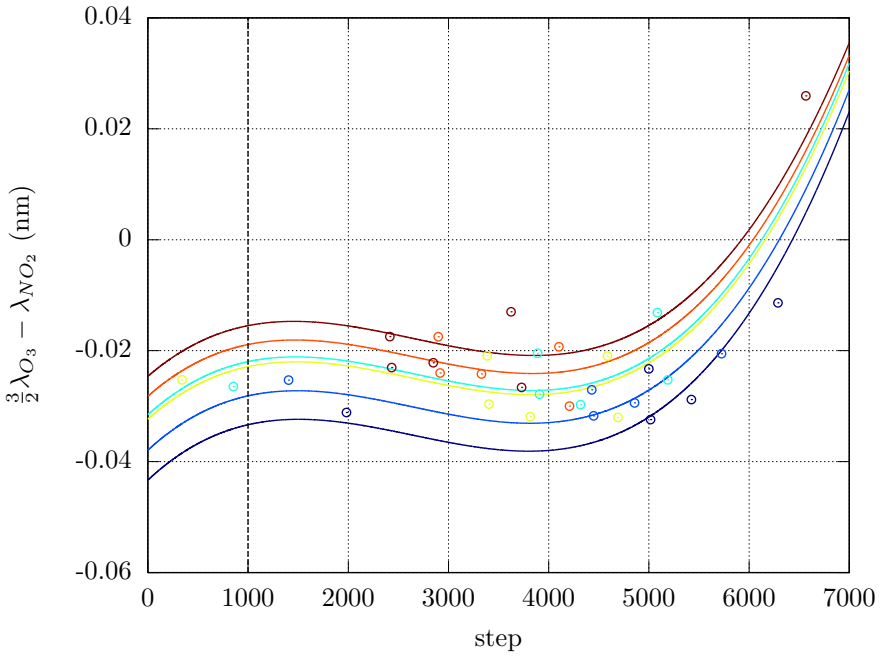

Figure 4.7: Brewer #066: difference between the wavelengths obtained from the UV dispersion function, multiplied by $\frac{3}{2}$ to take into account the diffraction orders used in `o3` and `n2` modes, and the dispersion function obtained in the visible, for each slit (lines), as a function of the grating position (micrometer step). Circles represent the difference between the wavelength of the emission lines retrieved from the UV dispersion function and the nominal wavelength. The colour convention is similar to the previous figures.

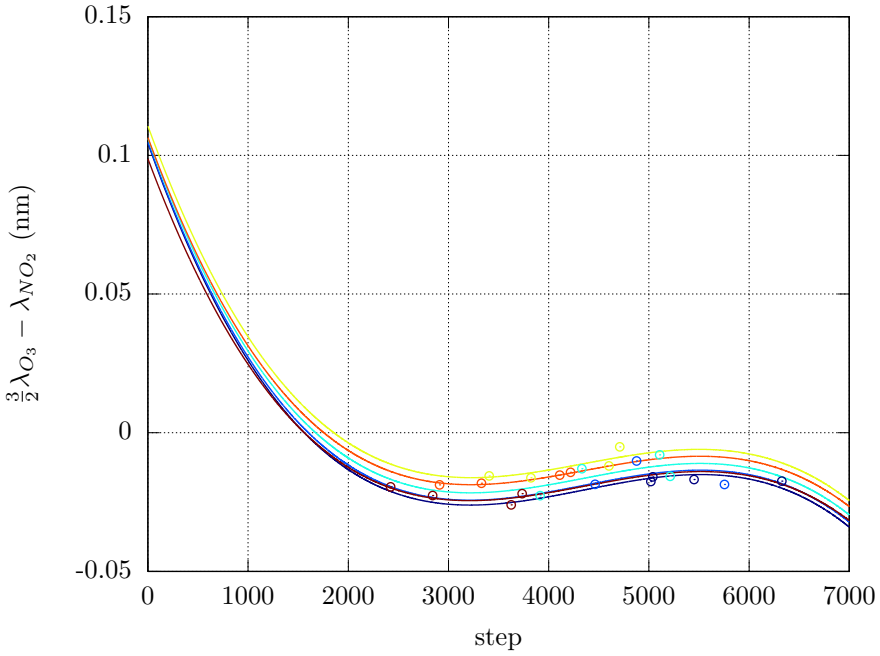

Figure 4.8: Same as 4.7, but for Brewer #067, operated in Rome.

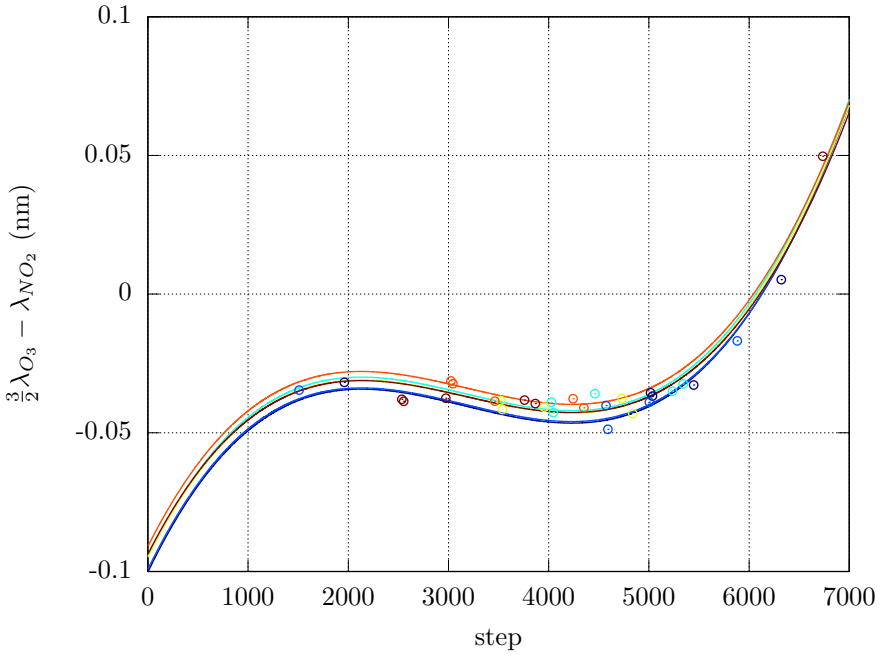

Figure 4.9: Same as 4.7, but for Brewer #098, operated in Hradec Králové.

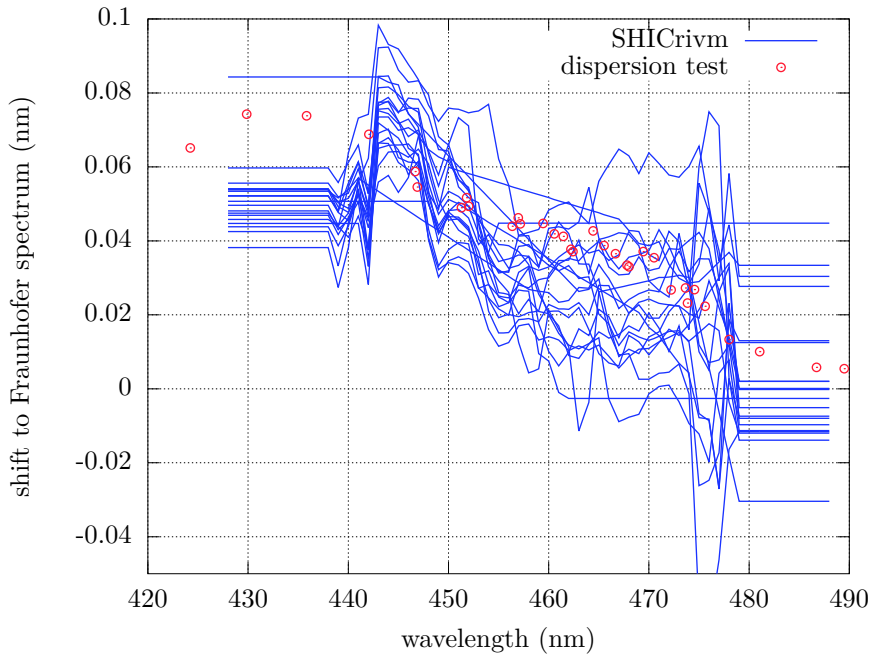

Figure 4.10: Output of the SHICrivm software applied on the visible spectra recorded by Brewer #066 in March, 2012 using the new routine `vi` (lines). The data from the dispersion test are displayed as circles.

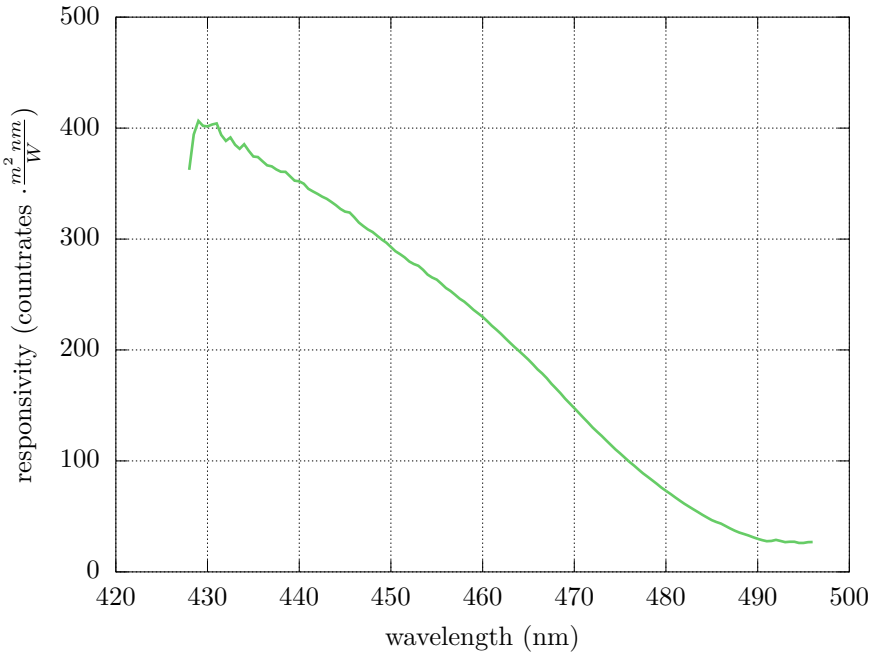

Figure 4.11: Spectral responsivity of Brewer #066 in the visible range, obtained by comparison against a well-tested double-monochromator spectroradiometer (Diémoz et al., 2011).

The effect, as from my calculations, could be as large as 1 step, which is still too low compared to the observed shifts;

further optical aberrations. Deviations from the grating law could arise in the monochromator from, e.g. the correction lens. Indeed, the latter could introduce small effects depending on the wavelength. However, a complete proof would require ray-tracing simulations, which are beyond the scope of my work.

The reasons of the discrepancies were not completely understood. Since the deviations are relevant, I preferred to use the dispersion function measured in the visible rather than the UV dispersion function multiplied by $\frac{3}{2}$.

Repeatability of the dispersion test

The dispersion test was performed many times during my Ph.D. activities, especially when the Brewer was moved from ARPA during the campaigns (Chap. 5). All results were nearly identical – well within ±1 micrometer step – which proves the stability of Brewer #066 after even long journeys.

4.1.2 Effect by internal filters

In principle, the filters used in the Brewer foreoptics (Sect. 3.3.2) to control the intensity of the light collected by the instrument should be neutral, i.e. they should attenuate irradiance at all wavelengths by the same amount. Nevertheless, it has been proven (Savastiouk, 2005) that this is not the case in the UV and that their effect on the ozone retrieval may be remarkable. The same issue could arise in the visible as well and deep investigations are required. Indeed, if either the attenuation is not constant with wavelength or its spectral dependency does not reflect one of the knows factors (Eq. 3.29), the linear combination is not able to remove the filter contribution. Therefore, Eq. 3.31 becomes

Table 4.3: Filter wheels (FW) and iris diaphragm settings during the test to characterise the filter attenuation. Positions 0 and 3h act as baselines for low- and high- intensities measurements, respectively. The test performs measurements at combinations 0 to 5h, then backwards from 5h to 0.

combination	FW#1	FW#2	iris diaphragm
0	GQ + ND2	0	open
1	GQ + ND2	1	open
2	GQ + ND2	2	open
3	GQ + ND2	3	open
4	GQ + ND2	4	open
5	GQ + ND2	5	open
3h	GQ	3	closed
4h	GQ	4	closed
5h	GQ	5	closed

$$\mathscr{F} = \mathscr{F}_0 - \frac{\sum_i \gamma_i \, AF_{pi}}{\Delta\alpha_{NO_2}} - \mu_{NO_2} X_{NO_2} \tag{4.2}$$

where AF_{pi} is the (spectrally varying) attenuation of filter p (defined in Eq. 3.22) at the wavelength relative to slit i. If the variation of the filter attenuation is not taken into account, the error on the retrieved nitrogen dioxide column will then be

$$\varepsilon_{AF_p} = \frac{1}{\mu_{NO_2}} \frac{\sum_i \gamma_i \, AF_{pi}}{\Delta\alpha_{NO_2}} \tag{4.3}$$

However, if the term ε_{AF_p} is known, it is possible to correct the measured linear combination, $\mathscr{F}$, by the same amount, which allows to greatly improve the accuracy of NO_2 estimations.

In order to characterise the spectral filter transmittance in the visible, a new routine was developed which uses the standard internal lamp as a source. Light emerging at the various slits from the monochromator was collected for several combinations of filters. The duration of each measurement was set up by taking into account the photon noise, assumed to follow Poisson statistics. Filter #4 and #5, which are the most difficult to characterise due to their high attenuation, were measured using two different settings: the first combination inserted a ground quartz (GQ) diffuser and a neutral density filter (ND2) on filter wheel #2, while the second employed only a ground quartz diffuser, in order to increase the recorded counts and reduce noise (Table 4.3). The test performed measurements switching between combinations from 0 to 5 at high intensity (hereafter referred as "5h") and then backwards from 5h to 0 in order to minimise the effect of slight variations of the lamp irradiance with time.

The results of the routine, in terms of $AF_{pi} - AF_p$, i.e. the mean difference between real (at slit i) and nominal attenuations, are depicted in Fig. 4.12 for all slits and all filters. The effect of the filters on the nitrogen dioxide column retrieved by the standard Brewer algorithm (Kerr's weighting coefficients, Table 3.1) is shown as a boxplot in Fig. 4.13. This corresponds to the error ε_{AF_p} (Eq. 4.3) for a unity air mass. As clear from the figure, the influence is very strong, especially for filters #4 and #5.

Since the measurement noise in the routine is remarkable, especially for the strongest filters, a rather long series must be recorded to accurately characterise the filters transmittance. The data used for the figures, for instance, belong to a three-months daily series (October – December 2012). Moreover, the new routine is able to measure the filter attenuation at whatever grating position. After introducing further positions in addition to the standard one (Sect. 4.3), the effect of filters was recalculated at the right micrometer step.

Finally, it should be stressed that the measured filters attenuation strongly depends on the given dead time of the photon counting system. Therefore, a careful investigation on the dead

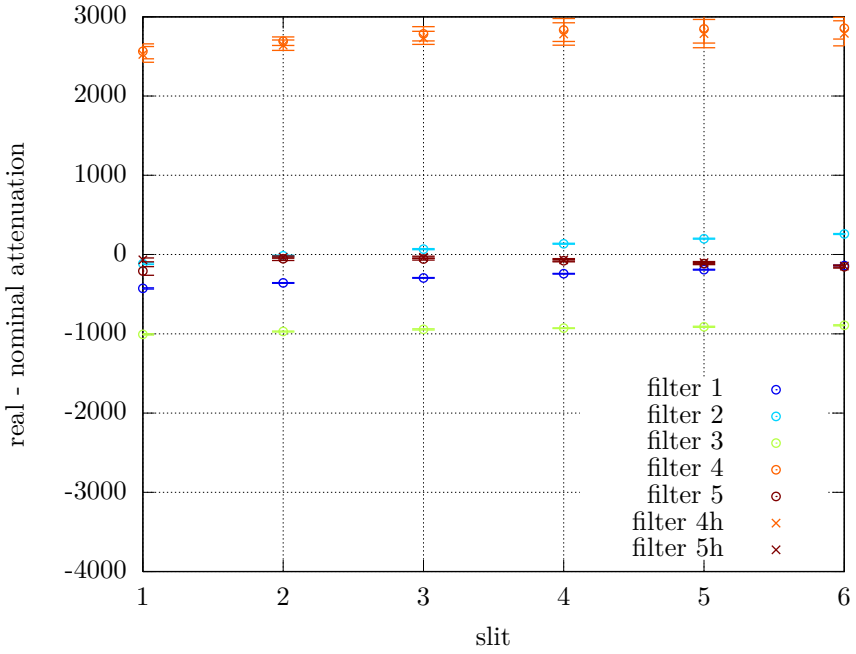

Figure 4.12: Difference between real and nominal spectral attenuations of filters, in the same units as F_i. Points were calculated as medians of many measurements. Standard deviations are represented as whiskers.

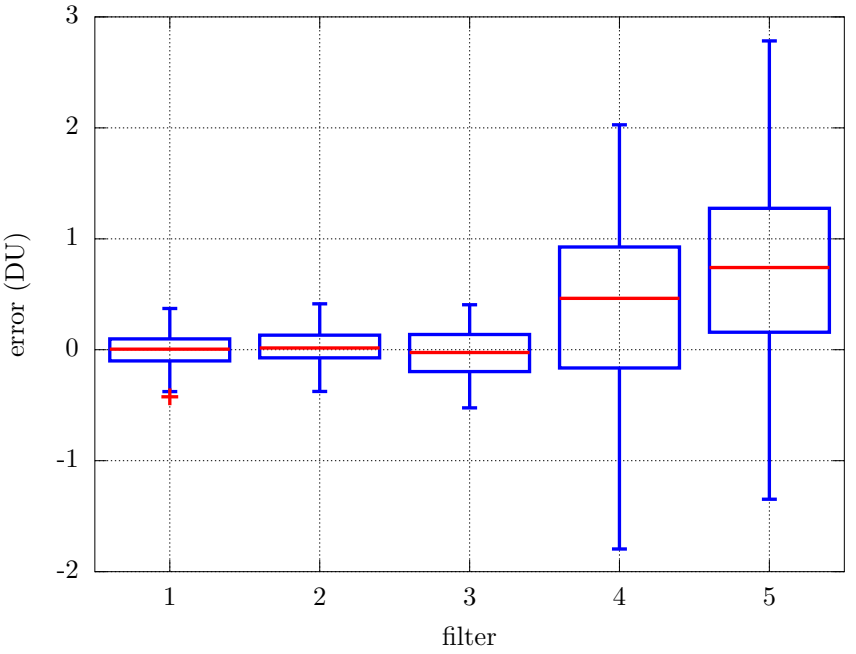

Figure 4.13: Boxplot of the effect (expressed in Dobson Units) introduced by the filters on the NO_2 retrieval. Attenuation of filter 1 is the weakest (about $10^{0.5}$), while filter 5 is the strongest (attenuation about $10^{2.5}$).

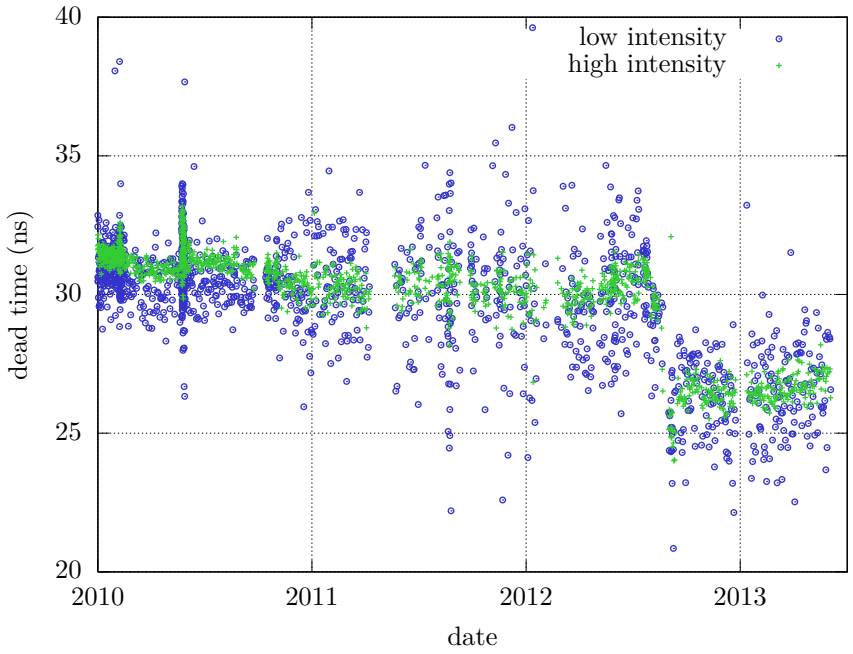

Figure 4.14: Series of the dead time recorded by Brewer #066 (`o3` mode, `dt` routine) for both high and low intensities. Due to noise, the low intensity series is more scattered. A discontinuity can be noticed in August 2012.

time, which is also essential to the data reduction process, was performed.

4.1.3 Dead time

The dead time (Sect. 3.3.2) of the photon counting system for Brewer #066 was determined using three different approaches, which approximately gave the same value, of about 27±1 ns (after August 2012):

using the standard lamp. The `dt` routine was scheduled in `n2` mode every night during the period of my Ph.D. Results in `n2` mode and `o3` mode are substantially identical;

using the sun. I modified the `dt` routine to use the sun as a source, as in the direct sun measurements, instead of the internal lamp. Indeed, the measured dead time may vary with different intensities. Since high intensities are characteristics of real measurements, this value should be more representative than the one from the `dt` routine using the internal lamp;

Langley plot. During a Langley calibration (next chapter), the suitability of the value used for the dead time was checked by looking at the continuity of the corrected count rates at the moment the Brewer inserts a different neutral density filter. Indeed, when the recorded intensity is close to the upper limit and the Brewer is nearly ready for a filter change, the photon number is very high and the dead time correction is maximum. Conversely, when the intensity is lower (filter with higher attenuation), the dead time correction is less important. If the data reduction is correctly performed, no "jumps" should be seen in the count rates.

Due to the overfilling of the PMT resulting from some experiments, the dead time permanently changed after August 2012 (Fig. 4.14), a phenomenon which has been rarely observed before (Savastiouk, personal communication, 2012). The variation will be taken into account in further analyses.

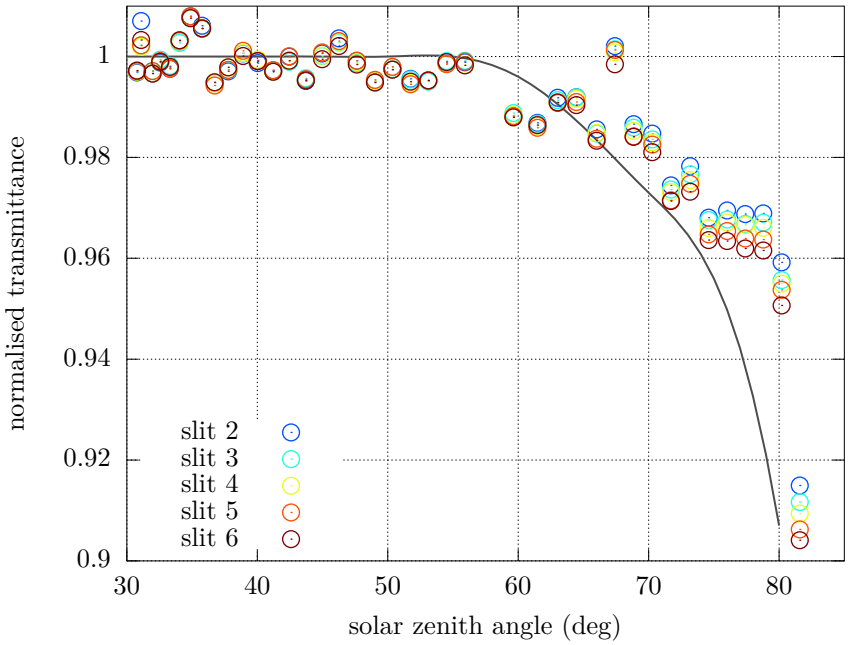

Figure 4.15: Effect of Brewer #066 internal polarisation on direct sun irradiances for `n2` mode. The thick line represents the polarisation effect expected by the theory, while circles are real data obtained from the ratio of the count rates with and without the quartz window.

4.1.4 Internal polarisation

As noticed by Cede et al. (2006b), some of the Brewer internal components (mainly the quartz window, through Fresnel effects, and the diffraction grating) are able to polarise the direct sun light entering in the instrument. As a result, an error is introduced, which depends on the angle between the sun and the normal to the quartz window plane. The effect must be taken into account when dealing with absolute irradiance levels, e.g. when measuring the aerosol optical depth and during a Langley plot (next chapter).

In order to characterise the internal polarisation effect in Brewer #066, "method 3" in the paper by Cede et al. (2006b) was used: I measured the solar direct spectral irradiance at several UV and visible wavelengths, corresponding to the slits used by the standard algorithm, with the quart window and removing it by hands (which is an unconventional procedure), for solar zenith angles ranging from 30° to 80°. Each measurement without the quartz window was preceded and followed by measurements through the window. The ratio of the measurements with and without quartz window at a solar zenith angle of 35° (i.e. sun perpendicular to the window and no Fresnel effects) represents the transmission of the quartz window.

Results for `n2` and `o3` modes are displayed in Figs. 4.15 and 4.16, respectively. While results in `n2` mode mostly lie on the line expected by the electromagnetic theory, data obtained in `o3` mode are very far from the expectations. This is probably to ascribe to the straylight present in the single monochromator of Brewer #066, which is larger for UV irradiances. Straylight has a small effect also in the visible range, which manifests as larger scatter among irradiances at different wavelengths for higher solar zenith angles.

The test also revealed that measurements for solar zenith angles higher than 78.3° are affected by edge effects due to shadow from the quartz window border.

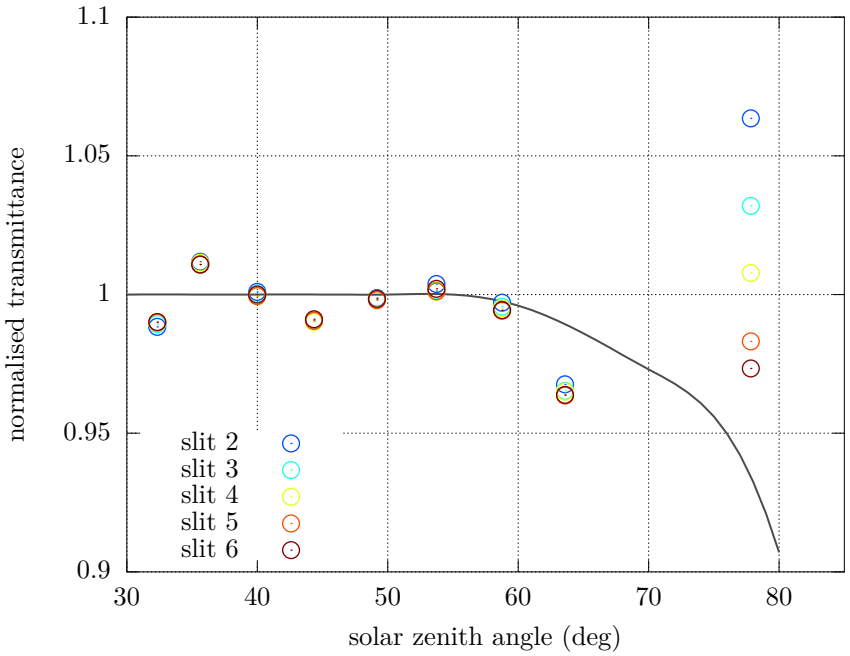

Figure 4.16: Same as Fig. 4.15, but for `o3` mode.

4.1.5 Effect of temperature

To analyse the effect of the Brewer internal temperature on the NO_2 retrieval, I reprocessed the full series of standard lamp measurements and calculated the linear combination, $\mathscr{F}$, from the count rates (Fig. 4.17). Any effect by the internal temperature should manifest as an annual cycle in the linear combination, since the internal temperature is influenced by the intensity of solar radiation and the external temperature, which both vary on an annual scale. However, no cycles were observed in the full series.

Moreover, I organised a second experiment: the Brewer was cooled down to 10 °C using several ice packs, then heated up to 40 °C by covering it with a blanket while exposing it to the sun. The standard lamp ratios were continually monitored. Again, no dependency on temperature was found.

The results agree with previous findings reported in literature (Meltzer et al., 2000; Weatherhead et al., 2001), i.e. the Brewer temperature dependency should be mostly attributed to the $NiSO_4$ filter, which is only used in UV measurements.

As a consequence, no temperature correction was performed in `n2` mode.

4.1.6 Light from viewing ports

Two viewing ports along the foreoptic assembly (Fig. 4.18) allow the user to view any images focused onto the iris diaphragm and the entrance slit. The viewing ports are covered with a plexiglass lid, which is opaque to the UV radiation (ozone measurements), but could be semitransparent to the visible radiation (nitrogen dioxide measurements with MKIV Brewer and ozone measurements with MKV models). In order to assess the influence of the light through the ports, I took several measurements with and without a thick piece of cardboard onto the plexiglass lid. Zenith sky measurements were performed for the purpose, which are probably more contaminated because of the lower intensity of the measured light.

Figure 4.19 shows the count rates observed with and without the cover on September, 6th 2011. Although the differences are less than 1%, the effect is clearly noticeable. Therefore, all following

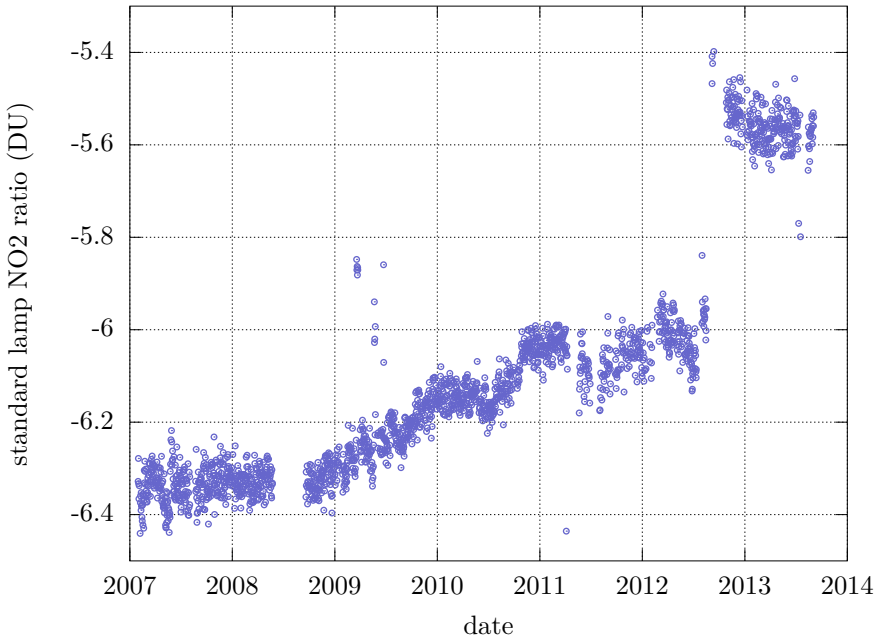

Figure 4.17: Full series of standard lamp ratios. No dependency on temperature is visible.

NO_2 measurements, especially during the calibration campaigns, were taken with a thick cover onto the viewing ports.

4.1.7 Straylight in the UV range

During the Izaña campaign (next chapter), a UV Helium-Cadmium laser was used to characterise the straylight in `o3` mode. Although this issue is not directly related to the measurement of nitrogen dioxide, the main findings are here described for completeness and because they can be useful for further research about the straylight effect in single monochromator Brewers.

The laser emitted a monochromatic beam at a wavelength of 325 nm and was switched on in a dark room together with Brewer #066. The Brewer was programmed to scan the line with slits 2–6 to retrieve not only the slit function (wavelengths close to the emission), but also the response at wavelengths far from 325 nm, which are connected to the straylight. After the data reduction process and normalisation to the maxima, Figs. 4.20 and 4.21 were obtained, in terms of wavelengths and micrometer steps, respectively. It is interesting to notice that the feature at the left "wing" of the graph is a function of the micrometer step, namely the grating position, and not of wavelength. Furthermore, its contribution varies with the slit. This proves that the effect of straylight cannot be simply calculated as a convolution between a "real" spectrum and the straylight function, since some features depends on the grating position and other on wavelength.

A visible laser would be required to determine the Brewer straylight in `n2` mode, which is however expected to be much lower than in the UV range. This could be an interesting integration to my Ph.D. work.

Figure 4.18: Brewer viewports with plexiglass lid.

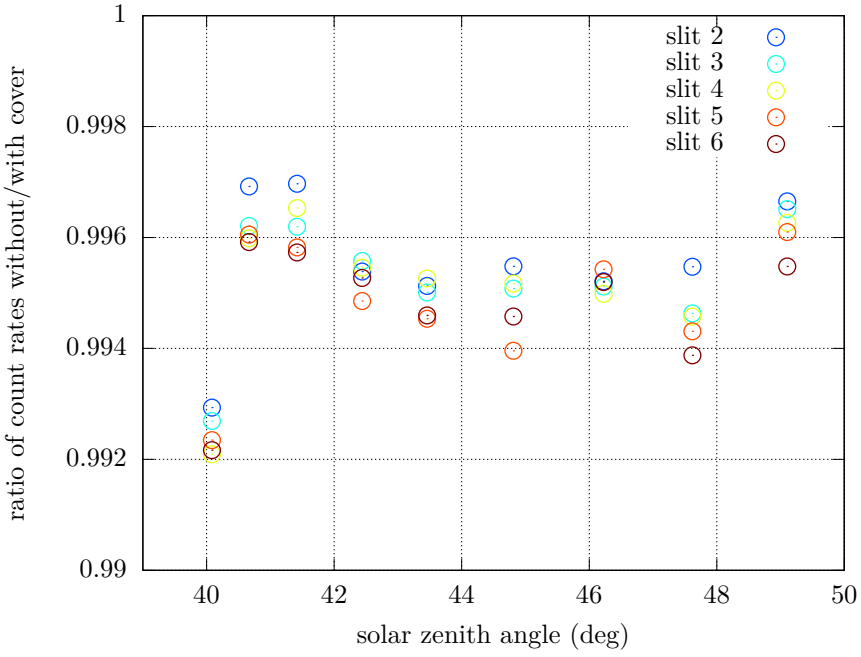

Figure 4.19: Ratio of recorded count rates without and with a thick cover on September, 6th 2011.

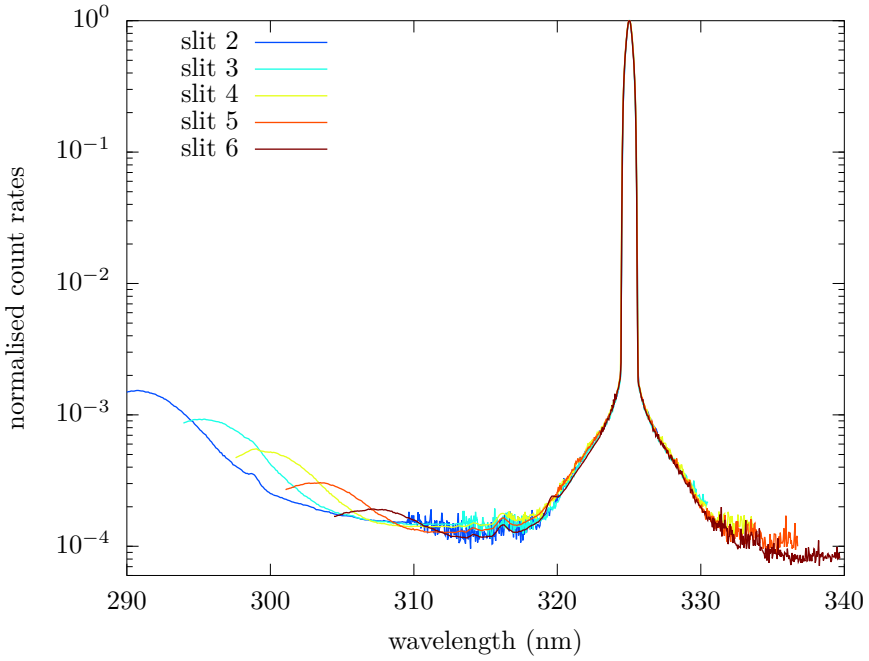

Figure 4.20: Semilogarithmic plot of the normalised count rates from slits 2–6 during the straylight assessment using a He-Cd laser.

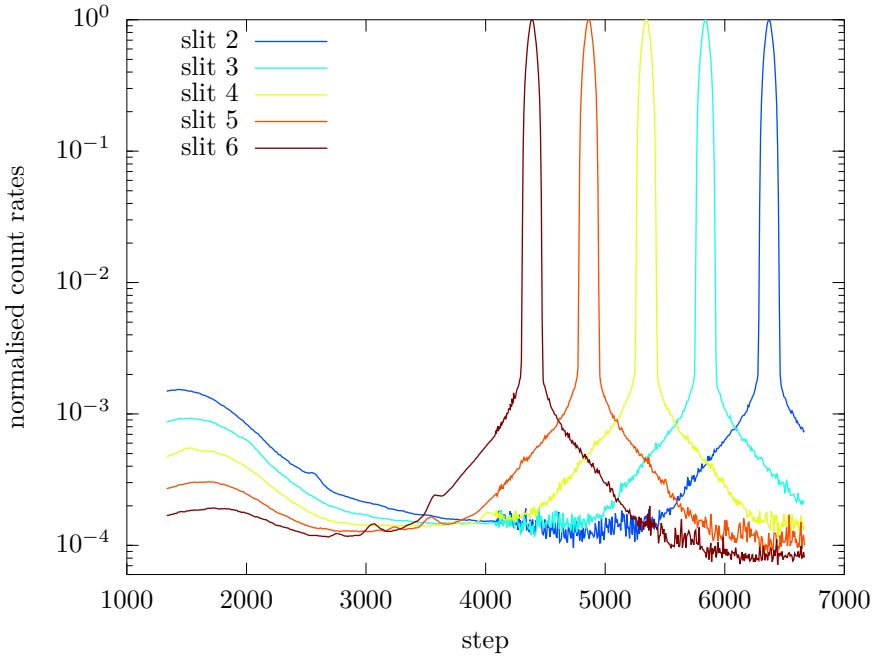

Figure 4.21: Same as 4.20, but in terms of micrometer steps instead of wavelength.

4.2 Updates to the NO_2 retrieval algorithm

A new mathematical framework was introduced in order to understand in more depth how the algorithm works and to easily introduce the necessary improvements. Then, the influence of several factors, both natural and instrumental, on the retrieved NO_2 was assessed based on the instrumental characterisation described in the previous section and by perturbing the Brewer equation (Eq. 3.35). This parameterisation revealed to be fundamental to "tune" the algorithm for best performances. Then, I introduced several innovations and I developed two different techniques to overcome the current limitations. Radiative transfer calculations, one of the fundamental tasks in my Ph.D. work, will be described in detail. The results of this section were presented at the SPIE meeting (Diémoz et al., 2013).

4.2.1 Mathematical framework

Let's start from the fundamental Brewer Eqs. 3.29, modified to include an arbitrary number of wavelengths, $i = 1...M$, and different atmospheric species in addition to ozone (j index):

$$\begin{cases} \sum_{i=1}^{M} \gamma_i \, \lambda_i^{-4} \equiv 0 \\ \sum_{i=1}^{M} \gamma_i \, \alpha_{ji} \equiv 0 \\ \sum_{i=1}^{M} \gamma_i \, \lambda_i^{-1} \equiv 0 \\ \sum_{i=1}^{M} \gamma_i \equiv 0 \end{cases} \tag{3.29}$$

Linear algebra may be of help in interpreting the above equations from a geometrical point of view. Indeed, the formulae express scalar products in an M-dimensional space:

$$\begin{cases} \vec{\gamma} \cdot \overrightarrow{\beta_R} \equiv 0 \\ \vec{\gamma} \cdot \overrightarrow{\alpha_j} \equiv 0 \\ \vec{\gamma} \cdot \overrightarrow{\delta_A} \equiv 0 \\ \vec{\gamma} \cdot \vec{1} \equiv 0 \end{cases} \tag{4.4}$$

where $\vec{1}$ is a vector of ones $(1, ..., 1)^{\mathrm{T}}$. The problem can then be reformulated by finding a vector $\vec{\gamma}$ that I will call "measurement vector", perpendicular to N given vectors:

$$\begin{cases} \vec{\gamma} \perp \overrightarrow{\beta_R} \\ \vec{\gamma} \perp \overrightarrow{\alpha_j} \\ \vec{\gamma} \perp \overrightarrow{\delta_A} \\ \vec{\gamma} \perp \vec{1} \end{cases} \tag{4.5}$$

$M - N$ should be at least 1, in order to allow solutions different from the trivial one ($\vec{\gamma} = \vec{0}$). Indeed, at least one degree of freedom is necessary for the normalisation of $\vec{\gamma}$.

In the standard Brewer algorithm, irradiances obtained at only $M = 5$ wavelengths are used, which leads to $M - N = 1$ degree of freedom. By adding one or more slits to the measurement, as I will show in the following sections, the $\vec{\gamma}$ vector is also allowed to turn (Fig. 4.22), which can be exploited to improve the quality of the measurement, as described in the next section.

4.2.2 Signal-to-noise ratio (SNR) maximisation

A further step is required to explain the geometrical interpretation of the measurement vector: in this section, I will show that the best SNR in the nitrogen dioxide retrieval is found when $\vec{\gamma}$ is as parallel as possible to the NO_2 absorption coefficient vector, $\overrightarrow{\alpha_{NO_2}}$.

A theoretical calculation of the expected noise in the determination of nitrogen dioxide can be performed by assuming Poisson noise in the measured count rates (including the dark signal) and propagating it through Eq. 3.35. The variance of the noise on the slant column density $S_{NO_2} = \mu_{NO_2} X_{NO_2}$ is then

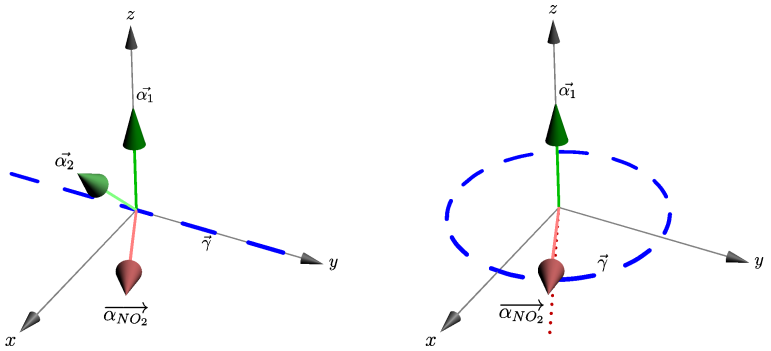

Figure 4.22: Simplified representation of the weightings optimisation in a 3-dimensional space. In the first case (left), two constraints ($\vec{\alpha_1}$ and $\vec{\alpha_2}$) are imposed. The $\vec{\gamma}$ vector, forced to be perpendicular to $\vec{\alpha_1}$ and $\vec{\alpha_2}$ (Eqs. 4.4), can only extend along the y direction (dashed blue line). When one of the constraints is loosen ($\vec{\alpha_2}$, right figure), one degree of freedom is added to the system and the $\vec{\gamma}$ vector can turn in the plane perpendicular to $\vec{\alpha_1}$. The best SNR, as explained in Sect. 4.2.2, is reached when $\vec{\gamma}$ is placed as parallel as possible to the NO_2 absorption coefficient vector (the projection of the NO_2 vector on the $x-y$ plane is shown as a dotted red line). This is the principle employed to reduce the measurement noise.

$$\sigma^2_{S_{NO_2}} = \left(\frac{1}{\sum \gamma_i \, \alpha_{NO_2 i}}\right)^2 \left[\sum \frac{{\gamma_i}^2}{p_i} + \left(\sum \frac{\gamma_i}{p_i}\right)^2 p_d\right] \tag{4.6}$$

where p_i is the number of photons passing through slit i and p_d is the number of photons forming the dark current during the measurement.

Derivation of Eq. 4.6. From Eq. 3.20, the count rates measured by the Brewer photon counting system at slit i are equal to the number of collected photons, p_i, in a given time interval, Δt

$$R_i = \frac{p_i}{\Delta t} \tag{4.7}$$

Assuming Poisson statistics for the photons distribution,

$$\sigma_{p_i} = \sqrt{p_i} \tag{4.8}$$

the resulting standard deviation of the signal will be

$$\sigma_{R_i} = \frac{\sigma_{p_i}}{\Delta t} = \sqrt{\frac{R_i}{\Delta t}} \tag{4.9}$$

The standard deviation of the retrieved NO_2 SCDs, S_{NO_2}, can be determined by propagating the count rates standard deviation through Eq. 3.35:

$$\frac{\partial S_{NO_2}}{\partial R_i} = -\frac{1}{\Delta \alpha_{NO_2}} \frac{\gamma_i}{R_i} \tag{4.10}$$

and

$$\sigma^2_{S_{NO_2}} = \sum_i \left(\frac{\partial S_{NO_2}}{\partial R_i} \right)^2 \sigma^2_{R_i} = \frac{1}{\Delta\alpha^2_{NO_2}} \sum_i \frac{\gamma_i^2}{R_i \, \Delta t} \tag{4.11}$$

The larger is the photons number p_i thought a slit, the lower will be the contribution of the slit to the total S_{NO_2} uncertainty.

Furthermore, when considering the contribution of the dark signal R_d,

$$\frac{\partial S_{NO_2}}{\partial R_i} = -\frac{1}{\Delta\alpha_{NO_2}} \frac{\gamma_i}{R_i - R_d} \tag{4.12}$$

$$\frac{\partial S_{NO_2}}{\partial R_d} = \frac{1}{\Delta\alpha_{NO_2}} \sum_i \frac{\gamma_i}{R_i - R_d} \tag{4.13}$$

$$\tag{4.14}$$

Simple calculations give Eq. 4.6. ■

If p_i is similar for all slits, then the variance is primarily driven by the term $\frac{\sum_i \gamma_i^2}{(\sum_i \gamma_i \, \alpha_{NO_2 i})^2}$ which should be minimised. Recalling that

$$\sum_i \gamma_i^2 = \|\vec{\gamma}\|^2 \tag{4.15}$$

$$(\sum_i \gamma_i \, \alpha_{NO_2 i})^2 = (\vec{\gamma} \cdot \overrightarrow{\alpha_{NO_2}})^2 \tag{4.16}$$

it is clear that a unit vector $\hat{\gamma}$ must be found which has the same direction of $\overrightarrow{\alpha_{NO_2}}$. In other terms, $\vec{\gamma}$ must be as parallel as possible to the NO_2 vector $\overrightarrow{\alpha_{NO_2}}$. This condition can be added to Eqs. 4.5:

$$\begin{cases} \vec{\gamma} \perp \overrightarrow{\beta_R} \\ \vec{\gamma} \perp \overrightarrow{\alpha_j} \\ \vec{\gamma} \perp \overrightarrow{\delta_A} 0 \\ \vec{\gamma} \perp \vec{1} \\ \vec{\gamma} \parallel \overrightarrow{\alpha_{NO_2}} \end{cases} \tag{4.17}$$

where the $\parallel$ symbol should be read "as parallel as possible" rather than "strictly parallel".

Interestingly, the supplementary condition also minimises the influence of unaccounted species, as will be shown in the Sect. 4.2.3. It is thus fundamental to leave some degrees of freedom, $M - N$, to the system, in order to allow the $\vec{\gamma}$ vector to turn and position itself as parallel as possible to $\overrightarrow{\alpha_{NO_2}}$ (Fig. 4.22).

Actually, p_i is different for each slits, which forces $\vec{\gamma}$ to rotate on an (hyper-)ellipsoid instead of on a (hyper-)sphere. However, numerical simulations give similar results in both cases.

In order to quantitatively determine the SNR term in Eq. 4.6 some scans in the visible range were taken with the Brewer on a clear summer day (July, 14th 2012) and are represented in Fig. 4.23. The dead time correction was not applied to estimate the noise, as suggested by Kiedron (2007). The data will be useful later in the text (e.g. Sect. 4.3).

4.2.3 Interference by unaccounted atmospheric species

The optical depths of major atmospheric absorbers for unity air mass in the MKIV Brewer wavelength range are depicted in Fig. 4.24. To determine them, I multiplied the respective cross sections, whose values are tabulated in the scientific literature, by the typical concentration of

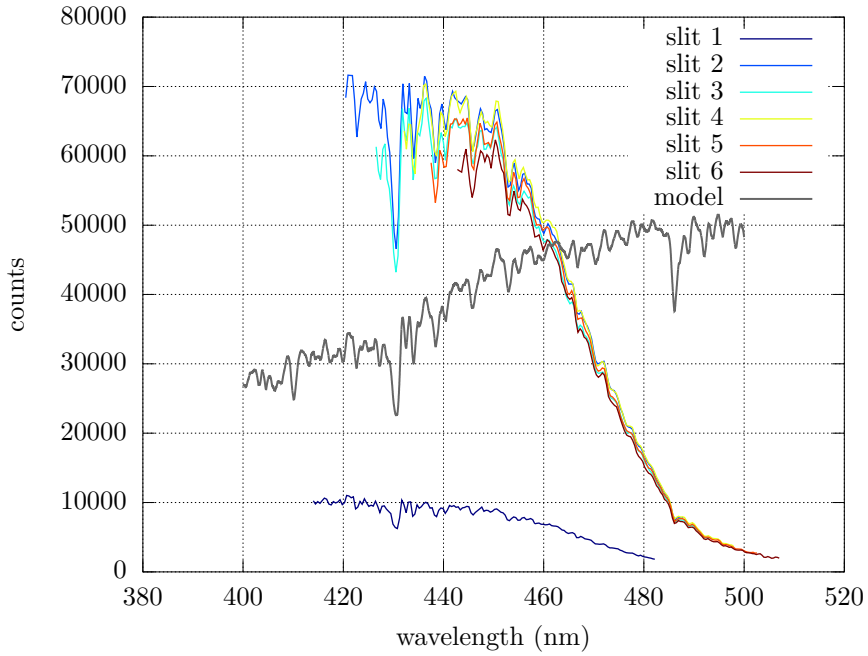

Figure 4.23: Raw counts measured by the Brewer on a sunny day through all slits in the visible range. The output from a radiative transfer model, calculated at the Brewer resolution, is also drawn, on the same scale of the graph, to highlight the correlation of the Fraunhofer structure with the measurements. The figure also clearly shows the decreasing Brewer responsivity at higher wavelengths.

the absorbers. In order to draw the graph, ozone and nitrogen dioxide concentrations were set to 315 DU and 1 DU, respectively, as in Cede et al. (2006a). I calculated the optical depth of water vapour by assuming a completely saturated atmosphere, as in Barton (2007), and the optical depth of the oxygen dimer for a U.S. standard atmosphere (NASA and USAF, 1976). Finally, typical concentrations of glyoxal (CHOCHO) from Wittrock et al. (2006) were used.

Then, I calculated the error on the NO_2 slant column retrieval if one of the absorbing species, denoted by x, is not accounted for in the algorithm:

$$\varepsilon_x = S_x \frac{\sum_i \gamma_i \, \alpha_{x\,i}}{\sum_i \gamma_i \, \alpha_{NO_2 i}} \tag{4.18}$$

where $\alpha_{x\,i}$ is the absorption coefficient of species x at the wavelength corresponding to slit i and S_x is the SCD of species x.

Derivation of Eq. 4.18. I rewrote Eq. 3.31 with and without taking account for the species x. Obviously, the NO_2 SCD obtained from the latter relation is erroneous, since the influence of x was neglected:

$$\mathscr{F} = \mathscr{F}_0 - S_{NO_2} - S_x \frac{\sum_i \gamma_i \, \alpha_{x\,i}}{\Delta\alpha_{NO_2}} \tag{4.19}$$

$$\mathscr{F} = \mathscr{F}_0 - S^{err}_{NO_2} \tag{4.20}$$

By subtracting the second equation from the first, the error is obtained:

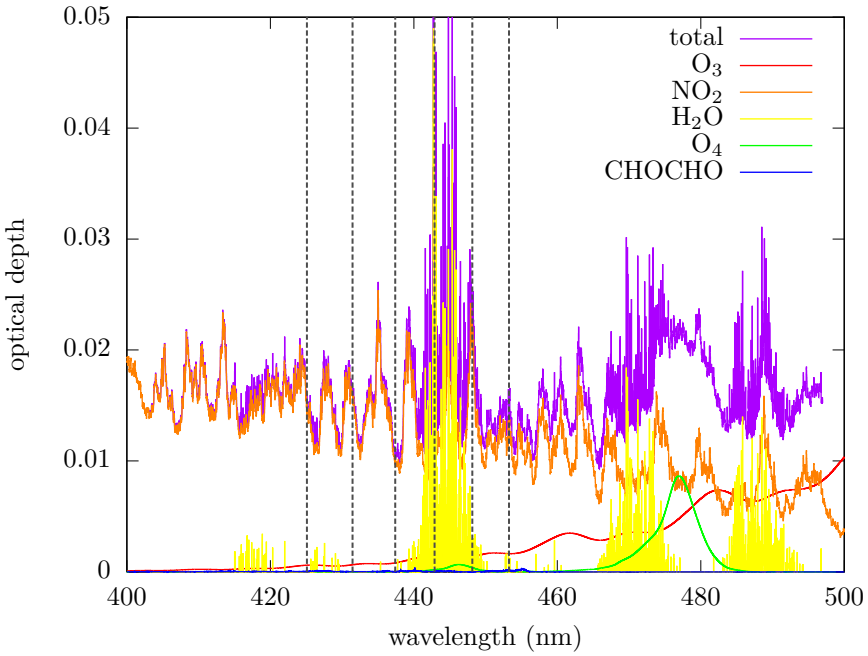

Figure 4.24: Optical depths of major atmospheric absorbers for AMF=1 in the MKIV Brewer wavelength range. The sum of all optical depths is drawn as a violet line. The wavelengths used by the Brewer at the standard grating position are shown as dashed vertical lines.

$$\varepsilon_x = S^{err}_{NO_2} - S_{NO_2} = S_x \frac{\sum_i \gamma_i \, \alpha_{x\,i}}{\sum_i \gamma_i \, \alpha_{NO_2 i}} \tag{4.21}$$

which is Eq. 4.18. ■

Again, Eq. 4.18 may be rewritten in terms of scalar products:

$$\varepsilon_x = S_x \frac{\vec{\gamma} \cdot \overrightarrow{\alpha_x}}{\vec{\gamma} \cdot \overrightarrow{\alpha_{NO_2}}} \tag{4.22}$$

Therefore, the error is maximum if the absorption coefficient vector of species x is parallel to the NO_2 absorption coefficient vector, namely in case of collinearity. This makes both S_x and S_{NO_2} unmeasurable. As we will see later in the text (Sect. 4.3.2), that will be the case of the effective temperature of nitrogen dioxide.

4.2.4 Parameterisation of Ring effect

The Ring effect in zenith sky measurements (Sect. 3.1.3) is not taken into account in the standard algorithm. To assess the error induced by neglecting the Ring effect and try to minimise it using the techniques explained further in the text, I again perturbed the Brewer equation and obtained:

$$\varepsilon_{Ring} = \frac{1}{\Delta\alpha_{NO_2}} \sum_i \gamma_i \left(\frac{I^{inel}(\lambda_i) - I^{el}(\lambda_i)}{I^{el}(\lambda_i)} \right) \tag{4.23}$$

where I_{inel} and I_{el} are the irradiances determined at wavelength λ_i with and without the contribution of the inelastic rotational Raman scattering, respectively.

Derivation of Eq. 4.23. Equation 3.30 may be written twice, once considering real inelastic scattering in the atmosphere and once considering only elastic scattering, as done in the standard algorithm. The NO_2 SCD obtained from the latter relation is erroneous, since the influence of the Ring scattering was neglected:

$$\sum_i \gamma_i F_i^{inel} = \sum_i \gamma_i F_{0i} - S_{NO_2} \Delta\alpha_{NO_2} \tag{4.24}$$

$$\sum_i \gamma_i F_i^{el} = \sum_i \gamma_i F_{0i} - S_{NO_2}^{err} \Delta\alpha_{NO_2} \tag{4.25}$$

After subtracting,

$$\varepsilon_{Ring} = S_{NO_2}^{err} - S_{NO_2} = \frac{1}{\Delta\alpha_{NO_2}} \sum_i \gamma_i \left(F_i^{inel} - F_i^{el}\right) \tag{4.26}$$

Recalling the logarithmic nature of F_i (Sect. 3.4.1), we can write

$$F_i^{inel} - F_i^{el} = \log \frac{I_i^{inel}}{I_i^{el}} = \log \frac{I_i^{el} + I_i^{inel} - I_i^{el}}{I_i^{el}} \tag{4.27}$$

where I_i is the measured solar irradiance at wavelength λ_i. Since the term $I_i^{inel} - I_i^{el}$ is a small perturbation compared to I_i^{el}, a Maclaurin expansion of the logarithm is allowed (Wagner et al., 2001):

$$\log \frac{I_i^{el} + I_i^{inel} - I_i^{el}}{I_i^{el}} = \log\left(1 + \frac{I_i^{inel} - I_i^{el}}{I_i^{el}}\right) \simeq \frac{I_i^{inel} - I_i^{el}}{I_i^{el}} \tag{4.28}$$

which gives Eq. 4.23. ■

By comparing Eqs. 4.23 and 4.18, it becomes evident that the Ring effect can be parameterised as an additional, fictitious absorber having its own "absorption coefficient".

From Eq. 4.23, I calculated the Raman scattering contribution at ground using a radiative transfer code (Kylling et al., 2011) and the extraterrestrial spectrum from Chance and Kurucz (2010). Calculations were performed in terms of unpolarised global irradiances, as no current model is able to couple the Raman effect with full spherical geometry and vector simulations (Barton, 2007; Rozanov, personal communication, 2013). However, since the aim of the calculations is to find the optimal instrumental settings to minimise the Ring effect, unpolarised calculations are adequate as well.

4.2.5 Effective temperature of nitrogen dioxide

Another factor may influence the accuracy of the determination of NO_2. The absolute values of the nitrogen dioxide cross section and its differential structure depend on temperature (Sanders, 1996; Vandaele et al., 2002), as shown in Fig. 3.6. However, neither the density profile of the absorber nor the atmospheric temperature profile - which are necessary for the estimation of the NO_2 effective temperature - are known *a priori*. If the real NO_2 effective temperature is different from the temperature of the cross section measured in the laboratory and used in the algorithm, the estimate of NO_2 is affected. The resulting error may be parameterised as

$$\varepsilon_T = S_{NO_2} \left(\frac{\sum \gamma_i \alpha_{NO_2 i}(T)}{\sum \gamma_i \alpha_{NO_2 i}(T^{err})} - 1 \right) \tag{4.29}$$

where T and T_{err} are the effective and assumed temperatures of nitrogen dioxide, respectively.

It must be noticed that the error depends on the NO_2 slant column. A linear dependence of the absorption coefficient on the temperature, as reported in the scientific literature (Vandaele et al., 2003), may be easily included in the above equation.

Derivation of Eq. 4.29. Let's write Eq. 3.30 and consider the "true" effective temperature T and the assumed temperature T^{err} of nitrogen dioxide in the atmosphere:

$$\sum_i \gamma_i F_i = \sum_i \gamma_i F_{0i} - S_{NO_2} \sum_i \gamma_i \alpha_{NO_2 i}(T) \tag{4.30}$$

$$\sum_i \gamma_i F_i = \sum_i \gamma_i F_{0i} - S^{err}_{NO_2} \sum_i \gamma_i \alpha_{NO_2 i}(T^{err}) \tag{4.31}$$

by subtracting every term of the first line to the second line,

$$S_{NO_2} \sum_i \gamma_i \alpha_{NO_2 i}(T) = S^{err}_{NO_2} \sum_i \gamma_i \alpha_{NO_2 i}(T^{err}) \tag{4.32}$$

and considering that $\varepsilon_T = S^{err}_{NO_2} - S_{NO_2}$, Eq. 4.29 is obtained. ■

4.2.6 Wavelength misalignments

Even some slight instrumental inaccuracies must be taken into account and their effect minimised by the algorithm. Such instrumental features can be parameterised and treated as fictitious absorbers as well. For instance, slight wavelength misalignments of the monochromator may occur during the day, even though the diagnostic tests are correctly performed. The error may be parameterised as

$$\varepsilon_{mis} = -\Delta\lambda \frac{\sum \gamma_i \Gamma_i}{\Delta\alpha_{NO_2}} \tag{4.33}$$

where $\Delta\lambda$ is the wavelength misalignment and Γ_i is the first derivative of the logarithm of the solar spectrum with respect to λ at wavelength λ_i.

Derivation of Eq. 4.33. I first considered a small wavelength misalignment, $\Delta\lambda$, in the recorded F_i – i.e. the logarithm of the count rates – and linearised at the first order the resulting function:

$$F(\lambda_i + \Delta\lambda) \simeq F(\lambda_i) + \frac{\partial F(\lambda)}{\partial \lambda}\Big|_{\lambda_i} \Delta\lambda \tag{4.34}$$

After applying the linear combination using the weighting factors,

$$\sum_i \gamma_i F_i \simeq \sum_i \gamma_i F_{0i} - S^{err}_{NO_2} \sum_i \gamma_i \alpha_{NO_2 i} - \Delta\lambda \sum_i \gamma_i \frac{\partial F(\lambda)}{\partial \lambda}\Big|_{\lambda_i} \tag{4.35}$$

The last term in the above equation can be interpreted as a fictitious absorber. From Eq. 4.18, we already know how to easily calculate the error resulting from an unaccounted species and Eq. 4.33 can be obtained. ■

4.2.7 New methods to retrieve nitrogen dioxide

From Table 4.4, it can be noticed that the number of the interfering factors in the Brewer MKIV spectral range is higher than the number of wavelengths used in the standard algorithm. The latter is thus a naive approximation and cannot take into account the complexity of the measurement.

Table 4.4: Influencing factors in the MKIV Brewer spectral range.

factor	accounted for in standard algorithm
absorption by O_3	X
absorption by NO_2	X
Rayleigh scattering	X
Mie scattering	X
spectrally-flat factors	X
absorption by O_4	
absorption by H_2O	
Ring effect	
NO_2 effective temperature	
wavelength misalignments	

In mathematical terms, the system is underdetermined, since the number of equations ($M = 5$) is lower than the number of the unknowns, N (at least, 10). Ideally, in such a situation two approaches can be chosen: either decreasing the unknowns, N, or increasing the equations, M. In the first case, I introduced one supplementary degree of freedom in the updated algorithm: the grating position, determined by the micrometer, is adjusted so that some of the previously listed effects are removed (or, at least, significantly reduced), thus decreasing the unknowns. In the second case, a new technique ("jump scan"), inspired by the "Umkehr" method for the estimation of the ozone profiles and the algorithm by Kerr (2002), was developed to increase the measured wavelengths.

In brief, the following two methods are proposed:

method 1. The first slit, which is routinely used in the `hg` test in the `o3` mode but not in the ozone measurements, was added in the algorithm as in Cede et al. (2006a) and Barton (2007). Solar irradiance is thus recorded at six wavelengths, one more than in the standard Brewer NO_2 algorithm. The influence of the oxygen dimer, water vapour, Ring effect, NO_2 effective temperature and wavelengths misalignments is minimised and the SNR is maximised by finding an optimal grating position. For this purpose, I made use of the parameterisations obtained in Eqs. 4.6–4.33. The residual influence by the oxygen dimer can be further reduced by calculating a correction factor using a radiative transfer model (Sect. 4.4) and knowing the atmospheric pressure at the measurement site. The number of the equations is $M = 6$ and the retrieved unknowns are $N = 4$, which leaves two degree of freedom: one for the normalisation of $\vec{\gamma}$ and one to optimise the SNR, as explained in Sect. 4.2.2.

method 2. A "jump scan" consisting of three phases at two different grating positions is performed (Fig. 4.25) in order to increase the measurements (M) and overconstrain the system ($M > N$). The two grating positions were chosen so that a selected pair of different slits superimpose, which can provide precious information about the variability of the atmosphere during the scan, e.g. because of changing cloud cover. In this way, the number of independent pieces of information is increased to $M = 12 - 1 = 11$. The absorption by the oxygen dimer and water vapour in the blue spectral range (Wagner et al., 2013) can thus be included in the retrieval, while the influence of the Ring effect, NO_2 effective temperature and wavelengths misalignments is minimised and the SNR is maximised as in method 1.

Both methods were implemented making use of pseudoinverse matrices and the singular value decomposition (SVD) technique (Meyer, 2000).

4.2.8 Updated spectroscopic data

All spectroscopic data used in the standard algorithm were updated using recent laboratory measurements.

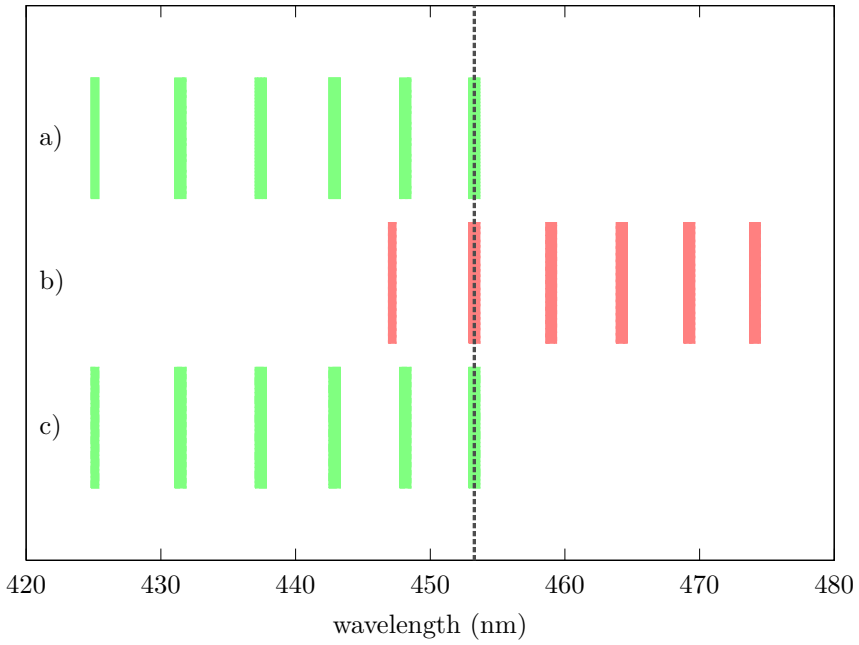

Figure 4.25: Example of wavelength settings in a "jump scan" (method 2). The measurement consists of three consecutive phases (`a`, `b`, `c`). The grating is moved so that wavelength 6 at position `a` corresponds to wavelength 2 at position `b` (dashed vertical line). Then, the grating is moved back to its initial position and the average of the irradiances measured during phases `a` and `c` is analysed together with irradiances at phase `b`. Irradiances at coincident wavelengths are compared (using a transfer function to take into account the slightly different slit widths) in order to assess the stability of the atmospheric conditions during the jump scan.

The cross sections of the gases were chosen according to the most recent recommendations for NO_2 column retrievals from NDACC (Van Roozendael and Hendrick, 2012). For NO_2, I chose the cross section measured by Vandaele et al. (2002), which are also used in SAOZ instruments and in the SCIAMACHY satellite radiometer. Bogumil et al. (2003) cross sections, which are known to have excellent SNR in the visible range, were selected for ozone. I calculated the cross section of the oxygen dimer by multiplicating the oxygen concentration (Greenblatt et al., 1990) by the laboratory data from Hermans et al. (2003). Then, the O_4 optical depth was determined by integrating the profiles of the U.S. standard atmosphere from the selected site altitude to the top of the atmosphere. For water vapor, the Py4CATS software (Schreier and García, 2013) was used to compute the optical depth due to molecular absorption from a line-by-line spectroscopic database (Rothman et al., 2009).

A remarkable update concerns the Rayleigh scattering. Namely, the Rayleigh coefficients traditionally used in the Brewer ozone algorithm in the UV range were replaced with the data provided by Bodhaine et al. (1999) in the visible range.

Resolution of spectroscopic data

An interesting issue concerns the conversion of the spectroscopic data to the resolution of the Brewer. In the Brewer community, the absorption coefficients are traditionally convolved directly with the instrumental slit functions (Eq. 3.24) and the resulting data are used as "effective absorption coefficients". However, this procedure is not correct in principle: in actual measurements, in effect, the spectra – and not their logarithm – are filtered by the slit function (Aliwell et al., 2002). This is the so-called "I0-effect".

The solution I proposed makes use of a more complex convolution:

$$\alpha^\star \equiv -\frac{1}{S}\ \log \frac{\int I_0(\lambda)\, f(\lambda)\, \exp\left[-S\,\alpha(\lambda)\right] \mathrm{d}\lambda}{\int I_0(\lambda)\, f(\lambda)\, \mathrm{d}\lambda} \tag{4.36}$$

where $\alpha^\star$ is the effective absorption coefficient of a given species at the right resolution, S is an *a priori* value of the SCD of an absorber in the atmosphere, $I_0(\lambda)$ is the extraterrestrial solar spectrum, $\alpha(\lambda)$ is an absorption coefficient calculated from high resolution laboratory cross section and $f(\lambda)$ the slit function of the instrument. A derivation of the above equation is not given for sake of brevity, but can be found, for instance, in Platt and Stutz (2008).

A complete list of the improvements included in the updated algorithm compared to the standard Brewer NO_2 algorithm is reported in Table 4.5.

Table 4.5: List of the improvements included in the updated algorithm, for both methods (Sect. 4.2.7).

	Standard algorithm	New algorithm (method 1)	New algorithm (method 2)
dispersion function	UV dispersion function, polynomial	improved dispersion (Gröbner et al., 1998) specific for the visible	
number of wavelengths used in the algorithm	5	6	11
effect of filters non-linearity	neglected	included	
weightings and differential absorption coefficient	Kerr (1989)	recalculated for specific instrument	
micrometer position	default (slit 2 at 431.4 nm)	optimised to reduce noise and influence of other factors	
air mass enhancement factor	direct sun only (geometrical)	direct sun and zenith sky (model), polarised	
I0-effect	neglected	included	
NO_2 cross sections	Johnston and Graham (1976)	Vandaele et al. (2002), 220 K	
Rayleigh scattering coefficients	coefficients used for ozone in the UV	Bodhaine et al. (1999)	
O_3 cross sections	Vigroux (1952)	Bogumil et al. (2003), 223 K	
O_4	neglected	minimised and corrected	retrieved, Hermans et al. (2003)
H_2O	neglected	minimised	retrieved, HITRAN using Py4CATS
Ring effect	neglected	minimised, using spectrum from Chance and Kurucz (2010)	
signal-to-noise ratio (SNR)	neglected	maximised	
effect from wavelength misalignments	neglected	minimised	

4.3 Choice of operating wavelengths

The instrumental characterisation of Brewer #066 and the updates to the retrieval algorithm were described in the previous sections. The next step will focus on the choice of the optimal grating position – and the resulting operating wavelengths – which minimises the interference by other factors and maximises the SNR.

I accomplished several calculations to assess the performances of the algorithms at different grating positions (micrometer steps). First, the wavelengths corresponding to the slits at each micrometer step were calculated using the dispersion function determined during the instrumental characterisation (Sect. 4.1). Then, the set of weighting factors was retrieved at the specified grating position using several algorithms:

1. the standard algorithm with updated cross sections. Five slits are employed in the measurement and four constraints are imposed (removal of effects by Rayleigh and Mie scattering, ozone and a constant factor);

2. the updated algorithm (method 1 and 2) described in Sect. 4.2.7, with six and eleven slits, respectively;

3. the algorithm developed by Barton (2007), using six slits and five constraints (the additional constraint is represented by the removal of the oxygen dimer within the linear combination).

Finally, Eqs. 4.6–4.33 were used to assess the contribution of each interfering factor with each method. The results were plotted as graphs and carefully analysed to find an optimal compromise.

As an example, the simulated noise in NO_2 measurements for a unity air mass (sun at the zenith) is shown in Fig. 4.26. The real photon counts shown in Fig. 4.23 were used as inputs in Eq. 4.6. The obtained values refer to only one sample: obviously, the measurement noise can be further decreased by averaging a set of measurements: usually, 100 repetitions for the direct sun and 140 repetitions for the zenith sky geometry are scheduled. Method 1 generally represents a noticeable improvement compared to the standard algorithm: the addition of one slit prevents collinearity at some grating positions, where the standard algorithm shows spikes and nitrogen dioxide cannot be retrieved. Method 2, using 11 slits, reveals even better results, which derive from the overconstrained system. Noise is generally much higher in Barton's algorithm (e.g. about four times higher at step 1000) due to the effects of an additional constraint – the inclusion of O_4 – and the inability to minimise the measurement noise, as explained in Sect. 4.2.1 and Fig. 4.22.

The influence by the oxygen dimer, which is unaccounted in some of the algorithms, is depicted in Fig. 4.27. As an encouraging check, the updated method 2 and Barton's algorithm show no influence at all steps, since the contribution by O_4 was taken into account in the algorithm. Conversely, absorption by water vapour was only included in the updated algorithm, method 2, which is the only one to show no influence in Fig. 4.28. The latter graph was calculated in the case of a completely saturated atmosphere, as Barton (2007) did for just the standard grating position.

As further examples, the errors induced by the Ring effect, calculated for unpolarised zenith radiance at 80° solar zenith angle, and by a wavelength misalignment of 0.01 nm (corresponding to about 1 micrometer step, in the `n2` measuring mode) are plotted in Fig. 4.29 and 4.30.

Finally, the sensitivity on the effective temperature of nitrogen dioxide (Fig. 4.31) was retrieved using the cross sections by Vandaele et al. (2002) at 220 K suggested by NDACC (Van Roozendael and Hendrick, 2012) and 294 K (room temperature), assuming a NO_2 column of 1 DU. This values are rather high and only serve the purpose to find an upper limit of the error.

After simulating the effects of all known factors, I chose three grating positions that optimise the NO_2 measurements. The default micrometer step (1000) for Brewer #066, which was used to collect the Aosta measurements series since 2007, turned out to be a rather good position for the updated algorithm. This represents a lucky circumstance, since it allows to reprocess a long term series with high accuracy, as shown in the next chapters. In addition, I selected a second position at 1012, which should reduce the Ring effect while being very close to the default one. A third position was identified at step 2554, which promises good results, but very far from the default position, in

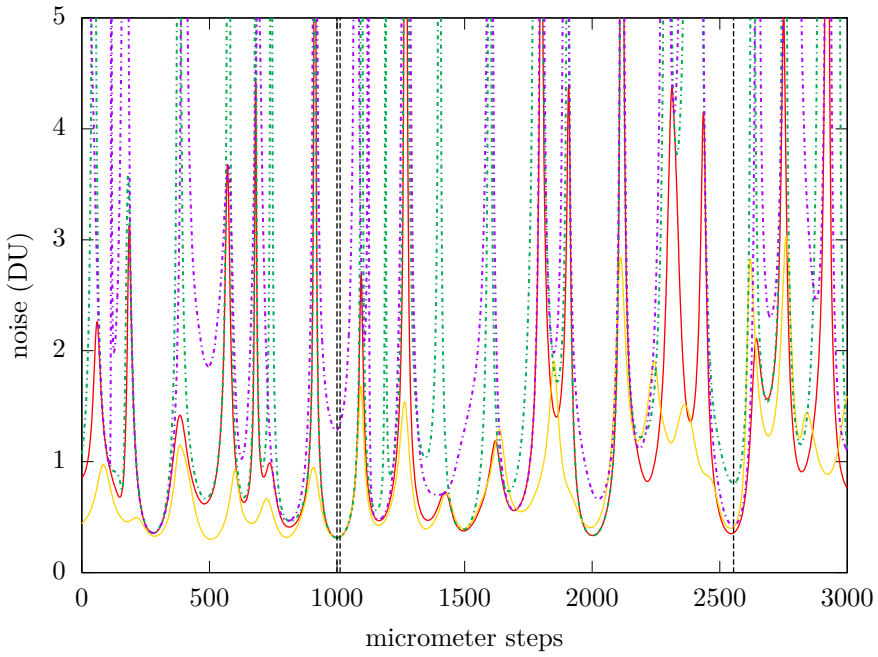

Figure 4.26: Diagram of expected measurement noise, expressed in the same units as the NO_2 column density, at different grating positions. The dashed green line refers to the standard algorithm. The solid lines identifies the updated algorithm using method 1 (red) and method 2 (yellow). Results using Barton's algorithm, are shown as a dashed violet line. The three dashed, vertical lines at steps 1000, 1012 and 2554 show the selected micrometer positions at the end of the analysis.

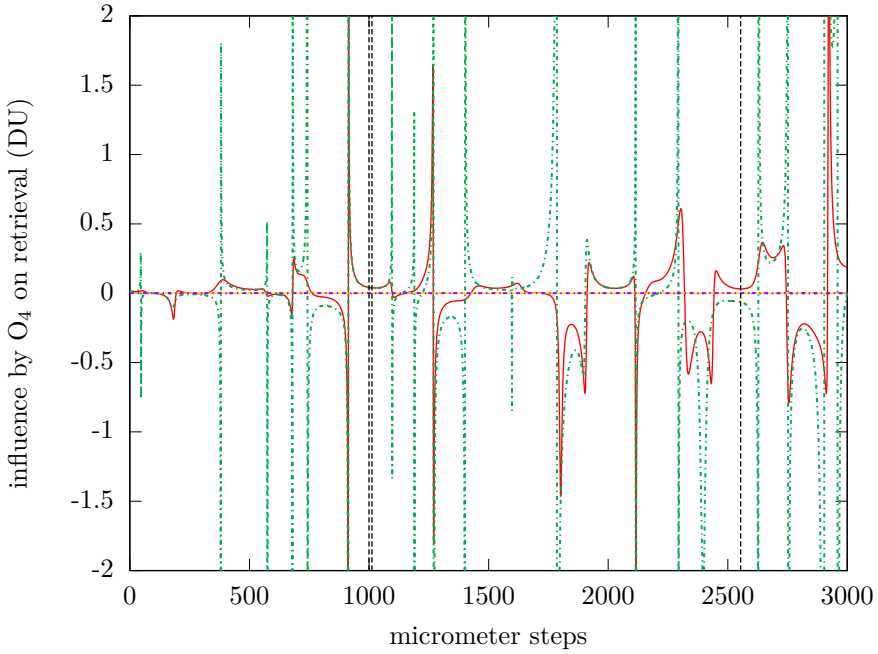

Figure 4.27: Diagram of the expected influence by the oxygen dimer, expressed in the same units as the NO_2 column density, at different grating positions. The colour convention is similar as in Fig. 4.26.

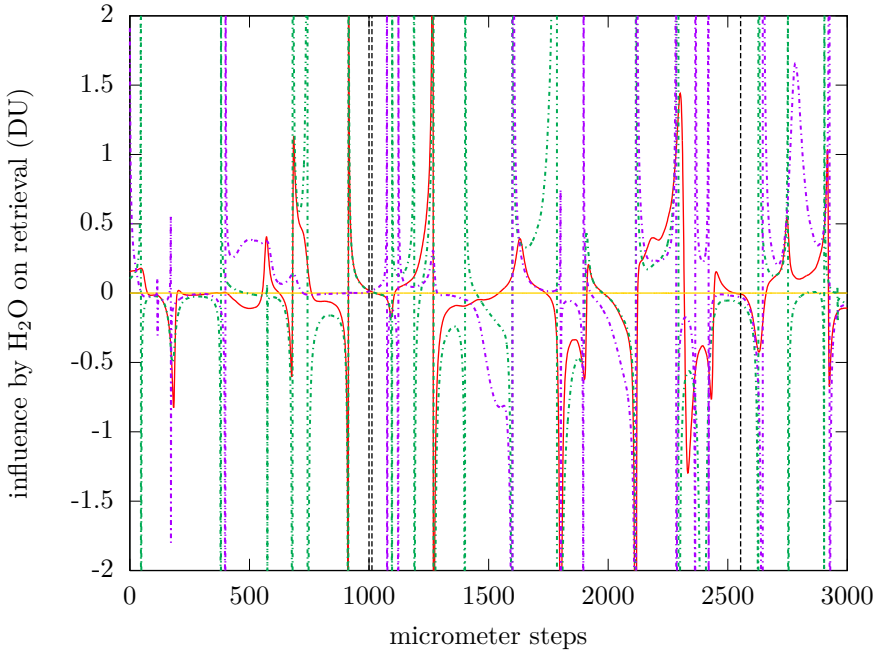

Figure 4.28: Diagram of the expected influence by water vapour, expressed in the same units as the NO_2 column density, at different grating positions. The colour convention is similar as in Fig. 4.26.

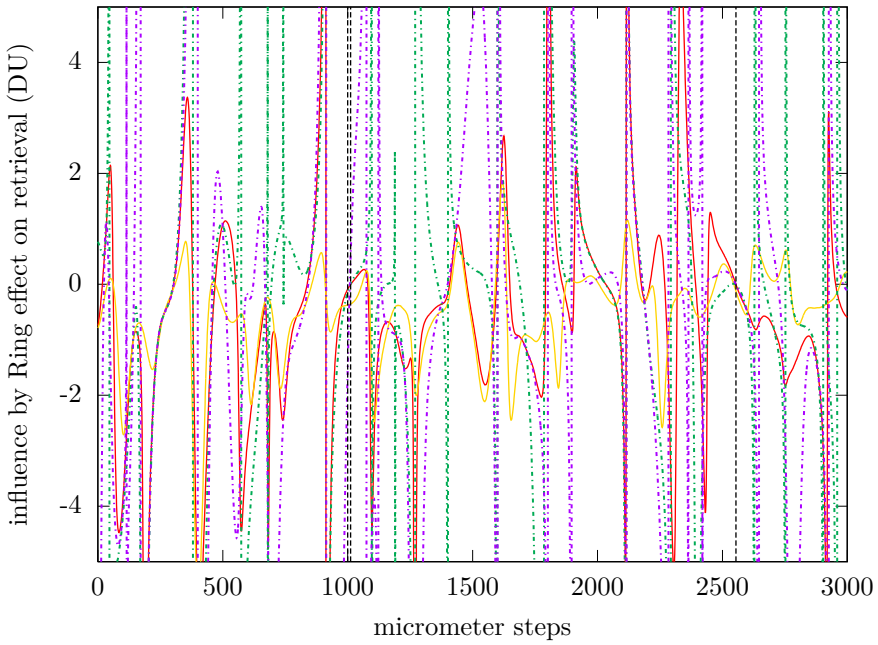

Figure 4.29: Diagram of the expected error induced by the Ring effect, expressed in the same units as the NO_2 column density, at different grating positions. The colour convention is similar as in Fig. 4.26.

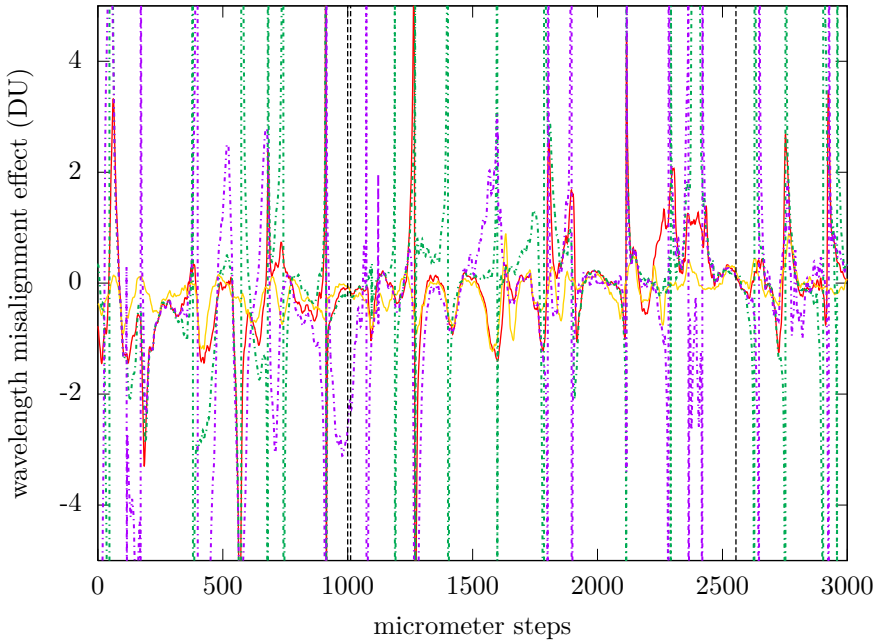

Figure 4.30: Diagram of the expected error induced by a wavelength misalignment of 0.01 nm, expressed in the same units as the NO_2 column density, at different grating positions. The colour convention is similar as in Fig. 4.26.

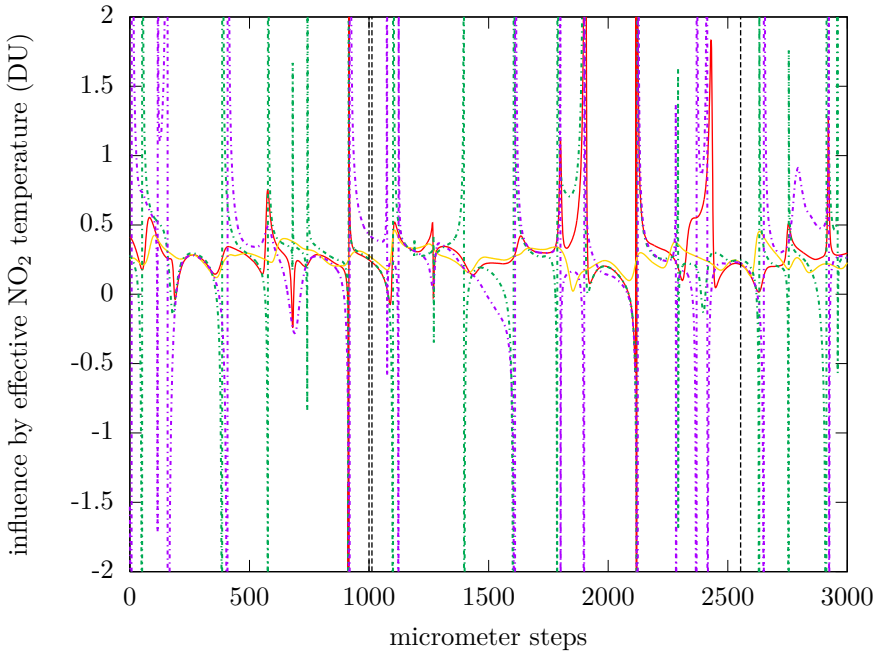

Figure 4.31: Diagram of the influence of a temperature error of +74 K, expressed in the same units as the NO_2 column density, at different grating positions. The colour convention is similar as in Fig. 4.26.

Table 4.6: Comparison among the weightings used by the various algorithms for Brewer #066 at step 1000.

Algorithm	slit 1	2	3	4	5	6	7	8	9	10	11
Kerr (1989)	0	0.1	-0.59	0.11	1.2	-0.82	0	0	0	0	0
Updated, method 1	0.04	0.17	-0.52	-0.03	0.74	-0.40	0	0	0	0	0
Updated, method 2	0.14	0.07	-0.63	-0.06	0.74	-0.09	-0.12	0.002	-0.02	-0.09	0.07

Table 4.7: List of the expected sensitivities to the known factors, expressed in Dobson Units, at step 1000.

Factor	Kerr (1989)	Barton (2007)	Updated, method 1	Updated, method 2
noise	0.4	1.3	0.3	0.3
wavelength misalignment	0.06	-3	-0.08	-0.05
O_4	0.05	0 (retrieved)	0.04	0 (retrieved)
H_2O	0.07	0.012	0.02	0 (retrieved)
Ring effect	0.15	-1.5	-0.09	-0.4
NO_2 temperature	0.2	0.4	0.2	0.3

the wavelengths range 442–469 nm for method 1 and 442–490 nm for method 2. These wavelengths had never been used before with MKIV Brewers, which made the experiment interesting. However, the effects induced by a steep variation of the PMT sensitivity (Figs. 4.11 and 4.23) in this range had to be accurately investigated in the following chapters. The new weighting factors at step 1000 are compared to the ones obtained by Kerr in Table 4.6.

The sensitivities to the known factors calculated at step 1000 for the various algorithms are shown in Table 4.7. The analysis revealed that method 2 is more affected by the Ring effect and slight wavelength misalignments due to the higher number of used slits, whose wavelengths partly fall very close to some strong Fraunhofer lines. It is worth noticing that the values in the table do not represent the uncertainty budget of the algorithms. For example, Kerr's algorithm is additionally affected by systematic errors due to the use of obsolete cross sections (Sect. 4.4.2).

4.3.1 Retrieval of the oxygen dimer and water vapour optical depths

I investigated the capability of the Brewer to measure O_4, which is an interesting parameter both in aerosol applications and for cloudscreening purposes (Wagner et al., 2002, 2004; Daniel et al., 2003), and H_2O within the MKIV spectral range. The retrieval may be performed by searching a set of weighting factors, such as for NO_2, which maximises the sensitivity to the desired absorber. I found that the retrieval of the oxygen dimer is possible at step 3769 (wavelengths in the range 455–481 nm, centred in the O_4 absorption band at about 477 nm) using six slits, by removing the contribution by ozone, Rayleigh and Mie scattering and a constant term and by minimising the other factors, including NO_2. The new set of weighting is shown in Table 4.8. Measurement noise should be less than about 7% with 100 samples (Fig. 4.32). An example of such a measurement during the Izaña campaign will be shown in the next chapter.

Conversely, the measurement noise when measuring water vapour cannot be decreased to less than 30% (with 100 samples) due to the weak absorption by water vapour in the blue spectral range (Wagner et al., 2013) and the interference of other absorbers.

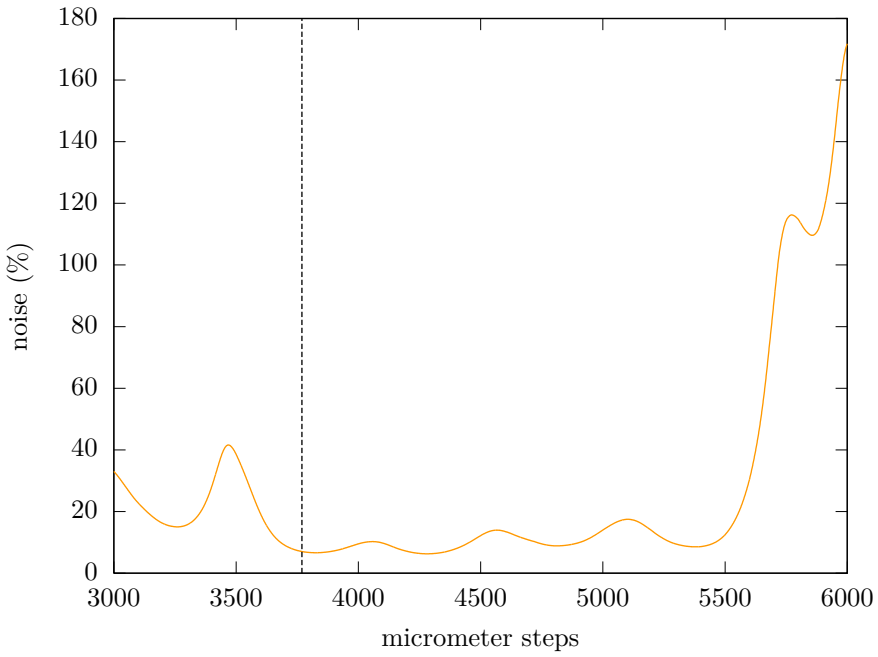

Figure 4.32: Diagram of the expected measurement noise for O_4, expressed as percentage, at different grating positions. The dashed vertical line at step 3769 shows the selected micrometer position at the end of the analysis.

Table 4.8: Weightings used for the retrieval of the oxygen dimer with Brewer #066 at step 3769.

slit 1	2	3	4	5	6
-0.08	0.37	-0.38	-0.33	0.72	-0.30

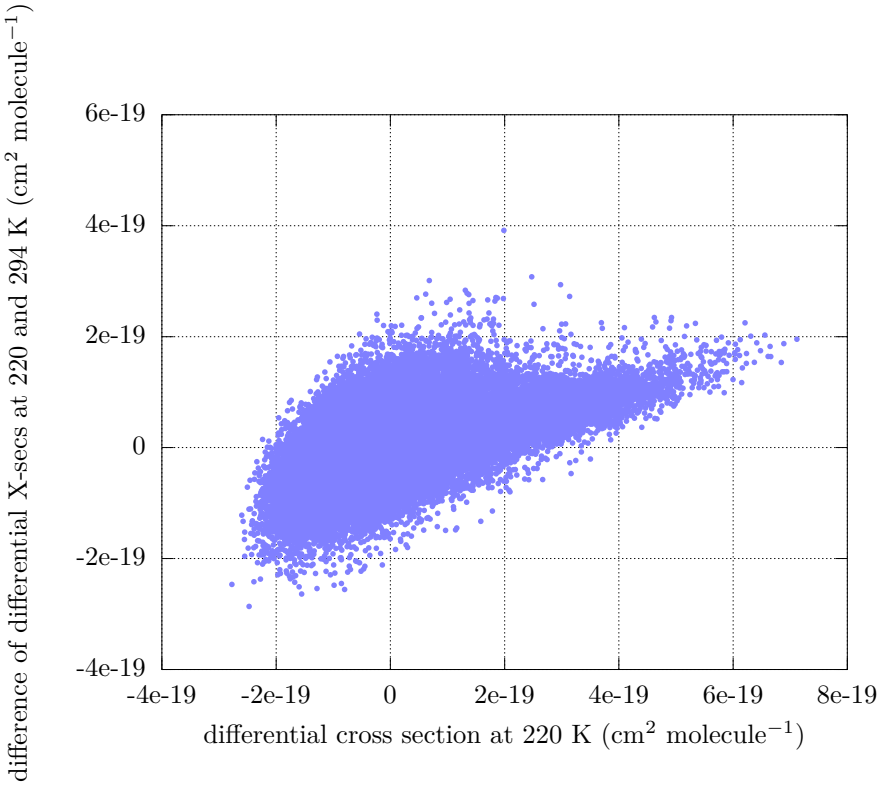

Figure 4.33: Scatterplot between the differential NO_2 absorption coefficient at 220 K and its difference with the differential absorption coefficient at 294 K.

4.3.2 Retrieval of NO_2 effective temperature

During the development of the algorithm, I incorporated the retrieval of NO_2 effective temperature in method 2. However, I found that the dependency of the NO_2 cross section with temperature is nearly collinear to the NO_2 cross section itself. Figure 4.33 shows a scatterplot between the differential NO_2 absorption coefficient at 220 K and its difference with the differential absorption coefficient at 294 K. Both differential absorption coefficients were calculated by detrending the absorption coefficients using a linear regression as a high-pass filter. As a consequence of the collinearity, not only the effective temperature of nitrogen dioxide is not retrievable, as already pointed out by Bucsela et al. (2013), but also the NO_2 retrieval was found to greatly worsen when including the effective temperature, as shown in Fig. 4.34 and expected from Eq. 4.18.

Despite the effective NO_2 temperature cannot be retrieved from the recorded irradiances, an estimate can be derived if the partitioning of nitrogen dioxide in the troposphere and in the stratosphere is known. A method will be suggested in the conclusions (Chap. 7) and possibly implemented in the future.

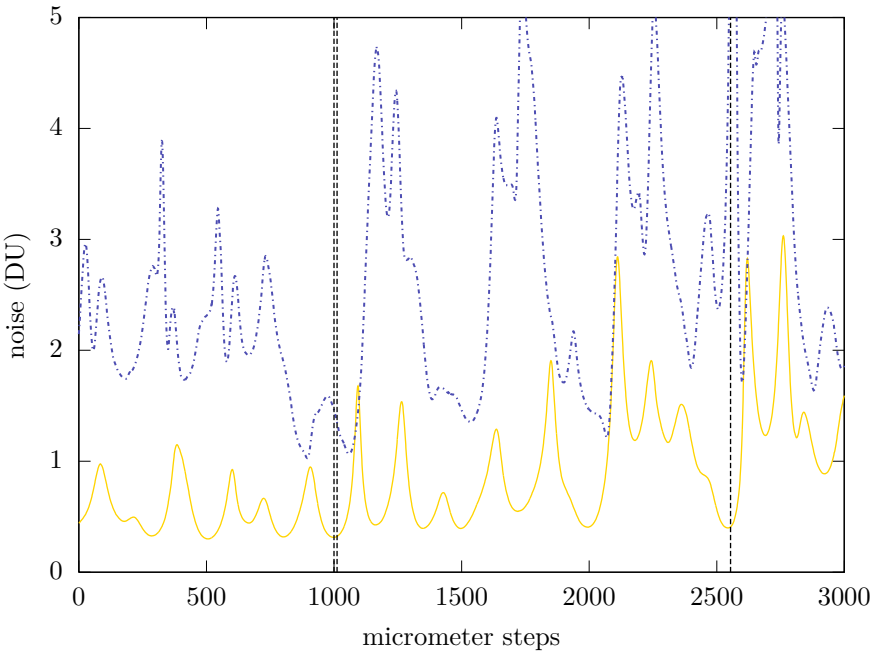

Figure 4.34: Diagram of expected measurement noise, expressed in the same units as the NO_2 column density, at different grating positions. The solid lines identifies the updated algorithm using method 2 (yellow) and the dashed blue line represents method 2 including the effective NO_2 temperature dependence. The three dashed, vertical lines at steps 1000, 1012 and 2554 show the selected micrometer positions at the end of the analysis.

4.4 Radiative transfer models

Radiative transfer models are able to simulate the radiance and the irradiance at whatever altitude in the atmosphere, given a set of input data describing the state of the atmosphere (gas concentrations, atmospheric profiles, aerosols, etc.), the position of the sun and some boundary conditions (such as ground albedo, for instance). Ideally, the perfect model for my research should include vector (i.e. polarised) irradiances, full-spherical geometry and Raman scattering. Unfortunately, no current model can satisfy all characteristics at the same time. I therefore decided to use two different models:

libRadtran (Mayer and Kylling, 2005), a well-known software which was recently modified to support rotational Raman scattering (Kylling et al., 2011). Pseudo-spherical geometry is supported by the DISORT solver and full-spherical geometry is supported by the much slower Monte Carlo solver. Polarised irradiances cannot be calculated together with non-plane-parallel geometries and with Raman scattering. The model was mainly used for fast simulations in pseudo-spherical geometry due to its user-friendly interface and its speed. The count rates registered by the Brewer, for instance, were simulated with the libRadtran model to check that the algorithm was working as desired;

SCIATRAN (Rozanov et al., 2014), a very complete model supporting polarisation, full-spherical geometry and Raman scattering. Unfortunately, the module for rotational Raman scattering is still under development and does not work properly with polarised irradiances (Rozanov, personal communication, 2013), thus the three characteristics cannot be used at the same time. I used it for the calculation of the air mass factors, since full-spherical calculations are much faster than the Monte Carlo solver of libRadtran and the model can take into account polarisation in this geometry. Also, the correction for the O_4 effect on the retrieval has been calculated using this model in full-spherical geometry.

Both models were repeatedly validated and successfully intercompared (Kokhanovsky et al., 2010).

4.4.1 Calculation of air mass enhancement factors

For the direct sun geometry, the geometrical AMFs were calculated as in the Brewer operating software (Savastiouk, 2005). Conversely, the AMFs for the zenith sky geometry were calculated with the help of the SCIATRAN model for both polarisations used by the Brewer. Indeed, photons of various polarisations reaching the ground have followed slightly different routes in the atmosphere, resulting in different AMFs. Vertical profiles obtained from a climatological database using a 2D chemo-dynamical model (Brühl and Crutzen, 1993) were employed. The air mass factors were retrieved for different solar zenith angle by differentiating Eq. 3.31 with respect to the vertical NO_2 density, X_{NO_2}. I calculated the derivative with the finite differences method, varying by 5% the NO_2 VCD, as in the work by Barton (2007).

As clear from Fig. 4.35, the zenith sky air mass enhancement factors slightly differ for both polarisations. Specifically, photons polarised parallel to the scattering plane are mainly multiple-scattered and have travelled more in the atmosphere before reaching ground than photons in the perpendicular polarisation (Sect. 3.3.2).

It is worth noticing that tropospheric NO_2 pollution can considerably alter the zenith AMFs calculated by the model. However, the issue may be solved in the future using nearly-simultaneous direct sun and zenith sky measurements to partition the tropospheric and stratospheric NO_2 contents.

4.4.2 Preliminary test of the algorithm

To check the ability of the updated algorithm to properly retrieve the NO_2 content in the atmosphere, I performed a direct sun retrieval on several synthetic spectra. I simulated the spectra using the

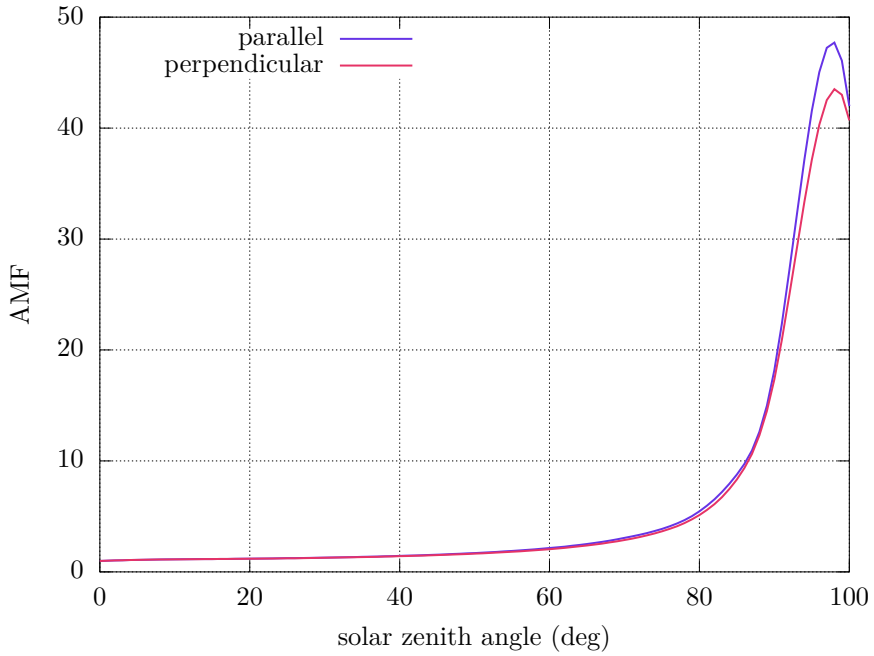

Figure 4.35: Zenith sky air mass enhancement factors retrieved using the SCIATRAN model for polarisations parallel and perpendicular to the scattering plane. The AMFs are calculated for the location of Izaña.

libRadtran radiative transfer model described above and taking into account the wavelengths and bandwidths measured at the default micrometer step (1000) with the dispersion test. I found that calculations over a very fine wavelength grid (< 0.005 nm) were necessary in order to reproduce the variability of the NO_2 cross section and the Fraunhofer solar structure. Then, I performed a Langley plot over the synthetic spectra, which were calculated at 0–80° solar zenith angles, to retrieve the extraterrestrial constants (Eq. 3.25). In addition, the simulations were repeated applying Kerr's coefficients to retrieve the NO_2 column as in the standard algorithm. Both the standard Brewer Rayleigh correction and the updated one were tested. Furthermore, the effect of lacking correction for filters non-linearity, as in the standard algorithm, was introduced in a fourth simulation (filters 3 and 2 are switched at 70° solar zenith angle, as in real measurements).

The comparison between the results and the concentration of nitrogen dioxide given as input to the model was fundamental to assess the magnitude of the systematic errors in the standard algorithm. The simulations were run with no NO_2 (to identify possible offsets), 0.1 DU (representative of the stratospheric content) and 1 DU (polluted conditions). As visible from Fig. 4.36, the results obtained using Kerr's coefficients can be up to 50% higher than the NO_2 concentration given as input to the model (e.g. case with 0.1 DU). As clear from the first graph, the standard Brewer Rayleigh correction and the filter non-linearity also introduce an offset in the retrieval. If the non-linearity of the filters is neglected, the effect on the retrieval is huge: the overestimation can be even larger than 200%. All values are in general agreement with the experimental results found during several intercomparison campaigns (Sect. 3.4.5).

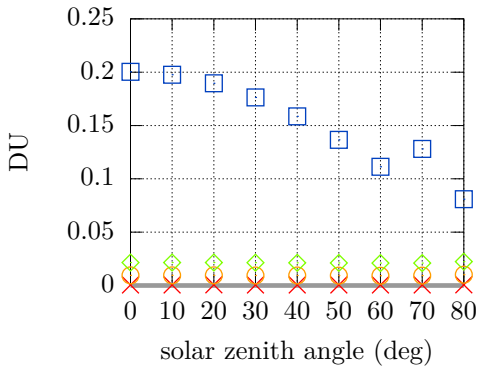

(a)

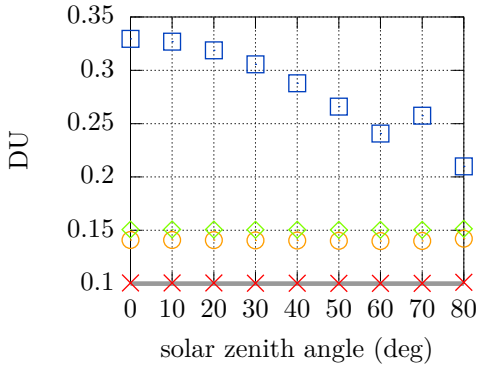

(b)

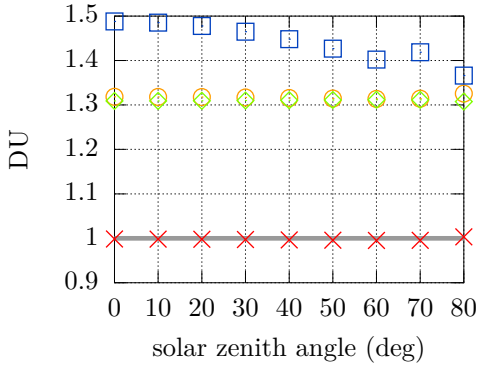

(c)

Figure 4.36: NO_2 retrieval from synthetic spectra using the updated algorithm (crosses) and Kerr's weighting factors with updated Rayleigh correction (circles) and the Brewer standard correction (diamonds). Squares identify the results using the standard algorithm without correction for filters non-linearity. The NO_2 concentration given as input to the model was 0 DU (a), 0.1 DU (b) and 1 DU (c) and is drawn as a thick grey horizontal line.

Chapter highlights

- for the first time, a MKIV Brewer spectrophotometer was accurately characterised in the visible range. For this purpose, I developed several new routines which are now available to the scientific community. Some unexpected issues came to light (e.g. dispersion function in the visible and UV regions, filter effects) and highlight the need of deeper understanding of the instrumental features;
- I updated the Brewer NO_2 algorithm and proposed two different solutions to overcome the main limitations of the standard method. Linear algebra was intensively used for this aim and an original mathematical framework has been developed;
- I determined the interference by the major factors on the NO_2 retrieval by perturbing the Brewer equation. This parameterisation turned out to be fundamental to optimise the algorithm and adapt it on Brewer #066. I also investigated the Brewer capability to measure the optical depths of other minor absorbers in the visible spectral range;
- I used top-level features of current radiative transfer models to determine the polarised air mass factors and to check the functioning of the algorithm. The simulations confirmed and clarified the overestimations by the standard Brewer algorithm observed during previous intercomparison campaigns.

CHAPTER 5

Field measurement campaigns

Field measurement campaigns are not only the decisive test bench to check the validity of a scientific theory and proper functioning of the instrumentation, but also a great challenge for the experimenter himself. During my Ph.D. I had the chance to attend – and organise – several campaigns. In fact, almost no other choice was possible to implement for the first time the updates to the algorithm that I introduced in my work: accurate comparisons and calibrations need peculiar conditions that can be fulfilled in few places on Earth, having unique environmental characteristics. Therefore, along with Brewer #066, I travelled from Saint-Christophe, at the bottom of the Aosta Valley, to the glacier of Plateau Rosa (3500 m a.s.l.), from the historical station of Arosa, Switzerland (1850 m a.s.l.), where ozone measurement were performed for the first time in 1926, to the pristine solar observatory at Izaña, Tenerife (2400 m a.s.l.).

The measurement techniques and algorithm updates proposed in the previous chapter are now applied to real data collected in the field. Sect. 5.1 deals with the explanation of the Langley calibration, which has been necessary to calibrate Brewer #066 for the first time. I will give an original contribution on that topic by introducing a novel approach to account for the daily variation of the nitrogen oxide due to the photochemistry (Sect. 5.4.4). The remaining sections, from 5.2 to 5.5, describe the measurement campaigns, with a particular focus on the Izaña calibration. The motivations, the measurement schedules as well as the numerous results of this campaign, along with some new products obtainable with the Brewer, such as the measurement of the degree of polarisation of the sky and the oxygen dimer optical depth, are discussed in Sect. 5.4. Additionally, the uncertainty of measurement is thoroughly addressed by applying the Monte Carlo technique for the first time on a Brewer, in Sect. 5.4.7. Finally, the last section illustrates a successful calibration transfer from Brewer #066 to a similar instrument.

5.1 Principles of Langley calibration

Let's recall the Brewer fundamental equation, which allows to retrieve the nitrogen dioxide vertical column density, X_{NO_2}, from a linear combination of radiances or irradiances measurements, $\mathscr{F}$:

$$\mathscr{F} = \mathscr{F}_0 - \mu_{NO_2} X_{NO_2} \tag{3.31}$$

The correct determination of the calibration factor (extraterrestrial constant) $\mathscr{F}_0$ is fundamental to accurately retrieve X_{NO_2}. If a slightly wrong value of the extraterrestrial constant is used in Eq. 3.31, the calculated NO_2 vertical column density will apparently vary during the day with a

typical "U" or "inverse-U" shape, centered at the local solar noon (explanation box further below). The error induced on the VCD will be maximum for lower air masses and minimum at sunset and sunrise (as an example, Fig. 5.29).

Explanation. If a wrong calibration factor $\mathscr{F}'_0$ is used instead of the real value $\mathscr{F}_0$, Eq. 3.31 will become

$$\mathscr{F} = \mathscr{F}'_0 - \mu_{NO_2} X'_{NO_2} \tag{5.1}$$

where X'_{NO_2} is an erroneous estimate for X_{NO_2}. By subtracting the above equation to Eq. 3.31, we get the error on the retrieved nitrogen dioxide:

$$X'_{NO_2} - X_{NO_2} = \frac{\mathscr{F}'_0 - \mathscr{F}_0}{\mu_{NO_2}} \tag{5.2}$$

Since μ_{NO_2} is symmetrical around noon, the induced error will also be dominated by the same symmetry. Most notably, if the extraterrestrial constant is too high, the nitrogen dioxide content at noon will also be higher than the "true" value and an inverse-U shape will be seen in the diurnal cycle. Conversely, a U-shaped daily cycle will be observed if the extraterrestrial constant is too low. ■

The extraterrestrial constant for an instrument can be determined essentially in two different ways. If a reference instrument is available, then simultaneous measurements allow to calculate a calibration factor optimising the performances of the tested instrument compared to the standard. This technique was employed in the Saint-Christophe campaign (Sect. 5.5) to calibrate Brewer #067 with respect to Brewer #066. If no reference is available, then a "Langley plot" (Langley, 1880) has to be carried out. This widely used technique, which takes the name from the American physicist and pioneer of aviation Samuel Pierpont Langley (1834–1906), is based on the fact that Eq. 3.31 is a linear relationship in the (μ_{NO_2},$\mathscr{F}$) plane. Specifically, X_{NO_2} is the slope of the line and $\mathscr{F}_0$ is the intercept. Therefore, if the solar intensity, or equivalently the linear combination of the intensities at various wavelengths, is recorded for at least half a day and plotted against the air mass (which varies as a function of the solar elevation), a simple linear regression can be used to determine the value of $\mathscr{F}_0$. Usually, half-day Langley plots are collected for several days and an average value of the intercepts is taken as the calibration constant. The only, but limiting, constraint to use this simple method is the fact that X_{NO_2}, and every other factor influencing the solar intensity, or the linear combination, must be stable for the duration of a Langley plot. Slopes vary among different days as a result of the changes of the absorber concentration in the atmosphere from day to day.

To obtain the greatest atmospheric stability, Langley calibrations are frequently performed at high-altitude and pristine sites (e.g., Mauna Loa, Hawaii, 3400 m a.s.l.), which are not influenced by the boundary layer pollution and by clouds. Specific criteria can additionally be applied to identify the best data for the fit (Harrison and Michalsky, 1994; Slusser et al., 2000; Kuester et al., 2003) and robust regression algorithms, less sensitive to the outliers, can be used (Redondas, 2007). Atmospheric conditions characterised by diurnal cycles should be avoided, since they induce systematic errors which are extremely difficult to detect (Marenco, 2007).

While the Langley plot technique is rigorously defined only for direct sun measurements, a generalisation of the method can be used for different observation geometries (Barton, 2007). In that case, the main issue is to correctly determine the air mass enhancement factor describing the average path of the solar beam in the atmosphere. Radiative transfer models must be used for the purpose. Moreover, for some observation geometries, the AMF may be strongly dependent on the concentration profile of the absorber.

Alternative formulations of the Langley plot were published in the scientific literature to overcome the limitations of the traditional technique. For instance, the bulk of the points in

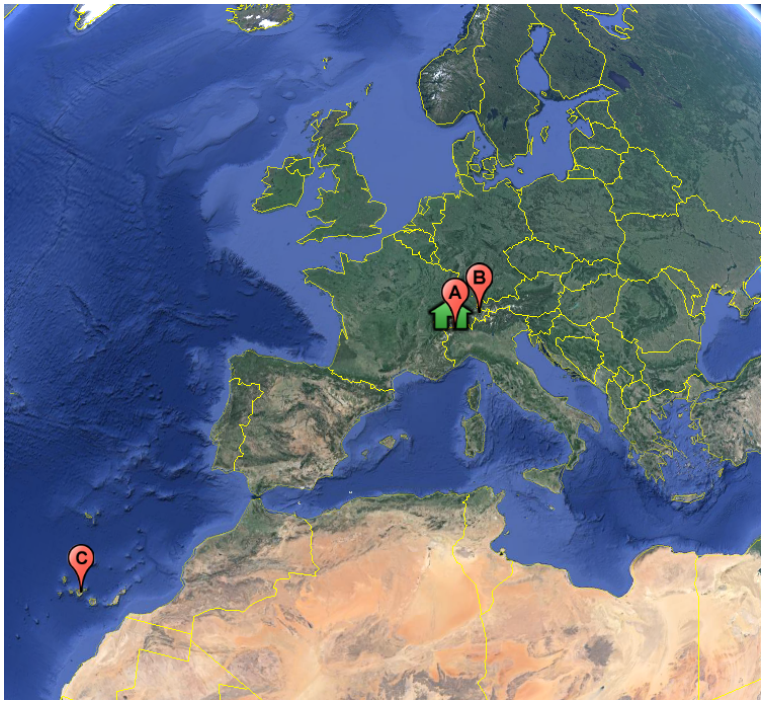

Figure 5.1: Measurement campaigns during my Ph.D. (picture taken from Google Earth). Plateau Rosa, Aosta Valley (A), Arosa, Switzerland (B), Izaña, Tenerife (C). The ARPA headquarter, which hosted the fourth campaign in 2013, is shows as a "house" marker.

a Langley plot accumulates at low air masses, when the sun "moves" more slowly. The $\mathscr{F}_0$ extrapolation is thus very sensitive to the data at the extremes of the fit. To homogenise the distribution of the points in the fit, Eq. 3.31 may be rewritten as

$$\mathscr{F}\,\frac{1}{\mu_{NO_2}} = -X_{NO_2} + \mathscr{F}_0\,\frac{1}{\mu_{NO_2}} \tag{5.3}$$

Therefore, in the $(\frac{1}{\mu_{NO_2}}, \frac{1}{\mu_{NO_2}}\,\mathscr{F})$ space, the slope is represented by $\mathscr{F}_0$ and the intercept by $-X_{NO_2}$, as opposed to the traditional method. Depending on the temporal scale of the fluctuations in the absorber density, the traditional or the alternative technique should be preferred (Adler-Golden and Slusser, 2007). More frequently, both methods are applied to the data and compared.

5.2 The Plateau Rosa campaign (2011)

I performed a Langley calibration during the first year of my Ph.D., with a twofold objective: to check the value of the extraterrestrial constant used at that time by the Brewer operating software and to learn the bases of the Langley method. For this purpose, the Brewer was installed to the Air Force measurement station at Plateau Rosa (45.94°N, 7.71°E, Fig. 5.1), one of the highest sites in the Aosta Valley reachable by cable car. The station is located on a permanent glacier at 3500 m a.s.l. (Fig. 5.2) and is therefore little affected by tropospheric pollution. The Brewer was equipped with a sky camera, which was able to shoot pictures of the full sky to remove the measurements potentially perturbed by clouds, and remotely operated for the whole month of July 2011. Unfortunately, due to both technical problems and, most of all, presence of clouds resulting from the strong atmospheric convection during the day (very frequent at that altitude in summer), all measurements were discarded and the Langley calibration was unsuccessful. However,

Figure 5.2: Brewer #066 on the platform of the Air Force station at Plateau Rosa (3500 m a.s.l.). A sky camera can be noticed on the top of the instrument.

the campaign turned out to be extremely useful to gain much experience, which was used during the Izaña campaign the following year.

5.3 The Arosa campaign (2012)

During the second year of my Ph.D., I participated as a European Brewer operator, together with the Brewer #066, to the seventh intercomparison of the Regional Brewer Calibration Centre for Europe (RBCC-E) (Fig. 5.3). The campaign, organised with the support of the Global Atmospheric Watch (GAW) program of the WMO and the European Space Agency (ESA), was held at the Lichtklimatisches Observatorium (LKO) of MeteoSwiss, Arosa (46.78°N, 9.68°E, 1850 m a.s.l.), Switzerland, during the period July, 16th-27th 2012. The location was chosen since the Arosa observatory hosts the longest series of total ozone measurements in the world, dating back to 1926, and several Dobson instruments are operated there. The intercomparison was a joint exercise of several (about 10) European operators to improve the accuracy of ozone measurements by Brewer spectrophotometers. The European Brewer reference, managed by the Agencia Estatal de Meteorologia (AEMET), Spain, the Brewer world travelling standard (#017), operated by International Ozone Services (IOS), and the world UV reference QASUME, run by the Physikalisch-Meteorologisches Observatorium Davos/World Radiation Centre (PMOD/WRC), also participated to the campaign. While the measurements were mainly focused on ozone and UV, and not on nitrogen dioxide, the campaign was very useful to verify the stability of Brewer #066 and its reliability compared to the reference instruments. For instance, although affected by straylight, like all single-monochromator spectrophotometers, the global UV irradiances measured by Brewer #066 turned out to be the closest to the world reference.

The Arosa intercomparison additionally allowed to discover some focusing problems in the monochromator of Brewer #067, which I used in the last part of my Ph.D. work.

Figure 5.3: Brewer #066 (centre) on the roof of the Arosa observatory during the European intercomparison.

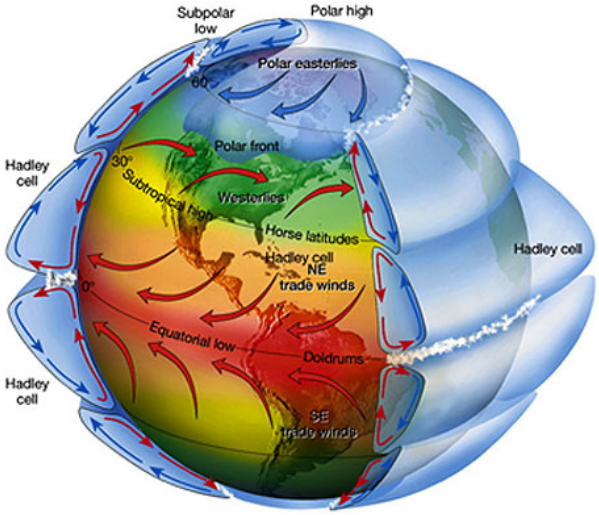

Figure 5.4: Three dimensional view of the global wind circulation patterns (credits: NASA's Remote Sensing Tutorial, `https://www.fas.org/irp/imint/docs/rst/Sect14/Sect14_1c.html`).

Figure 5.5: Sea of clouds from the Izaña observatory. Picture shot from the station at sunrise during the campaign on September, 15th 2012.

5.4 The Izaña campaign (2012)

5.4.1 Rationale

To achieve the maximum stability necessary for an accurate Langley plot, I decided, in agreement with AEMET, to organise an ad hoc campaign with Brewer #066 at the Izaña Atmospheric Research Center (IARC), in Tenerife, Canary Islands (28.31°N, 16.50°W), a GAW station, having unique features. First, it is located on the top of a mountain plateau (2400 m a.s.l.) in a pre-national park area (Teide National Park). The area is protected by a special "sky law", which preserves conditions of good visibility. Furthermore, the region is located below the descending branch of the Hadley cell (Fig. 5.4) and is affected by the southern side of the Azores Anticyclone, which has several consequences: the station experiences sunny conditions all the year; it is normally above the quasi-permanent "trade winds" temperature inversion layer between 800 and 1500 m a.s.l., which separates the moist marine boundary layer from the dry free troposphere, and thus free from local anthropogenic influences; even in case that clouds develop, the inversion keeps them below the station ("sea of stratocumulus", Fig. 5.5). The appearance of deep lows and cut-off lows, which could favour stratosphere-troposphere exchange, is limited to winter time (Gil et al., 2008). Finally, the Izaña observatory is well equipped with several solar instruments (photometers, radiometer, pyranometers, cloud camera, webcam, etc.), including the MKIII Brewer European ozone triad and can host foreign researchers for calibrations.

5.4.2 Brewer transport and installation

To ensure that Brewer #066 could remain stable, especially after the Langley calibration, and to prevent mechanical shocks, special care was taken during the the transportation of the instrument by aircraft. After the installation at the observatory, as well as after its return to Saint-Christophe, the necessary tests were performed (Sect. 3.3.2): step revolution (`sr`) and sighting (`si`), to check the proper functioning of the positioning system; standard lamp (`sl`) measurements, to verify the stability of the instrument; sun scans (`sc`) and dispersion (`dsp`) tests, to assess whether any change in the wavelength scale has occurred during the flight. A piece of cardboard was affixed on the viewports to avoid contamination by visible light entering through the plastic window. Figure 5.6 depicts the Brewer in its final, operating conditions.

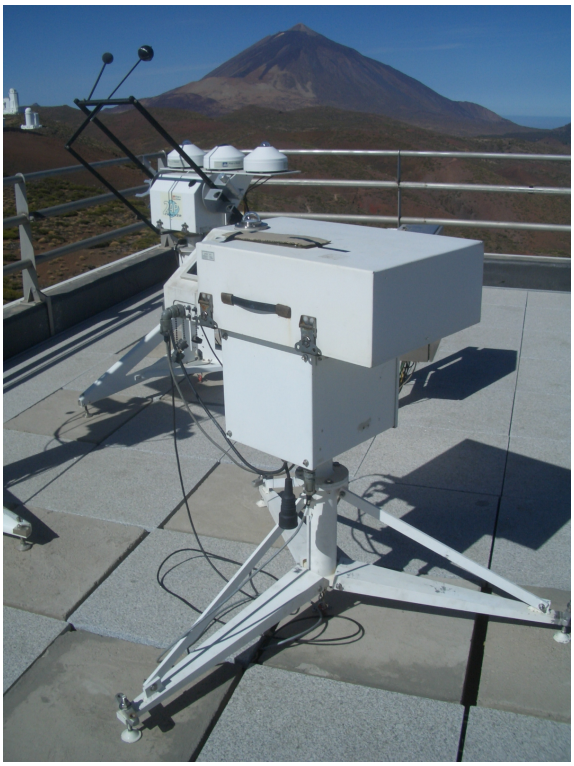

Figure 5.6: Brewer #066 on the roof of the Izaña observatory. On the background, other solar instruments and the Teide volcano.

5.4.3 Schedule of the campaign

The Langley campaign started at sunrise on September, 15th 2012, after few days of initial tests, and ended at sunset on October, 21st 2012. 38 days of measurements were collected and only 5 were discarded due to rain or fog. A few Saharan dust events (Fig. 5.7) were experienced at the station, but the analysis does not reveal any effect on the retrieved NO_2 values (see also Sect. 5.4.7 for a theoretical explanation).

The schedule (Sect. 3.3.2) I expressly designed before arriving in Izaña included measurements of both direct sun irradiances (at three different micrometer positions) and zenith sky radiances (at three micrometer positions and two different polarisations). Additionally, both method 1 (measurements at six slits) and 2 (eleven slits) were initially included in the schedule. After the first days of the campaign, I realised that the schedule was unfeasible: at the tropics, the sun "moves" very quickly on the horizon, especially at sunrise and sunset, and the schedule should be substantially reduced to obtain a large number of points, as needed for a good Langley plot. Measurements using method 2 were excluded after five days due to their large noise (Sect. 5.4.5) and I decided to split the campaign in two parts: in the first half, the Brewer only measured in direct-sun mode, in the second part, the measurements were performed along the zenith direction. The used schedules are reported in Appendix A.

The last days of the campaign were devoted to measurements of ozone, requested by the hosting agency for straylight studies, and estimates of the oxygen dimer optical depth (Sect. 5.4.11). Table 5.1 summarises some statistics about the weather conditions and the schedule during the campaign.

5.4.4 Variable Langley plot

In Sect. 5.1, I stated that a Langley calibration is possible only in the case that the concentration of the absorber to be measured is constant during the whole period of a plot event, since only

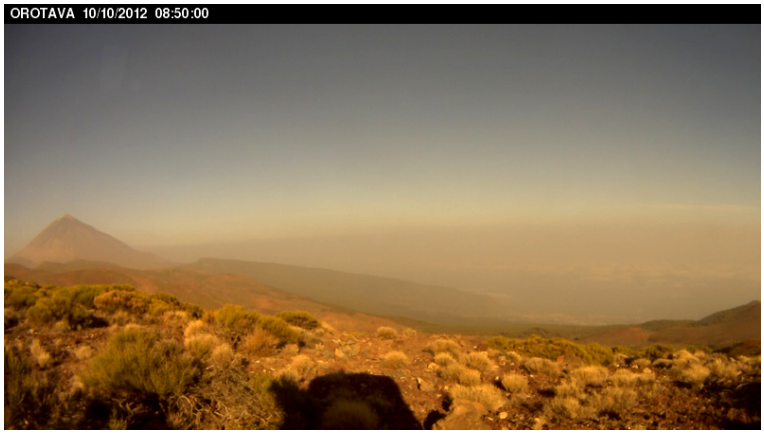

Figure 5.7: Saharan dust event at Izaña during the Langley campaign. Picture shot by a webcam looking towards the west.

Table 5.1: Statistics of the weather conditions and scheduled measurements during the Izaña campaign.

	days
whole campaign	38
rain/fog (excluded)	5
initial checks	2
direct sun measurements	16
zenith sky measurements (2 polarisations)	15
O_3 and O_4 measurements	5
Saharan dust contamination on NO_2	0

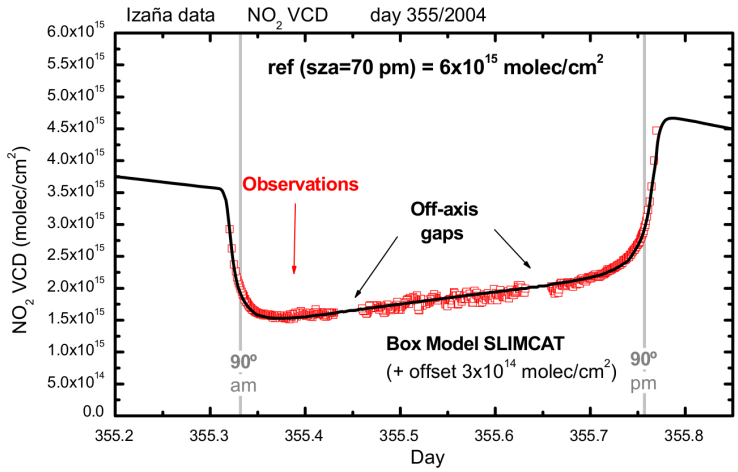

Figure 5.8: Daily evolution of NO_2 vertical column measurements (red squares) and SLIMCAT model estimates. The figure is taken from Gil et al. (2008).

measurements with a fixed concentration can be fitted by a straight line on the (μ_{NO_2},$\mathscr{F}$) plane. However, in Chap. 2 it was pointed out that photochemistry cannot be neglected for species such as NO_2, whose densities do vary during the day (e.g., Fig. 2.12). A traditional Langley is thus unfeasible.

In the scientific literature, this issue was frequently overcome by employing complex photochemical models (Vaughan et al., 1997; Roscoe et al., 2001; Schofield et al., 2004; Gil et al., 2008) and by including the dependency on the effects of the photochemistry in the AMFs. However, besides introducing considerable complications, even models are not exempt from uncertainties (Lee, 1994). A different approach, e.g. used with varying aerosols, could consist in improving the Langley plot to identify possible changes in the atmosphere and remove the points relative to those cases (Terez and Terez, 2003). However, this kind of techniques is useless when the absorber is already known to continuously vary during the day.

As a consequence, I developed a new method, which generalises the Langley plot in case of linear drifts of the absorber. Indeed, from previous measurements and model simulations in Izaña (Gil et al., 2008), the NO_2 column linearly increases with time during the day for solar zenith angles below 80°(Fig. 5.8). Therefore, Eq. 3.31 was rewritten by emphasising the dependence on time:

$$\mathscr{F}(t) = \mathscr{F}_0 - \mu_{NO_2}(t)\, X_{NO_2}(t) \tag{5.4}$$

and assuming that

$$X_{NO_2}(t) = \eta t + \zeta \tag{5.5}$$

The solution is provided by simply solving an overconstrained system, e.g. with pseudoinverse matrices.

Explanation. Equation 5.4 can be rewritten for each measurement as a system of linear equations,

$$\begin{cases} \mathscr{F}(t_1) = \mathscr{F}_0 - \mu_{NO_2}(t_1)\, X_{NO_2}(t_1) \\ \dots \\ \mathscr{F}(t_n) = \mathscr{F}_0 - \mu_{NO_2}(t_n)\, X_{NO_2}(t_n) \end{cases} \tag{5.6}$$

where $t_1 ... t_n$ are the times of the measurements. The system above can also be represented as a matrix equation:

$$\begin{bmatrix} \mathscr{F}(t_1) \\ ... \\ \mathscr{F}(t_n) \end{bmatrix} = \begin{bmatrix} 1 & -\mu_{NO_2}(t_1)t_1 & -\mu_{NO_2}(t_1) \\ & ... & \\ 1 & -\mu_{NO_2}(t_n)t_n & -\mu_{NO_2}(t_n) \end{bmatrix} \begin{bmatrix} \mathscr{F}_0 \\ \eta \\ \zeta \end{bmatrix} \tag{5.7}$$

or, in a shorter form,

$$Y = A\,X \tag{5.8}$$

The (rectangular) system is solved, in a least-square sense, as

$$X = A^{\dagger}\,Y \tag{5.9}$$

where $A^{\dagger}$ is the pseudoinverse matrix of A. Thus, the method not only provides an estimate of the extraterrestrial constant, but, at the same time, the rate of variation η and the average VCD ζ.

To avoid colinearity in the matrix and correctly separate the contribution by the temporal variation of the AMF and the linear drift of the NO_2 column due to photochemistry, a full day instead of half a day (as in traditional Langley calibrations) is needed. ■

Analogous derivations may be obtained using the $\frac{1}{\mu_{NO_2}}$ formulation (as in Eq. 5.3) and the Least Absolute Deviations (LAD) technique instead of least squares, for lower sensitivity to the outliers. Since not only the total column, but also the NO_2 profile changes (Gruzdev and Elokhov, 2011), the method could be further improved by recalculating $\mu_{NO_2}(t)$ with a new profile each time, but this solution would require profile measurements or, again, photochemical models.

Acceptance criteria

I had to define some acceptance criteria to filter only good measurements in the Langley calibration. First, only AMFs in the range 1.5–3.5 were accepted. The lower limit is necessary to avoid measurements with high noise due to the short photon path in the atmosphere, the weak NO_2 absorption signal and turbulence due to heat in the central hours of the day. Moreover, the AMF does not change relevantly when the sun is close to the solar noon (Harrison and Michalsky, 1994). Conversely, the higher limit was set to avoid straylight, shadows by the quartz window border, uncertainty caused by the increasing effect of atmospheric refraction and of atmospheric profiles and, finally, noise due to too few photons resulting from strong absorption. Additionally, points outside a certain limit from the fit (0.05 DU) were excluded from the Langley plot. Finally, Langley events with too large residuals (squared sum of the deviations from the fit above 0.2) or too few (< 9) morning or afternoon points were not considered in the analysis. Figure 5.9 shows an example of a Langley event, with both accepted and removed measurements from the fit.

Single measurements were used instead of time averages to obtain a larger numbers of points in the fit, as suggested by Lee (1994). Robust statistics (Least Absolute Deviations, LAD) were used to reduce the sensitivity to the remaining outliers.

5.4.5 Results using method 2 (eleven slits)

During the first days of the campaign, the new algorithm using method 2 (eleven slits) was implemented. Since measurements with method 2 at the standard grating position are very sensitive to the Ring effect (Table 4.7), a new micrometer step was chosen that reduced the influence by the Fraunhofer lines and, at the same time, kept low the retrieval noise. I determined that a jump scan at steps 1456 and 3485 could satisfy these criteria: the Ring effect is negligible and Poisson noise (for one sample) is 0.55 DU, a bit higher than with method 1. Therefore,

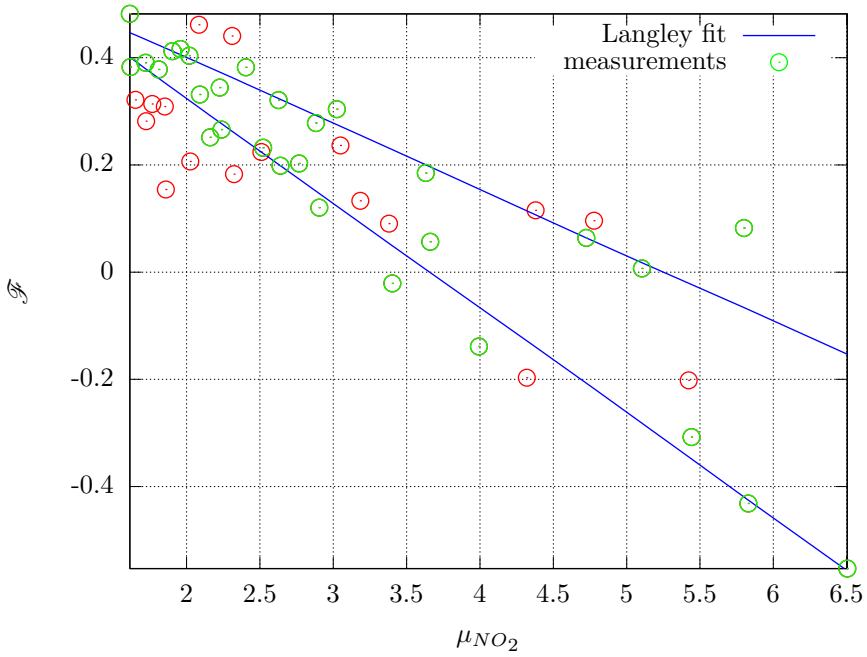

Figure 5.9: Example of a Langley calibration for one day (day 283, zenith sky geometry, parallel polarisation). Green circles represent the measurements which were taken into account in the regression, whereas red circles mark the measurements which are outside the acceptance criteria.

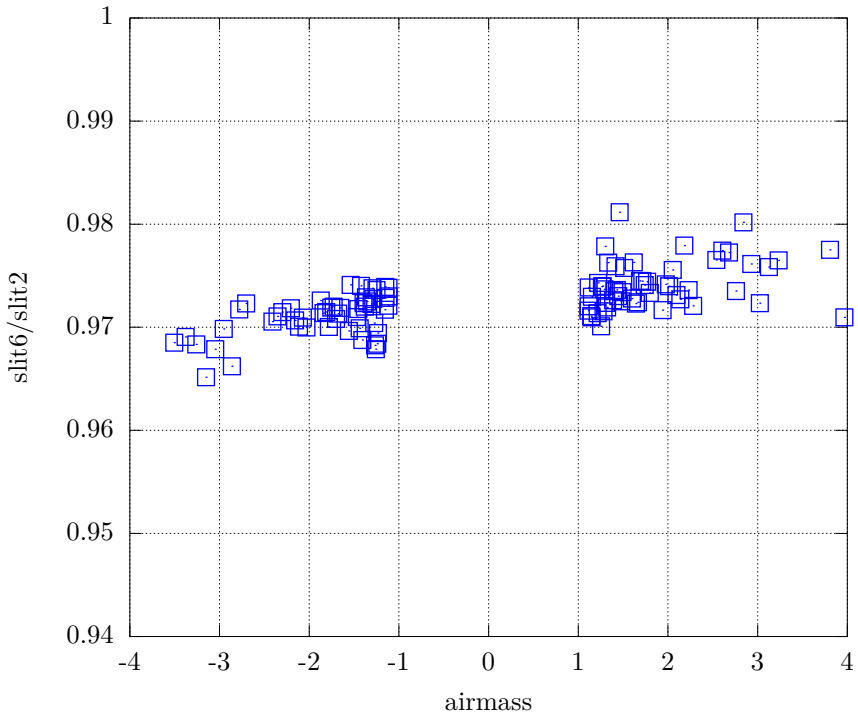

Figure 5.10: Ratio of the measured count rates at the same wavelength (458 nm) with slits 6 and 2 during a jump scan, as a function of the air mass (day 260).

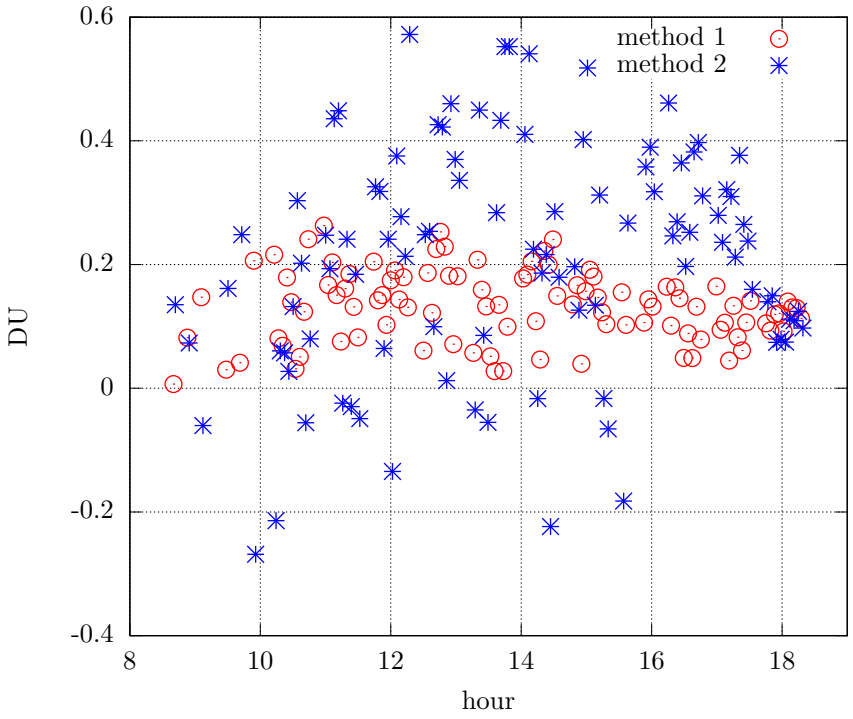

Figure 5.11: Series of NO_2 VCD for day 259 with the new algorithm and both methods. As noticeable, measurements obtained through a jump scan (blue asterisks) are much noisier than measurements using a more traditional six slits technique (red circles).

measurements were taken by swinging the micrometer at both positions, then the pair of (corrected) count rates collected at the first position (cf. Fig. 4.25) were linearly interpolated to the same air mass of the second position. Count rates at the sixth slit in the first position were compared to count rates at the second slit in the second position in order to find a transfer function between the two slits and to select only clear sky measurements. The ratios of the count rates at the two slits are plotted in Fig. 5.10.

When calculating the vertical column of nitrogen dioxide, I found that the estimates using eleven slits (method 2) were much noisier than using only six slits (method 1). As an instance, the series of NO_2 VCD for day 259 is depicted in Fig. 5.11. Higher noise was partially expected by theoretical calculations, due to the additional conditions imposed in the retrieval with method 2 (removal of interferences by O_4 and H_2O). However, I think that a significant, unexpected contribution comes from two other unaccounted factors:

1. the temporal interpolation between successive measurements at different grating positions, along with slight atmospheric variability, even in case of clear sky, can degrade the quality of the measurement;

2. step 3485 is very far from the default grating position. As already discussed (e.g., Fig. 4.11), the Brewer responsivity is lower and, additionally, very steep in this wavelength range (about 452–479 nm). As will be shown later in the text, this can make it very difficult to keep the Brewer in its linear regime (Sect. 5.4.6).

Since, as explained in Sect. 5.4.3, many points were needed for a Langley regression, I decided to exclude the measurements with method 2 from the schedule after the fifth day of the campaign and to increase the frequency of measurements with method 1. Therefore, from now on, only method 1 will be analysed.

5.4.6 Results using method 1 (six slits)

In principle, the extraterrestrial constant $\mathscr{F}_0$ should be the same for all observation geometries, if the AMFs are properly calculated. However, since the Brewer selects different filters for each geometry, which could introduce a slight spectral dependence, three distinct calibration constants were retrieved for direct sun and zenith sky (two polarisations) measurements.

The temporal series of the retrieved extraterrestrial constants with method 1 in the direct sun geometry are depicted, as instance, in Fig. 5.12 for each grating position (micrometer steps 1000, 1012, 2554). After detailed investigation, I did not find any correlation between the retrieved $\mathscr{F}_0$ values and other factors, such as atmospheric conditions (e.g., presence of thin cirrus clouds, aerosol optical depth, etc.) and statistical indexes (e.g., total number of measurements for each day). Therefore, only measurements during rain, fog or thick clouds were removed and the remaining were averaged to obtain a final estimate, along with its standard deviation, for each grating position and each observation geometry. Tables 5.2–5.4 report the median, the average and the standard deviations of the retrieved $\mathscr{F}_0$ in three geometries for each micrometer step.

Table 5.2: Final values for the extraterrestrial constants for grating position 1 (micrometer step 1000), expressed in DU.

	median	average	standard deviation
direct sun	0.82	0.82	0.08
zenith sky (parallel pol.)	0.70	0.72	0.09
zenith sky (perpendicular pol.)	0.75	0.75	0.06

Table 5.3: Final values for the extraterrestrial constants for grating position 2 (micrometer step 1012), expressed in DU.

	median	average	standard deviation
direct sun	3.18	3.18	0.10
zenith sky (parallel pol.)	3.05	3.04	0.12
zenith sky (perpendicular pol.)	3.08	3.08	0.08

Table 5.4: Final values for the extraterrestrial constants for grating position 3 (micrometer step 2554), expressed in DU.

	median	average	standard deviation
direct sun	74.37	74.41	0.10
zenith sky (parallel pol.)	74.40	74.32	0.33
zenith sky (perpendicular pol.)	74.46	74.42	0.16

Standard deviations are presented as an easy and well-known index of the spread of the data, although the distributions were far from normal (Fig. 5.13). In fact, two modes were present in some distributions. Probably, a large number of samples would provide better statistics. It is worth noticing that no relative standard deviation was reported, since it does not make sense with logarithmic values, as the $\mathscr{F}_0$'s are.

Generally speaking, the dispersion of the extraterrestrial constants was rather large. This is due to the weak absorption by NO_2 and the large noise in measurements as well as to the too short period of calibration. It is likely that a longer campaign would provide more accurate results. Moreover, it can be noticed that the standard deviations of the zenith sky measurements in the perpendicular polarisation were systematically lower than those in parallel polarisation. This is

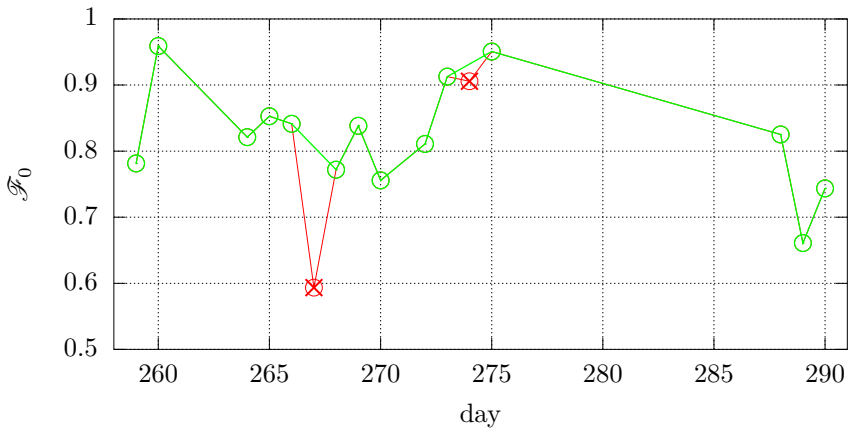

(a)

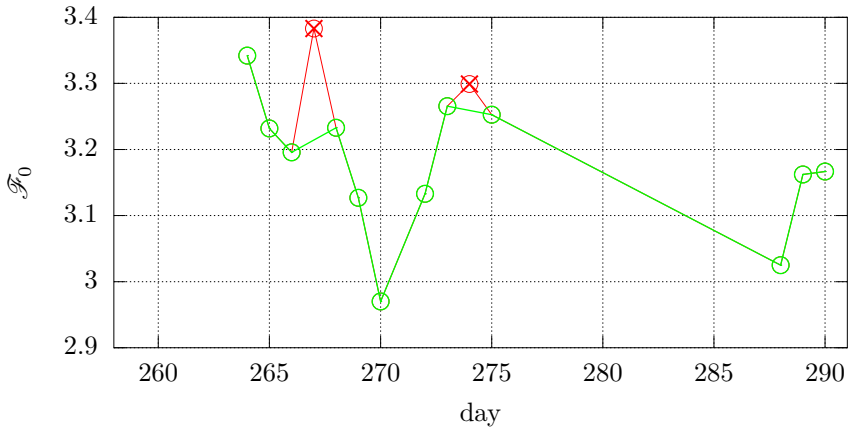

(b)

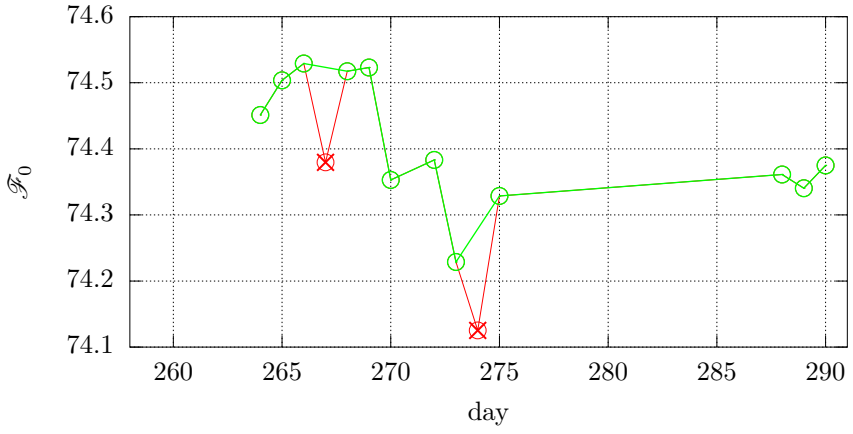

(c)

Figure 5.12: Temporal series of the retrieved extraterrestrial constants with method 1 in the direct sun geometry, for each micrometer step: 1000 (a), 1012 (b), 2554 (c). Green points are accepted values, red points are measurements removed because of fog, rain or thick clouds. Large gaps in the data occur when the schedule is switched to zenith sky measurements (not shown).

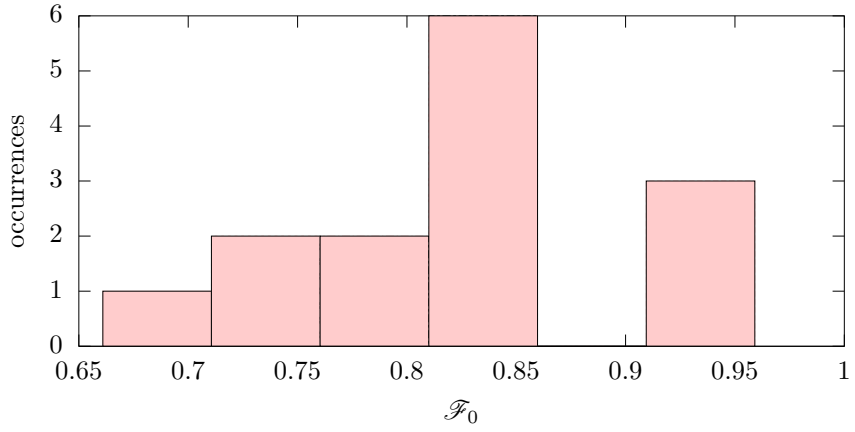

(a)

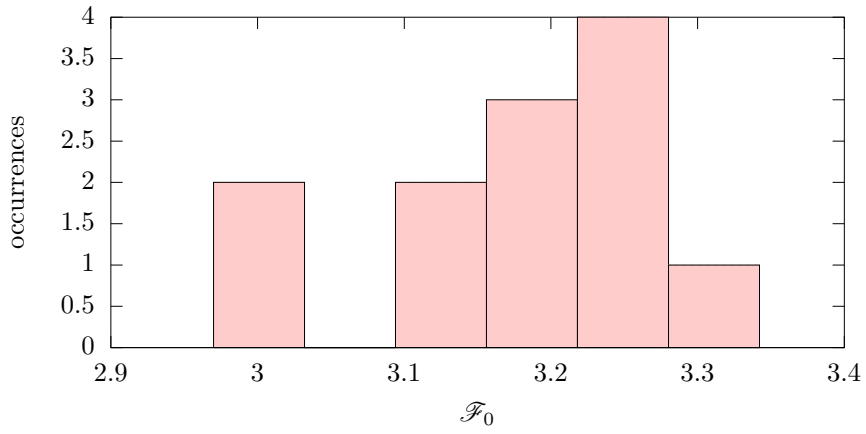

(b)

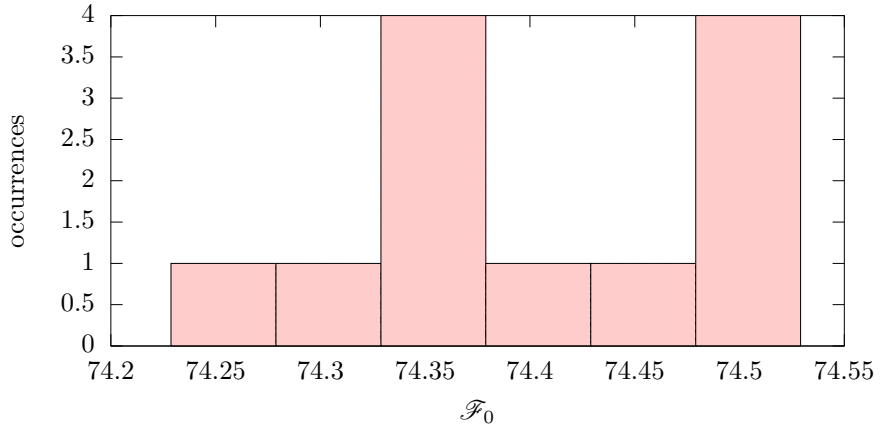

(c)

Figure 5.13: Distributions of the daily retrieved extraterrestrial constants with method 1 in the direct sun geometry, for each micrometer step: 1000 (a), 1012 (b), 2554 (c).

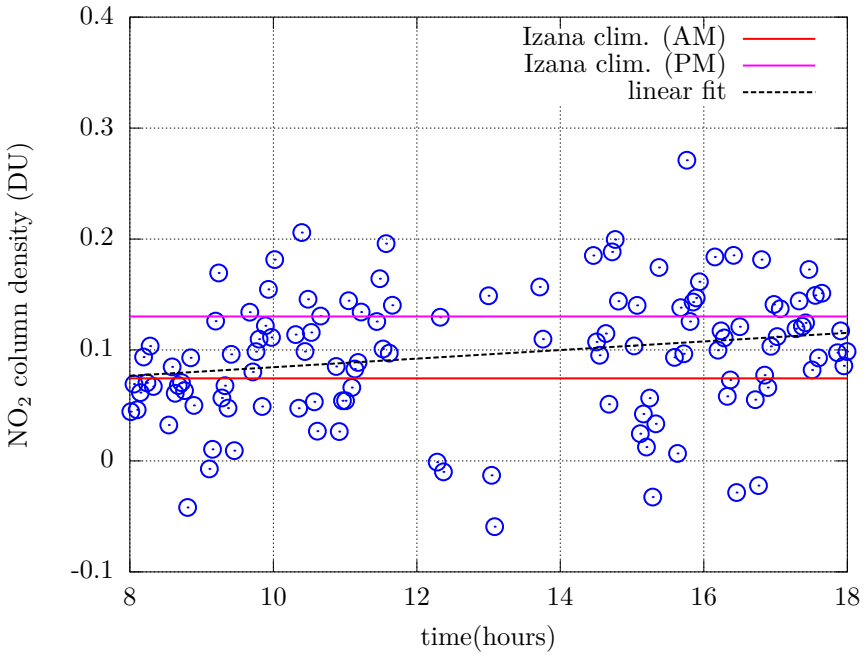

Figure 5.14: Daily NO_2 column evolution measured at Izaña (day 269, direct sun mode, micrometer step 1012). The horizontal lines delimit the theoretical daily evolution at Izaña from photochemistry calculations (Gil et al., 2008). The dashed line is a linear fit among data and represents the measured daily drift in NO_2 due to the photochemistry.

to ascribe to the higher number of photons, which results in lower Poisson noise, collected in the perpendicular polarisation compared to the parallel polarisation (Sect. 3.3.2).

After retrieving the extraterrestrial constants, I could finally calculate the NO_2 vertical columns. Figure 5.14, for instance, shows the measurements collected in direct sun mode during a clear sky day of the campaign. The scatter of the data was quite large, since the VCD of the absorber was low, as expected from unpolluted sites as Izaña. Indeed, only the stratospheric contribution, which is of the order of 0.1 DU, could be detected at this site. The measurements were promising and corresponded to the climatological values for Izaña in September-October from complex photochemical models (Gil et al., 2008). The daily NO_2 evolution, calculated using robust methods on all recorded data, is comparable to the values obtained in the scientific literature (Table 5.5). Specifically, I obtained rates between 7.0 and $12.5 \cdot 10^{13} \frac{molec}{cm^2\, h}$ using direct sun and zenith sky (parallel and perpendicular polarisations) geometries at the three steps.

Table 5.5: Daytime increasing rate of nitrogen dioxide due to the photochemistry, as reported in the scientific literature and in this study.

site	reference	daytime increasing rate ($10^{13} \frac{molec}{cm^2\, h}$)
Zugspitze/Garmisch	Sussmann et al. (2005)	5–15
Izaña	Gil et al. (2008)	6
Pacific Ocean	Peters et al. (2012)	8.7±0.5
Izaña	present study	7.0–12.5

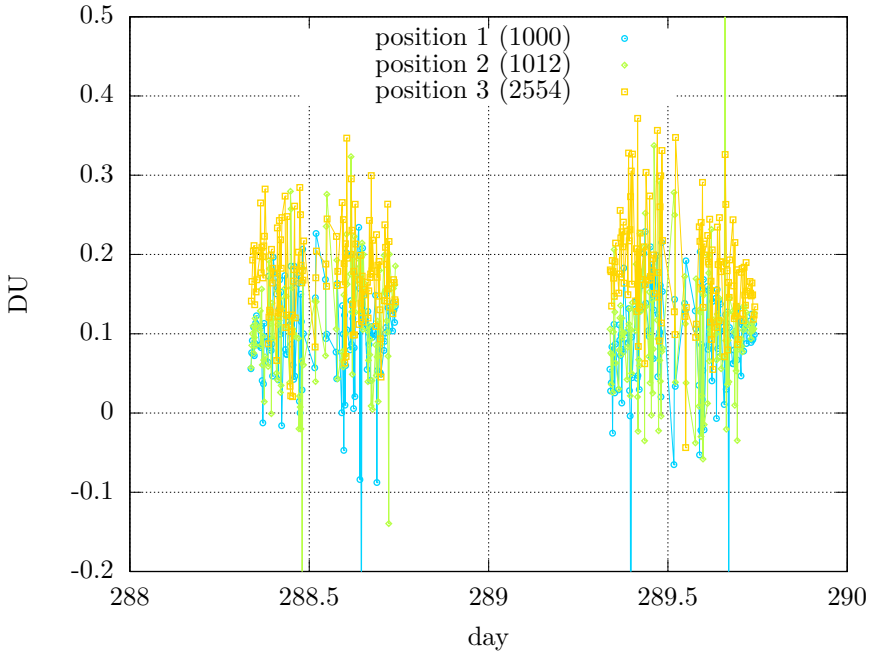

Figure 5.15: NO_2 direct sun estimates at three different grating positions for two sample days. Negative values may be due to noise or atmospheric variable conditions during the measurement.

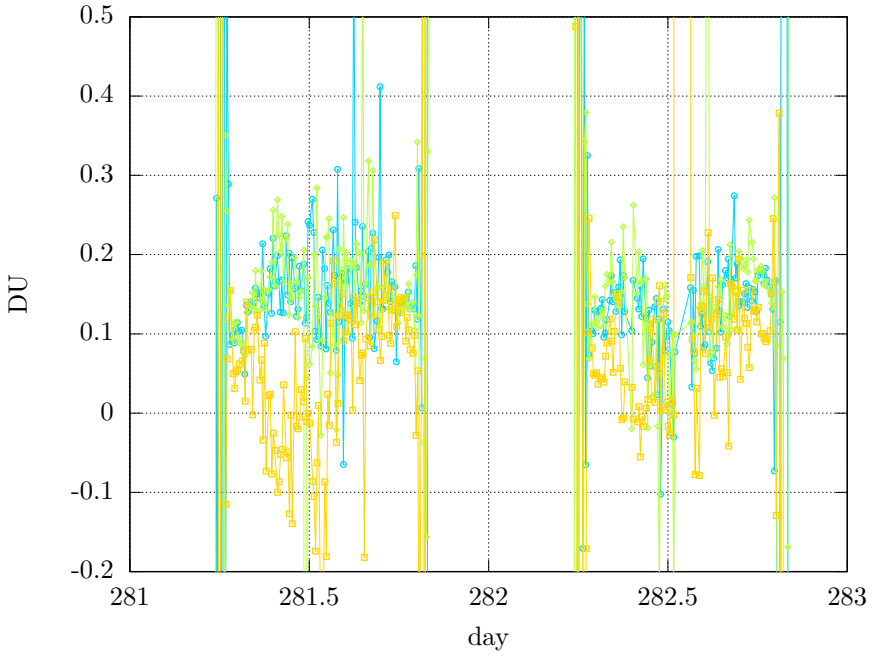

Figure 5.16: NO_2 zenith sky (parallel polarisation) estimates at three different grating positions for two sample days. The colour convention is similar as in Fig. 5.15.

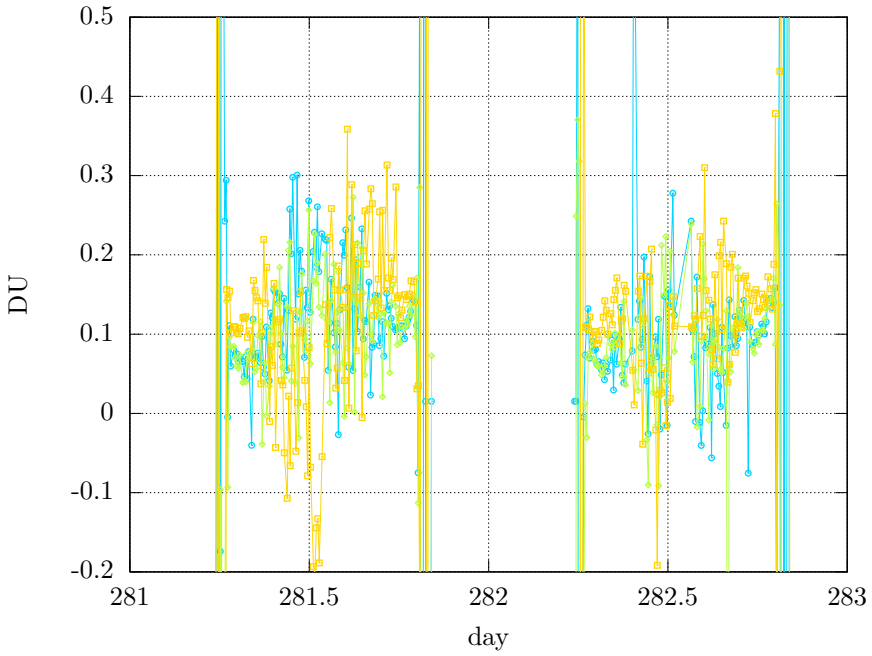

Figure 5.17: NO_2 zenith sky (perpendicular polarisation) estimates at three different grating positions for two sample days. The colour convention is similar as in Fig. 5.15.

Comparison among different grating positions

Estimates of the NO_2 VCD at the three different grating positions (micrometer steps 1000, 1012 and 2554), show similar results for the first two settings, while measurements at the third are systematically different. As an example, direct sun measurements for two days are plotted in Fig. 5.15. Results at grating position 1 and 2 are comparable, whereas measurements at position 3 are noticeably higher. Sometimes, sudden variations occur in the series obtained with the third grating position, as represented in Fig. 5.17 for the zenith sky geometry in the perpendicular polarisation. These jumps could be possibly explained by both the presence of thin cirrus clouds and the loss in instrumental linearity at that grating position. Indeed, the Brewer responsivity is very steep (Fig. 4.11) at the wavelengths selected at the step. For example, I calculated that NO_2 measurements at grating position 3 are about 20 times more sensitive to the dead time value than estimates at grating positions 1 and 2.

For this reason, although the wavelength range spanned by the third grating position is in principle interesting and unexplored by MKIV Brewers, the first two grating settings should be preferred for NO_2 measurements.

Comparison among different observation geometries

Since one of the objectives of my Ph.D. work was to compare the NO_2 estimates using different observation geometries, the Izaña campaign, held in an ideal environment, played a unique role in this task.

The full series of measurements in the three geometries for grating position 1 (step 1000) is represented, as an example, in Fig. 5.18. The figure depicts similar results for the three geometries. The effect of different schedules, leading to intermittent series for each geometry, is visible in the figure. Indeed, since the aim of the campaign was a Langley calibration, the schedule for each day included a prevalence of either direct sun or zenith sky measurements. Cloudy days measurements show a large spread. This is mostly due to changes in the path of the photons inside of clouds resulting in changes in the AMF, rather than real variations of the NO_2 VCD.

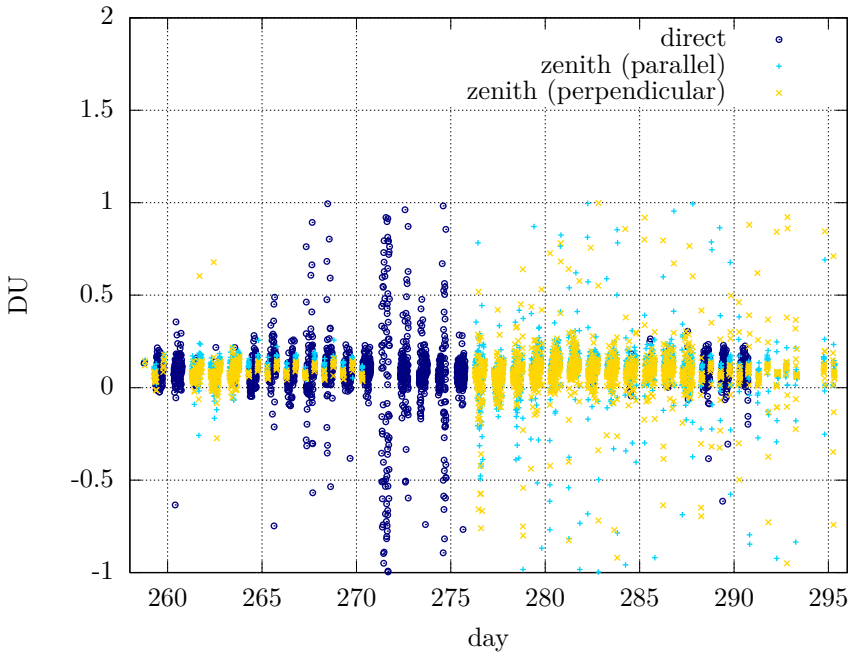

Figure 5.18: Full series of NO_2 VCD estimates during the Izaña campaign, using three observation geometries at grating position 1 (micrometer step 1000). Different schedules are visible in the figure, as gaps for each geometry. Cloudy days manifest as measurements with a large spread and negative values.

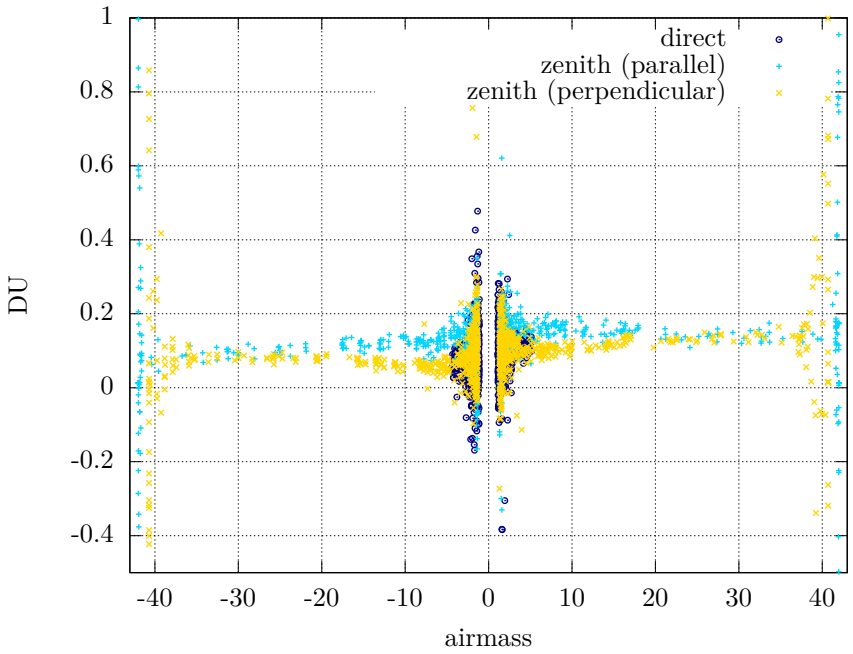

Figure 5.19: Clear sky measurements of NO_2 VCD estimates at grating position 1 during the Izaña campaign, using three different observation geometries, as a function of the AMF. Negative air masses refer to morning, positive to afternoon.

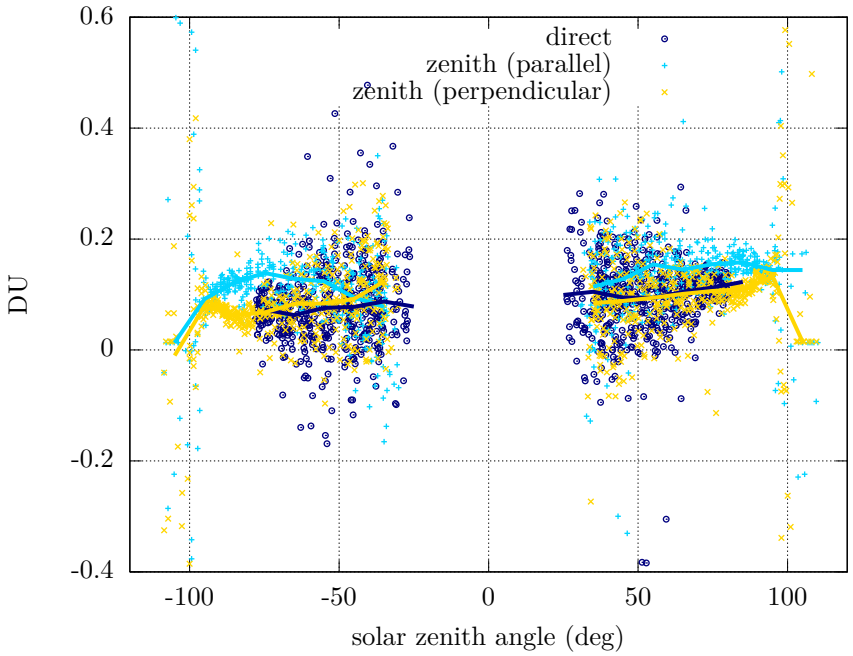

Figure 5.20: Clear sky measurements of NO_2 VCD estimates at grating position 1 during the Izaña campaign, using three different observation geometries, as a function of the solar zenith angle (negative angles refer to morning, positive to afternoon). Measurements were binned in several classes of solar zenith angles and the median values for each bin were plotted as solid lines.

The series of clear sky measurements at grating position 1 is presented in Fig. 5.19 as a function of the air mass factor. The figure nicely presents interesting characteristics. First, the estimates in direct sun and zenith sky at perpendicular polarisation geometries almost correspond, whereas measurements in zenith sky geometry with parallel polarisation are generally higher, although still within the uncertainty of the method (Sect. 5.4.7). Also, the figure shows that the measurement noise is remarkable high either at large or at small AMF. In the first case, the absorption signal due to NO_2 is high, but the number of photons is low, resulting in great uncertainty. Conversely, at low AMFs, the number of photons is high, but the absorption is weak due to the shorter photon path in the atmosphere. Additionally, the atmosphere is more turbulent at that moment because of heating. Noise can be further reduced by averaging a larger number of samples. This number was kept low (16) during the Izaña campaign to collect as many points as possible for the Langley plot.

Overestimation using zenith sky geometry in parallel polarisation are best visualised if the measurements are plotted against the solar zenith angle (Fig. 5.20). For ease of visualisation, the measurements were binned in several classes of solar zenith angles and the median values for each bin were plotted as solid lines. In principle, the overestimation can be attributed to several reasons: wrong extraterrestrial constant in the zenith sky geometry (parallel polarisation), wrong atmospheric profiles in AMF calculations or other effects. After careful investigations, I found that no value for the extraterrestrial constant exists which is able to flatten the shape of the curve for the zenith sky geometry (parallel polarisation): either estimates around noon get lower if the extraterrestrial constant is decreased or a maximum at about 70° forms if the constant is increased. Similarly, sensitivity analyses (not shown) reveals that no realistic atmospheric profile can substantially vary the AMF in Izaña and correct the wiggles in the graph.

Moreover, measurements in parallel polarisation just after sunrise and before sunset show an unphysical behaviour, namely increase at morning and decrease at afternoon, while the opposite tendency should result from the photochemical theory and is actually revealed in perpendicular polarisation.

At the end of a deep examination, I think that the most probable factor influencing zenith sky measurements in parallel polarisation is the Ring effect, as already noticed by Barton (2007). Among other things, two evidences are the most convincing:

1. data recorded in Saint-Christophe show that clouds give rise to sudden variations in zenith sky measurements in parallel polarisation, probably through the enhancement of the effect by rotational Raman scattering;

2. the curve is wavy for grating positions 1 and 2, which involve wavelengths close to a deep Fraunhofer line, whereas it is rather flat for grating position 3 (not shown), whose wavelengths are farther from strong Fraunhofer lines.

Unfortunately, no conclusive proof can be given through the use of radiative transfer models, since state-of-the-art algorithms are not yet capable to accurately simulate polarised radiances together with Raman scattering.

In brief, measurements of direct sun and zenith sky with perpendicular polarisation are to be preferred to zenith sky measurements with parallel polarisation.

5.4.7 Uncertainty estimation

The uncertainty estimate for Brewer measurements is a very complex task, since the retrieved VCD is the final product of a long chain of events: the measurement of the absorption cross sections (and their temperature dependence) in a laboratory, the evaluation of the weighting factors based on the instrument characterisation, the model calculation of the air mass factors, the calibration (by Langley plot or by comparison to a reference) and, at least, the measurement itself. Moreover, many influencing factor are correlated, in a clear or hidden way. Therefore, it is not surprising that only few works exist on that subject.

In this section, as a proof of concept, only a relatively simple case will be discussed: the uncertainty of NO_2 measurements in the direct sun geometry, in the same site where the Langley plot was performed and in the same time of the year. This case is likely to provide the minimum uncertainty attainable with the method proposed in my work. Conversely, different scenarios result in a larger uncertainty. For example, the zenith sky measurements are affected by almost the same factors as the direct sun geometry (actually, some of them are reduced due to the larger AMFs than the direct sun geometry) and, additionally, by the Ring effect, a more pronounced sensitivity to the atmospheric profiles, a more marked noise at large solar zenith angles, the little known efficiency of the polarising filter, etc. Also, direct sun measurements some time after the calibration will be affected by the uncertainties connected to the changes in the instrument response with time. Finally, even changing the Brewer location can add further uncertainty, since the operating conditions (e.g., the set of used filters) can be different compared to the calibration conditions and slight inaccuracies in the instrumental characterisation, which would be otherwise incorporated in the extraterrestrial constant, do not cancel out anymore.

Since an analytic assessment of the uncertainty is unfeasible and the influence of the various factors on the retrieved NO_2 can be non-linear, the traditional propagation of uncertainties in the framework of the Guide to the expression of uncertainty in measurements (GUM) (Gum, 1995) cannot be applied. Instead, I employed a Monte Carlo Method (MCM) (BIPM et al., 2008). Briefly, I developed a software able to reproduce the entire calibration, including the Langley plot (Sect. 4.4.2) over several days, and the processing of a series of measurements. Although it is possible to employ real measurements for the MCM uncertainty evaluation, I preferred to use the output data from a radiative transfer model, to additionally keep track of possible systematic deviations, compared to the "true" NO_2 (used as input value in the model), introduced by asymmetrical Probability Density Functions (PDFs) and non-linearities. The modelled values were transformed into raw counts by an inverse data reduction procedure (Sect. 3.4.1) and using Brewer #066 spectral response and characterisation (Sect. 4.1). The software generates a large number (1000) of input vectors, by sampling from the PDFs of the input quantities affected by uncertainties and considering them as possible realisations of the parameters. The standard deviation of the resulting

NO_2 values was taken as the standard (combined) uncertainty of the measurement as a function of the solar zenith angle.

The fundamental Brewer equation was used to express mathematically the relationship between the measurand, X_{NO_2}, and the input quantities on which X_{NO_2} depends:

$$\sum_i \gamma_i \cdot F_i = \sum_i \gamma_i \cdot F_{0i} - \mu_{NO_2} X_{NO_2} \sum_i \gamma_i \cdot \alpha_{NO_2 i} \tag{3.30}$$

it is essential to notice that, although not explicitly reported, Eq. 3.30 also includes other terms, such as the oxygen dimer correction. The latter will be taken into account in the next steps. Table 5.6 presents a complete list of the terms in the above equation, together with their most influencing factors. The uncertainty will thus be propagated from those factors to the retrieved NO_2 (Fig. 5.21):

Poisson noise was added to the signal during both the Langley calibration and the measurements, using samples from a Poisson distribution centred at the measured number of photons. Since the number of cycles in the direct sun routine at Izaña is $N = 16$, the same quantity of samples was then averaged to obtain a final value (this is equivalent to decrease the standard deviation of the photons PDF by $\sqrt{N}$). The resulting standard uncertainty of the output quantity, X_{NO_2}, which ranges from 0.02 to 0.08 DU, is compatible with the estimation reported in Table 4.7 which refers to only one cycle. The uncertainty decreases as the AMF increases, i.e. as the NO_2 absorption signal increases. Poisson noise is one of the main sources of uncertainty in the derived NO_2 in Izaña and could considerably be reduced by increasing the number of slit cycles. For example, if the number of collected samples (both in during the calibration and the measurements) were increased to 100, as in the standard direct sun routine (employed, for instance, in Saint-Christophe after the Izaña comparison), the standard uncertainty due to Poisson noise would decrease to 0.003–0.012 DU. This could be a remarkable improvement for future campaigns;

the uncertainty of the dark current is treated in a similar way as the uncertainty of the counts measured through other slits. The modelled dark count (and as a result, also the standard deviation of its PDF) was assumed to increase with the Brewer internal temperature. The resulting uncertainty on X_{NO_2} is negligible;

uncertainty of the filter correction. "Type A" (Gum, 1995) uncertainty, i.e. the standard deviation of the values obtained during the `jf` test (Fig. 4.13), is considered as normally distributed and affecting both the Langley calibration and the measurements. Interestingly, if the same set of filters is used in the calibration and in the measurements for each solar zenith angle, potential errors in the evaluation of the filter correction influence in the same way both $\mathscr{F}_0$ and $\mathscr{F}$ and cancel out. However, if a different filter is used at a specific solar zenith angle for the calibration and the measurement, then some uncertainty is introduced. This is the case when the Brewer is moved at a different location, with different solar intensities, or when measurements are performed in another time of year compared to the calibration or when clouds modify the solar irradiance. To take into account the latter point, I introduced some clouds in the modelled data. Both the cloud occurrence frequency and their maximum attenuation (assumed to be spectrally flat) were set to 30% (thin clouds). Since filter 3 is mostly used at lower ($< 65°$) solar zenith angles for both the calibration and the measurements, the effect on X_{NO_2} of the filter correction uncertainty is cancelled out. Then, at higher solar zenith angles, the contribution of (synthetic) clouds, together with the decreasing solar irradiance, originates a scatter of the used filters at a given solar angle and the associated uncertainty increases, up to 0.04 DU. If more thick clouds were considered, than the filter effect would have been relevant starting from lower zenith angles (however, the aim of a good cloud screening is indeed to remove the most disturbing clouds);

the **uncertainty of the wavelength alignment** translates in uncertainty in the measured spectral irradiance and, in turn, in the retrieved NO_2 VCD. The sensitivity of the spectral

Table 5.6: Factors analysed for the evaluation of the uncertainty of NO_2 measurements.

term	influencing factors	comments
F_i	Poisson noise	
	dark current	
	filter correction	the chosen filter depends on cloud cover
	wavelength misalignments	
	dead time	
	diffuse light in field of view	negligible in the visible range
	polarising filter efficiency	only relevant for zs geometry
	straylight	not considered
F_{0i}	same as for F_i	Langley interpolation and average of daily values
γ_i	ozone absorption coefficients	
	Ångström exponent	
	slit functions	
$\alpha_{NO_2 i}$	nitrogen dioxide absorption coefficients	
	NO_2 effective temperature	correlated to NO_2 effective height
	slit functions	
μ_{NO_2}	NO_2 effective height	
	profiles	only relevant for zs geometry
	solar zenith angle	negligible (NTP synchronisation)
O_4 correction	O_4 absorption coefficients	
others	Ring effect	only relevant for zs geometry
	H_2O	negligible
	unaccounted changes in response (sl correction)	not considered

irradiance to wavelength misalignments was already introduced in Sect. 4.2.6, but is here recalculated for the various solar zenith angles. Only the uncertainty in the offset of the wavelength scale was considered, even though the dispersion test could introduce some uncertainties on the mutual distance between the various slits. Then, I tried to assess the potential uncertainty of the operational wavelengths (in terms of steps), based on previous knowledge:

1. the `hg` test has an accuracy of 1 micrometer step;
2. the analysis of the wavelength adjustments of the `hg` test during the Izaña campaign provided normally distributed statistics with a standard deviation of 0.5 steps;
3. the SHICrivm software (Sect. 4.1.1), correlating the structures of the measured spectra to the Fraunhofer lines, gives deviations within the uncertainty of the algorithm itself, less than 0.02 nm (i.e. about 2 steps, in the visible), when the right dispersion function is used;
4. larger deviations (i.e. 4 steps for Brewer #066) were identified when using the dispersion function measured in the UV as a reference for the visible (Sect. 4.1.1);
5. Kerr and Davis (2007) provide much larger deviations, up to 12 steps, revealed through a step scan method. I think that these results, which seems a bit unrealistic, could be due to the wavelength used for their `hg` test, 302.1 nm. Indeed, this actually is a group of emission lines, whose central wavelength changes as their relative irradiances change, causing larger uncertainty.

On the basis of these considerations, a maximum uncertainty of 2 micrometer steps was given as input in the model together with a rectangular PDF. The resulting contribution to the combined uncertainty on X_{NO_2}, ranging from 0.02 to 0.12 DU, is the largest among all factors, as it has already been pointed out by many authors about NO_2 measurements (Orphal, 2003; Cede et al., 2006a). The magnitude of the uncertainty due to wavelength misalignments is compatible with the theoretical estimation reported in Table 4.7 (referring to only one step). Interestingly, the uncertainty decreases for larger solar zenith angles.

uncertainty of the dead time. An uncertainty of 10% (Gröbner, 1998) in the determination of the dead time was propagated to the irradiances (both during the Langley calibration and in the following measurements) and to the NO_2 final estimation. The influence on X_{NO_2} is negligible. However, this estimate does not take into account that the filter correction factor is also sensitive to the dead time;

diffuse light in the field of view. Diffuse light collected in the field of view of the instrument was considered by many authors as a potential source of error for the retrievals in the UV range (Cede et al., 2006a; Arola and Koskela, 2004). I added the diffuse radiance calculated at various zenith angles by a radiative transfer model, multiplied for the solid angle relative to a full field of view of 2.6° (Cede et al., 2003), to the direct sun irradiance. The effect on the retrieved NO_2 was negligible at all angles for the Izaña conditions. However, the effect may be noticeable for high aerosol loads, resulting in larger fraction of diffuse light;

the **uncertainty in the polarising filter efficiency** was not considered for direct sun measurements, but can represent a remarkable source of uncertainty in zenith sky NO_2 estimates, since, especially in the parallel polarisation, it can be considered a source of straylight;

straylight was not considered, since the corresponding characterisation was not performed. I think that the effect of straylight in the visible is considerably smaller than in the UV range because of the smaller solar irradiance variation with wavelength;

the **uncertainty of ozone absorption coefficients** propagates to the weighting factors and, consequently, to the linear combinations of both F_{0i} and F_i. An absorption coefficient uncertainty of 3%, based on the work by Burrows et al. (1999), was set. The uncertainty

propagated to X_{NO_2} is rather low (about 0.01 DU when considering also uncertainties in the NO_2 absorption coefficients);

uncertainty in the aerosol extinction. Aerosol extinction is treated in the Brewer algorithm using the Ångström formula (Eq. 3.10) with unit exponent. Uncertainty in the Ångström exponent translates to uncertainty into the calculated weighting coefficients. Based on the AERONET data gathered at Izaña in October 2012, the Ångström exponent varied from about 0.2 (Saharan dust) to 1.6 (smaller particles). A rectangular PDF with these two limits was used and a negligible influence on the final NO_2 VCD was obtained. This confirms the experimental finding that the NO_2 retrievals during the campaign were not influenced by Saharan dust events (Sect. 5.4.3). However, presence of a thick aerosol layer does affect the estimation of the AMF, especially in the zenith sky geometry (not considered here);

uncertainty of the slit functions. Since the ozone laboratory cross sections are convoluted using the Brewer slit functions (Sect. 4.2.8), an uncertainty in the slit measurements propagates to the calculation of the weighting coefficients. Furthermore, also the nitrogen dioxide cross section are convoluted by the same slit functions and the uncertainty is propagated to the differential absorption coefficient, $\sum_i \gamma_i \alpha_{NO_2 i}$. To assess the magnitude of these effects, the FWHM of the slit functions was perturbed by a lengthening factor (with gaussian PDF and standard deviation of 10%) and new effective absorption coefficients for both NO_2 and O_3 were recalculated at every MCM trial. The resulting effect on NO_2 is negligible (0.004 DU);

uncertainty of nitrogen dioxide absorption coefficients. Laboratory data describing the cross sections is affected by uncertainty, which is however not simple to quantify. Orphal (2003) reports deviations of 2.6% among the most recent data; Bogumil et al. (2003) states 3.4%; estimates by Burrows et al. (1998) and Vandaele et al. (2002) are about 4–5%. A conservative estimation of 4% was thus used, but small effect was observed on the retrieved NO_2 content (the standard uncertainty is about 0.01 DU when considering also the uncertainties of the O_3 absorption coefficients);

the **uncertainty of NO_2 effective temperature** translates into uncertainty in the NO_2 absorption coefficients. A standard uncertainty of 20 K (Redondas and Cede, 2007), which seems realistic for the Izaña conditions, was considered in the MCM. This corresponds to an uncertainty of about 0.005 DU on the NO_2 column, which is compatible with the value determined previously (Table 4.7 refers to the error due to a temperature difference of 74 K with a NO_2 column of 1 DU). Clearly, the uncertainty of the NO_2 effective temperature remarkably increases in polluted sites due to a twofold effect:

1. nitrogen dioxide in the polluted layer, which is close to the ground, has a much higher temperature than NO_2 in the stratosphere;
2. the effect of the NO_2 effective temperature is proportional to the total NO_2 column;

NO_2 effective height is a necessary input for the calculation of the AMF in the direct sun geometry. An uncertainty in the effective height of 5 km (Redondas and Cede, 2007) translates to a very low standard uncertainty of 0.001–0.002 DU, depending on the solar zenith angle. The low sensitivity on the NO_2 height distribution has already been listed as an important characteristic of the direct sun measurements. A detailed analysis of the effect of different profiles on zenith sky measurements is not provided here;

uncertainty of time, and its propagation to the calculation of the solar zenith angle, is not considered since all personal computers connected to the Brewers were synchronised by NTP protocol to the standard Internet time;

uncertainty of O_4 correction. The oxygen dimer correction (Sect. 4.2.7) is very useful to avoid overestimations in the NO_2 content. However, every correction brings along a corresponding uncertainty. The same correction factor was calculated starting from the cross sections by

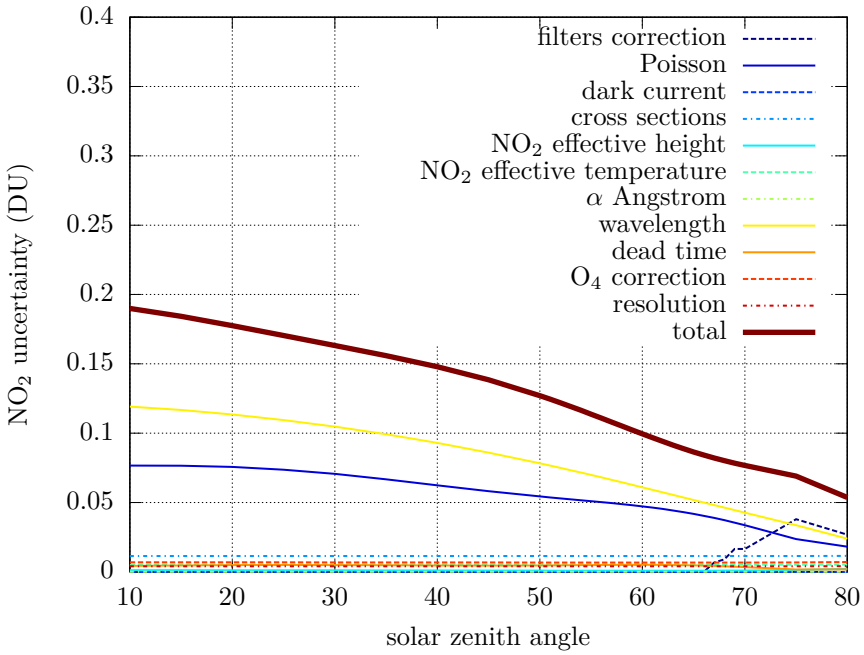

Figure 5.21: Monte Carlo standard uncertainty for Brewer NO_2 measurements in direct sun geometry in Izaña. The MCM was repeated allowing each influencing factor to vary within its uncertainty (thin lines), then a run (1000 MCM trials) with all uncertainties together was performed (thick line) to evaluate the combined uncertainty.

Greenblatt et al. (1990) and by Hermans et al. (2003) (suggested by NDACC) and differences of 30% were found. The same value is used as an estimation of the uncertainty of the correction, leading to an NO_2 uncertainty of about 0.007 DU;

other sources of uncertainties. Effective heights of absorbers different from NO_2 (ozone, aerosol, Rayleigh, etc.) have no influence on the calculation of the weightings, since only the shape of the cross section influences the weightings, and not their absolute values. The same is true for the Rayleigh dependence on pressure. The influence by water vapour was already found to be negligible with the new algorithm (Table 4.7). The Ring effect was not considered here since it only affects zenith sky measurements. Changes of the Brewer response with time which are not completely compensated by the `sl` test are not taken into account in the present MCM uncertainty assessment.

The combined standard uncertainty (Fig. 5.21) ranges from 0.05 to 0.19 DU with smaller values for large solar zenith angles. It is worth noticing that the standard uncertainty can be approximately twice the value of the measurand in Izaña for small solar zenith angles. This is compatible with the spread visible, for example, in Fig. 5.20. A plot of the PDFs is represented in Fig. 5.22 for several solar elevations.

A second simulation was repeated using a concentration of 0.1 DU during the Langley calibration and 1 DU during measurements to assess the effect of the total NO_2 concentration on the combined uncertainty. While some components increase with the concentration (for instance, the effect of the cross sections, effective temperature and resolution uncertainties), the combined standard uncertainty does not change proportionally (0.14–0.25 DU). Therefore, since the relative standard uncertainty decreases with increasing X_{NO_2}, the direct sun method is more accurate when large NO_2 concentrations are to be measured.

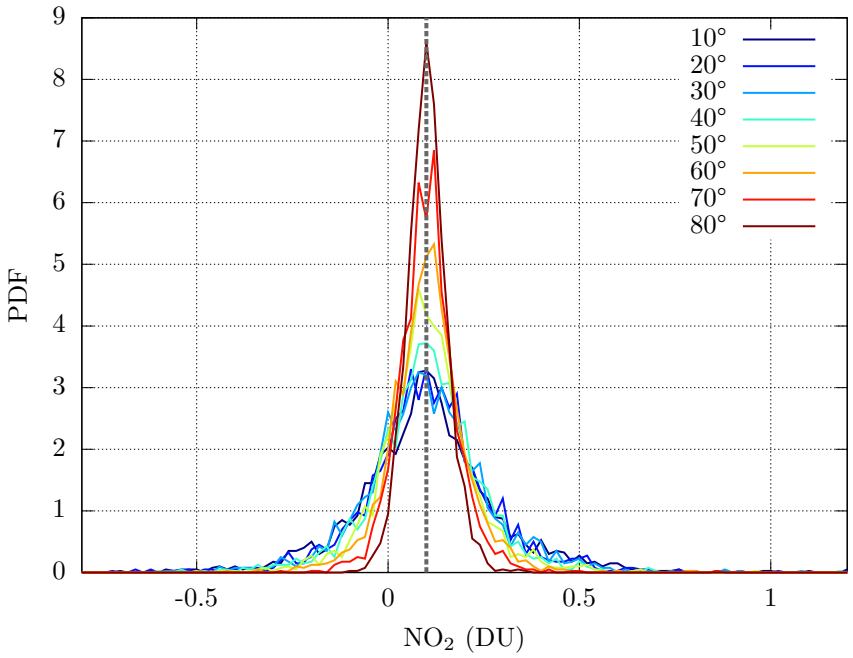

Figure 5.22: The MCM probability density functions for several solar zenith angles. The vertical line represent a NO_2 column density of 0.1 DU, corresponding to the value given into the radiative transfer model.

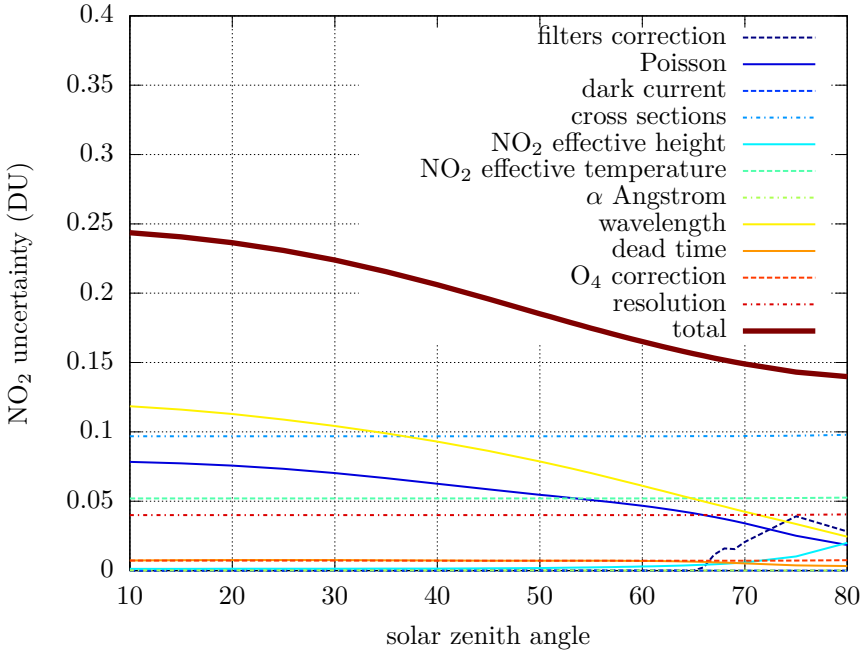

Figure 5.23: Same as in Fig. 5.21, but, after the Izaña calibration, the Brewer is assumed to be moved in a more polluted site with $X_{NO_2} = 1$ DU.

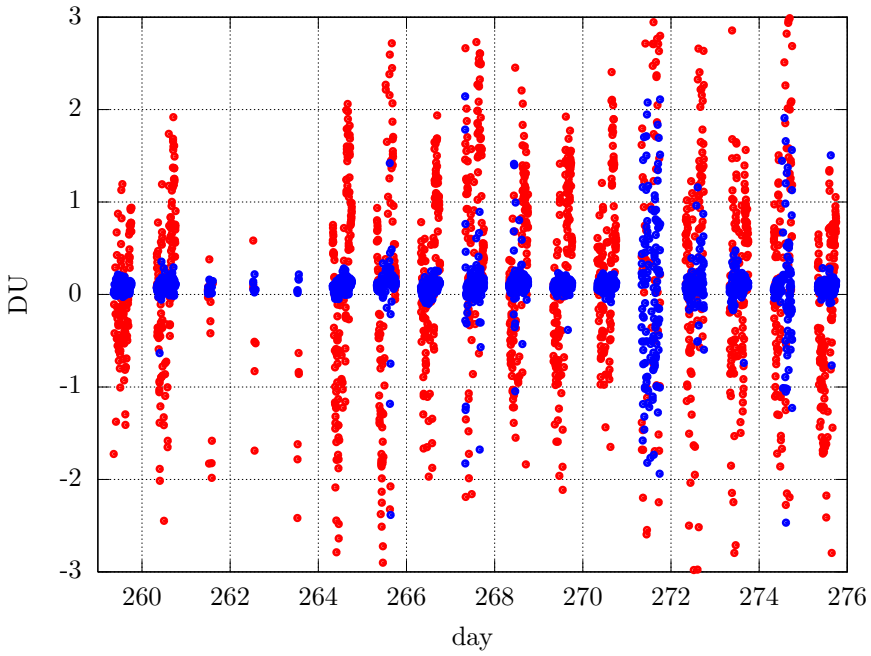

Figure 5.24: Comparison of the results using David Barton's algorithm (red dots) and the new algorithm (blue dots). Data are taken from direct sun measurements during the first days of the Izaña campaign (all weather conditions, including cloudy days, e.g. day 271). Default micrometer motor step 1000 for both series.

5.4.8 Comparison between different algorithms

As in Sect. 4.4.2, I present a comparison between different algorithms, but this time using the real data from the Izaña campaign instead of the estimates by radiative transfer models. As before, the methods included in the comparison are:

the standard algorithm by Kerr (1989), namely the algorithm used by the standard Brewer software;

an improved standard algorithm based on Kerr (1989), but with updated Rayleigh coefficients (Bodhaine et al., 1999) and inclusion of filters corrections;

the algorithm by Barton (2007), using six slits and removing the effect of the oxygen dimer;

the new algorithm (method 1) developed in this work.

All methods are applied after calculating the extraterrestrial constants appropriate for each algorithm through Langley plots.

For graphical reasons, the comparison between Barton's algorithm and the new one is shown separately (Fig. 5.24). It can be easily noticed that Barton's algorithm is remarkably noisier than the new one at the default Brewer motor step. This is to ascribe to the supplementary condition defined in Barton's algorithm to remove the O_4 effect, as already explained in Sect. 4.4.2. Furthermore, Barton's algorithm is extremely sensitive to wavelength misalignments, as expected from Table 4.7. As visible from Fig. 5.25, the results from the `hg` test (black crosses), representative of the wavelength misalignments, and NO_2 estimates using this algorithm are clearly correlated. Noise in Barton's algorithm may be reduced by changing the micrometer position, as in Fig. 5.26. In this way, the results become more similar to the new algorithm.

The comparison with the standard and improved standard algorithms is presented in Fig. 5.27 and 5.28. As may be noticed, results with both algorithms using Kerr's coefficients are higher

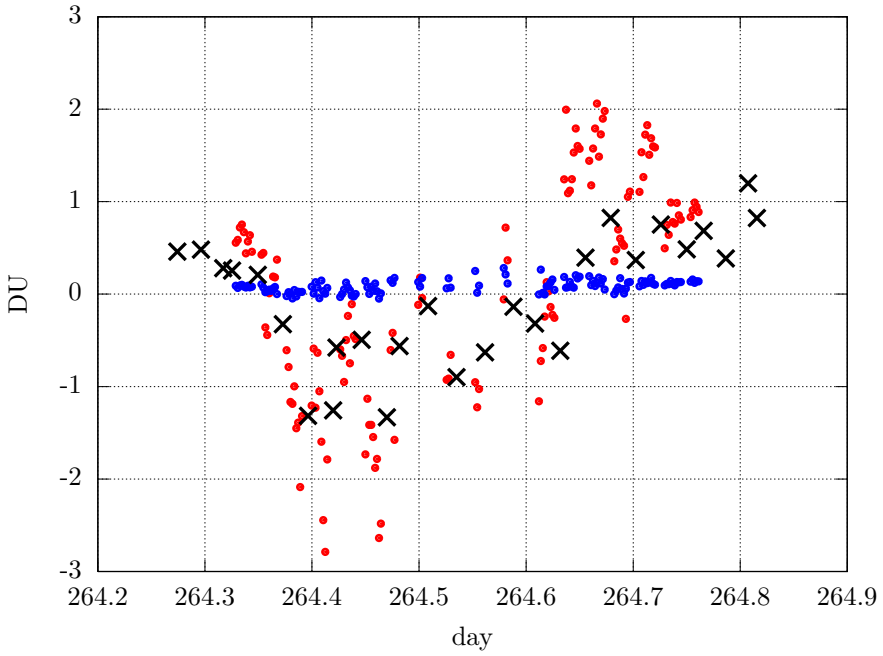

Figure 5.25: Same as previous for the clear-sky day 264. Black crosses are the results from the `hg` test (decreased by the nominal step 932 to allow visual comparison against NO_2 measurements).

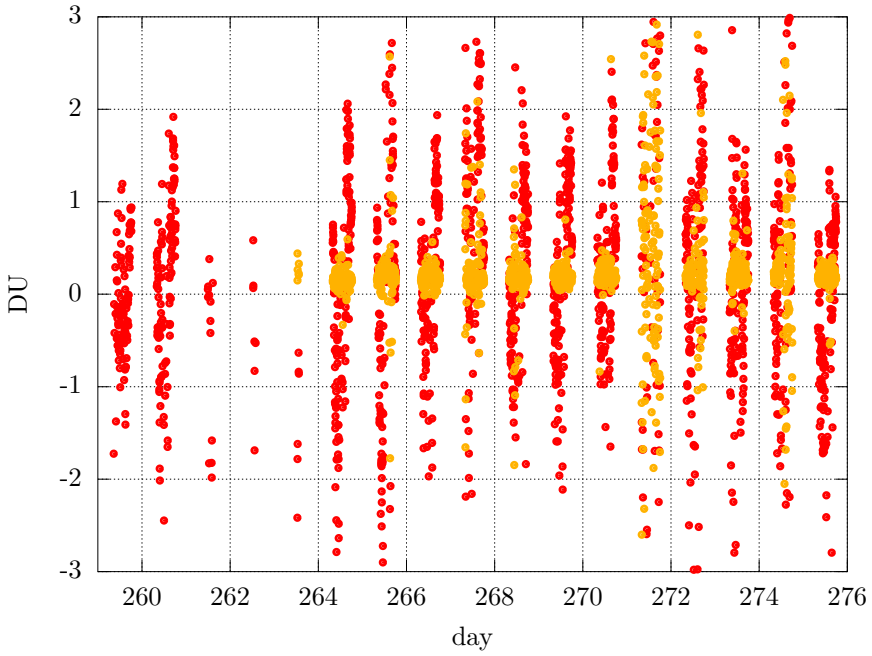

Figure 5.26: Results with Barton's algorithm using measurements at default micrometer position (1000), red dots, and at step 2554, orange dots.

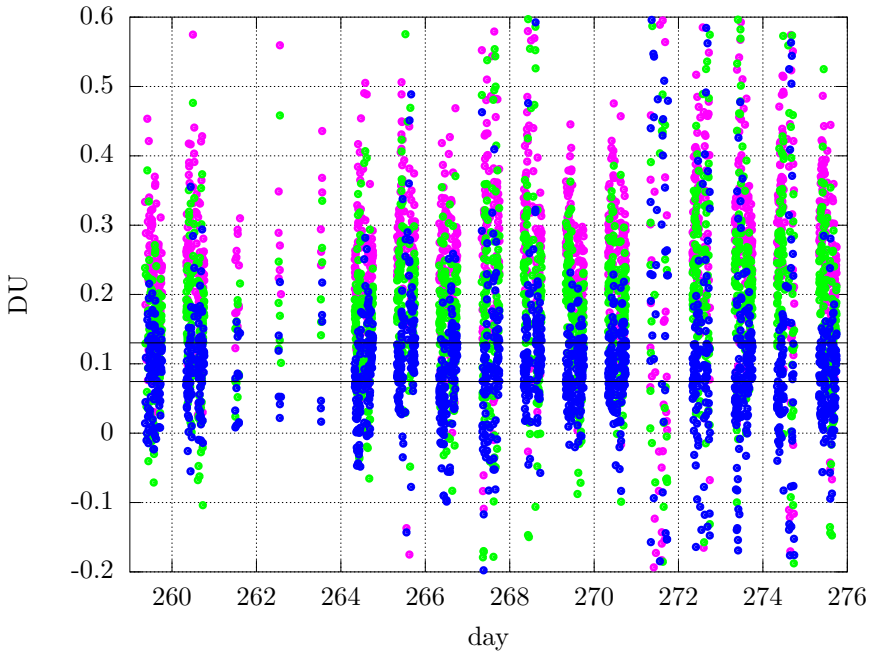

Figure 5.27: Comparison of the results using the standard Brewer algorithm (pink dots), the improved standard algorithm still with Kerr's coefficients (green dots) and the new algorithm developed in this work (blue dots). Data are taken from direct sun measurements during the first days of the Izaña campaign (all weather conditions, including cloudy days). Default micrometer motor step 1000 for both series. The NO_2 climatological content measured in September at the Izaña observatory is drawn as horizontal lines, for morning (lower line) and afternoon (higher line).

(more than 200%) than the estimates with the new one. The latter, on the contrary, perfectly fits the climatological NO_2 content measured at the Izaña observatory in September (black lines). The difference between the improved standard algorithm and my algorithm is approximately a scaling factor. However, the differences between the standard algorithm and the improved standard algorithm, due to the different Rayleigh coefficients and the filters correction, is a constant offset.

It should be emphasised that all previous experimental results were perfectly predicted by modelling studies in Chap. 4.

As a last comparison, Fig. 5.29 shows the values which would have been measured at Izaña if the obsolete extraterrestrial constants (as taken from the original instrument constants - ICF - file) had been used along with the standard Brewer algorithm. The (inverted) U-shaped daily evolution in the first series is a clear clue revealing wrong ETC values.

5.4.9 Comparison with a reference NDACC instrument

A UV-visible DOAS spectrometer owned by INTA (Spain) has been operating at Izaña since 1992. The instrument is certified by the NDACC (`http://www.ndsc.ncep.noaa.gov/sites/stat_reps/izana/`). Zenith measurements at twilight by this instrument can be compared to the Brewer estimates for the period of the campaign. A qualitative comparison is offered in Fig. 5.30, where zenith sky measurements at the default grating position (micrometer step 1000) along with data gathered by the reference instruments are presented. Overall good performances can be noticed also from Fig. 5.31, where the differences between nearly-simultaneous (within 10 minutes) measurements by both instruments are plotted. Differences are in the range -0.03–0.005 DU, well within the uncertainties of the Brewer (Sect. 5.4.7). Furthermore, it should be stressed that the comparison is performed for the zenith sky geometry, where the Brewer is affected by the Ring

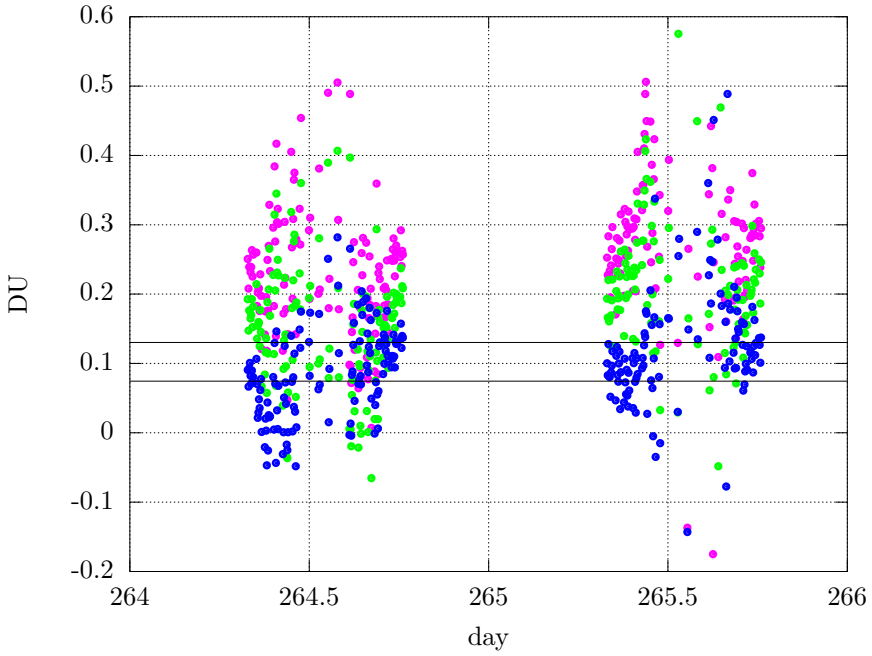

Figure 5.28: Same as Fig. 5.27, zoom on days 264 and 265.

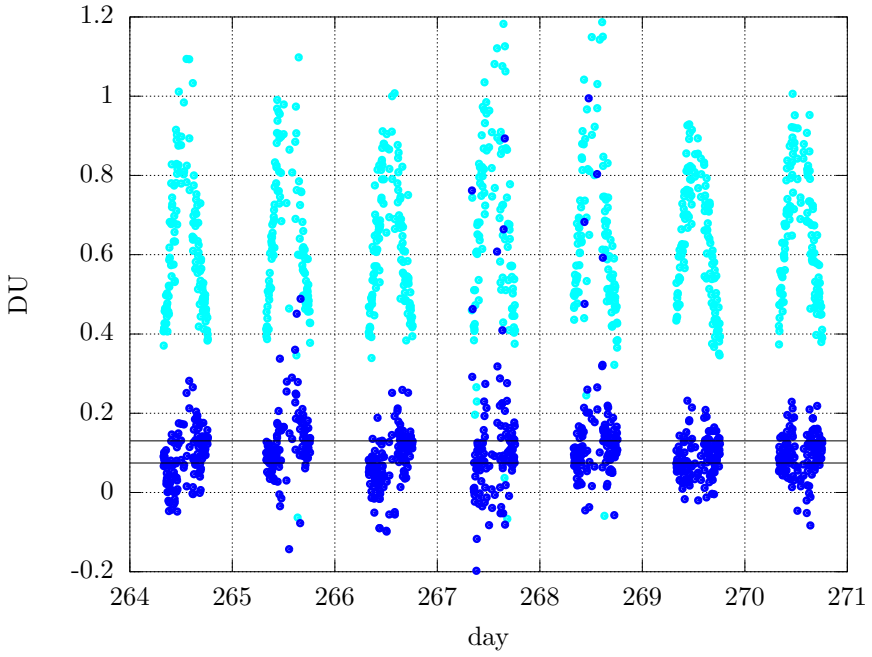

Figure 5.29: NO_2 estimates using the original Brewer algorithm with an obsolete extraterrestrial constant (light blue), showing typical inverse-U shape, and the new algorithm with updated extraterrestrial constant (blue dots).

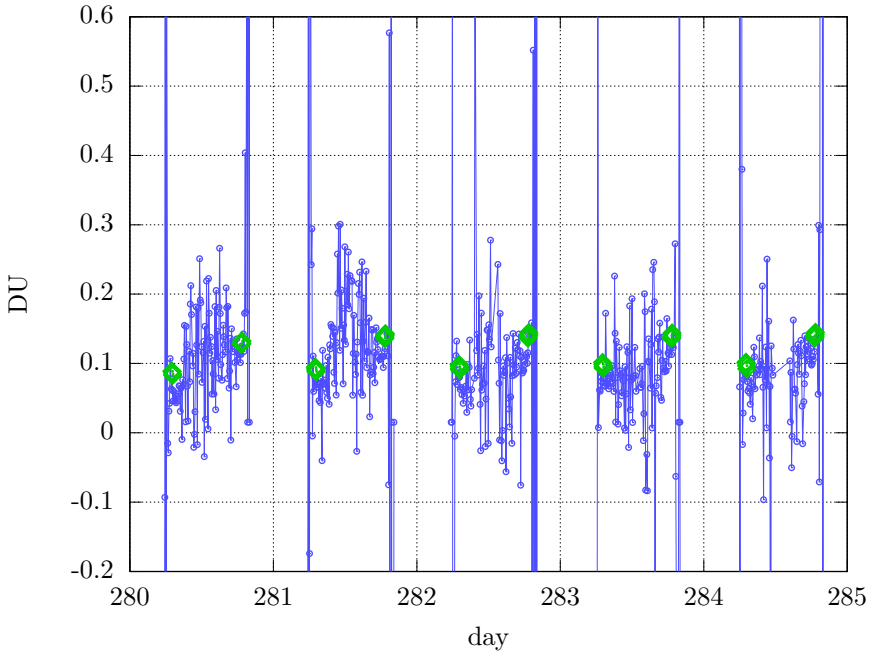

Figure 5.30: NO_2 estimates by the Brewer (blue line), in zenith sky geometry with perpendicular polarisation, and by the NDACC reference instrument at twilight (green diamonds).

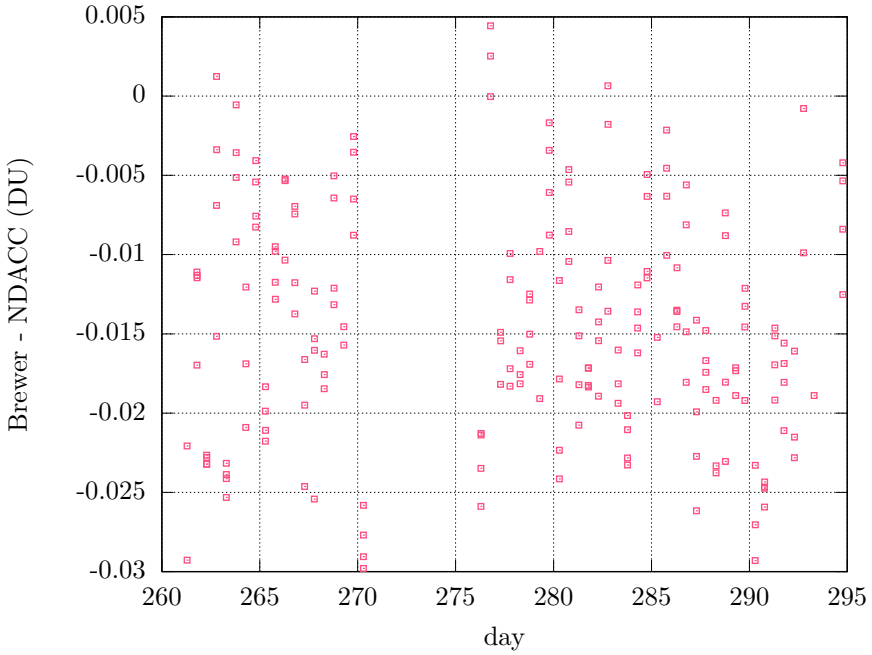

Figure 5.31: Differences between nearly-simultaneous measurements by the Brewer, in zenith sky geometry with perpendicular polarisation, and by the NDACC reference instrument at twilight.

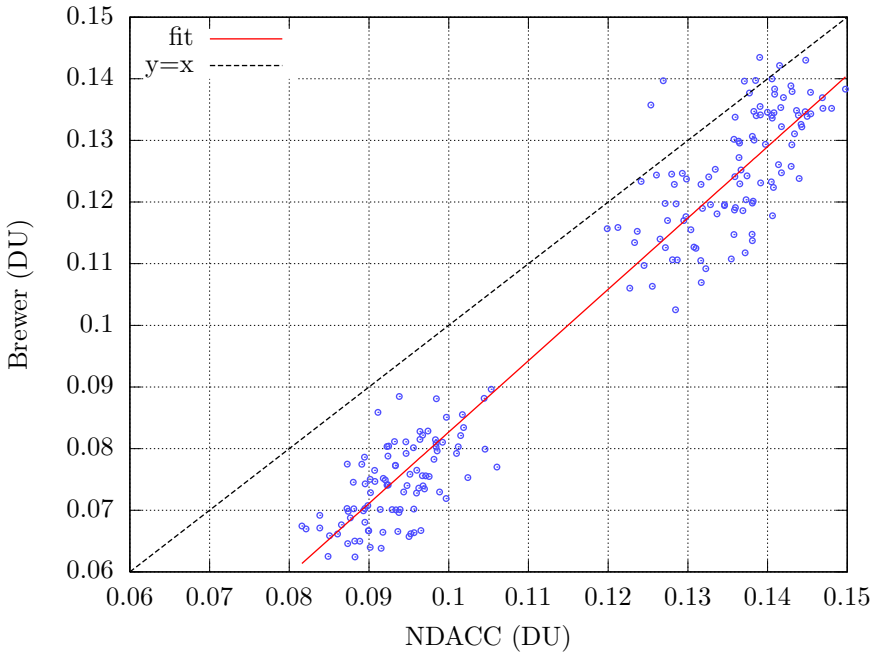

Figure 5.32: Scatterplot of NO_2 estimates by the Brewer, in zenith sky geometry with perpendicular polarisation, and by the NDACC reference instrument at twilight. The red line represents the fit of the data and the black, dotted line the bisectrix of 1st and 3rd quadrant (see Table 5.7 for the parameters of the fit).

interference. A scatterplot for the same series of nearly-simultaneous measurements is displayed in Fig. 5.32. Table 5.7 presents the results of the intercomparison in the same terms used by the NDACC guidelines (Piters et al., 2012; NDACC, 2013). A few characteristics can be mentioned. First, the slope of the comparison for parallel polarisation is generally lower than the slope with perpendicular polarisation, but the deviation from unity (reference value) with both geometries is almost similar. However, residuals with perpendicular polarisation are remarkably better. This can be due both to the highest number of photons and to the lower Ring effect in this polarisation. The residuals may be further improved by collecting and averaging more samples. Although promising, results are still outside the strict limits of NDACC protocols and the deviations are higher than the attainable accuracy with state-of-the-art instrument, of about 5–10% (Roscoe et al., 2010). However, it should be pointed out that those thresholds apply when comparing slant column densities, and different methods to calculate the air mass factors could make the comparison worse. Also, percentage deviations, as expressed by Roscoe et al., generally decrease when high NO_2 columns are measured (as during the Cabauw intercomparison campaign reported on the cited papers). Finally, NO_2 data in Izaña during the campaign showed very small variations and the bulk of the data accumulated in a narrow range of values. Thus, a scatterplot is rather risky, since the uncertainty of the parameters of the fit in such a short range can be very large.

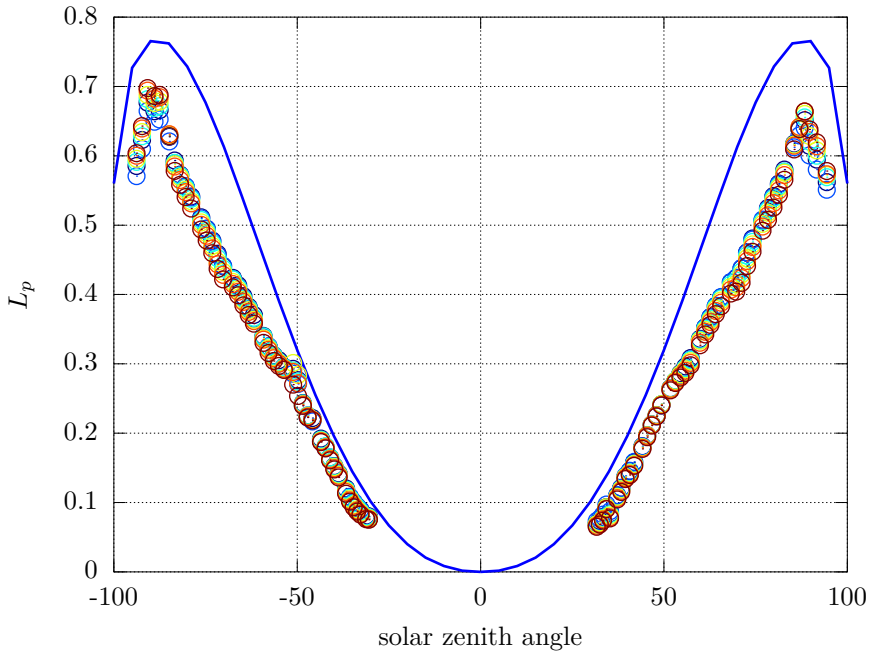

Figure 5.33: Degree of linear polarisation at the zenith for a clear sky day (263) calculated by the SCIATRAN radiative transfer model (line) and measured by the Brewer (circles, each slit is drawn with a different colour).

Table 5.7: Results of the intercomparison between the Brewer and the NDACC instrument. NDACC recommendations are written between parentheses in the first line. The first number for each cell is relative to the parallel polarisation, the second to the perpendicular polarisation.

micrometer step	slope (1.00±0.05)		intercept 10^{15} molec/cm^2 (1 ± 10^{15} molec/cm^2)		residual 10^{15} molec/cm^2 (< 0.5 10^{15} molec/cm^2)	
1000	1.01	1.15	0.39	-0.89	5.4	2.6
1012	0.84	1.20	0.91	-1.10	5.4	4.1
2554	0.88	1.08	-0.72	0.12	7.3	2.6

5.4.10 Degree of polarisation of the sky

Measurements at two different polarisations allow for the determination of the degree of linear polarisation of the sky, defined as (Coulson, 1988)

$$L_p(\lambda) \equiv \frac{I_\perp - I_\parallel}{I_\perp + I_\parallel} \tag{5.10}$$

where $I_\perp$ and $I_\parallel$ are the radiances measured in the perpendicular and parallel polarisations, respectively. Although L_p is not a standard Brewer product, it can give useful information about aerosols properties (optical depth and effective radius of particles) in the atmosphere (McLinden et al., 2001a) as well as about the cloud cover, since both factors affect the scattering characteristics in the atmosphere. Also, such measurements in the MKIV Brewer range would be even more interesting than in the UV, since the interference by the Rayleigh scattering is less strong in the former case compared to the latter.

Figures 5.33–5.35 show the degree of linear polarisation along the zenith as a function of the solar zenith angle, as calculated with the SCIATRAN radiative transfer model and measured by the

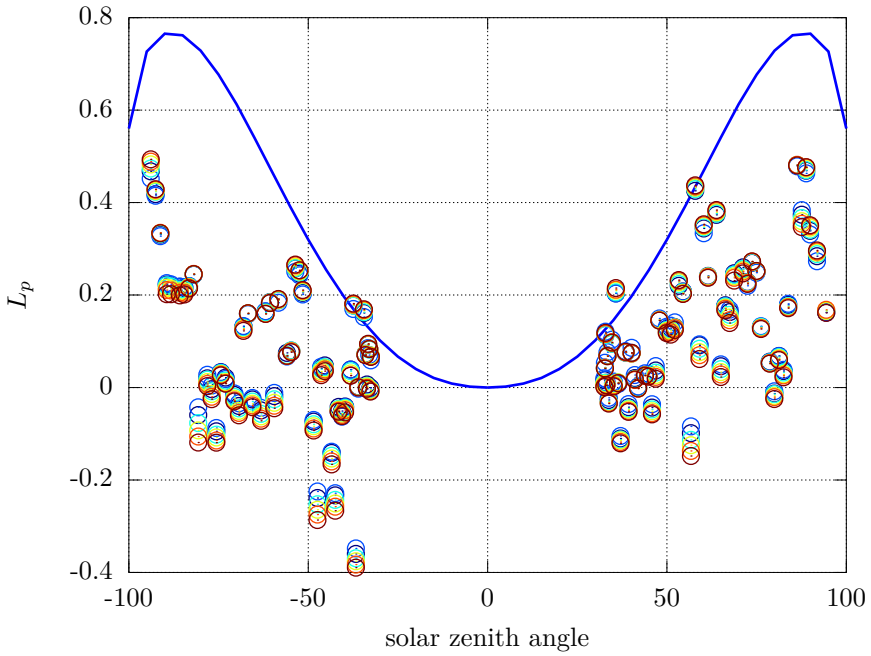

Figure 5.34: Degree of linear polarisation for a foggy day (277).

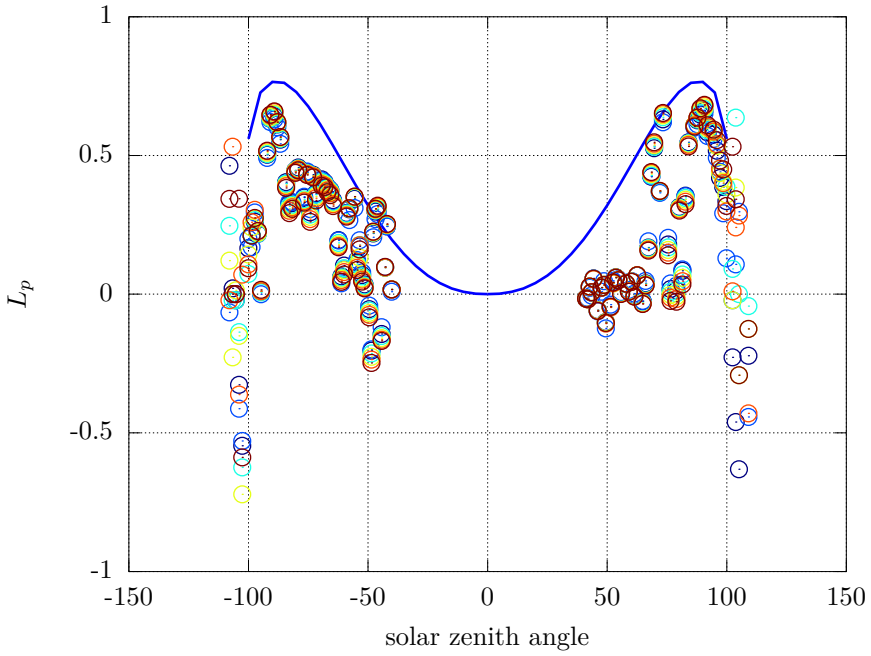

Figure 5.35: Degree of linear polarisation for a day with cirrus clouds in the sky (287).

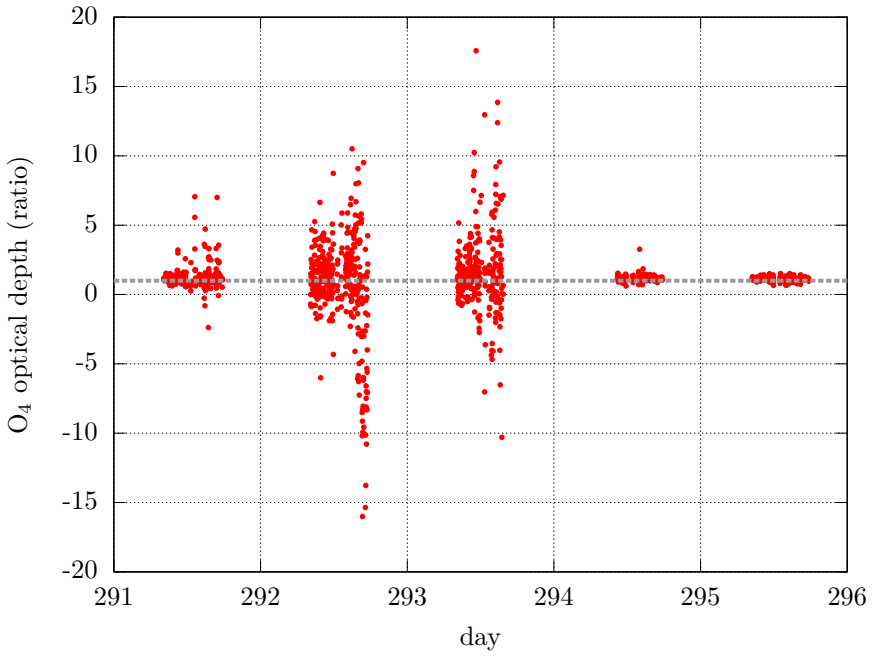

Figure 5.36: Ratio of O_4 optical depth measured with the Brewer and expected for clear sky from model calculations, during the last days of the Izaña campaign. Clouds in the sky can be easily revealed based on the oxygen dimer estimates. The dashed horizontal line indicates a unit ratio, i.e. perfect agreement between measurements and model expectations.

Brewer. The figures represent a clear sky day, a foggy day and a day with cirrus clouds, respectively. The effects of the different atmospheric conditions on L_p are remarkable. Even in the clear sky case, some deviations between the model and the measurements persist. I found that the deviations are compatible with a polarising efficiency of 95% of the polarising filter, which is realistic. A characterisation of the efficiency could be carried out, for instance, through laser measurements.

5.4.11 Measurements of the oxygen dimer optical depth

In the last days of the campaign, O_4 measurements were included in the schedule. Such estimates can provide useful information both in aerosol applications and for cloud screening purposes (Wagner et al., 2002, 2004; Daniel et al., 2003). Indeed, since the oxygen dimer optical depth depends on the oxygen concentration, which is known and stable, sudden apparent variations in the O_4 optical depth can only be due to changes in the AMF, mainly because of clouds and aerosols. Figure 5.36 summarises the results, expressed as ratios of the measured and expected O_4 optical depth in case of clear sky. Presence of clouds may be easily revealed from the plot as large scatter of the data, whereas clear sky measurements approach to unity, as expected.

5.5 The Saint-Christophe campaign (2013)

Brewer #067, operated by Sapienza – University of Rome, was moved to Saint-Christophe (Aosta) for about one month in summer 2013. The campaign aimed at checking whether a NO_2 calibration transfer is feasible from a Brewer to another. Brewer #067 was characterised in the same way as Brewer #066 (Sect. 6.3.1) and proper weighting factors were calculated, then both instruments were exposed to the sun with the same schedule to take simultaneous direct sun and zenith sky measurements.

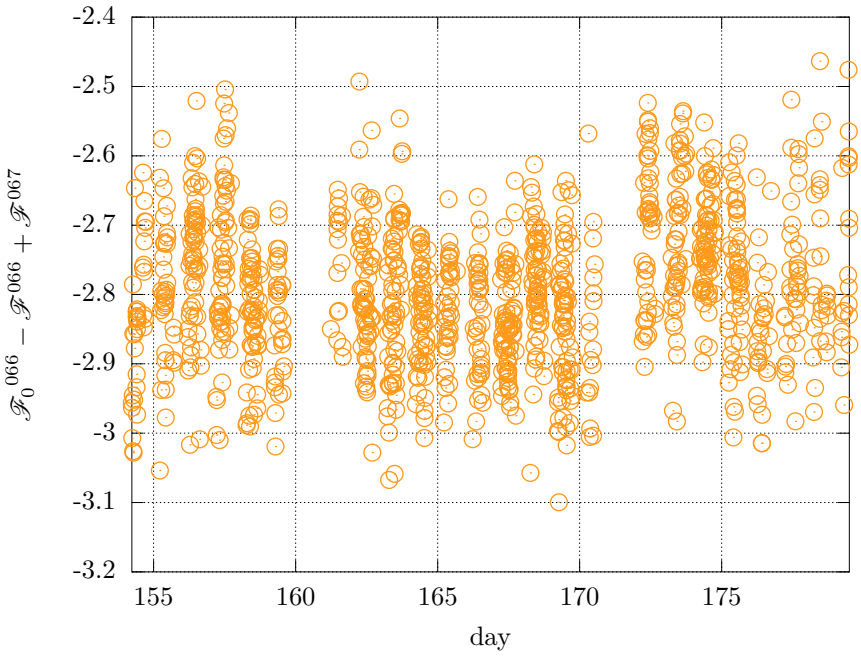

Figure 5.37: Temporal series of the estimates of the extraterrestrial calibration constant for Brewer #067.

Since the NO_2 VCD must be the same for coincident measurements with both instruments, it follows from Eq. 3.31 that

$$\mathscr{F}_0{}^{066} - \mathscr{F}^{066} \equiv \mathscr{F}_0{}^{067} - \mathscr{F}^{067} \tag{5.11}$$

Therefore, the calibration constant for Brewer #067 can be determined as $\mathscr{F}_0{}^{067} = \mathscr{F}_0{}^{066} - \mathscr{F}^{066} + \mathscr{F}^{067}$. This value is plotted in Fig. 5.37 as a temporal series and in Fig. 5.38 as a distribution histogram (whose shape is nearly gaussian, with mean -2.79 DU and standard deviation 0.11 DU). No dependency on the AMF was found (not shown). The best estimate for the extraterrestrial calibration constant for Brewer #067 is thus $\mathscr{F}_0{}^{067} = -2.79$ DU.

After the calibration, the NO_2 series of Brewer #067 was compared with the reference (Fig. 5.39). The average offset between both series is negligible and the standard deviation of the differences is 0.08 DU. The Pearson correlation coefficient between the series is 0.70 (1130 measurements), which indicates that both data series very likely belong to the same distribution.

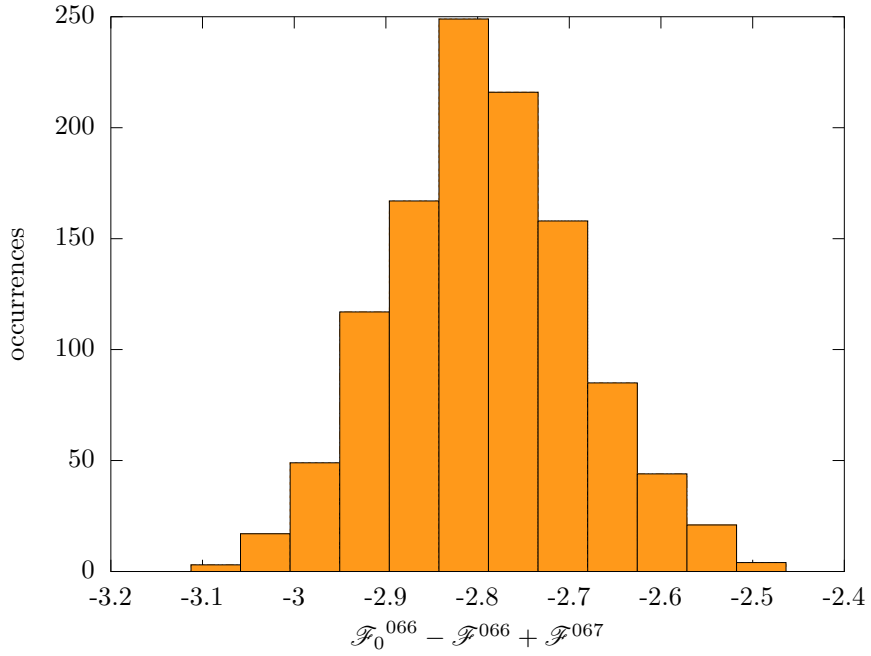

Figure 5.38: Histogram of the estimates of the extraterrestrial calibration constant for Brewer #067.

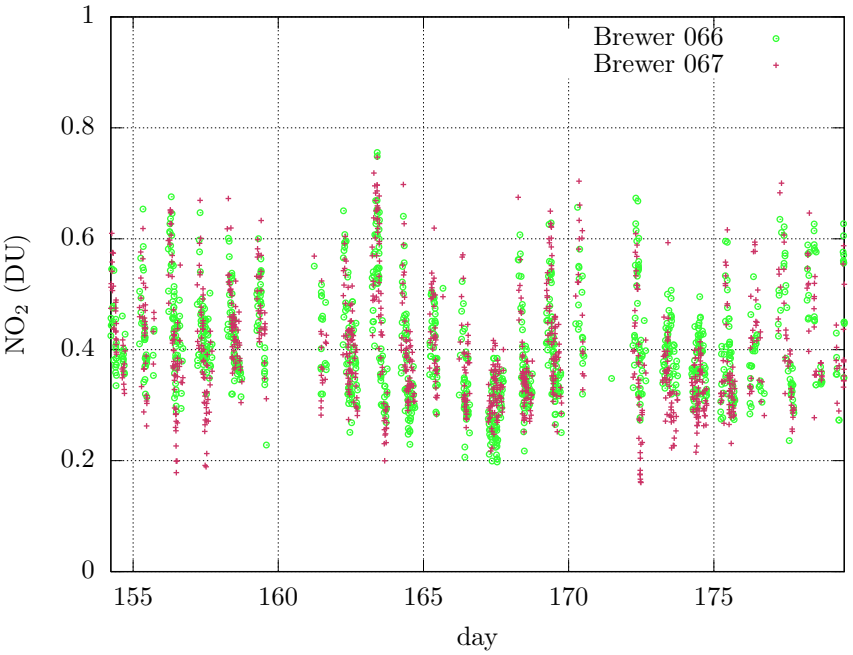

Figure 5.39: Series of NO_2 measurements with Brewers #066 (reference) and #067 in Saint-Christophe.

Chapter highlights

- I participated, together with Brewer #066, to four campaigns throughout my Ph.D. The Brewer showed very good performances compared to reference instruments and excellent stability during the journeys. The most important campaign was in Izaña, Tenerife, where Brewer #066 was calibrated through a Langley plot, becoming a (probably unique in the world) Brewer standard for NO_2. I additionally showed, during the Saint-Christophe campaign, that the calibration of Brewer #066 can be easily transferred to another instrument;
- I developed a new technique to take into account the daily evolution of NO_2 due to the photochemistry in the Langley calibration. This methods is very general (the only constraint is a linear NO_2 trend with time) and does not require complex photochemical models. The daily evolution retrieved by the new technique is coherent with the results published in the previous scientific literature;
- I performed a complete estimation of the NO_2 measurement uncertainty, using for the first time the Monte Carlo method together with Brewer retrievals, for the Izaña series in the direct sun geometry;
- I proved that measurements in the different geometries (direct sun and zenith sky) provide good results well within the uncertainty of the method. Method 2 (eleven slits) was found to provide noisier data than method 1 (six slits), which should be considered the preferred technique;
- I showed that useful quantities different from the nitrogen dioxide VCD can be retrieved using MKIV Brewer spectrophotometers in the visible range, such as the degree of linear polarisation of the sky and the oxygen dimer optical depth.

CHAPTER 6

Reprocessing of long-term data series

The algorithm and techniques I developed during my work can not only contribute to perform measurements with higher accuracy, but also to reprocess NO_2 data sets at stations collecting long-term observations. Indeed, all data needed for the retrieval, for instance the instrumental configuration and the photons revealed by the detector, are saved by the Brewer in the "B-files". These so-called "raw data" remain accessible in an electronic form and allow to reprocess a series with whatever algorithm.

One of the greatest capabilities of Brewer spectrophotometers is their organisation within a global network. Several instruments belonging to the network have been measuring NO_2 for a long time, up to twenty years. This represents an enormous resource for the scientific community, but – surprisingly – most series have not been adequately analysed, yet.

During the years of my Ph.D., the results of my research have progressively drawn large attention and some operators accepted to send their raw data for a reprocessing with the new algorithm. In such context, this chapter is dedicated to the use of some empirical methods to calibrate a Brewer without performing a Langley plot, thus avoiding to move the Brewers from their station. The long-term series of measurements at Saint-Christophe and Rome (Italy), Athens (Greece) and Hradec Králové (Czech Republic) are then reprocessed using my algorithm. Although a complete statistical investigation of the NO_2 trends and short-term fluctuations is beyond the scope of my work, exploratory data analysis and the study of the middle-term nitrogen dioxide evolution (loosely called "trend") is performed as an example of the possible applications using the new data. Finally, the Brewer measurements are compared to the estimates by three spaceborne radiometers.

6.1 Alternative calibration methods

In the previous chapter, two methods to calibrate a MKIV Brewer were introduced: the Langley plot technique and the transfer from a reference instrument to a target instrument. However, neither of the two techniques can be often applied. Indeed, few Brewers can be moved to a high-altitude site for a calibration and Langley plots at the ordinary measurement sites may be affected by tropospheric pollution. On the other hand, any travelling Brewer standard do not yet exist to provide an accurate NO_2 calibration by comparison. Nevertheless, if a long-term data series is available, alternative methods based on a statistical approach and some realistic assumptions turn out to be very useful and, frequently, the only possible solution.

Some interesting examples are provided by Herman et al. (2009), who developed two original algorithms:

the **Minimum-Amount Langley Extrapolation (MLE)**. When the tropospheric pollution is considerable and the NO_2 VCD is not constant during the day, the $(\mathscr{F}, \mu_{NO_2})$ plot, which in more pristine conditions would be a straight line, resembles a broad strip of points. Nevertheless, the higher envelope of this Langley-like plot is often well defined (see details in the box further below). This is the case when the minimum of the NO_2 VCD, instead of the VCD itself, is constant during the measurement period (or at least some portion of it) and independent of the AMF. The intercept of the line fitting the envelope may be considered as the extraterrestrial constant, just as in the standard Langley plot;

Detailed description of the MLE technique. Again, taking into consideration the Brewer fundamental equation:

$$\mathscr{F} = \mathscr{F}_0 - \mu_{NO_2} X_{NO_2} \tag{3.31}$$

For a fixed AMF, μ_{NO_2}, the maximum $\mathscr{F}$ corresponds to the minimum X_{NO_2}. If $\min X_{NO_2}$ is constant during the measurement period and independent of the AMF, then the higher envelope of the points distribution is a line whose intercept is $\mathscr{F}_0$. In order to fit it, the data can be binned in classes of similar μ_{NO_2} and the maximum of each group can be determined. To avoid possible outliers, however, a high percentile is used instead of the maximum.

Herman et al. (2009) describe an application of the MLE method to the DOAS technique, which implies slightly different laws and reverse graphs. To make my plots look like as in the reference paper, I analysed $-\mathscr{F}$ instead of $\mathscr{F}$. Accordingly, the lower envelope of the plot, identified by a low percentile (e.g., the third) of each class, is fitted instead of a higher percentile. ■

the **Bootstrap Estimation (BE)**. The method relies on the hypothesis that, in a sufficiently long data set, there will be at least few measurements when the tropospheric contribution is negligible and the NO_2 VCD is comparable to the stratospheric column. The latter is approximately known, e.g. from photochemical models, for each site as a function of latitude. The extraterrestrial constant can be adjusted so that the measured minima, or again a low percentile of the measurements (e.g., the third), correspond to a certain a-priori stratospheric value.

Detailed description of the BE technique. Let's assume that the minimum amount of NO_2 measurable at a specific location is the stratospheric content, $X^0_{NO_2}$, and let's study the quantity:

$$\max\left(\mathscr{F} + X^0_{NO_2}\,\mu_{NO_2}\right)$$

From Eq. 3.31, this is equal to

$$\max\left[\mathscr{F}_0 - \mu_{NO_2}\left(X_{NO_2} - X^0_{NO_2}\right)\right] = \mathscr{F}_0 - \min\left[\mu_{NO_2}\left(X_{NO_2} - X^0_{NO_2}\right)\right] \tag{6.1}$$

Since $\mu_{NO_2} \geq 1$ and $X_{NO_2} \geq X^0_{NO_2}$, the minimum in the second term is zero. Therefore,

$$\mathscr{F}_0 = \max\left(\mathscr{F} + X^0_{NO_2}\,\mu_{NO_2}\right) \tag{6.2}$$

Again, to make my plots consistent with the reference paper, I analysed

$\min\left(-\mathscr{F} - X^0_{NO_2}\,\mu_{NO_2}\right)$ instead of $\max\left(\mathscr{F} + X^0_{NO_2}\,\mu_{NO_2}\right)$. Moreover, to remove possible outliers from the analysis, a low percentile (e.g., the third) was used instead of the minimum. ■

Clearly, those empirical methods are much less accurate than a Langley calibration at a pristine site, which still represents the reference technique. For example, uncertainties are introduced when the a-priori VCDs and, to a lesser extent, the lower percentile, are chosen. Moreover, the underlying assumptions could be not completely fulfilled, for instance in case of a varying NO_2 baseline, which would compromise the MLE, or residual tropospheric contribution for the entire measurement period, which would make the BE fail. For this reason, an optimal length of the calibration period must be chosen: sufficiently long to allow the assumptions to come true and short enough to track real changes in the instrumental response.

I adapted both methods to the $1/\mu$ formulation introduced in Sect. 5.1 and I employed them to reprocess some long-term data series in Europe where MKIV Brewers are operated. The methods were validated in Saint-Christophe for the case of Brewer #066, the extraterrestrial constant of which was determined through an independent method (Langley campaign, Sect. 5.4). Then, the series of Rome (Italy), Athens (Greece) and Hradec Králové (Czech Republic) were analysed. The measuring sites are depicted in Fig. 6.1. As a proof of concept, only direct sun measurements will be taken into account.

6.2 The Saint-Christophe series

The series started in 2007, when the Brewer was moved from the European Joint Research Centre at Ispra (Italy) to the Environmental Protection Agency of the Aosta Valley (Diémoz et al., 2007). Measurements are performed on the roof of the agency building, at low altitude (570 m a.s.l.). The site is in a large valley floor with a wide field of view, up to 70° zenith angle. The location is in a semi-rural context, just out of town, partially influenced by anthropogenic activity on a local scale (emissions from cars from a nearby main road, heating systems, steel mill). The prevalent wind circulation is forced by mountain-valley and mountain-plain breezes.

A preliminary study on UV-visible spectra showed that the NO_2 absorption signal is clearly detectable in Saint-Christophe. To the purpose, I ratioed the spectra gathered by a Bentham spectroradiometer by the results of a radiative transfer model (not including any NO_2 contribution) and I performed a Principal Component Analysis (PCA) on the ratios (Wilks, 1995). The first component, rotated using the Varimax technique, is plotted in Fig. 6.2 together with the NO_2 cross section, detrended and convoluted with the spectroradiometer slit function. As clear from the graph, the two curves correlate well, proving that NO_2 strongly affects the solar irradiance spectrum measured at ground.

6.2.1 Validation of the Minimum-Amount Langley Extrapolation and Bootstrap Estimation

To check the accuracy of the extraterrestrial constants obtained by the MLE and BE, the results by the MLE and BE methods were compared to the Langley extrapolation in Izaña. For the purpose, I used six months of direct sun measurements taken in Saint-Christophe at micrometer step 1000 (standard position) just after the Izaña campaign. To screen only meaningful data, some empirical criteria were applied:

1. the AMF had to lie in the interval 1.5–3, for the same reasons explained in Sect. 5.4.4 (the maximum was slightly decreased to avoid any shadow by the mountains);

2. the count rates through the second slit must be above the first quartile of all count rates, to remove thick clouds;

Figure 6.1: Measurement stations of the data series reprocessed in this chapter: Saint-Christophe (1) and Rome (2), Italy, Athens (3), Greece, and Hradec Králové (4), Czech Republic.

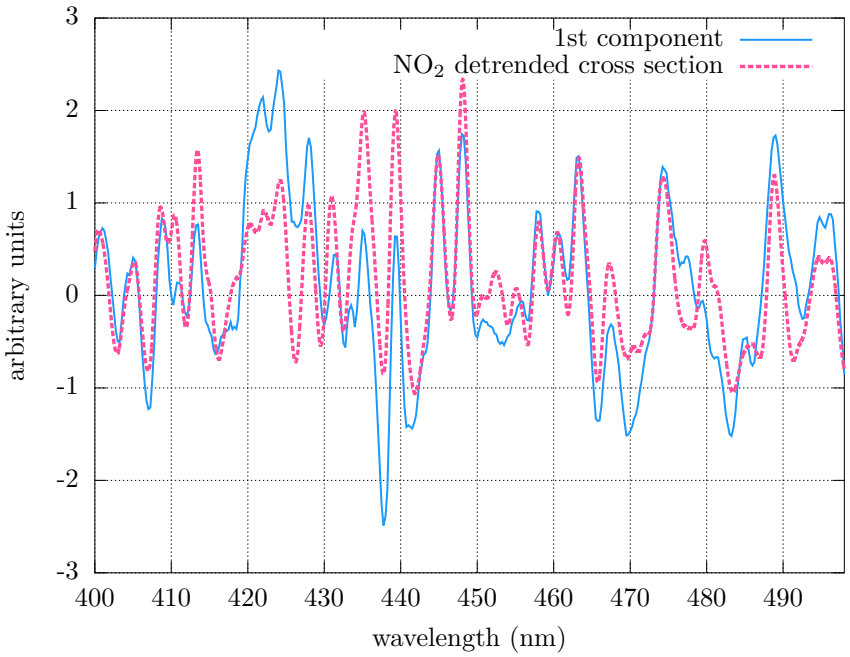

Figure 6.2: Blue line: first component resulting from Principal Component Analysis of the ratios between measured and modelled global irradiance spectra. Pink, dashed line: NO_2 cross section, detrended and convoluted with the spectroradiometer slit function. Both series were scaled to a unit standard deviation to allow visual comparison.

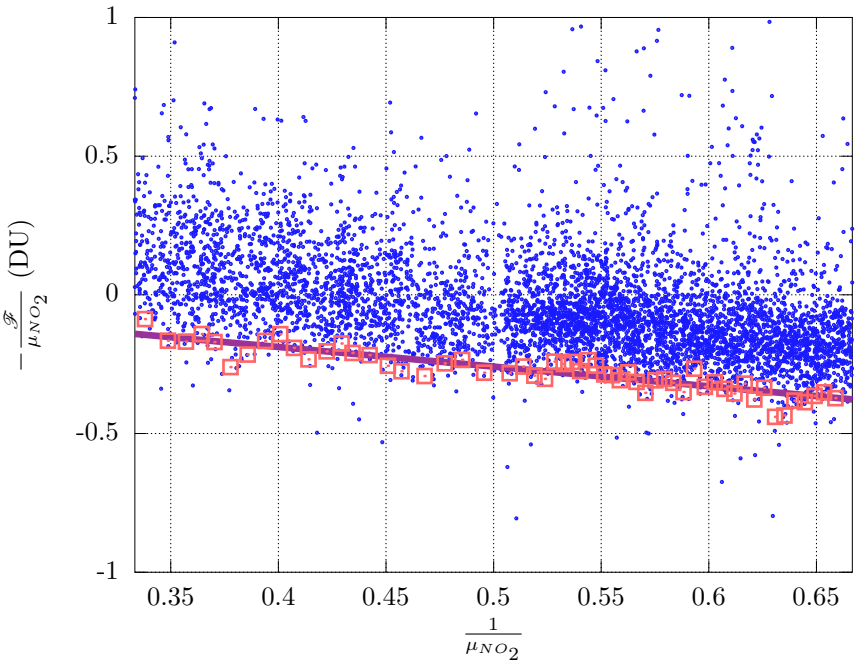

Figure 6.3: Minimum-Amount Langley Extrapolation applied to the Saint-Christophe data series after the Izaña campaign (measurements from about six months). NO_2 measurements are plotted as points on a $(-\frac{\mathscr{F}}{\mu_{NO_2}}, \frac{1}{\mu_{NO_2}})$ plane and the third percentile of each bin as a red square. Under the assumption that the minimum NO_2 is constant during the measurement period and independent of the AMF, the squares are fitted (violet line) and the negative slope of the regression line is the estimate of the extraterrestrial constant.

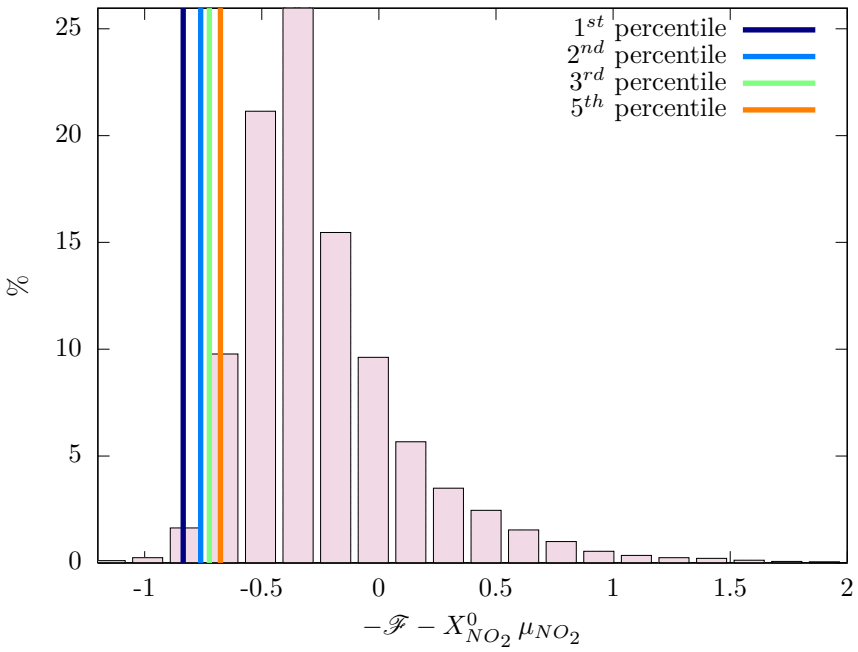

Figure 6.4: Bootstrap Estimation applied to the Saint-Christophe data series after the Izaña campaign (measurements from about six months). The distribution of $-\mathscr{F} - X^0_{NO_2}\,\mu_{NO_2}$ is plotted as an histogram. Some estimates of the extraterrestrial constant, as a function of the chosen percentile, are represented as vertical lines.

3. since the new routine `ns` was used for some months after the Izaña campaign, no criterion based on the standard deviation of the samples could be used (the `ns` routine only saved the average, not the standard deviation, of the samples in the output file).

A plot of the Minimum-Amount Langley Extrapolation technique is shown in Fig. 6.3. NO_2 measurements were plotted as points on a $({\mu_{NO_2}}^{-1}, -\mathscr{F}\,{\mu_{NO_2}}^{-1})$ plane. Bins containing a minimum of 100 points were identified and the third percentile of each bin was calculated. This points refer to the minimum NO_2 amount at a given AMF. Under the assumption that the minimum NO_2 is constant during the measurement period and independent of the AMF, the third percentiles are fitted and the negative slope of the regression line is taken as the estimate of the extraterrestrial constant, as from Eq. 5.3. Points lying too far from the fit were identified as outliers and removed and the fit was iterated. The retrieved calibration constant, using both least squares and least absolute deviations techniques, is 0.72 DU, slightly lower than the Langley estimate, but still well within the Brewer uncertainty. The choice of the percentile does not relevantly affect the extraterrestrial constant estimated by the MLE, as already noticed by Herman et al. (2009). As instance, switching from the third to the tenth percentile increases the estimate of the extraterrestrial constant by only 0.04 DU. Finally, using the MLE technique on the $(-\mathscr{F}, \mu_{NO_2})$ plane gives only slightly lower (0.70 DU) results compared to the $\frac{1}{\mu_{NO_2}}$ formulation.

The application of the BE to the same series is summarised in Fig. 6.4. A stratospheric content of $X^0_{NO_2} = 0.1$ DU was assumed and the distribution of the quantity $-\mathscr{F} - X^0_{NO_2}\,\mu_{NO_2}$ was plotted, together with the first, second, third and fifth percentile, which represent the (negative) estimates of the extraterrestrial constant, as explained in the previous section. As already noticed by Herman et al. (2009), the left side of the histogram is rather steep, which helps in accurately identifying the desired minimum. Therefore, the retrieval only slightly depends on the chosen percentile. As an example, the estimate of the extraterrestrial constant is 0.84, 0.76, 0.72 and 0.68 DU for the first, second, third and fifth percentiles, respectively. It is worth noticing that the

Table 6.1: Estimates of the extraterrestrial constant at micrometer step 1000 using different techniques.

method	extraterrestrial constant (DU)
Langley calibration (Izaña)	0.82
MLE	0.72
BE	0.72

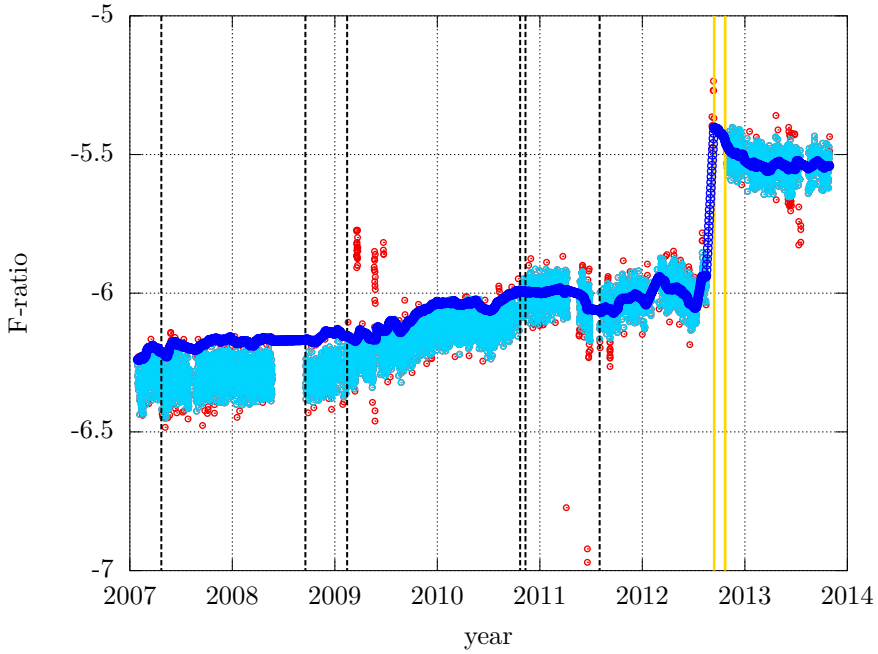

Figure 6.5: Results of `sl` test for Brewer #066. Light blue points represents the linear combination, $\mathscr{F}$, obtained using the lamp as a source, red points are outliers removed from the analysis by my software. The Izaña campaign is delimited by orange vertical lines. The final `sl` series (blue points) is obtained by imposing continuity before and after standard lamp replacements (black vertical dashed lines) and applying a running average filter. A steep change is visible just before the Izaña campaign as a consequence of a PMT overfilling.

estimate with the third percentile perfectly matches the result of the MLE retrieval. To assess the sensitivity of the retrieval to the assumed stratospheric column, the latter was changed by ±0.03 DU. Accordingly, the calibration constant became 0.67 and 0.78 DU, respectively.

Table 6.1 summarises the estimates of the Brewer #066 extraterrestrial constant at micrometer step 1000 using different techniques.

6.2.2 Reprocessing of standard lamp test series

As explained in Sect. 3.4.4, the internal `sl` diagnostic test is an efficient way to accurately track any variation of the Brewer sensitivity. Therefore, I reprocessed the full series of lamp measurements with the new set of weightings (Table 4.6). Sudden variations of the `sl` results may occur when the lamp is replaced after burning out, because the spectral emission of a new lamp may be different from the older. Since the Brewer response is supposed not to change just before and after the replacement, any discontinuity in the `sl` series caused by a standard lamp replacement must be removed. To this purpose, I calculated the averages of the F-ratio 15 days before and after

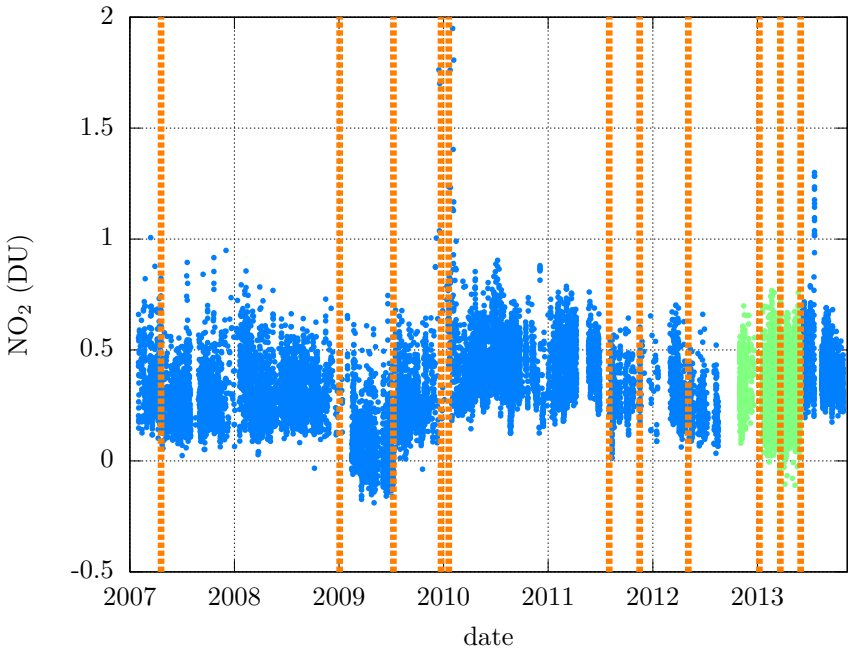

Figure 6.6: Series of NO_2 measurements in Saint-Christophe after first reprocessing with the new algorithm. Blue points: direct sun measurements with the standard `ds` routine; green points: direct sun measurements using the multistep `ns` routine; vertical dashed lines: events that may affect the wavelength alignment of the Brewer.

the replacement and applied an offset to the first part of the series to allow the first average to correspond to the second. Finally, a running average with a window of ± 15 days was applied to the series. Results are shown in Fig. 6.5. The final F-ratio is rather smooth, confirming the overall stability of Brewer #066. The only remaining steep variation is visible before the Izaña campaign, as a consequence of a PMT overfilling and the resulting change in the Brewer spectral responsivity.

6.2.3 First reprocessing of the NO_2 series

A first reprocessing of the direct sun Saint-Christophe series was attempted, using the new algorithm developed in this work and the extraterrestrial constant determined during the Izaña campaign. Only good data were selected based on three different criteria, empirically determined from the measurements series themselves:

- the standard deviation of the VCDs retrieved from the five samples collected by the `ds` routine for each measurement had to be < 0.07 DU;
- the count rates through slit 2 had to be higher than their first quartile to ensure good signal and to exclude thick clouds or sun below the mountain horizon;
- the solar zenith angle had to be $< 70°$ to exclude shadows by the mountains or by the quartz window border.

The standard lamp correction, described in the previous section, was employed to track and correct the Brewer calibration drifts. Results are presented in Fig. 6.6 and are far below the expectations: most of all, some sudden jumps in the NO_2 baseline can be clearly distinguished. These unexpected variations are not visible in the standard lamp measurements (Fig. 6.5), which means that a change in the Brewer spectral sensitivity is not likely the reason of the jumps.

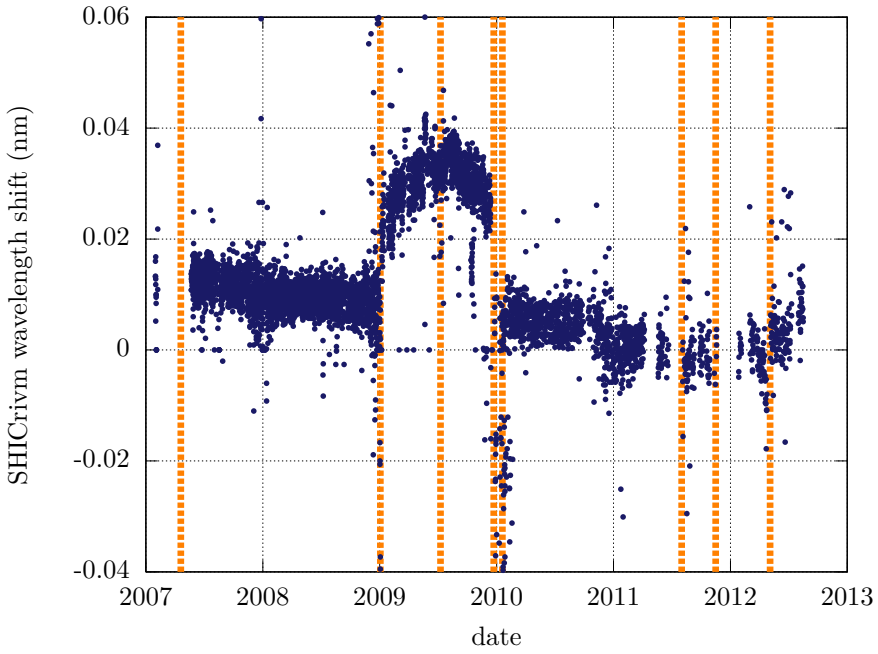

Figure 6.7: Wavelength shifts of Brewer #066 obtained by the SHICrivm software by correlation with the Fraunhofer solar spectrum. The vertical lines are the same as in Fig. 6.6

Additionally, in situ measurements of nitrogen dioxide local concentrations by the Environmental Protection Agency (Sect. 6.2.6) where examined to exclude any abrupt changes in the tropospheric NO_2 column and, as expected, no correspondence was observed.

6.2.4 Sensitivity to wavelength misalignments

After careful investigation, I found that all variations correspond to slight changes in the wavelength scale of the Brewer: if the mercury lamp is replaced (or even simply removed and inserted again!) or the calibration step of the Brewer is changed by few units, based for example on a `sc` test, the influence on the retrieved NO_2 is enormous. This kind of events are represented as vertical lines in Fig. 6.6 and are listed in Table 6.2. The wavelength shifts are also confirmed by the SHICrivm software, already used in Sect. 4.1.1, for the days where UV irradiance spectra were recorded. In Fig. 6.7 the average shifts in the wavelength range 308–312 nm are plotted for each UV measurement. The Brewer sensitivity to the wavelength, as expected from the discussion in the previous chapters (e.g., Sects. 4.2.6 and 5.4.7), is compatible with the values reported in Table 4.7 and represents a great limitation of Brewer NO_2 measurements. As will be shown in the next sections, the sensitivity of NO_2 measurements to wavelength misalignments is a common characteristic of all Brewer instruments, not only of Brewer #066.

In order to try to overcome the issue and to correctly reprocess the series taking into account the wavelength shift, I first evaluated the magnitude of the variations in the wavelength scale. Based on the `sc` results and the SHICrivm calculations, I could go back to the effective operating step, i.e. the step identifying the real operating wavelengths with reference to a fixed dispersion function (e.g., the dispersion measured in the last dispersion test). Periods with effective step as low as 998 and as high as 1003, compared to the reference step 1000, were revealed. When the effective step is low, the retrieved NO_2 VCD is high, while the retrieval is lower when the effective step is high. This behaviour is confirmed using the results of the radiative transfer calculations from the previous chapter. Figure 6.8 depicts the influence of a ± 2 steps discrepancy on the retrieved NO_2, as a function of the AMF. For all the three runs, the NO_2 was retrieved with the same

Table 6.2: Events able to change the wavelength alignment of the Brewer #066.

date	event
19/04/2007	IOS calibration and micrometer maintenance
02/01/2009	hg lamp replacement
09/07/2009	IOS calibration and cal. step change (3 units)
22/12/2009	hg lamp removed and inserted again
18/01/2010	hg lamp replacement
01/08/2011	IOS calibration and cal. step change (2 units)
15/11/2011	hg lamp replacement
03/05/2012	hg lamp replacement
07/01/2013	hg lamp replacement
21/03/2013	change of software settings (SWITCH% variable)
31/05/2013	IOS calibration and cal. step change (2 units)

algorithm (same weightings and same extraterrestrial constant) as for the reference step. The radiative transfer results are in good agreement with the observations (Fig. 6.6).

6.2.5 Feasibility of piecewise calibration

Theoretically, every parameter within the algorithm should be varied accordingly to the effective operating step: the extraterrestrial constant, the weightings, the differential cross section, the filter correction, the Rayleigh compensation, the O_4 correction, etc. Some of these factors, however, are slow functions of the wavelength, such as the Rayleigh and filter corrections and the instrumental bandwidth. The O_4 correction was recalculated at steps 998 and 1003 and negligible differences were found (about 1–2% of the correction term, which is already small). Even the differential coefficient does not relevantly change ($< 0.05\%$). Nevertheless, although the single weightings apparently vary little with the effective step, their impact on the linear combination and the extraterrestrial constant is crucial. This would imply to recalculate not only the extraterrestrial constant, but also the weightings (and thus the linear combination) as a function of the effective operating step, for each period of the series. This procedure is rather thorny and, above all, unfeasible at the stations where the evolution of the effective operating step is not accurately tracked.

Fortunately, from both simulated and measured data, I found that a very good approximation consists in using the weightings calculated at a reference step (e.g. 1000), even if it is slightly different from the effective step, provided that a suitable extraterrestrial constant is found. In this way, as instance, the results in Fig. 6.8 get to an agreement $< 5 \cdot 10^{-4}$ DU (not shown). This procedure is not completely new in the way of thinking of the Brewer users community, where a standard set of weighting coefficients is used for all Brewers. In our case, this procedure makes unnecessary to exactly know the effective step and only implies to recalculate the extraterrestrial constants on limited portions of the series, for example using the MLE or BE method. The piecewise extraterrestrial constants obtained with the BE method are plotted in Fig. 6.9.

6.2.6 Final reprocessing and exploratory data analysis

The reprocessed series is displayed in Fig. 6.10. The results are much better and no baseline jump is visible as a result of the extraterrestrial constant recalculations. The retrieved amounts of nitrogen dioxide are representative of a typical semi-rural site, such as Saint-Christophe. A histogram of the distribution of NO_2 column densities is plotted in Fig. 6.11 and shows that half of the measurements fall in the interval 0.19–0.3 DU, calculated as the Inter-Quartile Range (IQR), with median 0.25 DU (Table 6.6). These are remarkably higher values than Izaña, due to both different altitudes, latitudes and environments. In Table 6.6 the NO_2 estimates using the old algorithm (but the same quality screening criteria) are additionally reported, as recorded in the

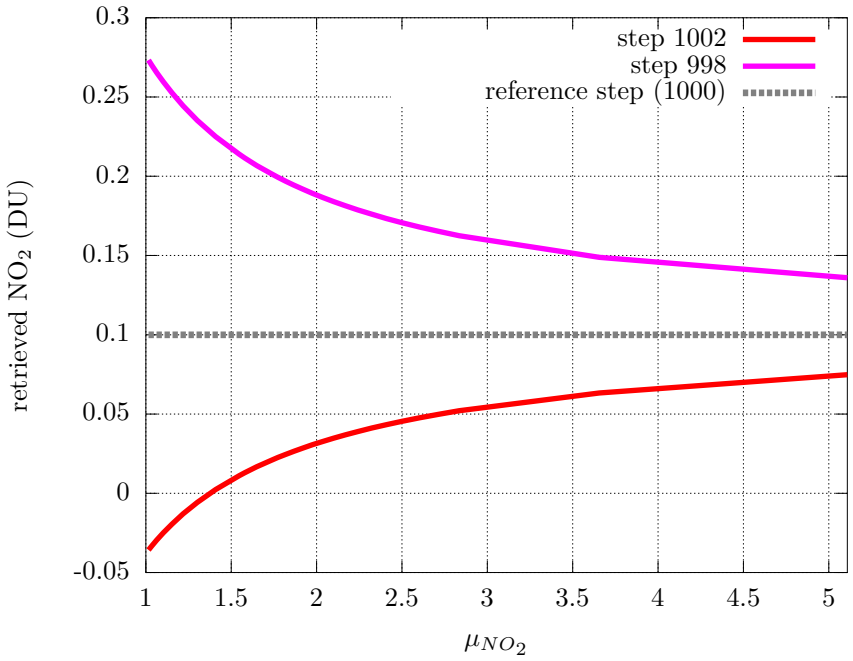

Figure 6.8: Synthetic NO_2 VCD retrieval using modelled data at the reference step (1000), resulting in the same amount as given as input into the model (0.1 DU), and at ± 2 steps far from the reference.

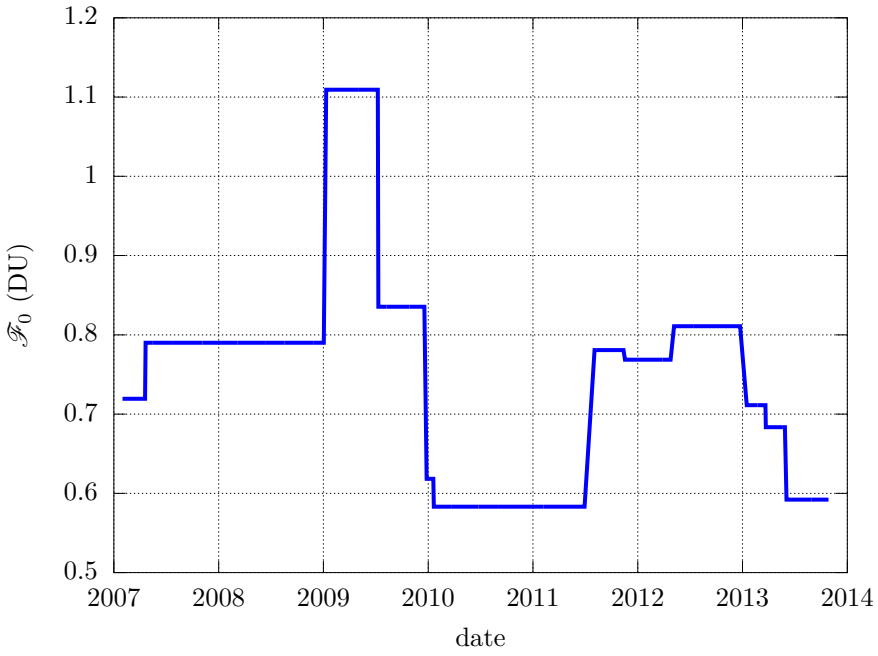

Figure 6.9: Series of extraterrestrial constants determined using the piecewise BE technique from the Saint-Christophe data series.

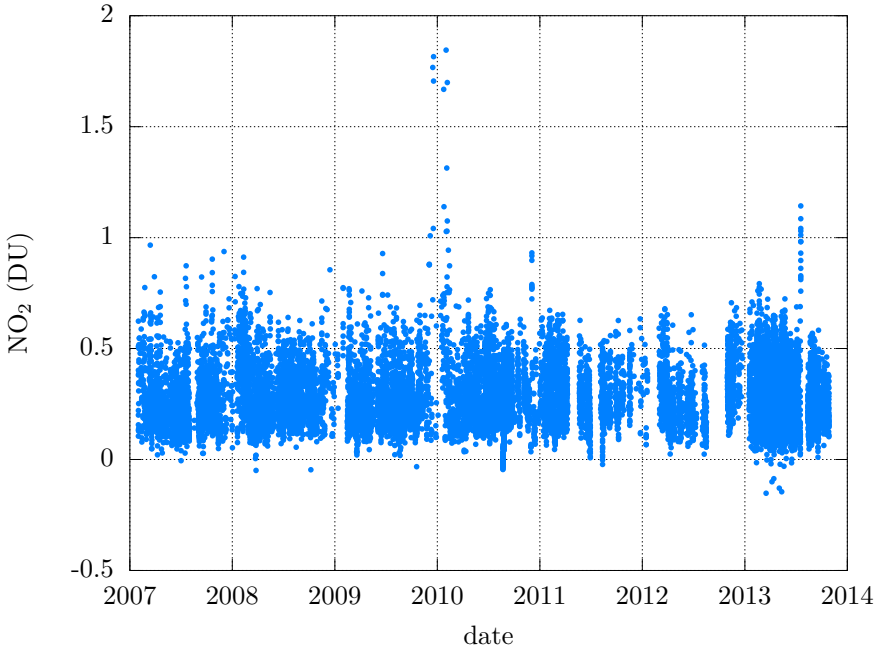

Figure 6.10: The NO_2 data series in Saint-Christophe, reprocessed using the variable calibration factors displayed in Fig. 6.9. No jumps in the baseline are visible, now.

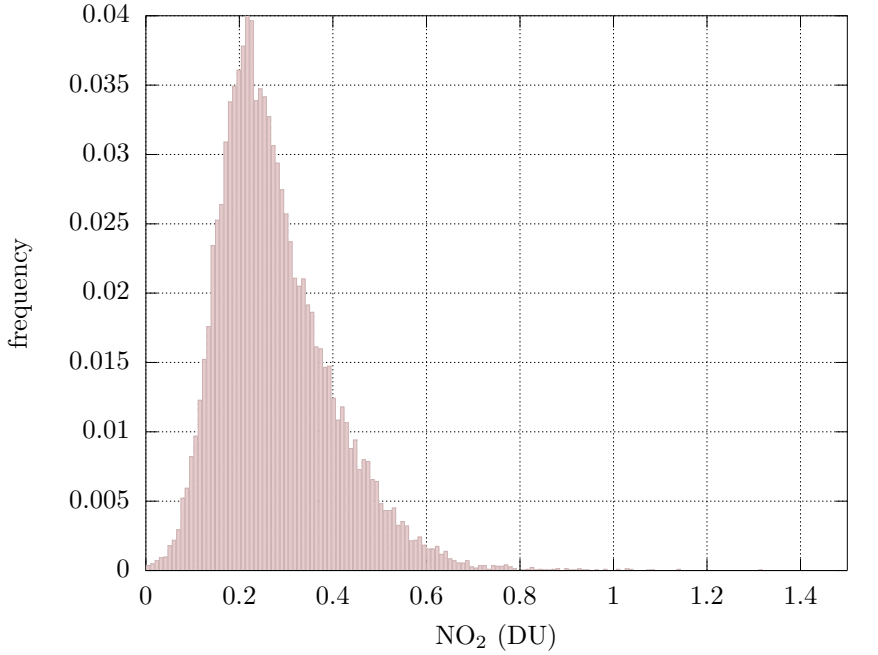

Figure 6.11: Distribution of NO_2 column densities measured in Saint-Christophe.

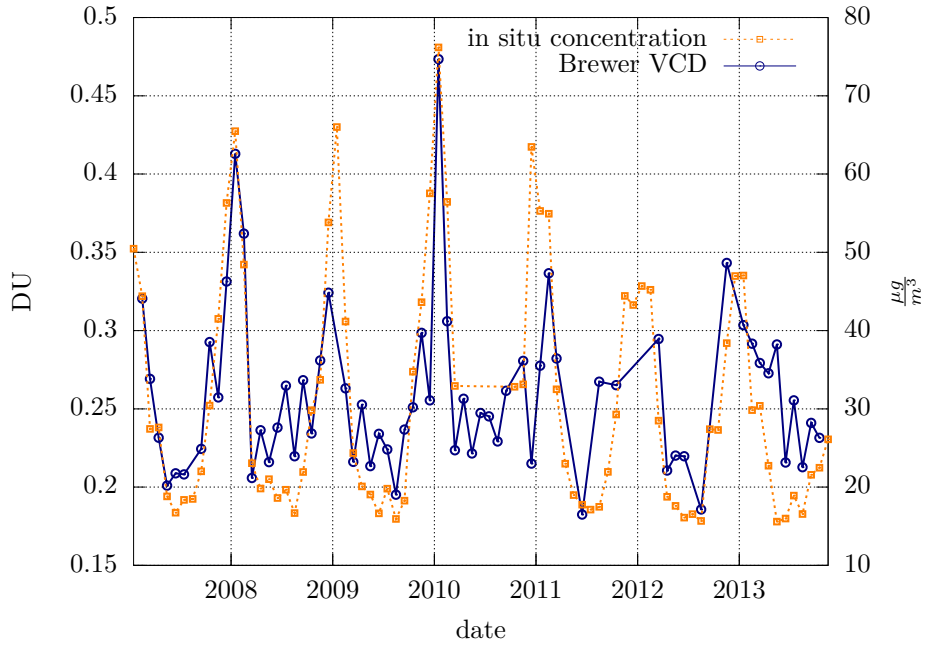

Figure 6.12: Blue points and left axis: monthly means of the NO_2 VCDs measured in Saint-Christophe by the Brewer. Orange points and right axis: monthly means of in-situ NO_2 concentrations revealed by the Environmental Protection Agency.

B-file. An overestimation of more than 300% by the old algorithm is found on average.

Correlation with in-situ measurements and trends

In situ NO_2 concentration measurements, performed by the Environmental Protection Agency, are available at Dora station, about 1.3 km far from the Brewer observatory, towards downtown. Monthly means of both series (VCDs from the Brewer and local concentrations from chemiluminescence measurements) are plotted together in Fig. 6.12. Large correlation (e.g., Pearson's coefficient 0.75) between the two data sets can be noticed. Table 6.7 summarises the results of the correlation analysis based on several estimators: the Pearson's correlation coefficient assumes linearity, homoscedasticity and that the two variables are normally distributed, whereas the Kendall's and Spearman's rank correlations are non-parametric tests that measure the strength of the dependence between two variables without making any assumption about the distribution. The high correlation indexes prove that a relevant part of the total nitrogen dioxide measured by the Brewer along the line of sight is located in the troposphere, and thus also detected by the in situ instrumentation. However, perfect correlation between the techniques is not expected, due to many factors:

1. the Brewer estimates the total column (stratosphere and troposphere), while the in situ measurements only probe the lowest levels of the troposphere. Moreover, due to the inclined path of the sun beam, the spatial area probed by the Brewer is large and depends on the altitude of the NO_2 layer;

2. in situ concentration measurements are strongly influenced by temperature inversions, which are common in the Aosta Valley, especially in winter;

3. the in situ measurements are performed in downtown Aosta, while the Brewer operates in Saint-Christophe. Remarkable variability is found even among different in situ sampling points in the city, therefore large scatter is to be expected between Aosta and Saint-Christophe data. Also, the correlation could depend on the wind direction and speed;

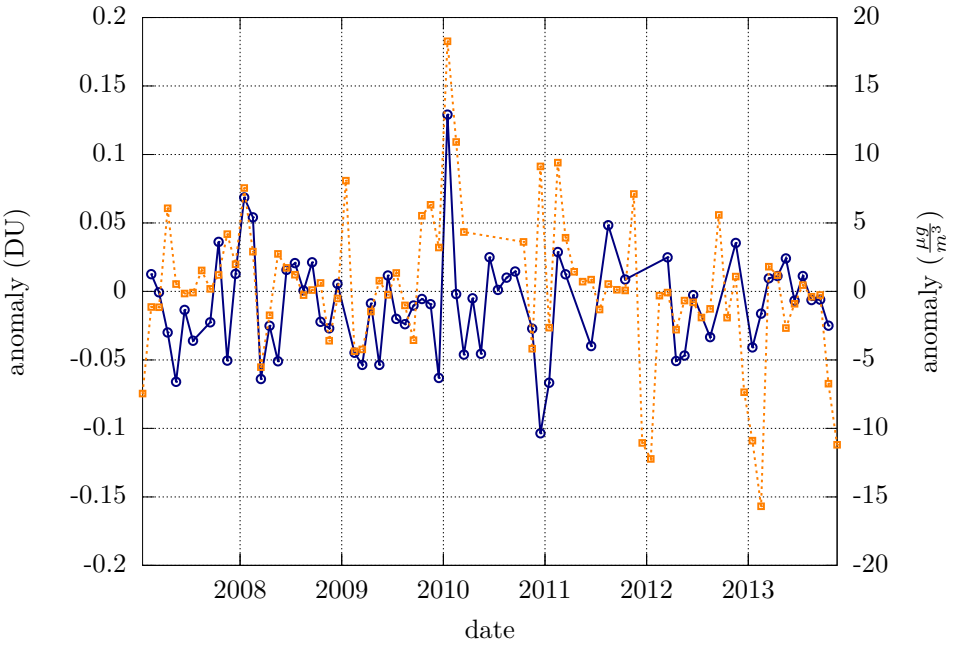

Figure 6.13: Blue points and left axis: monthly anomalies, with respect to the climatological values, of the NO_2 VCDs measured in Saint-Christophe. Orange points and right axis: monthly anomalies of the in-situ NO_2 concentrations revealed by the Environmental Protection Agency.

4. when the sun is obscured by the clouds, the Brewer measurements are removed by the algorithm, whereas in situ measurements are unperturbed by bad weather. Therefore, the two kinds of instruments do not always measure at the same time;

5. few NO_2 VCD daily measurements were scheduled before the starting of my Ph.D. (2011) and the diurnal variability could be not fully captured by the Brewer before that date.

Then, monthly climatological reference values for both the Brewer and the in situ series were calculated based on all available data and subtracted to the monthly means of each year, thus obtaining the VCD anomalies. The results are displayed in Fig. 6.13 and the respective correlation analysis in Table 6.8. On the same graph, the anomalies of the NO_2 concentration from in situ measurements by the Environmental Protection Agency were plotted. Though lower than the one reported for absolute values, remarkable correlation between both anomaly series is still visible.

Although a rigorous determination of the climatological trends would require a longer measurement series, the tendency of the NO_2 anomalies in the analysed period was calculated and the term "trend" is however used, in a broadest sense. A linear fit was applied to the data to determine the evolution of both series during the measurement period (Table 6.9). A raw estimate of 0.1 DU was assumed for the fraction of the monthly anomaly uncertainty relevant to the calculation of the trends, based on the uncertainty analysis of the previous chapter (with part of the combined uncertainty connected to the random effects approaching zero when averaged over a month and an additional part of the uncertainty linked to systematic effects not affecting the trend estimation) and on the differences between the extraterrestrial constants determined using different methods. Then, the anomaly uncertainty was propagated to the calculated trend and the resulting uncertainty is given in the same table for the trends determined by the Brewer. Both the Student's t-test and the Mann-Kendall's test were applied to the data, revealing a statistically insignificant trend (under the null hypothesis that the trend is zero and a significance level of 0.05, the p-values of the tests are respectively 0.9 and 0.6, thus the null hypothesis cannot be rejected).

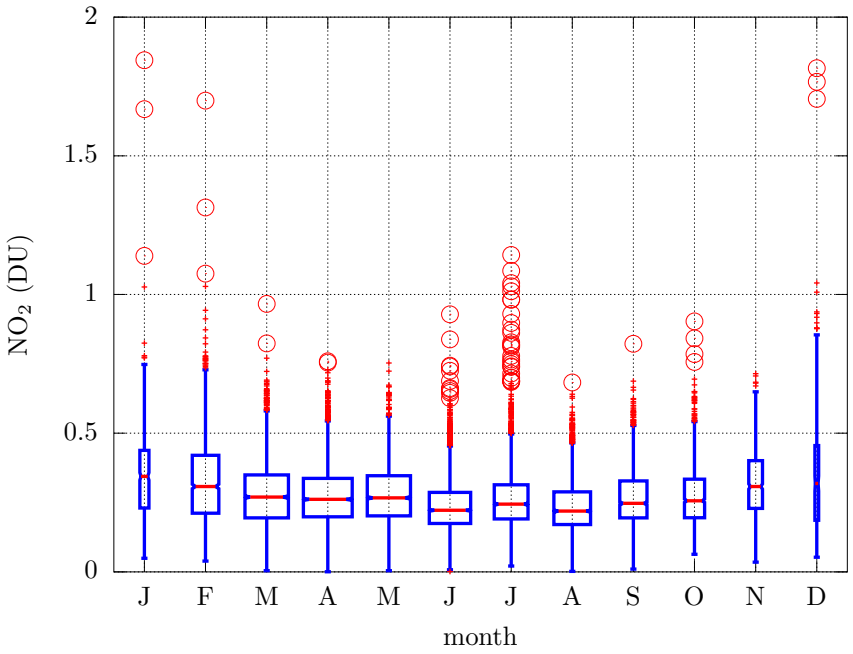

Figure 6.14: Boxplot of the annual cycle of total column nitrogen dioxide in Saint-Christophe. The horizontal axis represents the months, from January to December.

Short-term temporal variability

The annual cycle revealed by the Brewer is represented as a notched boxplot in Fig. 6.14. Due to the semi-rural context in Saint-Christophe, any seasonal cycle could be potentially masked by two concurrent effects: the stratospheric density, as explained in Chap. 2, shows a maximum in summer and a minimum in winter, while the opposite is true for the tropospheric VCD. However, even in the relatively unpolluted site of Saint-Christophe, the influence of tropospheric nitrogen dioxide dominates and a maximum emerges in wintertime. The narrow notches prove that the differences of the medians are statistically significant. The average amplitude of the seasonal cycle is 0.13 DU, but several outliers are visible, identifying critical situations associated with high NO_2 concentrations.

Several concomitant factors contribute to the observed seasonal cycle, as already pointed out in Chap.2:

1. higher NO_2 emissions in winter than in summer, due to residential heating and industry;
2. temperature inversions, which favour stagnation and limit the cleaning effect of the winds;
3. increased photolysis during summer, which decreases the concentration of NO_2 relative to NO. The increased photolysis of the hydroxyl radical (OH) precursor species (such as O_3) also decreases the summertime NO_2 concentration via its reaction with OH to yield nitric acid (HNO_3) (Mendolia et al., 2013);
4. increased lifetime of NO_2 during winter months due to the decreased temperature.

Additionally, the anthropogenic influence is clearly revealed when the NO_2 Brewer measurements are plotted as a function of the day of the week, as in Fig. 6.15: large quantities of nitrogen dioxide are progressively injected in the atmosphere during working days, while the VCDs decrease during weekends. Again, the differences of the medians are statistically significant. The weekly cycle is noticeable in several ground-based series and even from satellite radiometers (Beirle et al.,

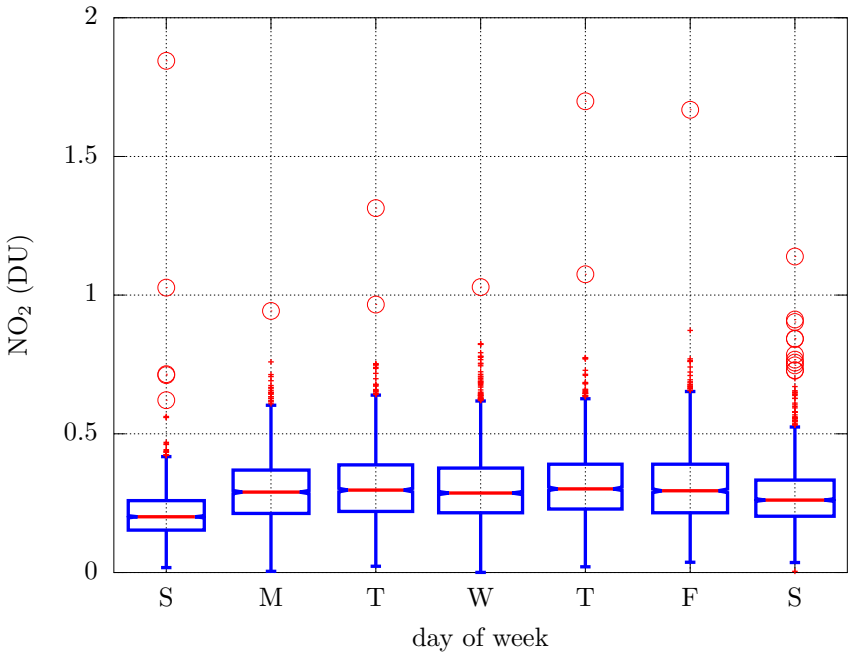

Figure 6.15: Weekly cycle of nitrogen dioxide measured by the Brewer in Saint-Christophe. The horizontal axis represents the day of the week, from Sunday to Saturday.

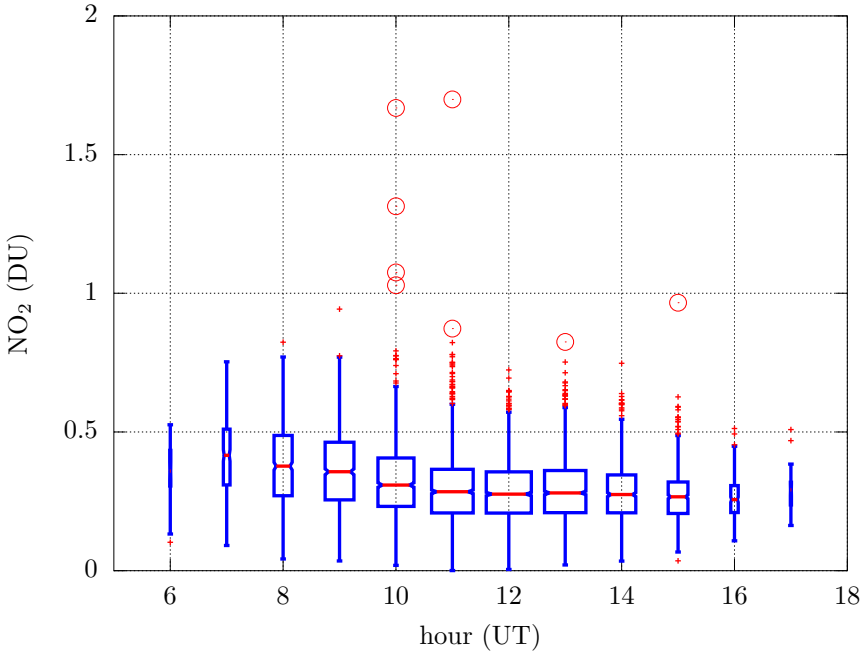

Figure 6.16: Daily cycle of nitrogen dioxide measured by the Brewer in Saint-Christophe on working days (Monday–Friday, October–May). The horizontal axis represents the hour of the day. A peak in the morning due to traffic in the rush hours is noticeable.

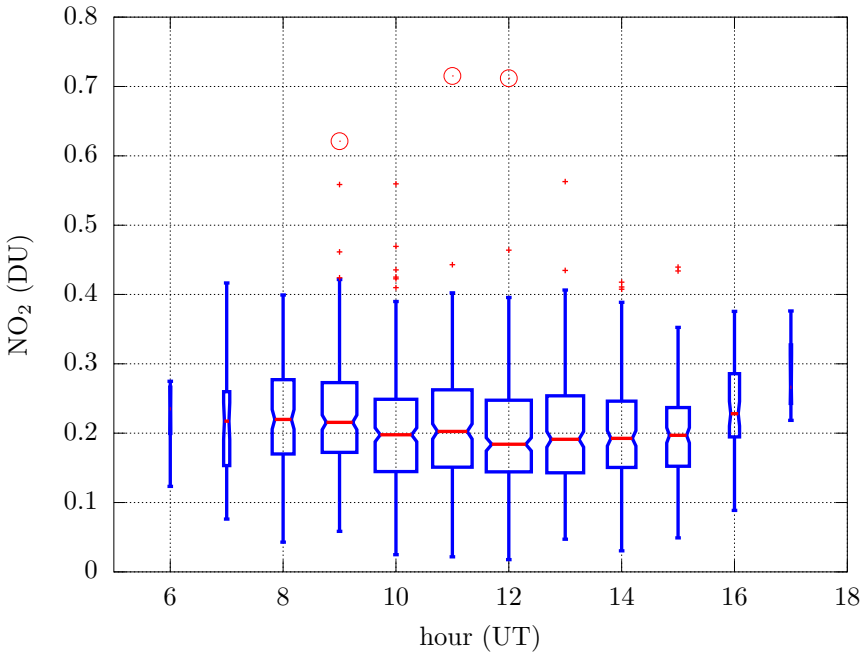

Figure 6.17: Daily cycle of nitrogen dioxide measured by the Brewer in Saint-Christophe on Sundays (during the same period as in Fig. 6.16 to allow a coherent comparison). The horizontal axis represents the hour of the day.

2003). Moreover, the pattern of the weekday–weekend variations is a useful diagnostic of emission inventories and chemical models (Valin et al., 2014).

On an even finer scale, the daily cycle of a typical working day, obtained by averaging all days from Monday to Friday in the period October–May, is represented in Fig. 6.16. Lack of any (inverse-)U shape may be interpreted as an evidence of the accuracy of the used extraterrestrial constants (Sect. 5.1). Nitrogen dioxide is high in the morning probably due to vehicle traffic during the rush hours and gently decreases during the rest of the day. As a further evidence, the daily cycle obtained on Sundays during the same period of the year is displayed in Fig. 6.17 and presents a completely different pattern due to different personal habits on non-working days.

6.3 The Rome series

The station of Rome (41.9°N, 12.5°E, 75 m a.s.l) has been providing estimates of atmospheric ozone and nitrogen dioxide total columns by means of the MKIV Brewer #067 since 1992 (Francesconi et al., 2004). The spectrophotometer is located on the roof of the Fermi building of the Physics department at Sapienza University, in the city centre, and is thus influenced by typical urban conditions. The Brewer participated in several WMO/GO_3OS (World Meteorological Organisation / Global Ozone Observing System) ozone monitoring campaigns and is calibrated for ozone measurements every second year by comparison with the travelling standard #017. Some instabilities and focusing problems of Brewer #067 came up in the last years. Also, I found during my work that the attenuation of the neutral density filter used for the `n2` mode, located on the first filter wheel, is too low and the Brewer usually operates outside its linearity range. The respective data were identified and removed from the following analysis.

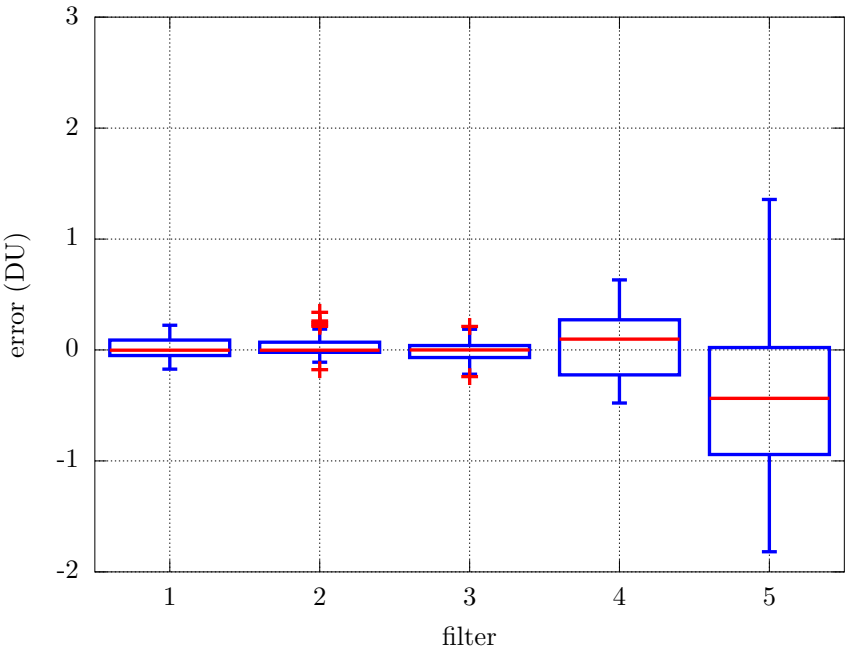

Figure 6.18: Effect of filters non-linearity for Brewer #067.

Table 6.3: Results from dispersion tests run on all Brewers used in the analysis. The operating wavelengths for each slit and the respective resolutions, in parentheses, are expressed in nm.

	Brewer #066	#067	#001	#098
operating step	1000	969	985	1104
λ_1 ($\Delta\lambda_1$)	425.10 (0.58)	425.02 (0.70)	425.03 (0.61)	426.61 (0.91)
λ_2 ($\Delta\lambda_2$)	431.46 (0.84)	431.40 (0.90)	431.40 (0.86)	431.50 (0.88)
λ_3 ($\Delta\lambda_3$)	437.41 (0.84)	437.35 (0.88)	437.36 (0.85)	437.44 (0.88)
λ_4 ($\Delta\lambda_4$)	442.89 (0.86)	442.83 (0.89)	442.86 (0.86)	442.91 (0.87)
λ_5 ($\Delta\lambda_5$)	448.15 (0.84)	448.08 (0.89)	448.12 (0.86)	448.16 (0.88)
λ_6 ($\Delta\lambda_6$)	453.27 (0.83)	453.20 (0.88)	453.26 (0.85)	453.29 (0.85)

6.3.1 Characterisation of Brewer #067

The dispersion test in the visible range was executed during both the Arosa and the Saint-Christophe campaigns (Sects. 5.3 and 5.5) in 2012, using my new dispersion routine. The resulting wavelengths and resolutions at the operating step 969 are listed in Table 6.3. The NO_2 weighting coefficients, calculated as illustrated in Chap. 4, are shown in Table 6.4. The sensitivities to the factors affecting the NO_2 estimates were calculated and are shown in Table 6.5. A dead time of 42 ns, as employed in the ozone measurements, was used. The effect of the filters non-linearity, assessed with the new routine in the visible, is represented in Fig. 6.18. Since the more absorbing filter apparently shows an unrealistic deviation from linearity, probably due to completely different issues (e.g., dead time correction), the corresponding value was set to zero. The O_4 correction was determined for an altitude of 75 m a.s.l.

6.3.2 Reprocessing of standard lamp test series

I used the standard lamp measurements, corrected for any lamp replacement, to take into account the variations of the Brewer sensitivity. The series is displayed in Fig. 6.19. Unlike the `sl` measurements for Brewer #066, some seasonal dependence is visible in the results for Brewer #067.

Table 6.4: NO_2 weighting coefficients and differential absorption coefficients.

	Brewer #066	#067	#001	#098
γ_1	0.038	0.044	0.040	-0.015
γ_2	0.168	0.155	0.163	0.290
γ_3	-0.518	-0.517	-0.517	-0.575
γ_4	-0.027	-0.017	-0.025	-0.024
γ_5	0.737	0.738	0.738	0.678
γ_6	-0.398	-0.402	-0.399	-0.353
$\Delta\alpha_{NO_2}$ $(10^{-19}\frac{cm^2}{molec})$	2.368	2.297	2.348	2.304

Table 6.5: Same as Table 4.7, with results from all Brewers used in the analysis, expressed in Dobson Units.

	Brewer #066	#067	#001	#098
noise	0.32	0.32	0.32	0.33
wavelength misalignment	-0.08	-0.09	-0.10	-0.20
O_4	0.04	0.05	0.04	0.04
H_2O	0.02	0.03	0.02	0.02
Ring effect	-0.09	-0.12	-0.14	-0.11

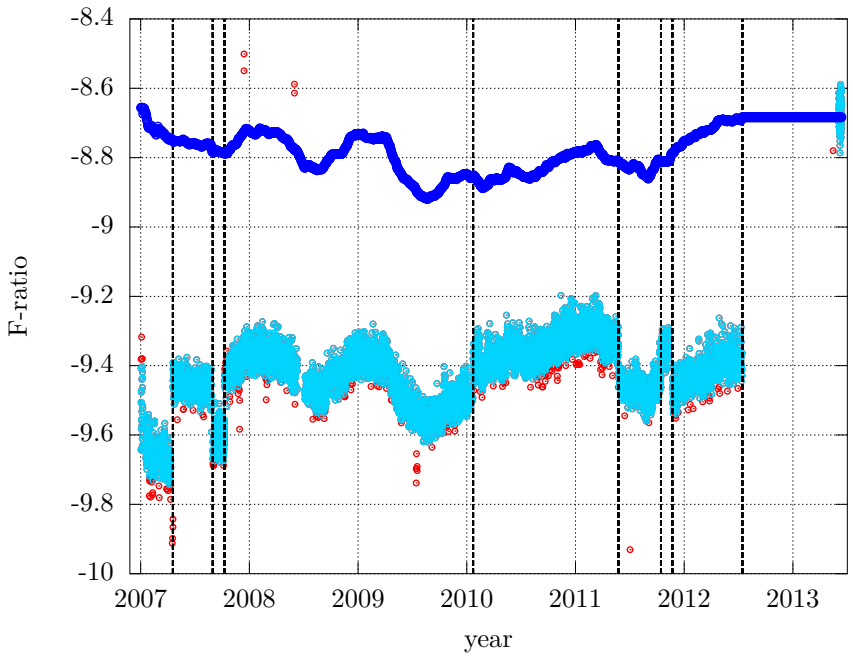

Figure 6.19: Results of `sl` test for Brewer #067. Light blue points represents the linear combination obtained using the lamp as a source, red points are outliers removed from the analysis by my software. The final `sl` series (blue points) is obtained by imposing continuity before and after lamp replacements (black vertical dashed lines) and applying a running average filter.

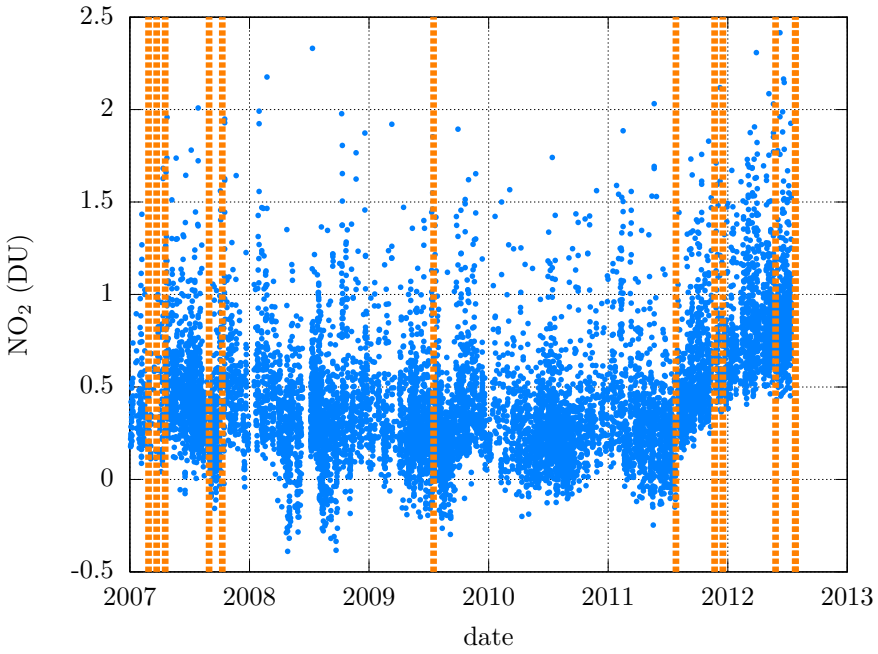

Figure 6.20: Series of NO_2 measurements in Rome after first reprocessing with the new algorithm. Blue points: direct sun measurements; vertical dashed lines: events that may affect the wavelength alignment of the Brewer.

6.3.3 First reprocessing of the NO_2 series

The standard lamp correction, described in the previous section, was employed to track and correct the Brewer calibration drifts. Results are presented in Fig. 6.20 and are clearly affected by factors that cannot be simply solved by a simple correction using the `sl` test: an example is the unjustified increase starting from the second half of 2012. Therefore, new extraterrestrial constants were calculated, as in Saint-Christophe, using the BE method on portions of the series between the several events that altered the Brewer wavelength scale (Fig. 6.21).

6.3.4 Final reprocessing and exploratory data analysis

The final NO_2 series, which is much better, is displayed in Fig. 6.22. The retrieved amounts of nitrogen dioxide are representative of a urban site. A histogram of the distribution of NO_2 column densities measured in Rome is plotted in Fig. 6.23 and shows that half of the measurements fall in the range 0.28–0.6 DU, with median 0.4 DU (Table 6.6). As expected, the measured VCD are higher than Saint-Christophe (Fig. 6.11). In Table 6.6 the NO_2 estimates using the old algorithm (but the same quality screening criteria) are additionally reported, as recorded in the B-file. An overestimation of more than 270% by the old algorithm is found on average. This can explain the mean value of 1.63 DU at Rome reported by Francesconi et al. (2004), which should be revised on the basis of my work.

Correlation with in-situ measurements and trends

In situ NO_2 concentration measurements, performed by the Environmental Protection Agency, are available at Magna Grecia station, about 2.6 km far from the Brewer observatory. Monthly means of both series (VCDs from the Brewer and local concentrations from chemiluminescence measurements) are plotted together in Fig. 6.24. Table 6.7 summarises the results of the correlation analysis based on several estimators.

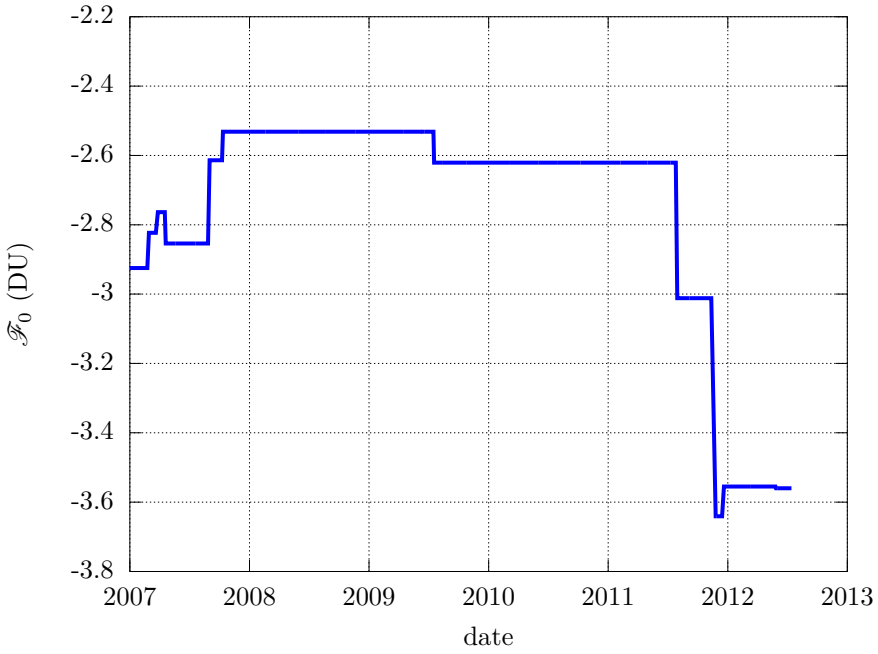

Figure 6.21: Series of extraterrestrial constants determined using the BE technique from the Rome data series.

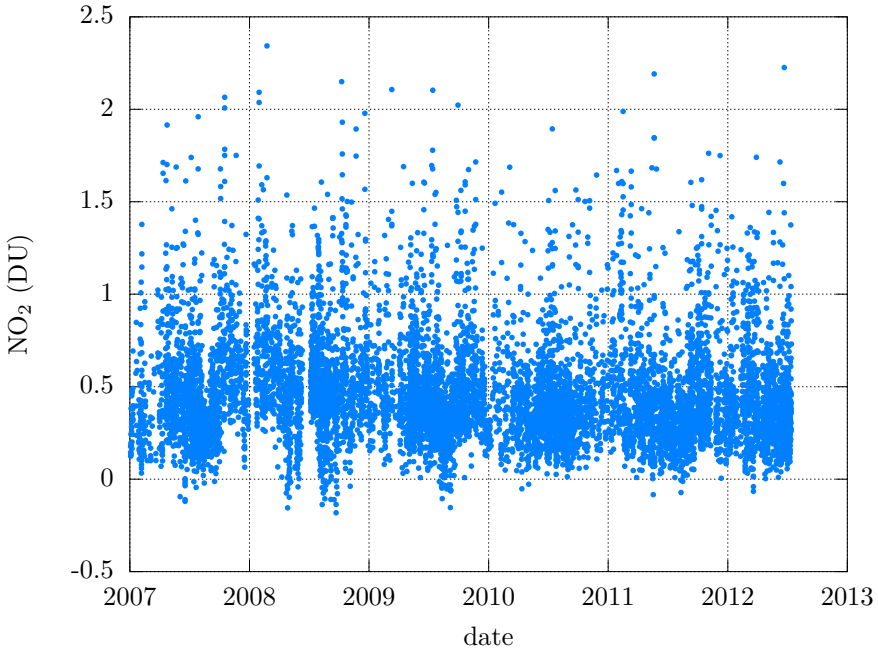

Figure 6.22: The NO_2 data series in Rome, reprocessed using the variable calibration factors displayed in Fig. 6.21.

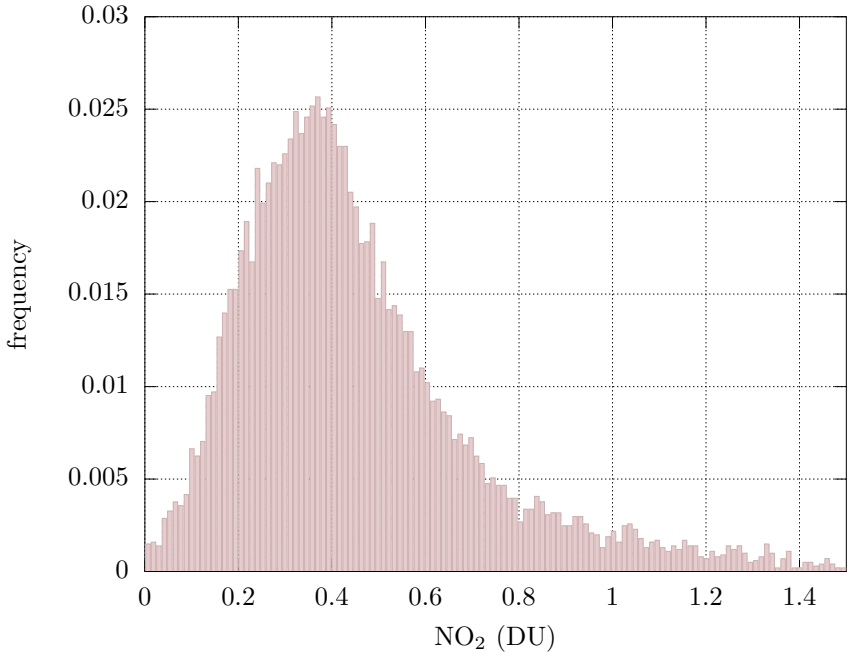

Figure 6.23: Distribution of NO_2 column densities measured in Rome.

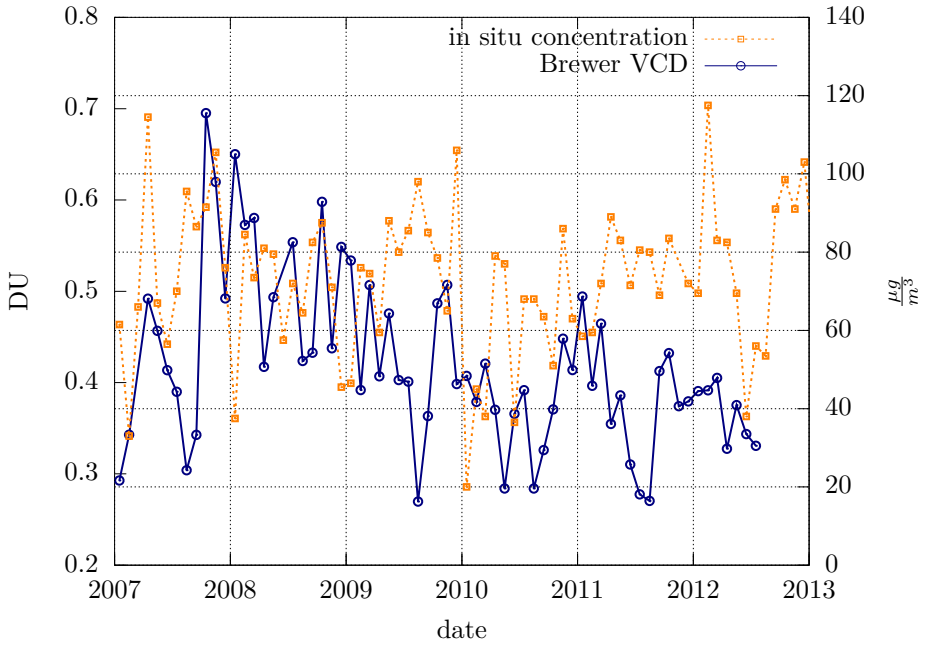

Figure 6.24: Blue points and left axis: monthly means of the NO_2 VCDs measured in Rome by the Brewer. Orange points and right axis: monthly means of in-situ NO_2 concentrations revealed by the Environmental Protection Agency.

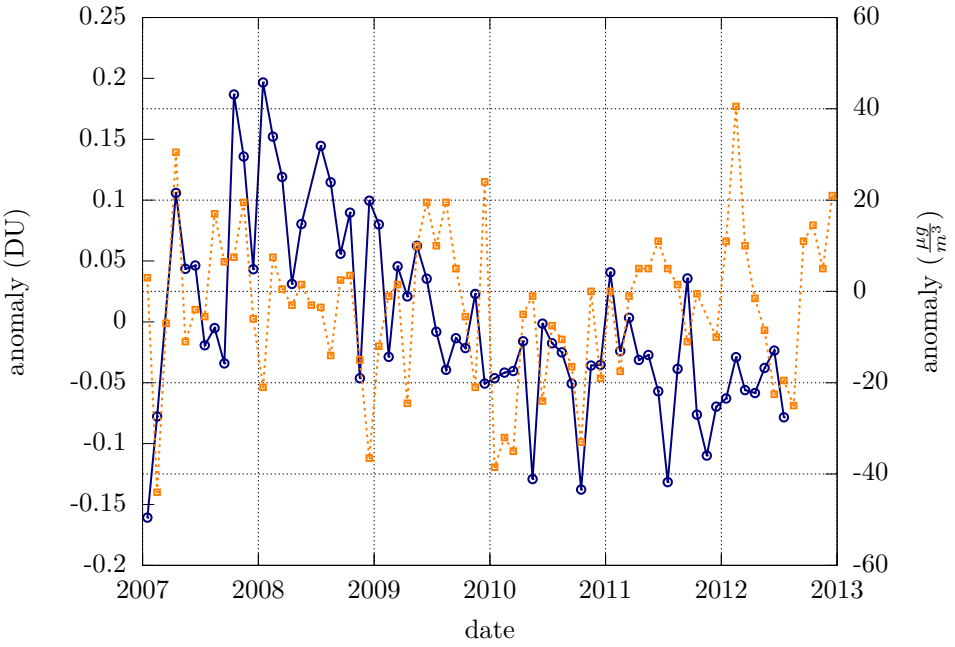

Figure 6.25: Blue points and left axis: monthly anomalies, with respect to the climatological values, of the NO_2 VCDs measured in Rome. Orange points and right axis: monthly anomalies of the in-situ NO_2 concentrations revealed by the Environmental Protection Agency.

The VCD anomalies are displayed in Fig. 6.25. On the same graph, the anomalies of the NO_2 concentration from in situ measurements by the Environmental Protection Agency were plotted (for ease of visibility, a multiplying factor was applied to the in situ measurements) and the respective correlation analysis is displayed in Table 6.8. The point-to-point correlation between the total column estimates by the Brewer and the in situ measurements is much lower than in Saint-Christophe. On the other hand, Rome is a much larger city with more pronounced and heterogeneous pollution sources and a loss of correlation was to be expected.

A linear fit was applied to the Brewer data, revealing a trend of (-5.0±1.6) %/year (Table 6.9). Both the Student's t-test and the Mann-Kendall's test found that the Brewer trend is statistically significant (significance level of 0.05, p-values less than 0.002).

Short-term temporal variability

The annual cycle is represented as a boxplot in Fig. 6.26. The influence of tropospheric nitrogen dioxide can be noticed from the seasonal cycle with amplitude 0.20 DU and maximum in wintertime as well as from the weekly cycle, plotted in Fig. 6.27, with the same dynamics as in Saint-Christophe (Fig. 6.15). The daily cycle of a typical working day is represented in Fig. 6.28 and shows that the NO_2 levels remains high during all day, not only in the morning rush hours. The same graph for Sunday measurements, with a slightly different shape than working days, is displayed in Fig. 6.29.

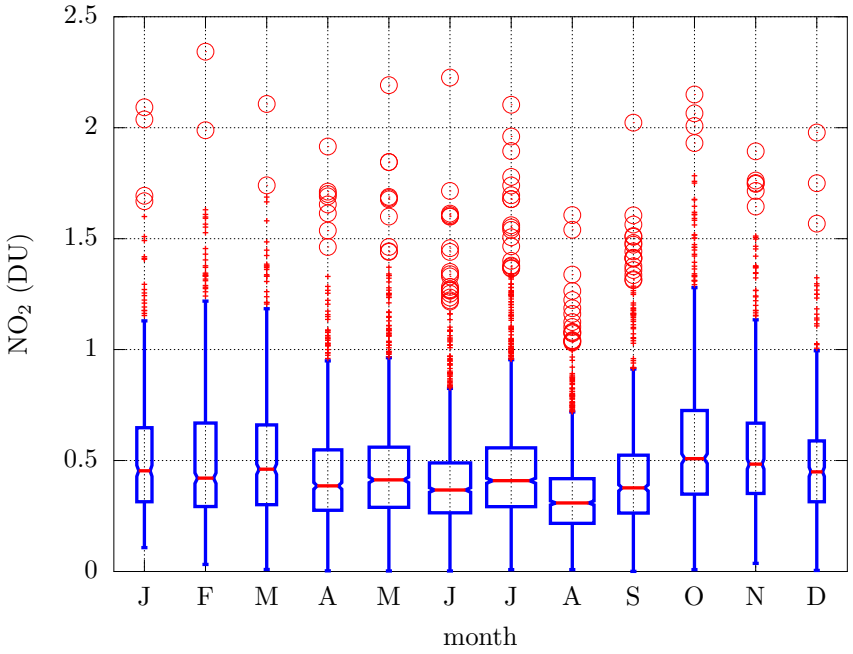

Figure 6.26: Boxplot of the annual cycle of nitrogen dioxide VCDs in Rome. The horizontal axis represents the months, from January to December.

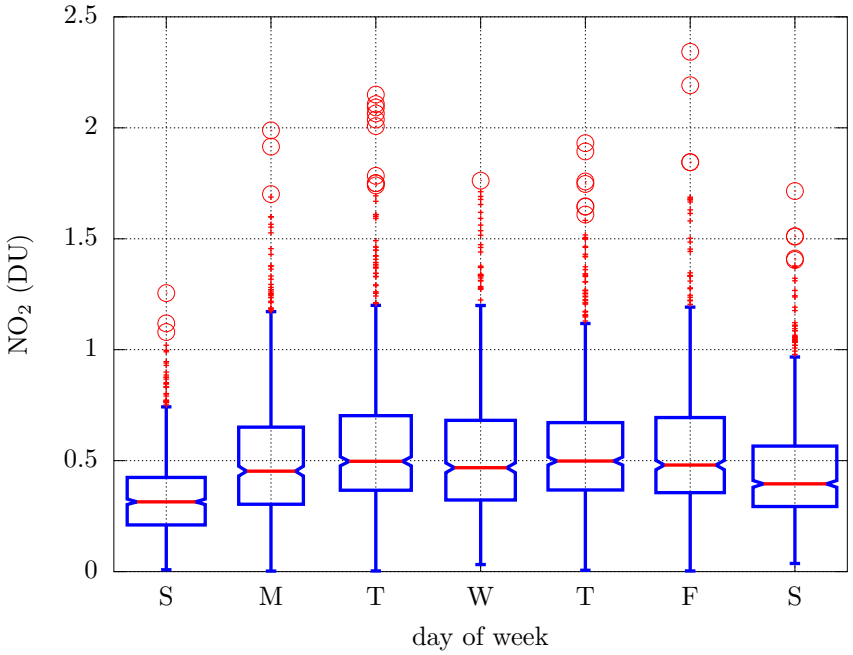

Figure 6.27: Weekly cycle of nitrogen dioxide measured by the Brewer in Rome. The horizontal axis represents the day of the week, from Sunday to Saturday.

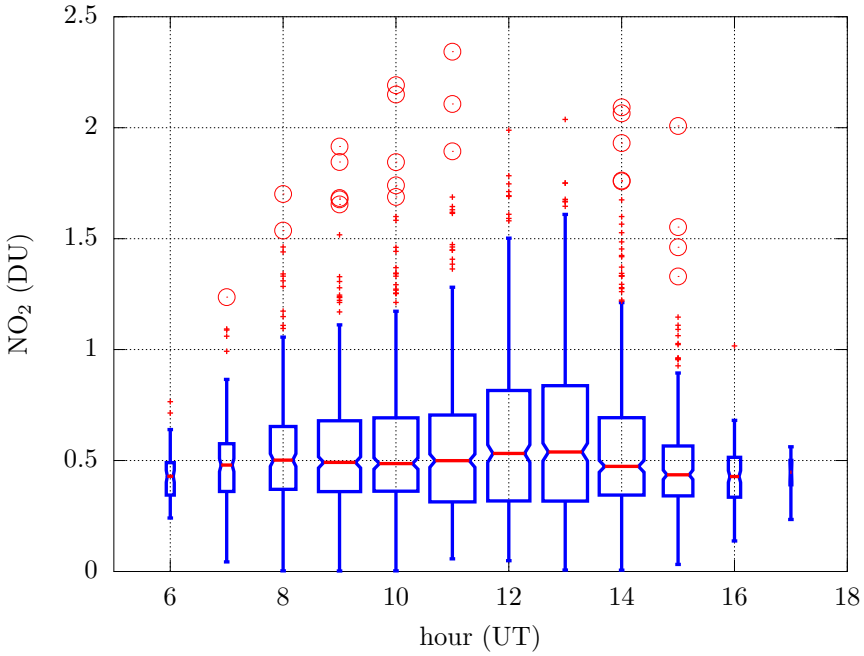

Figure 6.28: Daily cycle of nitrogen dioxide measured by the Brewer in Rome on working days (Monday–Friday, October–May). The horizontal axis represents the hour of the day.

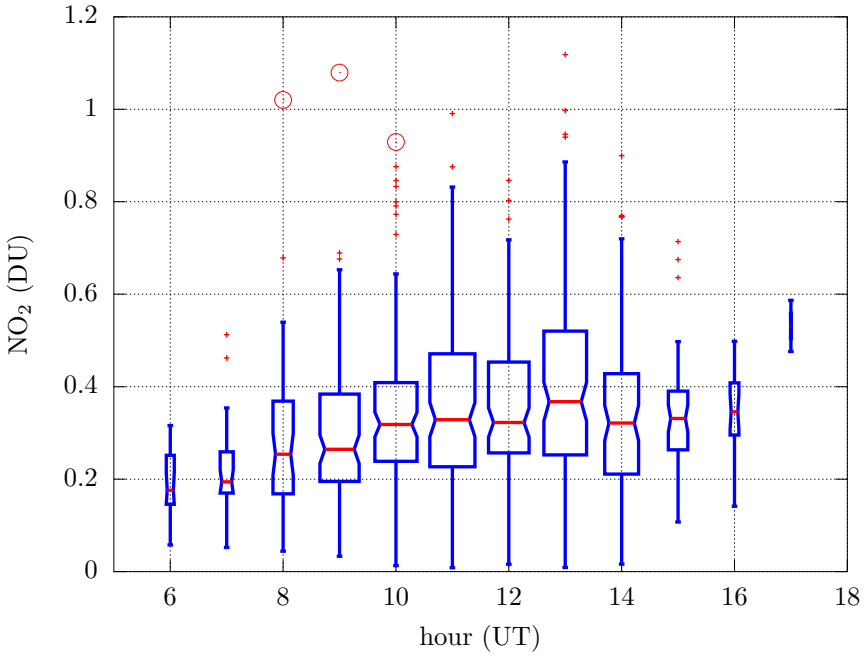

Figure 6.29: Daily cycle of nitrogen dioxide measured by the Brewer in Rome on Sundays (October–May). The horizontal axis represents the hour of the day.

6.4 The Athens series

The measurements are performed on the roof of the Biomedical Research Foundation of the Academy of Athens (38.0°N, 23.8°E, 190 m a.s.l). The campus is located in a green area at a distance of about 4 km from the centre of the city and it is thus partly influenced by urban emissions. Some mountains surround the station to the east (Mount Hymetteus, at a distance of about 1 km) and to the north and northeast (Attica, Parnes and Penteli, at a distance of 15–20 km). To the south, the Saronic Gulf is found at a distance of about 10 km. Brewer #001 has been providing estimates of atmospheric ozone and nitrogen dioxide total columns since 2004. Ozone calibrations through the travelling standard Brewer #017 and extraordinary maintenance by IOS are performed every second or third year. The operator's logbook often reports about considerable instability of Brewer #001 (`sl` ratios, filter wheel problems, etc.).

During my work, a period of micrometer malfunctioning was also identified for the first time and the corresponding data were removed from the analysis.

6.4.1 Characterisation of Brewer #001

Since the Athens laboratory does not own the necessary lamps for the dispersion test, it was not possible to run the new `dsp` routine in the visible range. Therefore, the UV dispersion coefficients from the last IOS calibration were multiplied by $\frac{3}{2}$ to approximately determine the operating wavelengths and resolutions at a step of 985 (Table 6.3). The NO_2 weighting coefficients, calculated as illustrated in Chap. 4, are shown in Table 6.4. The sensitivities to the factors affecting the NO_2 estimates were calculated and are shown in Table 6.5. A dead time of 44 ns, as employed in the ozone measurements, was used. The effect of the filters non-linearity, assessed with the new routine in the visible, is represented in Fig. 6.30. The O_4 correction was determined for an altitude of 190 m a.s.l.

6.4.2 Reprocessing of standard lamp test series

I used the standard lamp measurements, corrected for any lamp replacement, to take into account the variations of the Brewer sensitivity. The series is displayed in Fig. 6.31 and shows a much larger scatter compared to Brewer #066 and #067 that could be due either to low lamp intensity or problems in the third filter wheel mechanism. Therefore, `sl` results for Athens were smoothed using a much longer period compared to the other series (±30 days).

6.4.3 First reprocessing of the NO_2 series

Results using a first guess extraterrestrial constant are presented in Fig. 6.32. This is a very interesting data set, since it manifestly shows that the jumps in the series are well correlated with changes in the wavelength scale. New extraterrestrial constants were calculated using the BE method on portions of the series (Fig. 6.33).

6.4.4 Final reprocessing and exploratory data analysis

The final NO_2 series, which does not show the previous discontinuities, is displayed in Fig. 6.34. The retrieved amounts of nitrogen dioxide are representative of a urban site. A histogram of the distribution of NO_2 column densities measured in Athens is plotted in Fig. 6.35 and shows that half of the measurements fall in the range 0.3–0.7 DU, with median 0.5 DU (Table 6.6). The measured VCD are slightly higher than in Rome (Fig. 6.23). In Table 6.6 the NO_2 estimates using the old algorithm (but the same quality screening criteria) are additionally reported, as recorded in the B-file. An overestimation of 120% by the old algorithm is found on average.

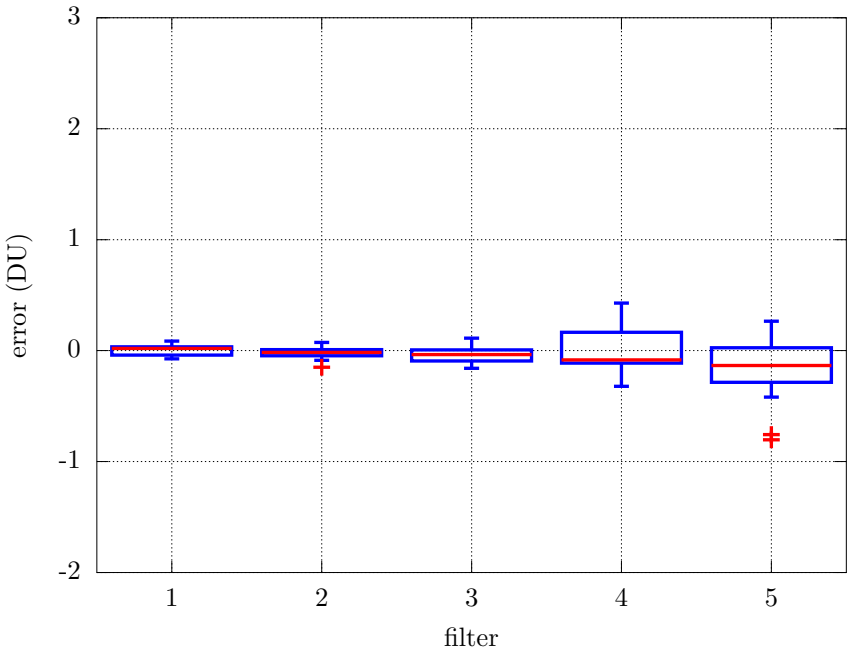

Figure 6.30: Effect of filters non-linearity for Brewer #001.

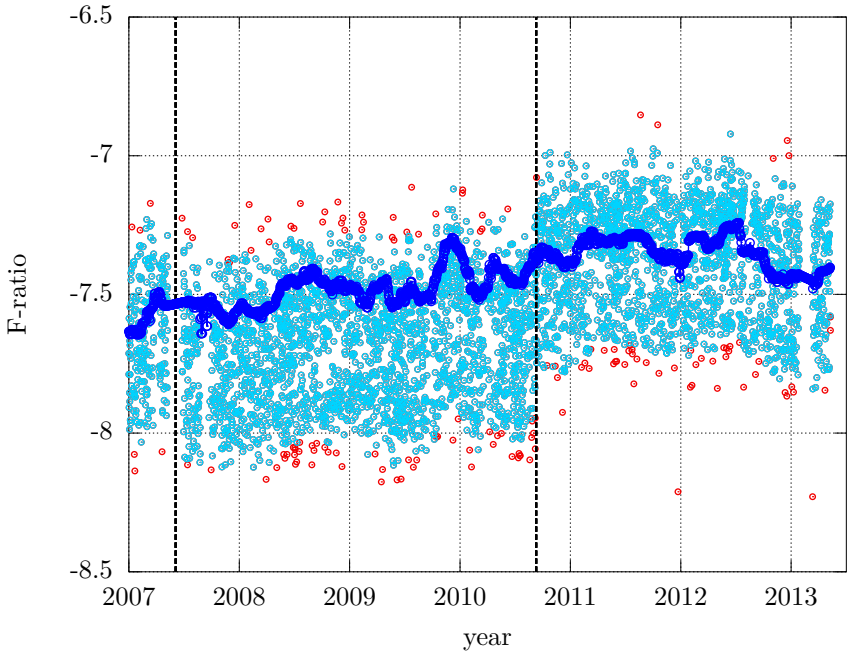

Figure 6.31: Results of `sl` test for Brewer #001. Light blue points represents the linear combination obtained using the lamp as a source, red points are outliers removed from the analysis by my software. The final `sl` series (blue points) is obtained by imposing continuity before and after lamp replacements (black vertical dashed lines) and applying a running average filter.

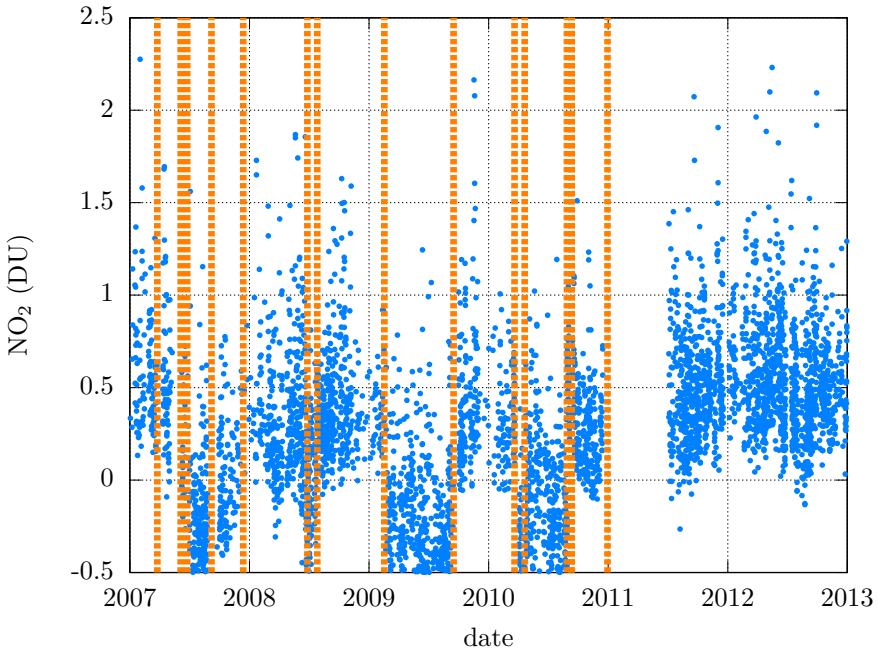

Figure 6.32: Series of NO_2 measurements in Athens after first reprocessing with the new algorithm. Blue points: direct sun measurements; vertical dashed lines: events that may affect the wavelength alignment of the Brewer.

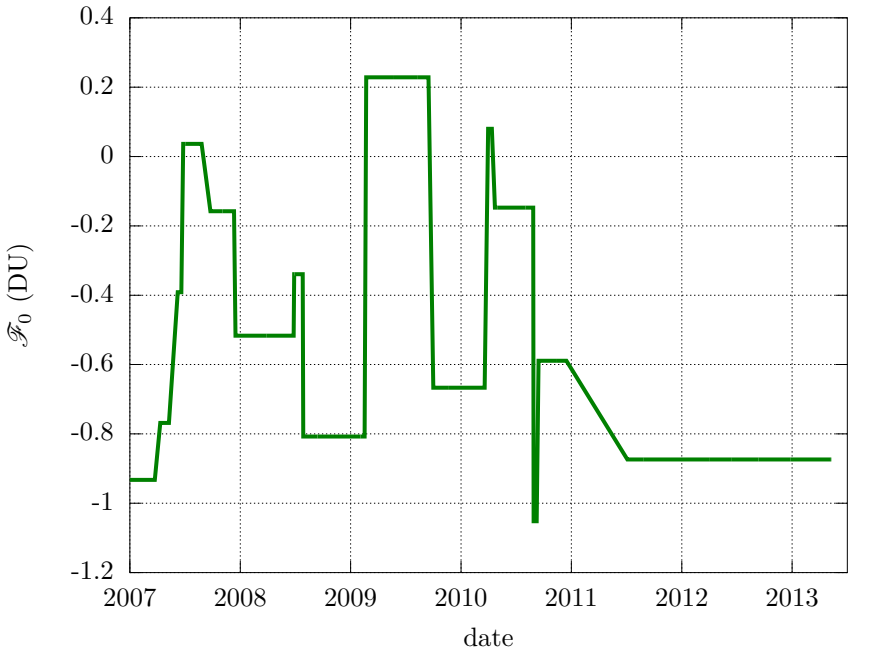

Figure 6.33: Series of extraterrestrial constants determined using the BE technique from the Athens data series.

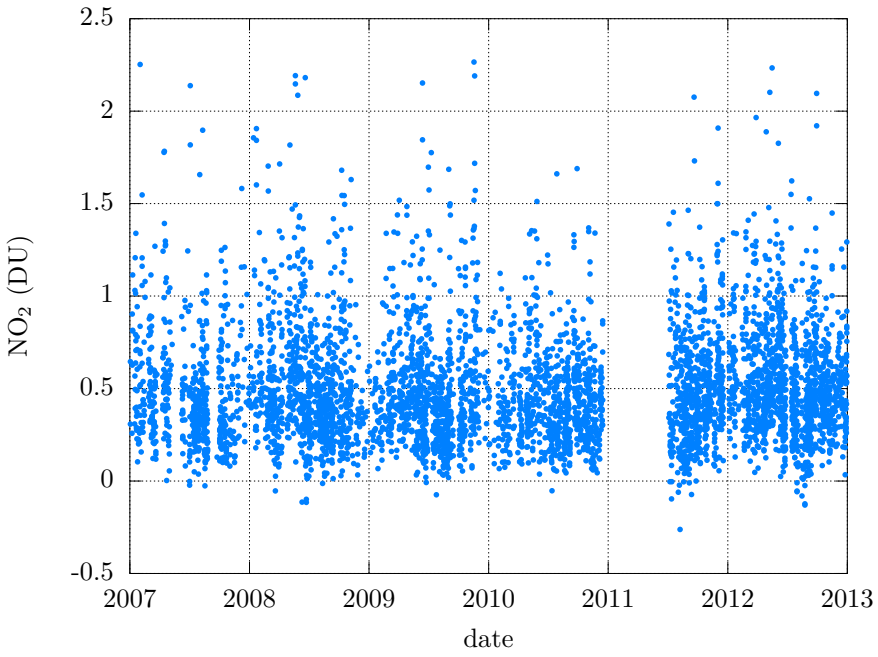

Figure 6.34: The NO_2 data series in Athens, reprocessed using the variable calibration factors displayed in Fig. 6.33.

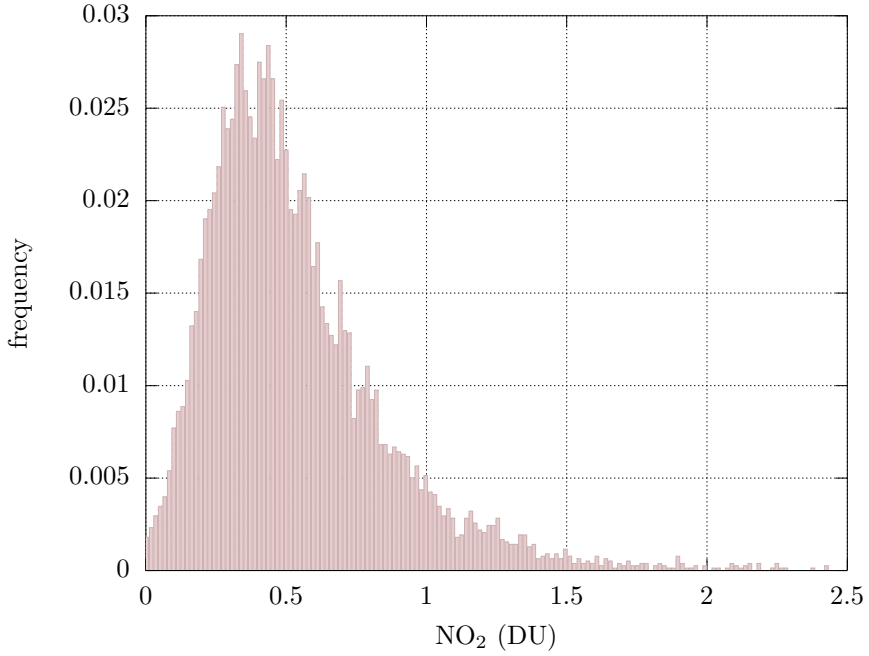

Figure 6.35: Distribution of NO_2 column densities measured in Athens.

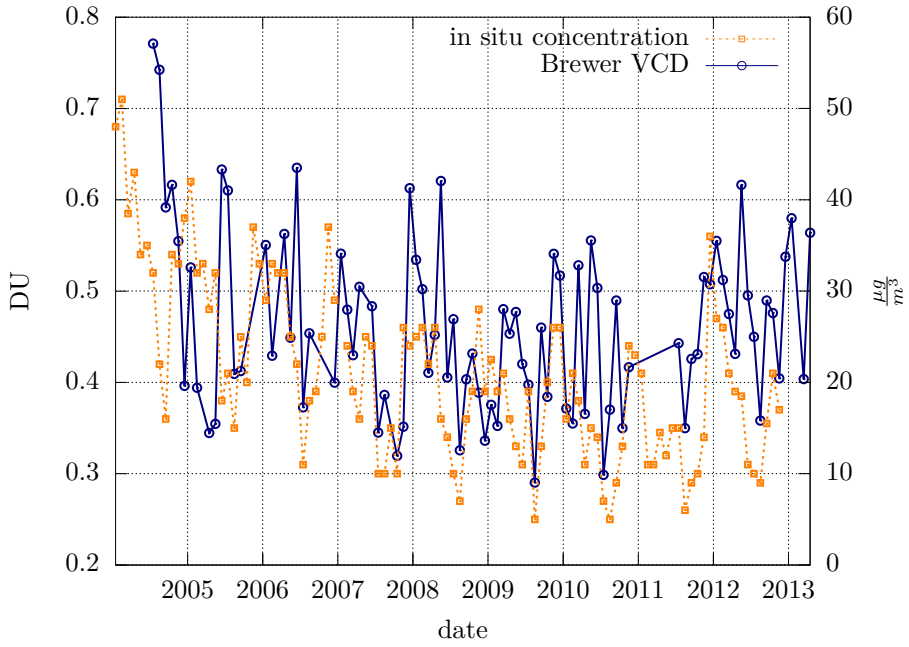

Figure 6.36: Blue points and left axis: monthly means of the NO_2 VCDs measured in Athens by the Brewer. Orange points and right axis: monthly means of in-situ NO_2 concentrations in a nearby station.

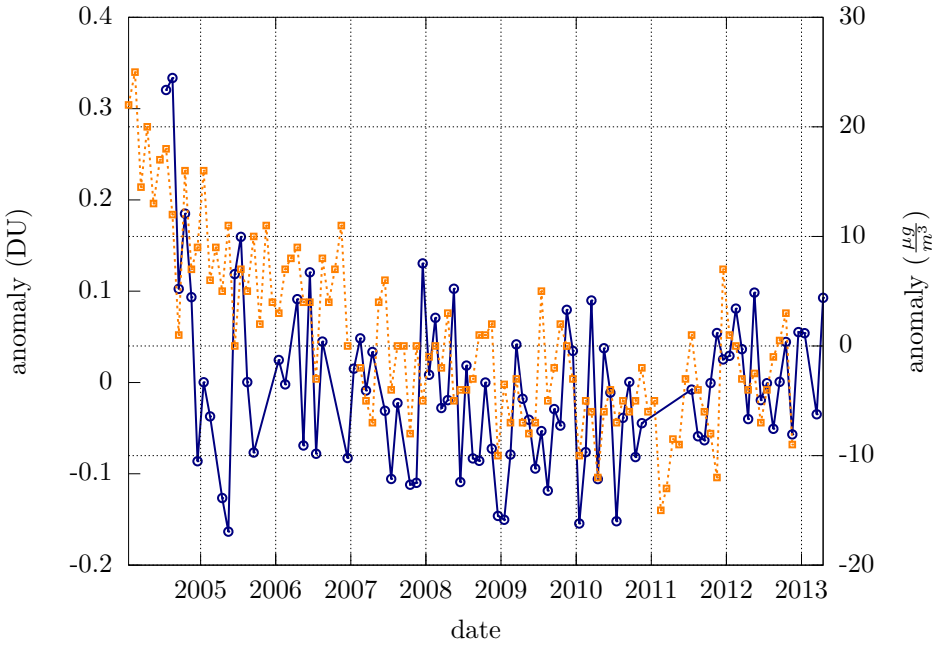

Figure 6.37: Blue points and left axis: monthly anomalies, with respect to the climatological values, of the NO_2 VCDs measured in Athens. Orange points and right axis: monthly anomalies of the in-situ NO_2 concentrations.

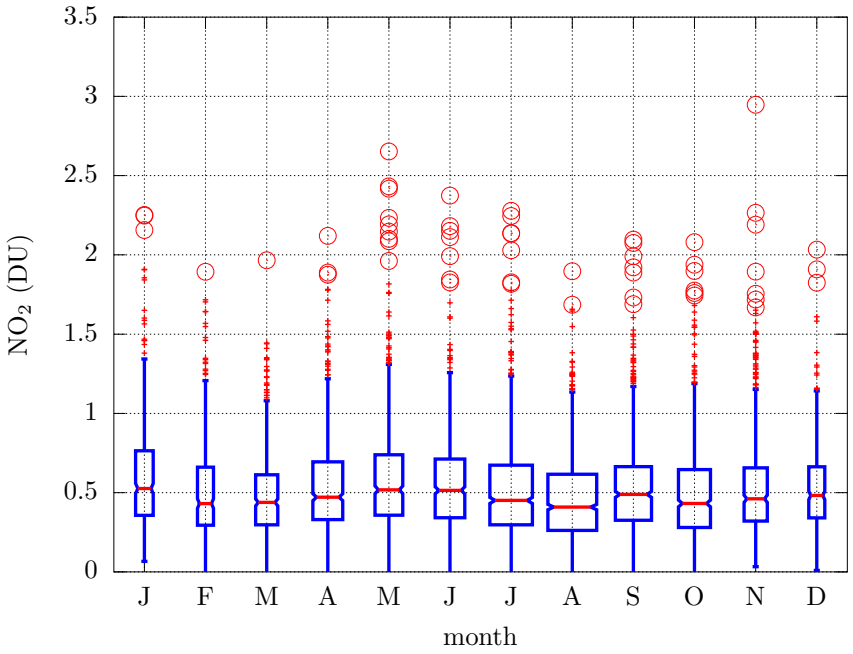

Figure 6.38: Boxplot of the annual cycle of nitrogen dioxide VCDs in Athens. The horizontal axis represents the months, from January to December.

Correlation with in-situ measurements and trends

In situ NO_2 concentration measurements are performed at Marousi station, about 8 km far from the Brewer observatory, but with similar environment. Monthly means of both series (VCDs from the Brewer and local concentrations from chemiluminescence measurements) are plotted together in Fig. 6.36. Table 6.7 summarises the results of the correlation analysis based on several estimators.

The VCD anomalies are displayed in Fig. 6.37 and the respective correlation analysis Table 6.8. The calculated linear trends for both series, which are negative in agreement with, e.g., Vrekoussis et al. (2013), are reported in Table 6.9. Neverthess, the revealed trend of (-1.3±0.8)% is not statistically significant, based on both the Student's t-test and the Mann-Kendall's test (significance level of 0.05, p-values of 0.13 and 0.6 respectively).

Short-term temporal variability

The annual cycle is represented as a boxplot in Fig. 6.38 and is less pronouced (average amplitude 0.12 DU) compared to Saint-Christophe and Rome, probably due to the lower latitude and milder climate. The weekly cycle is plotted in Fig. 6.39. The daily cycle of a typical working day is represented in Fig. 6.40 and shows a maximum at midday. In principle, this behaviour could be a sign of a wrong extraterrestrial constant. However, the same graph for Sunday measurements (Fig. 6.41) is more flat, which implies that the shape in Fig. 6.39 has physical reasons.

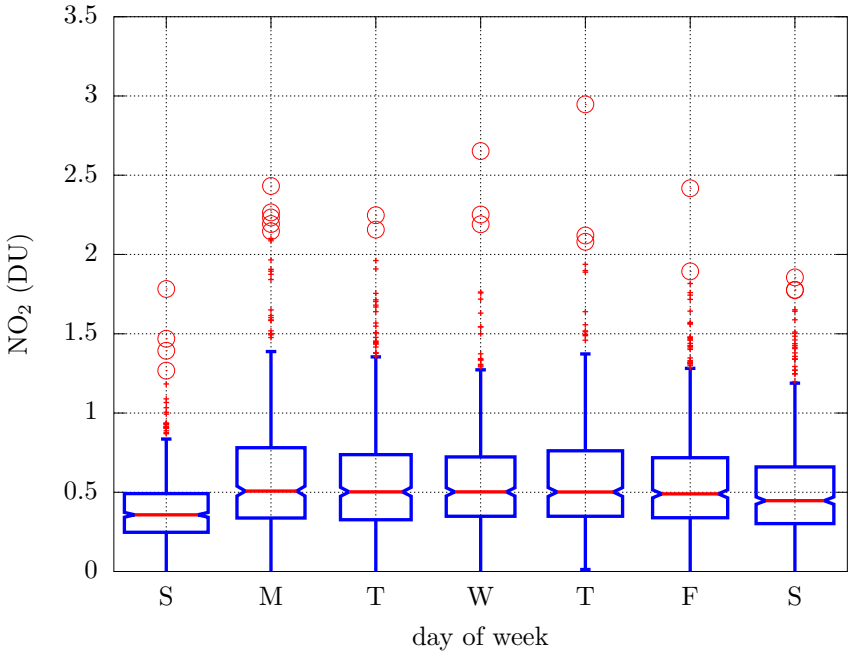

Figure 6.39: Weekly cycle of nitrogen dioxide measured by the Brewer in Athens. The horizontal axis represents the day of the week, from Sunday to Saturday.

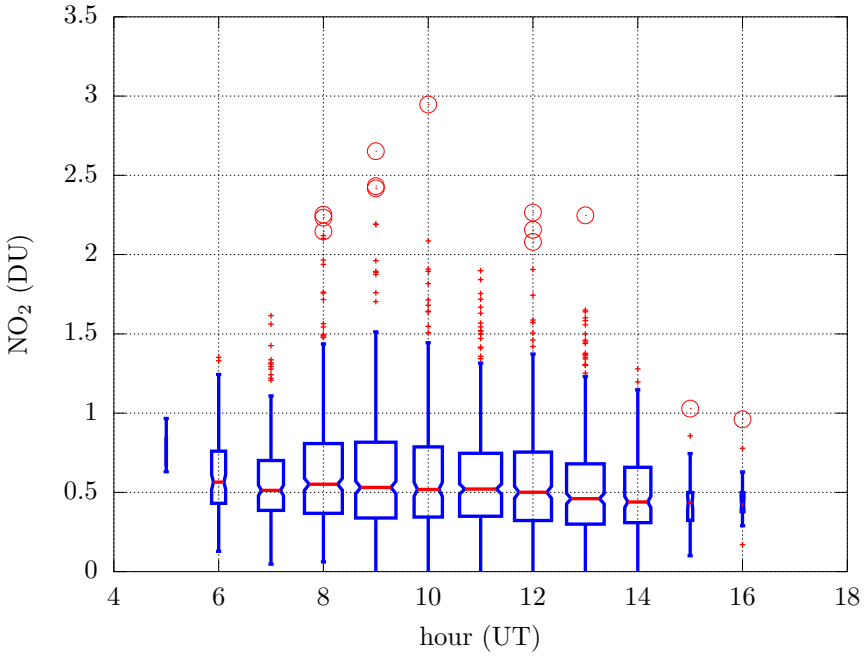

Figure 6.40: Daily cycle of nitrogen dioxide measured by the Brewer in Athens on working days (Monday–Friday, October–May). The horizontal axis represents the hour of the day.

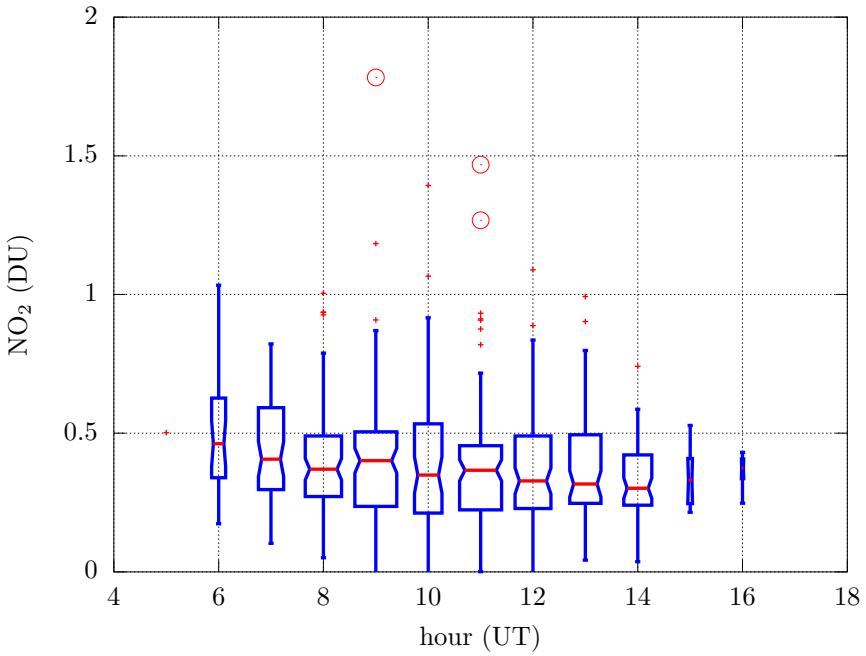

Figure 6.41: Daily cycle of nitrogen dioxide measured by the Brewer in Athens on Sundays (October–May). The horizontal axis represents the hour of the day.

6.5 The Hradec Králové series

Dobson ozone measurements started in 1962 in the GAW station of Hradec Králové (No. 096, 50.18°N, 15.833°E, 280 m a.s.l). The MKIV Brewer #098 has been providing estimates of atmospheric ozone and nitrogen dioxide total columns since 1993. The spectrophotometer is located on the roof of the Solar and Ozone Observatory of the Czech Hydrometeorological Institude in the outskirts of the city of Hradec Králové, a typical central Europe lowland site. Quite heavy traffic around the town, as well as a coal-fired power plant nearby – about 15 km from the observatory – could affect the NO_2 measurements at the station. The owner of the Brewer is also responsible for the ozone calibrations in Europe with the reference Brewer #017 and the instrument is well maintained and stable.

6.5.1 Characterisation of Brewer #098

The dispersion test in the visible range was executed by the operator at the measurement site, using my new dispersion routine. The resulting wavelengths and resolutions at the operating step 1104 are listed in Table 6.3. The new NO_2 weighting coefficients are shown in Table 6.4. The sensitivities to the factors affecting the NO_2 estimates were calculated and are shown in Table 6.5. A dead time of 34 ns, as employed in the ozone measurements, was used. The effect of the filters non-linearity, assessed with the new routine in the visible, is represented in Fig. 6.42. The O_4 correction was determined for an altitude of 280 m a.s.l.

6.5.2 Reprocessing of standard lamp test series

I used the standard lamp measurements, corrected for any lamp replacement, to take into account the variations of the Brewer sensitivity. The series is displayed in Fig. 6.43.

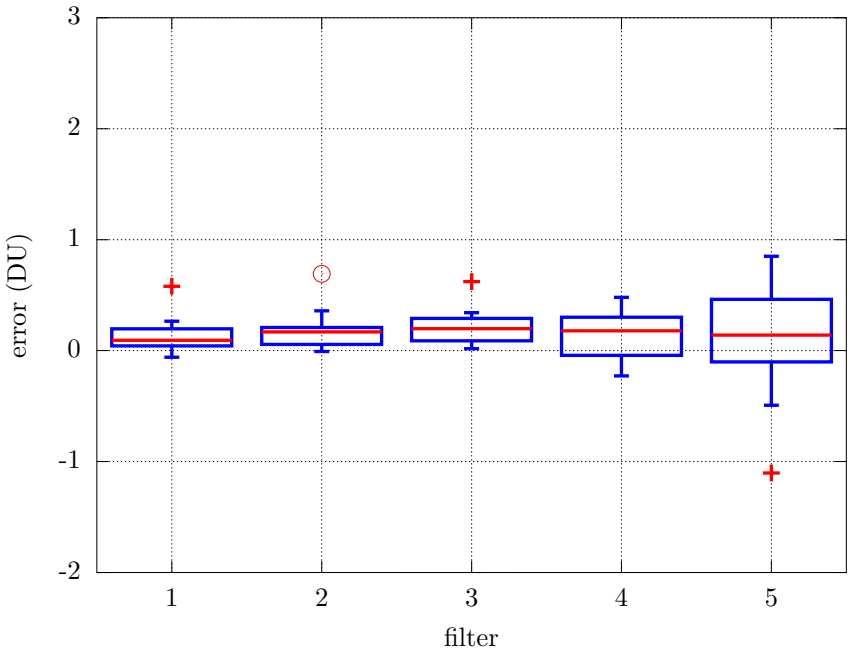

Figure 6.42: Effect for filter non-linearity for Brewer #098.

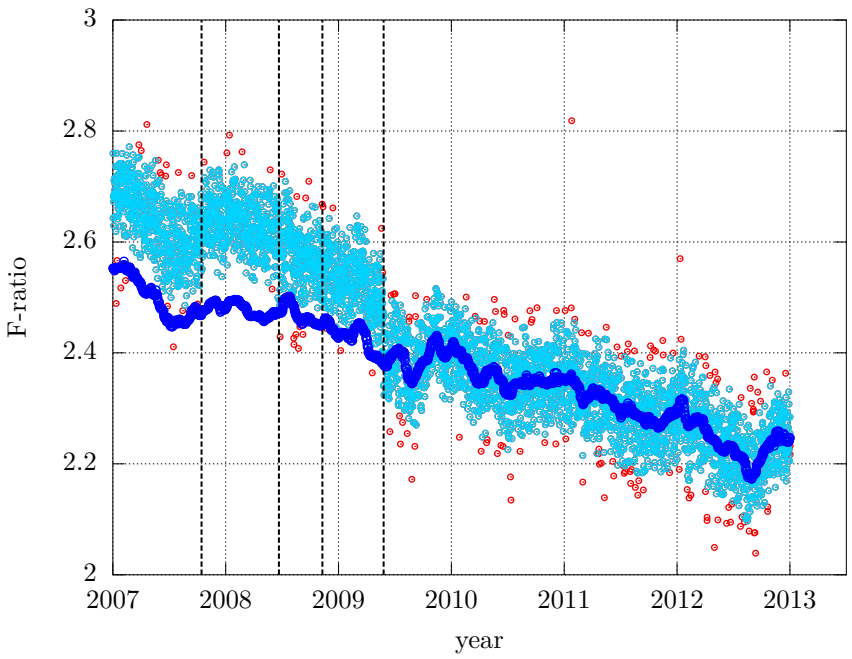

Figure 6.43: Results of `sl` test for Brewer #098. Light blue points represents the linear combination obtained using the lamp as a source, red points are outliers removed from the analysis by my software. The final `sl` series (blue points) is obtained by imposing continuity before and after lamp replacements (black vertical dashed lines) and applying a running average filter.

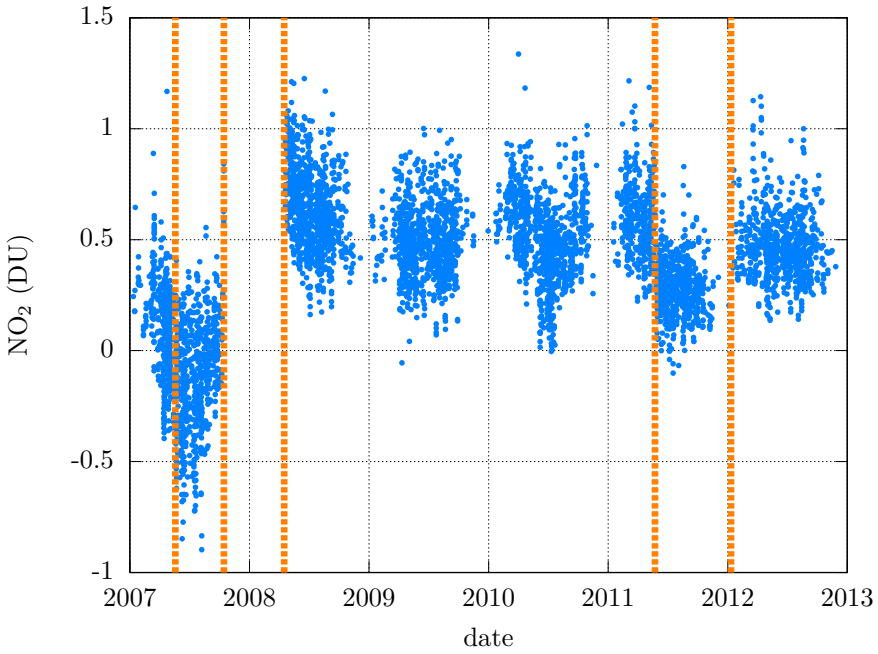

Figure 6.44: Series of NO_2 measurements in Hradec Králové after first reprocessing with the new algorithm. Blue points: direct sun measurements; vertical dashed lines: events that may affect the wavelength alignment of the Brewer.

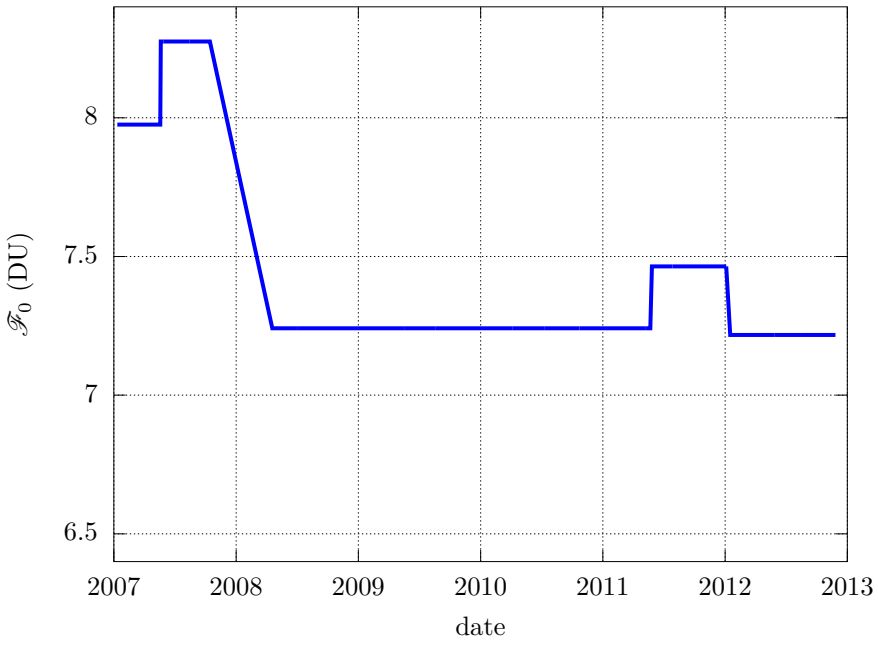

Figure 6.45: Series of extraterrestrial constants determined using the BE technique from the Hradec Králové data series.

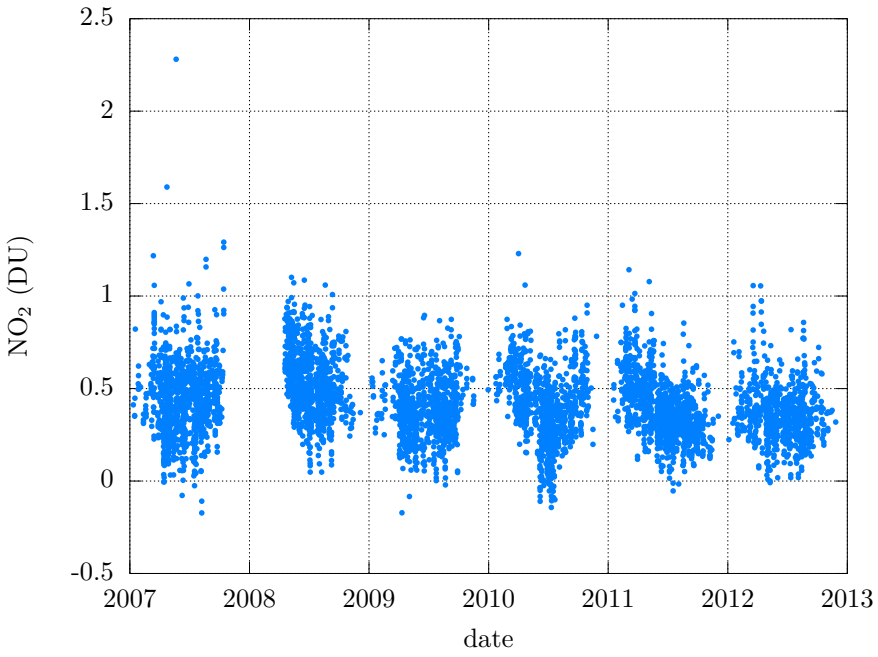

Figure 6.46: The NO_2 data series in Hradec Králové, reprocessed using the variable calibration factors displayed in Fig. 6.45.

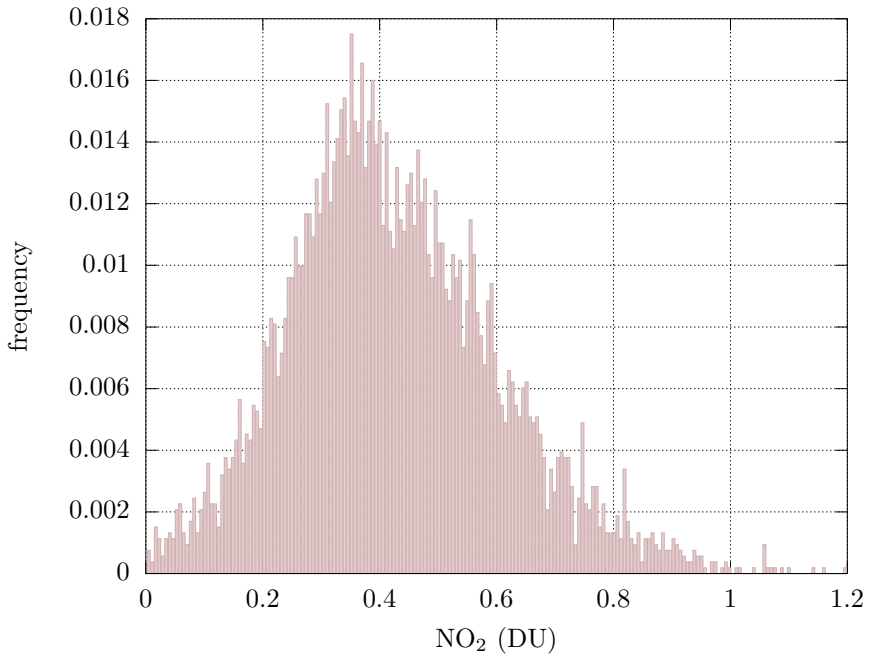

Figure 6.47: Distribution of NO_2 column densities measured in Hradec Králové.

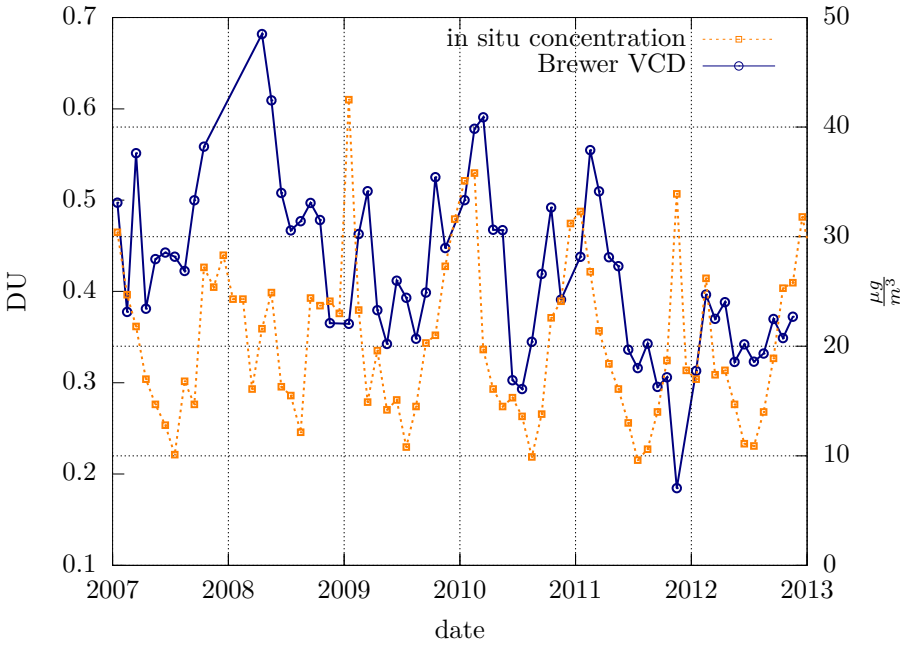

Figure 6.48: Blue points and left axis: monthly means of the NO_2 VCDs measured in Hradec Králové by the Brewer. Orange points and right axis: monthly means of in-situ NO_2 concentrations in a downtown station.

6.5.3 First reprocessing of the NO_2 series

Results using a first guess extraterrestrial constant are presented in Fig. 6.44. A very pronounced dependence on wavelength misalignments is visible, due to the high sensitivity (the higher among the analysed series) of Brewer #098 (Table 6.5). New extraterrestrial constants were calculated using the BE method on portions of the series between the events that altered the Brewer wavelength scale (Fig. 6.45).

6.5.4 Final reprocessing and exploratory data analysis

The final NO_2 series, which does not show the previous discontinuities, is displayed in Fig. 6.46. The retrieved amounts of nitrogen dioxide are higher than expected from a semi-rural site, probably due to emissions by the traffic and the power plant. A histogram of the distribution of NO_2 column densities measured in Hradec Králové is plotted in Fig. 6.47 and shows that half of the measurements fall in the range 0.3–0.5 DU, with median 0.4 DU (Table 6.6). Therefore, the VCD measurements in Hradec Králové are found to be between the Saint-Christophe and Rome levels. In Table 6.6 the NO_2 estimates using the old algorithm (but the same quality screening criteria) are additionally reported, as recorded in the B-file. An overestimation of more than 370% by the old algorithm is found on average.

Correlation with in-situ measurements and trends

In situ NO_2 concentration measurements, performed in the town center, are available. Monthly means of both series (VCDs from the Brewer and local concentrations from chemiluminescence measurements) are plotted together in Fig. 6.48. Table 6.7 summarises the results of the correlation analysis based on several estimators.

The VCD anomalies are displayed in Fig. 6.49 and the respective correlation analysis Table 6.8. The calculated linear trends for both series are reported in Table 6.9. Both the Student's t-test

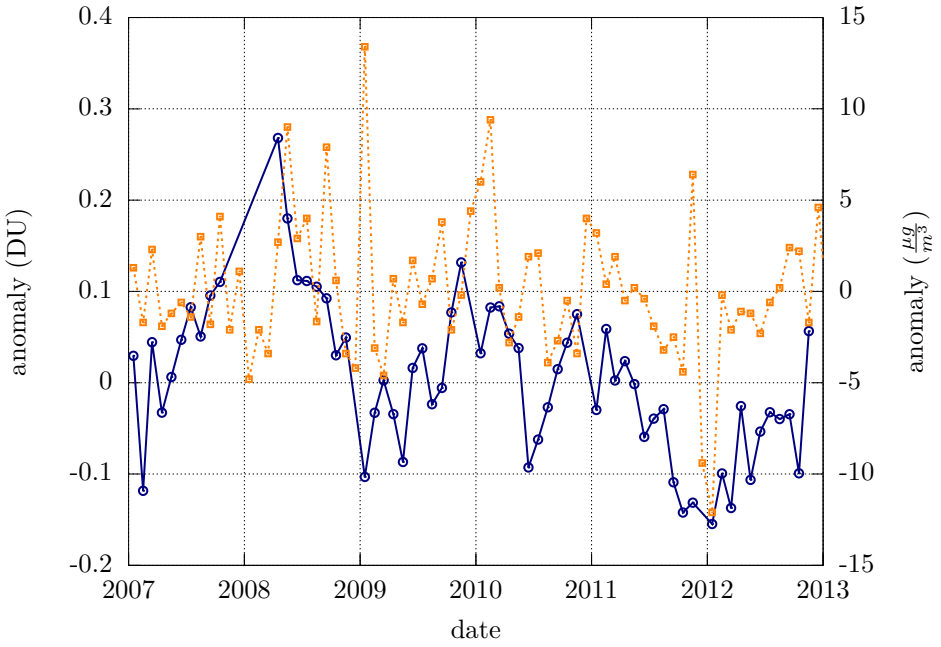

Figure 6.49: Blue points and left axis: monthly anomalies, with respect to the climatological values, of the NO_2 VCDs measured in Hradec Králové. Orange points and right axis: monthly anomalies of the in-situ NO_2 concentrations.

Table 6.6: IQR and median of the reprocessed NO_2 series, using both the new algorithm described in my work and the old algorithm by the Brewer operating software.

station	IQR (DU) new algorithm	median (DU) new algorithm	IQR (DU) old algorithm	median (DU) old algorithm
Saint-Christophe	0.19–0.3	0.25	1.0–1.3	1.1
Rome	0.28–0.6	0.4	1.2–1.8	1.5
Athens	0.3–0.7	0.5	0.8–1.5	1.1
Hradec Králové	0.3–0.5	0.4	1.3–1.9	1.5

and the Mann-Kendall's test found that the Brewer trend of (-5.0±1.5)% is statistically significant (significance level of 0.05, p-values less than 0.002).

Short-term temporal variability

The annual cycle is represented as a boxplot in Fig. 6.50 and is characterised by an average amplitude of 0.19 DU, with maximum values in the winter season. In this period, in addition to the other sources, the power plant works to the full. The weekly cycle is shown in Fig. 6.51, the daily cycle of a typical working day is represented in Fig. 6.52 and the same graph for Sundays measurements is displayed in Fig. 6.53. Absence of any (inverse) U-shape is a promising sign of the accuracy of the used extraterrestrial constants.

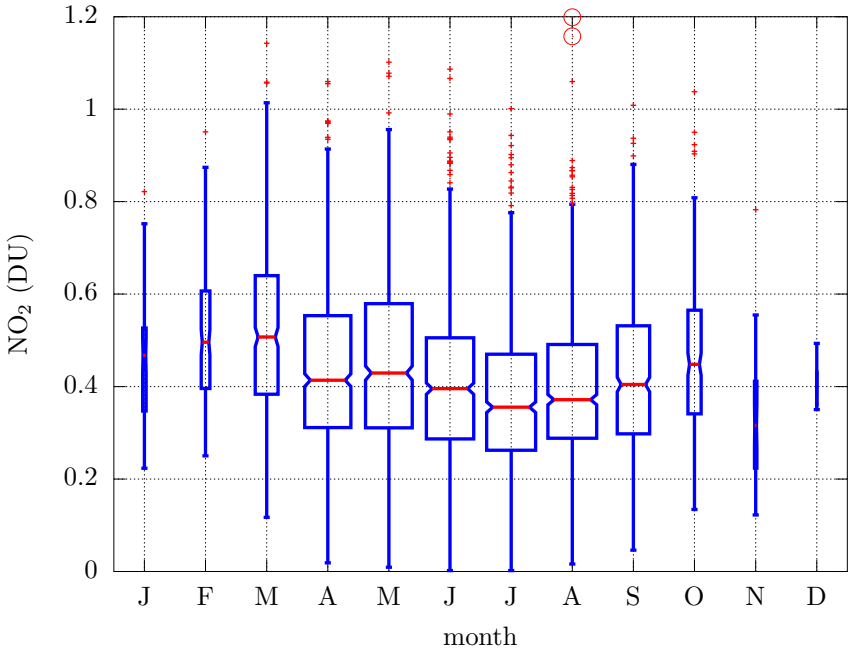

Figure 6.50: Boxplot of the annual cycle of nitrogen dioxide VCDs in Hradec Králové. The horizontal axis represents the months, from January to December.

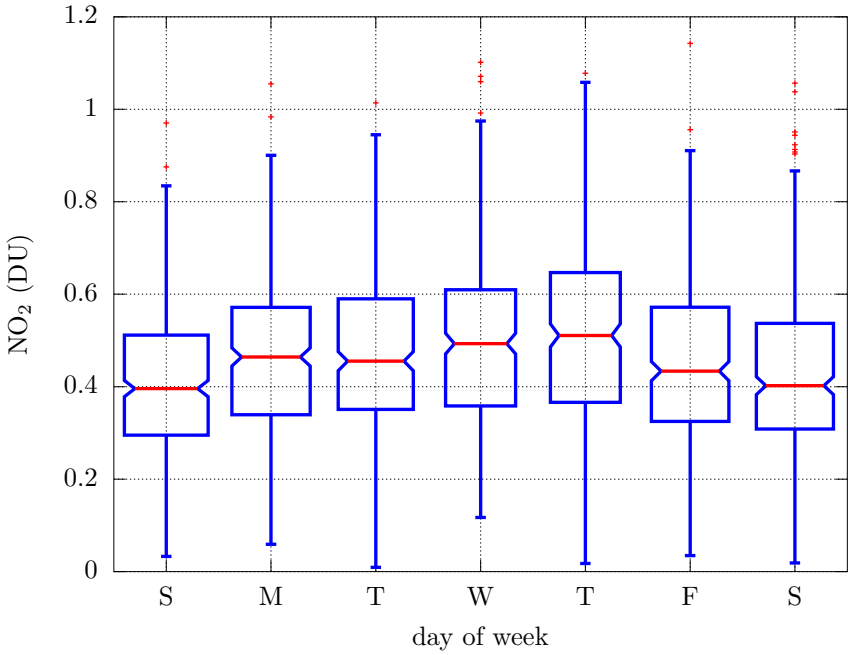

Figure 6.51: Weekly cycle of nitrogen dioxide measured by the Brewer in Hradec Králové. The horizontal axis represents the day of the week, from Sunday to Saturday.

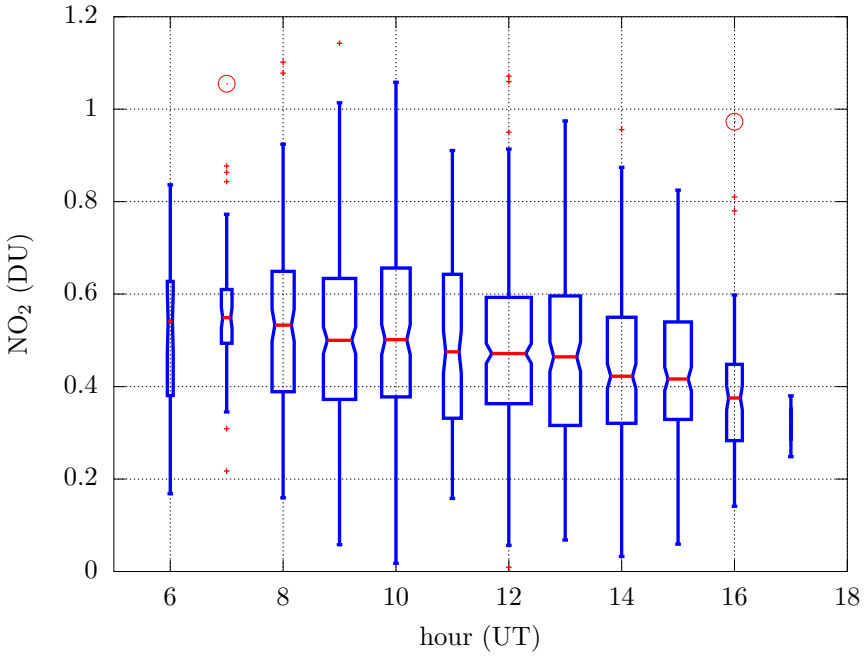

Figure 6.52: Daily cycle of nitrogen dioxide measured by the Brewer in Hradec Králové on working days (Monday–Friday, October–May). The horizontal axis represents the hour of the day.

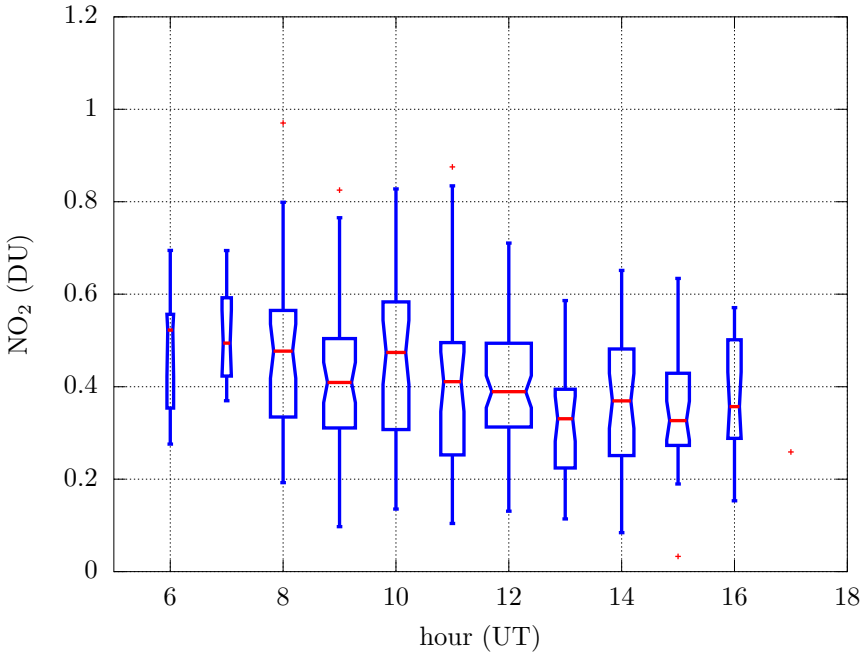

Figure 6.53: Daily cycle of nitrogen dioxide measured by the Brewer in Hradec Králové on Sundays (October–May). The horizontal axis represents the hour of the day.

Table 6.7: Correlation coefficients between the Brewer VCDs and the in situ concentrations in the European locations considered in the study.

station	Pearson's ρ_P	Kendall's τ	Spearman's ρ_S
Saint-Christophe	0.75	0.53	0.69
Rome	0.05	0.02	0.04
Athens	0.37	0.26	0.36
Hradec Králové	0.22	0.16	0.23

Table 6.8: Correlation coefficients for the anomalies of Brewer and the in situ concentration series in the European locations considered in the study.

station	Pearson's ρ_P	Kendall's τ	Spearman's ρ_S
Saint-Christophe	0.36	0.23	0.31
Rome	0.12	0.08	0.10
Athens	0.42	0.22	0.30
Hradec Králové	0.26	0.15	0.23

Table 6.9: Linear trends revealed by different sources (Brewer VCD retrievals, in situ measurements and satellite estimates, Sect. 6.6) in the analysed series. The quantities after the ± sign are the uncertainties (k=1, in percent) of the trends, obtained assuming that the fraction of the uncertainty of the monthly anomalies relevant to the calculation of the trend is 0.1 DU.

source	Saint-Christophe %/year	Rome %/year	Athens %/year	Hradec Králové %/year
Brewer	0.4±2.5	-5.0±1.6	-1.3±0.8	-5.0±1.5
in situ	-1.9	2.3	-7	-0.7
OMI	2.8	-1.0	-4	2.3
SCIAMACHY	-0.3	1.1	-3	-0.3
GOME2a	-1.4	-0.8	-6	5

6.6 Satellite estimates

As a further example of application of the results provided by the new algorithm, the ground-based measurements with the Brewer were compared to the satellite estimates of tropospheric nitrogen dioxide by three spaceborne radiometers: OMI, SCIAMACHY and GOME-2 (Bovensmann et al., 1999; Levelt et al., 2006; Burrows et al., 1999; Noel et al., 1999; Celarier et al., 2008; Wenig et al., 2008; Schneider and van der A, 2012). Their main technical characteristics are reported in Table 6.10.

Table 6.10: Technical characteristics of satellite radiometers used in the study.

	OMI	SCIAMACHY	GOME-2
satellite platform	EOS Aura	Envisat	MetOp-A
spectral range (nm)	270–500	240–2380	240–790
FWHM (nm)	0.45–1.0	0.2–1.5	0.5
spatial resolution (km^2)	13×24	30×60	80×40

Monthly averages of total nitrogen dioxide retrievals from the Brewers and from satellite radiometers are displayed in Figs. 6.54, 6.56, 6.58 and 6.60. Moreover, the bias and the Root Mean Square Deviation (RMSD) between satellite and Brewer estimates is shown in Table 6.11. Generally, the magnitude of the NO_2 estimates with the new algorithm agree much better than with the old algorithm: the mean bias over all stations is about -6% (the satellite data being slightly lower than the Brewer measurements) or -2.4% when the Saint-Christophe series is excluded from the average. Indeed, satellite retrievals are remarkably lower than ground-based measurements at Saint-Christophe, in agreement with previous studies in mountain regions (Zhou et al., 2009): the satellite pixel is probably too large and the spaceborne instrument cannot pierce the lower atmospheric layers of the Aosta Valley.

A feature common to all graphs is the less marked seasonal dependence by the Brewers compared to spaceborne instruments. For example, the winter maxima in Hradec Králové measured from the space are sometimes unnaturally high. This could be due to the power plant, running to the full during winter, entering in the satellite pixel or even to failure in snow detection on ground with consequent inaccuracies on NO_2 retrievals (Hilboll, personal communication, 2014). On the Brewer side, an additional reason could be the application of the BE algorithm over too short periods, tending to flatten the series based on the assumption of a constant NO_2 baseline. This subject would require deeper analysis, which is not the aim of my thesis.

Table 6.11: Bias between satellite and Brewer monthly NO_2 VCD estimates, in DU, and RMSD, between parentheses.

satellite	Saint-Christophe DU	Rome DU	Athens DU	Hradec Králové DU
OMI	-0.03 (0.08)	0.05 (0.20)	-0.04 (0.17)	-0.04 (0.27)
SCIAMACHY	-0.04 (0.06)	0.06 (0.20)	-0.01 (0.17)	-0.06 (0.17)
GOME2a	-0.06 (0.09)	0.03 (0.15)	-0.04 (0.11)	-0.05 (0.50)

A correlation analysis of the absolute NO_2 monthly values from the Brewers and the satellite radiometers and the respective monthly anomalies is presented in Tables 6.12 and 6.13. Table 6.14 shows the correlation indexes between satellites and in situ monthly anomalies. Correlations are generally rather poor, probably reflecting the different spatial resolutions of the three techniques

(Hilboll et al., 2013). Also, the non-homogenised database used could be a further reason of low correlations: the monthly means from the satellite sensors depend on the overpass of the satellite at the location of interest (around 6 overpasses per month for the SCIAMACHY intrument, around almost 3–4 per week for the GOME-2 and one per day for OMI). Therefore, one should identify more carefully the days being used to provide the satellite monthly means to have a direct comparison between. Additionally, the Brewer data at the exact overpass time of the satellites should be compared. Further analyses on these issues, which are not the main subject of the present work, are planned in the future.

Interestingly, the performances of the satellite radiometers depend on the location and there is no "best" spaceborne instrument in an absolute sense. The overall correlation between satellite and in situ anomalies is not better than the one between Brewers and in situ anomalies (Table 6.8).

Finally, nitrogen dioxide trends measured from the space over the four locations are presented in Table 6.9. They mostly show inconsistent tendencies in Saint-Christophe, Rome and Hradec Králové, with remarkable differences both in the magnitude and sign. Over Athens, satellites measure a general negative trend of about -4%, which is consistent with the results published in the scientific literature (Vrekoussis et al., 2013). Again, the lower magnitude of the trend detected by Brewer #001 in Athens could be due to the application of the BE method.

Table 6.12: Spearman's rank correlation between Brewer and satellite monthly NO_2 VCD estimates for all analysed stations.

satellite	Saint-Christophe	Rome	Athens	Hradec Králové
OMI	-0.07	0.40	0.25	0.19
SCIAMACHY	0.11	0.20	0.33	0.11
GOME2a	-0.11	0.21	0.48	0.15

Table 6.13: Spearman's rank correlation between Brewer and satellite monthly NO_2 anomalies for all analysed stations.

satellite	Saint-Christophe	Rome	Athens	Hradec Králové
OMI	0.01	0.27	0.09	-0.07
SCIAMACHY	0.23	0.10	0.36	-0.11
GOME2a	-0.15	0.02	0.22	-0.16

Table 6.14: Spearman's rank correlation between in situ and satellite monthly NO_2 anomalies for all analysed stations.

satellite	Saint-Christophe	Rome	Athens	Hradec Králové
OMI	0.09	0.03	0.50	0.22
SCIAMACHY	0.02	0.13	0.38	0.03
GOME2a	0.01	0.16	0.37	0.25

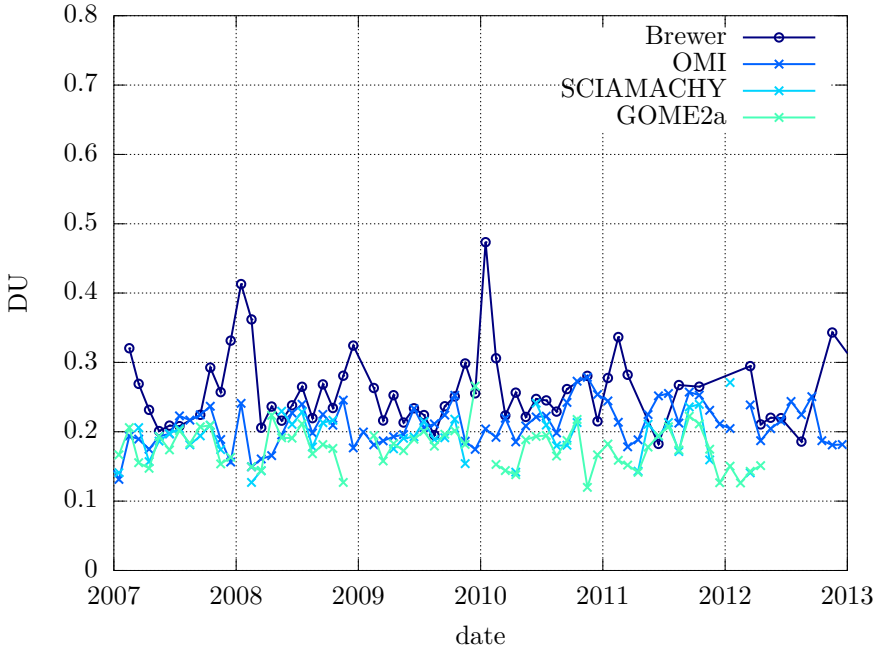

Figure 6.54: Monthly averages of total NO_2 VCD estimates by the Brewer and the satellites over Saint-Christophe.

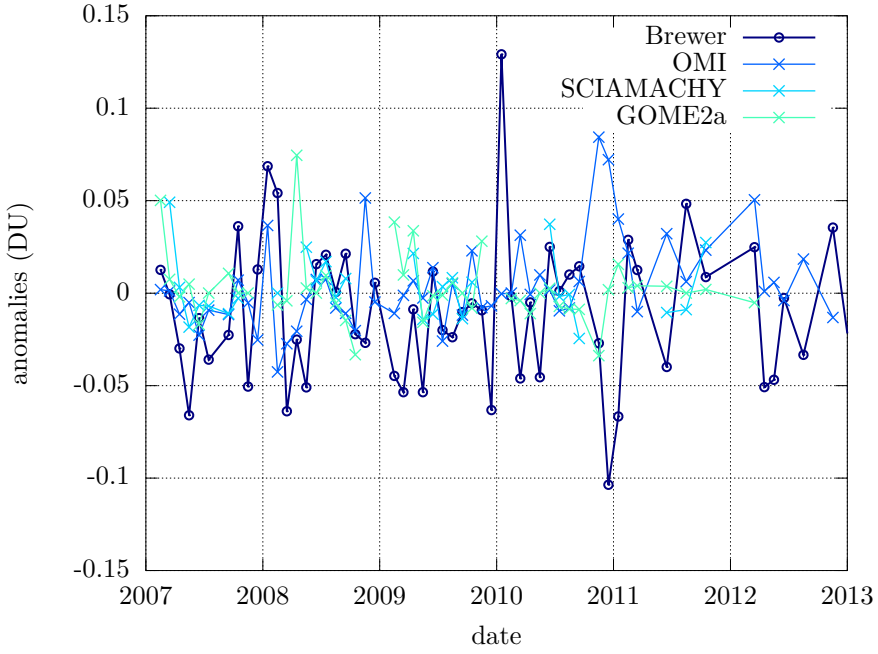

Figure 6.55: Monthly anomalies measured by the Brewer and satellites over Saint-Christophe.

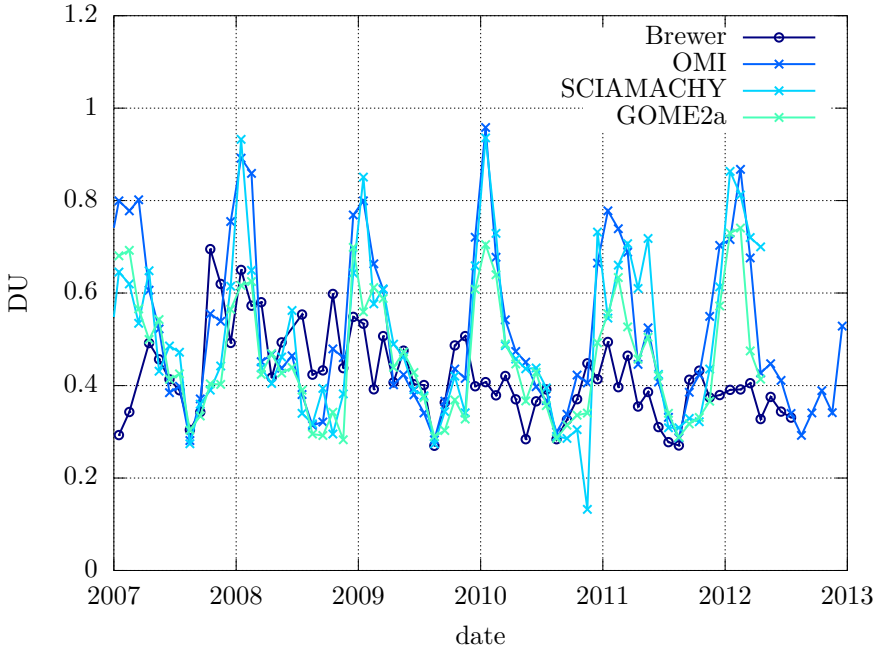

Figure 6.56: Monthly averages of total NO_2 VCD estimates by the Brewer and the satellites over Rome.

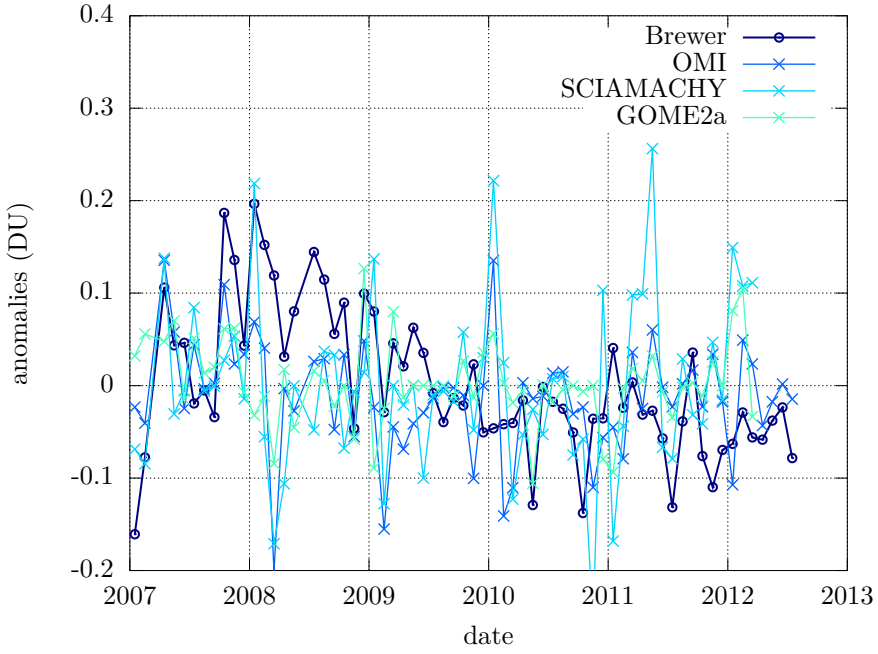

Figure 6.57: Monthly anomalies measured by the Brewer and satellites over Rome.

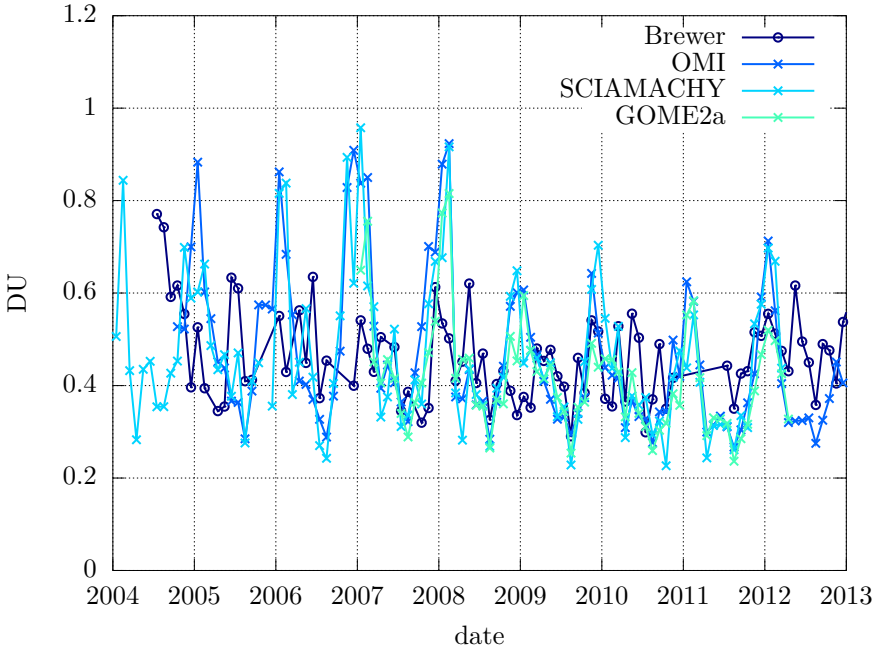

Figure 6.58: Monthly averages of total NO_2 VCD estimates by the Brewer and the satellites over Athens.

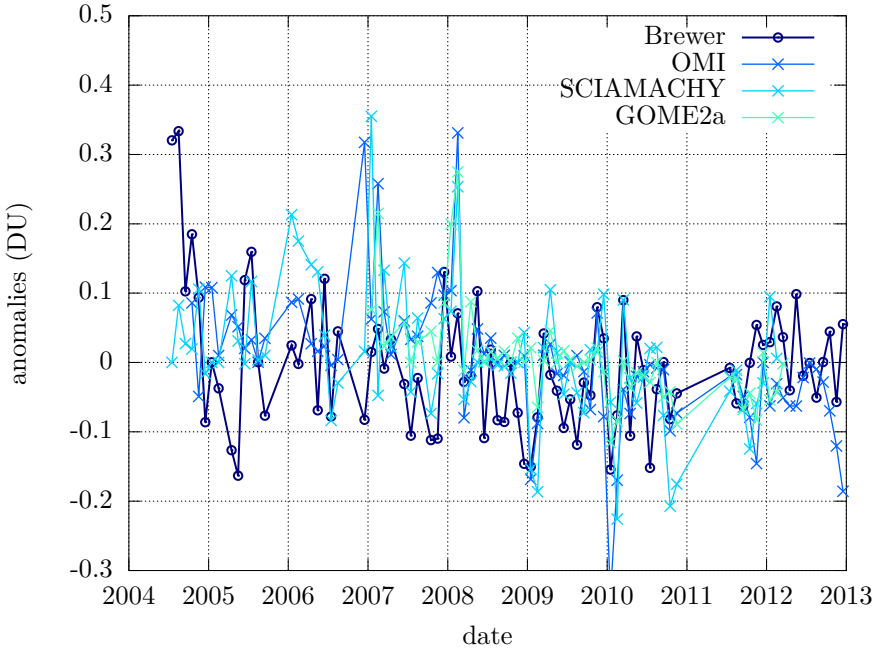

Figure 6.59: Monthly anomalies measured by the Brewer and satellites over Athens.

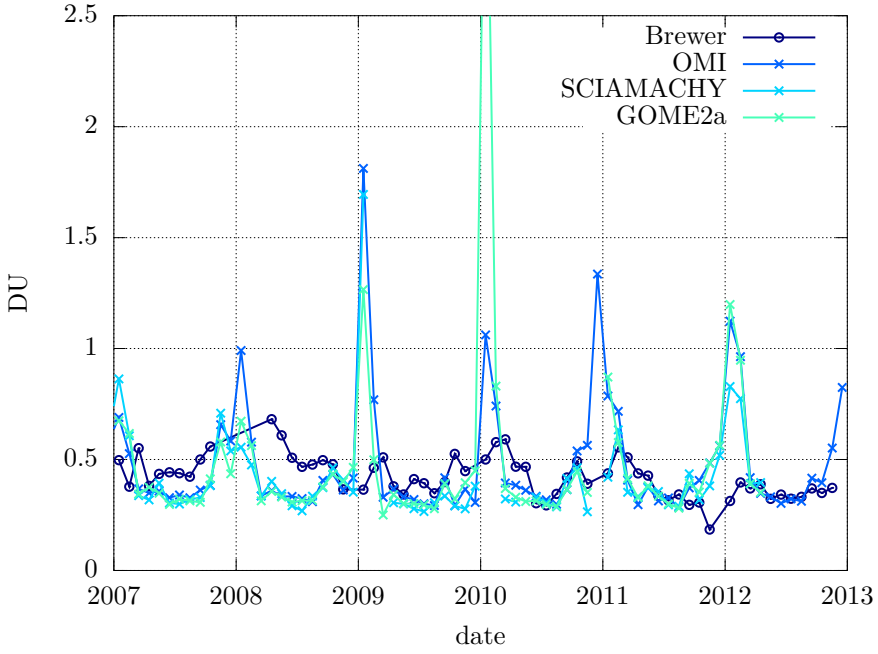

Figure 6.60: Monthly averages of total NO_2 VCD estimates by the Brewer and the satellites over Hradec Králové.

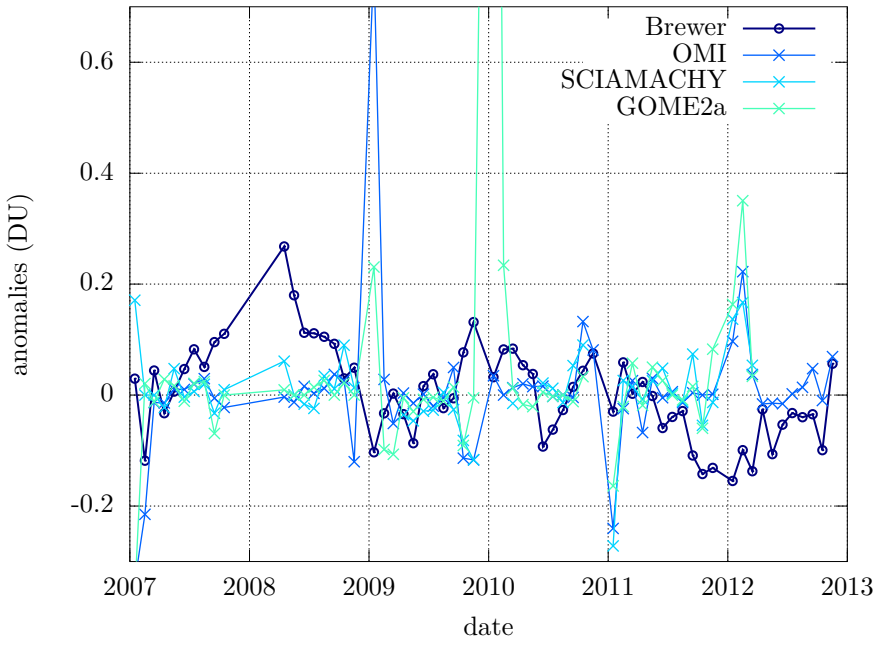

Figure 6.61: Monthly anomalies measured by the Brewer and satellites over Hradec Králové.

Chapter highlights

- two alternative methods to calibrate a Brewer spectrophotometer from the statistical analysis of a long-term data set (the Minimum-Amount Langley Extrapolation and the Bootstrap Estimation techniques) were validated using the Saint-Christophe (Italy) series;
- four European Brewers, operating in Italy, Greece and in the Czech Republic, were thoroughly characterised and their respective long-term data sets were successfully reprocessed with the new algorithm. As expected, the average values were found to be representative of the environmental characteristics around the respective measuring stations. Large overestimations, up to 370% compared to the new algorithm, were obtained when applying the old algorithm;
- the series were affected by serious errors that are not simple to correct in a trivial way. Most of all, slight wavelength inaccuracies, e.g. after mercury lamp replacements, were confirmed to be the main source of the inconsistencies. The piecewise recalculation of the extraterrestrial constant was proven to be an effective correction method, providing accurate results;
- high correlation was found between the Brewer retrievals and nearby measured in situ concentrations in the Saint-Christophe series, proving that most of the NO_2 variability detected from ground-based instrumentation is due to the tropospheric column. The anthropogenic influence is also noticeable in the seasonal, weekly and daily cycles of all series. Medium to large negative tendencies, up to -5%/year, were discovered in the analysed data sets, which is in agreement with the recent scientific literature. Nevertheless, the trends are only significant for the Rome and Hradec Králové stations;
- data reprocessed with the new algorithm get in much closer agreement to the nitrogen dioxide estimations from space (OMI, SCIAMACHY and GOME-2 satellite radiometers) than with the old algorithm, with an overall bias as low as -2.4% when mountainous regions are excluded from the analysis. Short-term correlations are rather poor, probably reflecting the different spatial resolutions of the various techniques (e.g. the large satellite pixels) and inherently limitations of the Bootstrap Estimation technique.

CHAPTER 7

Conclusions and perspectives

7.1 Outcomes

During the three years of Ph.D., I faced several issues. A summary of the specific outcomes of my research is given below.

The operating principles and instrumental characteristics of the MKIV Brewer spectrophotometer #066, installed in Saint-Christophe (Italy), were thoroughly analysed. This was the first instrument to be characterised in the visible range. To the purpose, innovative software was developed, which is now available to the whole Brewer users community;

the Brewer algorithm for the retrieval of nitrogen dioxide in the direct sun and zenith sky geometries was improved and two solutions to overcome the main limitations of the standard method were proposed, making use of solar intensity measurements at six and eleven wavelengths. An innovative mathematical framework, making use of linear algebra, was developed and intensively used to understand in depth the capabilities and limitations of the Brewer retrieval technique;

based on the instrumental characterisation and numerical simulations, optimal instrumental settings (e.g., micrometer position) for Brewer #066 were found, increasing the Signal-to-Noise Ratio (SNR) of NO_2 estimates and reducing, if not removing, the interference of factors perturbing the nitrogen dioxide retrieval (e.g., oxygen dimer, wavelength sensitivity, water vapour, etc.);

Brewer #066 participated to four field measurement campaigns, proving its reliability and its ability to behave as a reference instrument for nitrogen dioxide measurements. During the ad-hoc field campaign carried out in the unique environment of Izaña (Tenerife), the Brewer was calibrated for NO_2 estimates through the Langley plot technique. The latter was enhanced, using a novel approach, to take into account the daily NO_2 variability. Comparison with an NDACC reference spectrophotometer provided results within the uncertainty of the two instruments;

the Monte Carlo method was used to assess the combined uncertainty of each factor affecting the Brewer NO_2 retrieval in the direct sun geometry. The combined uncertainty ranges from 0.05 to 0.25 DU, depending on the solar zenith angle and the environmental conditions of the measuring site;

using newly developed techniques, other atmospheric parameters were effectively retrieved by the MKIV Brewer, such as the oxygen dimer optical depth and the degree of linear polarisation of the zenith skylight. These parameters are useful in studying the effects of aerosols and clouds in the atmosphere;

serious errors were found to affect the long-term series recorded in four European Brewer stations (two in Italy, one in Greece and one the Czech Republic), most of all wavelength misalignments, which are not simple to remove by ordinary techniques. A piecewise calibration was successfully applied to overcome this issue;

the series were reprocessed using my newly developed algorithm. To this purpose, two statistical techniques making use of historical data were applied to calibrate the Brewers even in the highly polluted environment of urban sites. It was found that the NO_2 estimates with the new algorithm are much lower than those obtained with the old algorithm and closer to the retrievals from space employing satellite radiometers;

the anthropogenic influence was assessed by comparing, although different quantities, the Brewer NO_2 vertical column density retrievals with in situ concentrations revealed by chemiluminescence detectors. When the respective stations are close to each other, high correlation was found. Also, the pollution effect was observed in the seasonal, weekly and daily cycles of Brewer measurements. Despite the analysed period is limited in time, medium to large negative nitrogen dioxide tendencies (%/year) were detected over the urban sites. The trends were found to be statistically significant for the Rome and Hradec Králové stations.

7.2 Theses

The research presented in this work was developed with the aim of providing the answer to the hypotheses stated in the Introduction and reported further below.

A better instrumental characterisation allows to improve the Brewer performances (accepted as is). Since nitrogen dioxide is a weak absorber, great care must be taken to characterise the measuring instrumentation. As instance, it was proved that the effect of the neutral density filters is remarkable (up to 200%) on NO_2 estimates. Additionally, a fine tuning of each instrument (e.g., the grating position) was found to be necessary in order to increase the retrieval content and reduce the influence of perturbing factors which could degrade the measurement accuracy;

the observed overestimations by the Brewer can be reduced by employing more recent spectroscopic data (accepted as is). The most recent spectroscopic data sets published in the scientific literature were included in the new algorithm. Overestimations of about 50% were identified when using the obsolete data instead of the new ones. Additionally, wrong extraterrestrial constants such as those currently used by the European Brewers can lead to huge overestimations, e.g. up to 370% on average;

better techniques are available to reduce the measurement noise and increase the information content of the retrieval (partly accepted). Two methods were developed to improve the retrieval quality, using six and eleven slits. I showed that the latter algorithm is noisier than the former, which should be preferred. Noise reduction was performed using the newly formulated mathematical framework and trying to "turn" the measurement vector as parallel as possible to the NO_2 cross section vector, while setting it orthogonal to the vectors of other influencing factors;

direct sun and zenith sky estimates by the Brewer are consistent within their respective uncertainties (accepted as is). During the Izaña campaign, quasi-simultaneous measurements of direct sun and zenith sky (in the parallel and perpendicular polarisation)

light intensity were performed and compared. Although some residual effect, probably due to the Rotational Raman Scattering (RRS), is visible in the zenith measurements, the estimates are within the expected uncertainty. It is worth noticing that this occurs in the pristine conditions of the Izaña station, where the only contribution comes from the nitrogen dioxide stratospheric column. When the tropospheric column is not negligible, e.g. in polluted sites, then a proper choice of the Air Mass Factors (AMFs) is fundamental, since the direct sun measurements are more sensitive to the total column, while the zenith sky estimates are more representative of the stratosphere;

reliable information about the NO_2 trends can be derived by reprocessing existing long-term data sets (partly accepted). It was found that the combined uncertainty of direct sun NO_2 estimates by the Brewer can reach more than 200% of the stratospheric column and is thus too large for assessing long-term trends of the stratospheric content. The uncertainty should decrease when using the zenith sky geometry instead of direct sun retrievals, but other errors arise, such as the Ring effect. On the other hand, the Brewer can be effectively used to study the tropospheric trends, which are remarkably higher than the stated uncertainty and thus detectable. A preliminary analysis of the general NO_2 tendency in some European sites, in a limited period of few years, was carried out in the last chapter of this work;

satellite total column estimates and in-situ concentration measurements are not always representative of the nitrogen dioxide density in the atmosphere (accepted as is). Although the magnitude of satellite radiometers and Brewer estimates are consistent when using the new algorithm, with an overall satellite–Brewer bias as low as -2.4% when considering all stations except the mountainous site of Saint-Christophe (-6% when including it), low correlation was generally observed when comparing the short-term variations from the space with the Brewer retrievals and in situ concentrations. This can be justified by the low satellite resolution, while in situ measurements are also influenced by the mixing layer height and local wind circulation. However, further analyses are required on this issue and a more homogenised dataset, calculated on the basis of proper overpass days and times, could provide better results.

7.3 Future research

More research is needed on the topic of nitrogen dioxide estimations by the Brewers. Some challenging questions are offered further below.

Some instrumental characterisation issues must be further investigated, such as the determination of the straylight effect in the visible range and the polarising efficiency of the filters. This could lead to more accurate estimations of nitrogen dioxide in the atmosphere as well as of other quantities measurable by the Brewer, such as the degree of linear polarisation of the sky. The inconsistencies between the dispersion functions determined in the UV and visible range should be faced and solved;

further studies about the Ring effect are needed to assess the quality of zenith sky retrievals and to increase their accuracy. This could be achieved once the radiative transfer models are able to support polarised calculations, rotational Raman scattering and full spherical geometry at the same time, to correctly simulate the zenith sky radiances measured by the Brewer;

after the Ring effect is taken into account, historical series of zenith sky measurements can then be reprocessed and provide valuable information about the stratospheric trends, due to the high NO_2 signal resulting from enhanced AMFs;

the new algorithm developed in the present work can be applied to the European and global series to analyse them with more refined statistical technique. This could also allow to find better agreement between the retrievals with the Brewer, spaceborne and in situ instrumentation;

nearly simultaneous zenith sky and direct sun measurements could be used to partition the tropospheric and stratospheric NO_2 columns, taking advantage of the different atmospheric regions probed by the two geometries (Twomey et al., 1977; Jiang et al., 1997; Schofield et al., 2004). The simplest method consists in assuming that, at large solar zenith angles, the main contribution of the nitrogen dioxide column in the zenith sky measurements comes from the stratosphere (Chen et al., 2009; Gruzdev and Elokhov, 2009). Then, assuming a constant stratospheric VCD, or linearly varying with time from the morning to the afternoon, the tropospheric column could be determined by subtracting the stratospheric VCD, obtained from zenith sky retrievals, to the total VCD from direct sun measurements. A more refined approach is represented by the optimal estimation method (Rodgers, 2000) applied on nearly simultaneous measurements of direct sun and zenith sky or even zenith sky measurements in two different polarisations (Jiang et al., 2004; Guo et al., 2007). A correct partitioning would also allow to better determine the nitrogen dioxide effective temperature, which can influence the choice of the NO_2 cross sections and, in turn, the retrieval;

better estimates of nitrogen dioxide can be used to improve the quality of Aerosol Optical Depth (AOD) retrievals by the Brewer in the visible range. By analysing them together with the AODs measured in the UV, the Ångström exponent could be determined (Gröbner and Meleti, 2004);

finally, an interesting application of the method would be to use the moon, instead of the sun, as a source. In effect, the Brewer is able to perform "focused moon" measurements, which are however rarely used for ozone and have never been done for NO_2. This could allow to measure the nitrogen dioxide column densities at night, when the photochemistry is almost absent. Nighttime nitrogen dioxide retrieval would be even simpler than the ozone retrieval, since more photons can be collected in the visible range than in the UV at night.

Appendices

APPENDIX A

Measurement schedules used during the Izaña campaign

In this appendix, the three Brewer schedules used during the Izaña campaign are reported. In addition to the standard Brewer commands, the schedules include some user-defined routines:

`ns`: NO_2 measurements in direct sun geometry at various diffraction grating positions (micrometer steps);

`nz`: NO_2 measurements in zenith sky geometry (polarisation parallel to the scattering plane) at various diffraction grating positions (micrometer steps);

`nw`: NO_2 measurements in zenith sky geometry (polarisation perpendicular to the scattering plane) at various diffraction grating positions (micrometer steps);

`os`: direct sun measurements of the oxygen dimer;

`jl`: standard lamp measurements at various grating positions;

`jf`: measurements of the filters attenuation at various grating positions.

A.1 Direct sun measurements (langns.skd)

```
-180
pdo3hgslslsldtrsappohgb2w1cihgczhgn2slslsldtrsjfo3hgn2jljljlpf
-110
pdo3aphgn2nwnznwnznwnznwb1nzpf99
-70
pdo3aphgdsn2nsnsnsnsnsnsnsnsb1nsfvpf99
-50
pdo3aphgdsn2nsnsnsnsnsnsnsnsb1nsfvpf99
-40
pdo3aphgdzdzn2jljljlnsnsb1nsfvpf99
40
pdo3aphgdsn2nsnsnsnsnsnsnsnsb1nsfvpf99
70
pdo3aphgn2nwnznwnznwnznwb1nzpf99
110
pdo3aphgn2jljljlo3pf
```

```
130
pdo3appzzepf
180
langns
```

A.2 Zenith sky measurements (langnz.skd)

```
-180
pdo3hgslslsldtrsappohgb2w1cihgczhgn2slslsldtrsjfo3hgn2jljljlpf
-110
pdo3aphgn2nznwnznwnznwnznwnzb1nwpf99
-40
pdo3aphgdzdzn2jljljlnsnsb1nsfvpf99
40
pdo3aphgn2nznwnznwnznwnznwnzb1nwpf99
110
pdo3aphgn2jljljlo3pf
120
pdo3appzzepf
180
langnz
```

A.3 Oxygen dimer measurements (langos.skd)

```
-180
pdo3hgslslsldtrsappohgb2w1cihgczhgn2slslsldtrsjfo3hgn2jljljlpf
-110
pdo3aphgn2nwnznwnznwnznwb1nzpf99
-80
pdo3aphgdsn2ososososososososb1osfvpf99
-50
pdo3aphgdsn2ososososososososb1osfvpf99
-40
pdo3aphgdzdzn2jljljlososb1osfvpf99
40
pdo3aphgdsn2ososososososososb1osfvpf99
80
pdo3aphgn2nwnznwnznwnznwb1nzpf99
110
pdo3aphgn2jljljlo3pf
130
pdo3appzzepf
180
langos
```

APPENDIX B

Publication list

B.1 Peer-reviewed papers

1. Diémoz, H., Siani, A.M., Casale, G.R., di Sarra, A., Serpillo, B., Petkov, B., Scaglione, S., Bonino, A., Facta, S., Fedele, F., Grifoni, D., Verdi, L. and Zipoli, G.: First national intercomparison of solar ultraviolet radiometers in Italy, Atmos. Meas. Tech., 4, 1689–1703, 2011

2. Casale, G.R., Siani, A.M., Diémoz, H., Kimlin, M.G. and Colosimo, A.: Applicability of the Polysulphone Horizontal Calibration to Differently Inclined Dosimeters, Photochem. Photobiol., 2012, 88, 207–214, doi: 10.1111/j.1751-1097.2011.01006.x

3. Diémoz, H., Egli, L., Gröbner, J. and Siani, A.M.: Solar ultraviolet measurements in Aosta (Italy): an analysis of short- and middle-term spectral variability, Radiation Processes in the Atmosphere and Ocean (IRS2012) AIP Conf. Proc. 1531, 856–859 (2013); doi: 10.1063/1.4804905

4. Siani, A.M., Modesti, S., Casale, G.R., Diémoz, H. and Colosimo, A.: Biologically effective surface UV climatology at Rome and Aosta, Italy, Radiation Processes in the Atmosphere and Ocean (IRS2012) AIP Conf. Proc. 1531, 903–906 (2013); doi: 10.1063/1.4804917

5. Diémoz, H., Savastiouk, V. and Siani, A.M.: Capability and limitations in measuring atmospheric nitrogen dioxide column amounts by means of the MKIV Brewer spectrophotometers, SPIE Remote Sensing 2013 "Remote Sensing of Clouds and the Atmosphere XVIII; and Optics in Atmospheric Propagation and Adaptive Systems XVI", doi: 10.1117/12.2028704

6. Diémoz, H., Campanelli, M. and Estelles, V.: One Year of Measurements with a POM-02 Sky Radiometer at an Alpine EuroSkyRad Station, J. Meteorol. Soc. Jpn. (accepted)

7. Petkov, B.H., Vitale, V., Tomasi, C., Siani, A.M., Seckmeyer, G., Webb, A., Smedley, A.R.D., Lanconelli, C., Mazzola, M., Lupi, A., Busetto, M., Diémoz, H., Casale, G.R., Goutail, F., Köhler, U., Mendeva,B.T., Werner, R., Josefsson, W., Moore, D., Bartolomé, M.L., Moreta González, J.R., Mišaga, O., Dahlback, A., Tóth, Z., Varghese, S., De Backer, H., Stübi, R. and Vanícek, K.: Response of the ozone column over West Europe to the 2011 Arctic springtime ozone depletion event according to ground-based observations, Atmos. Environ., 2014, 85, 169–178, doi: 10.1016/j.atmosenv.2013.12.005

8. Diémoz, H., Siani, A.M., Redondas, A., Savastiouk, V., McElroy, C.T.: Improved retrieval of nitrogen dioxide (NO_2) column densities by means of MKIV Brewer spectrophotometers, Atmos. Meas. Tech. (submitted)

B.2 Conference proceedings

1. Diémoz, H.: Characterization of MKIV Brewer #066 for NO2 measurements, 13th Biennial WMO-GAW Brewer Users Group Meeting, 12-16 September 2011, Beijing (China) (To be published in a WMO/GAW report)

2. Diémoz, H.: Brewers and NO2: algorithms and calibration issues, 13th Biennial WMO-GAW Brewer Users Group Meeting, 12-16 September 2011, Beijing (China) (To be published in a WMO/GAW report)

3. Diémoz, H., Siani, A. M. and Agnesod G.: Il monitoraggio ambientale della radiazione ultravioletta, Proceedings of Convegno nazionale di radioprotezione (invited talk): Radiazioni naturali e artificiali nell'ambiente, 12-14 October 2011, Reggio Calabria, pp. 36-37, ISBN 978-88-88-648-29-3

4. Casale, G.R., Siani, A.M., Diémoz, H. and Colosimo, A.: Personal exposure studies by means of polysulphone dosimeters, XXV NOG (Nordic Ozone and UV Group Meeting), 8-10 February 2012, Helsinki (Finland)

5. Casale, G.R., Siani, A.M., Diémoz, H., Colosimo, A.: When does the PS horizontal calibration apply to inclined dosimeters?, XXV NOG (Nordic Ozone and UV Group Meeting), 8-10 February 2012, Helsinki (Finland)

6. Diémoz, H. et al.: Primo interconfronto nazionale di radiometri ultravioletti solari, Proceedings of V Convegno nazionale degli agenti fisici: Il controllo degli agenti fisici: ambiente, salute e qualità della vita, 6-8 June 2012, Novara

7. Diémoz, H., Gröbner J. and Hülsen, G.: Tracciabilità delle misure ultraviolette solari presso le stazioni di ARPA Valle d'Aosta, Proceedings of V Convegno nazionale degli agenti fisici: Il controllo degli agenti fisici: ambiente, salute e qualità della vita, 6-8 June 2012, Novara

8. Diémoz, H., Siani, A. M. and Campanelli, M.: Due applicazioni della fotometria solare allo studio della qualità dell'aria: determinazione del diossido d'azoto e delle proprietà ottiche degli aerosol, Processing of V Convegno nazionale degli agenti fisici: Il controllo degli agenti fisici: ambiente, salute e qualità della vita, 6-8 June 2012, Novara

9. Facta, S., Saudino Fusette, S., Bonino, A., Diémoz, H., Anglesio, L. and d'Amore, G.: Caratterizzazione di radiometri ultravioletti solari a banda larga presso il laboratorio di ottica dell'ARPA Piemonte, Proceedings of V Convegno nazionale degli agenti fisici: Il controllo degli agenti fisici: ambiente, salute e qualità della vita, 6-8 June 2012, Novara

10. Petkov, B., Vitale, V., Tomasi, C., Laconelli, C., Diémoz, H., Mazzola, M., Busetto, M. and Lupi, A.: Variazioni dell'ozono colonnare sopra l'Europa occidentale dovute alla deplezione nell'Artico durante la primavera 2011, Proceedings of V Convegno nazionale degli agenti fisici: Il controllo degli agenti fisici: ambiente, salute e qualità della vita, 6-8 June 2012, Novara

11. Siani, A.M., Casale, G. R., Colosimo, A., Diémoz, H. and Agnesod, G.: Quantificazione dell'esposizione personale alla radiazione solare ultravioletta mediante dosimetria a polisolfone, Proceedings of V Convegno nazionale degli agenti fisici: Il controllo degli agenti fisici: ambiente, salute e qualità della vita, 6-8 June 2012, Novara

12. Diémoz, H.: Tecniche di misura della radiazione UV solare, Invited talk at Scuola superiore di radioprotezione Carlo Polvani "Strumenti e metodi di indagine per la valutazione dell'esposizione umana a radiazione ottica non coerente", 14-15 February 2013, Ivrea

13. Diémoz, H. and Campanelli, M.: One year of measurements with a POM02 sun-sky radiometer at an Alpine Euroskyrad station, International SKYNET Workshop 2013, Chiba (Japan)

14. Diémoz, H.: Variazioni nell'irraggiamento solare e possibili impatti, Invited talk, Convegno nazionale AIRM/AIRP "Radiazioni naturali: tra conoscenza e ricerca", 2013, Vulcano

15. Diémoz, H.: Misure di radiazione ultravioletta solare in continuo, Invited talk, Convegno nazionale AIRM/AIRP "Radiazioni naturali: tra conoscenza e ricerca", 2013, Vulcano

16. Casale, G.R., Siani, A.M., Diémoz, H. and Colosimo, A.: Do solar UV daily doses allow water treatment at mediterranean latitudes?, International Conference for Energy and Meteorology (ICEM 2013), 25-28 June 2013, Tolosa

17. Casale, G.R., Siani, A.M., Diémoz, H., Parisi, A.V. and Colosimo, A.: Extreme UV Index and solar exposures at Plateau Rosa (3500 m asl) in Valle d'Aosta region, Italy, Davos Atmosphere and Cryosphere Assembly DACA-13, 8-12 July 2013, Davos (CH)

18. Hülsen, G., Gröbner, J., Diémoz, H., Blumthaler, M., Vuilleumier, L., Sánchez, R. and Ccora, O.: UV measurements at mountain sites, Davos Atmosphere and Cryosphere Assembly DACA-13, 8-12 July 2013, Davos (CH)

19. Facta, S., Saudino Fusette, S., Bonino, A., Diémoz, H., Anglesio, L., d'Amore, G., Hülsen, G. and Gröbner, J.: Characterization of broadband UV radiometers in the Arpa Piedmont Optical Laboratory and intercomparison with the World Calibration Center for UV (WCC-UV), Thematic Network for Ultraviolet Measurement - UVnet, August 27-28, 2013, Davos (CH)

20. Diémoz, H., Siani, A.M., Savastiouk, V., Redondas, A., Eleftheratos, K., Zerefos, C.S., Vrekoussis, M., Casale, G.R., Stanek, M., Burrows, J.P., Richter A. and Hilboll, A.: Improvements to the nitrogen dioxide observations by means of the MKIV Brewer spectrophotometer, 14th WMO-GAW Brewer Users Group Meeting, 24-28 March 2014 Tenerife (ES)

21. Diémoz, H.: Other Brewer measurements: NO_2, Brewer operator course, 24-28 March 2014 Tenerife (ES)

22. Religi, A., Siani, A.M., Casale, G.R., Diémoz, H., Petkov, B.: Trend and variability in total ozone content at three measurement stations in Italy, 14th WMO-GAW Brewer Users Group Meeting, 24-28 March 2014 Tenerife (ES)

23. Casale, G.R., Siani, A.M., Colosimo, A., Diémoz, H.: La radiazione solare ultravioletta alle latitudini del Mediterraneo nel trattamento di acque microbiologicamente contaminate, Convegno Gestione sostenibile del mediterraneo, Accademia nazionale dei Lincei, 21 March 2014

24. Diémoz, H., Eleftheratos, K., Zerefos, C.S., Vrekoussis, M., Siani, A.M., Burrows, J.P., Richter A. and Hilboll, A.: Reprocessing of nitrogen dioxide total column densities recorded with a Brewer spectrophotometer in Athens, The Mediterranean City Conference, 10-11 June 2014, Athens (GR) (submitted)

B.3 Other publications

1. Diémoz, H., Siani, A.M., Casale, G.R., di Sarra, A., Serpillo, B., Petkov, B., Scaglione, S., Bonino, A., Facta, S., Fedele, F., Grifoni, D., Verdi, L. and Zipoli, G.: Risultati della prima campagna di interconfronto italiana di strumentazione per la misura della radiazione ultravioletta solare, Italian Radiation Protection Association bulletin, 2013

2. Casale, G.R., Siani, A.M., Modesti, S., Diémoz, H., Agnesod, G. and Colosimo, A.: Misure mediante dosimetria a polisolfone per la quantificazione dell'esposizione individuale alla radiazione solare ultravioletta, Italian Radiation Protection Association bulletin, 2013

3. Egli, L., Gröbner, J., Shapiro, A., Blumthaler, M. and Diémoz, H.: Development of a new high resolution extraterrestrial spectrum, PMOD/WRC Annual report 2012, printed 2013

Bibliography

Adler-Golden, S. and Slusser, J.: Comparison of plotting methods for solar radiometer calibration, J. Atmos. Ocean. Tech., 24, 935–938, 2007. (Cited on page 99)

Aliwell, S., Van Roozendael, M., Johnston, P., Richter, A., Wagner, T., Arlander, D., Burrows, J., Fish, D., Jones, R., Tørnkvist, K., et al.: Analysis for BrO in zenith-sky spectra: An intercomparison exercise for analysis improvement, J. Geophys. Res., 107, ACH–10, 2002. (Cited on page 82)

Alvarez, R., Weilenmann, M., and Favez, J.-Y.: Real-world NO and NO2 emission factors of modern light vehicles, derived from reliable online measurements, in: Proceedings of the 6th International Conference on Urban Air Quality Limassol, Cyprus, 27-29 March 2007, 2007. (Cited on pages 2, 3, 24, and 26)

Ångström, A.: On the atmospheric transmission of sun radiation and on dust in the air, Geografiska Annaler, 11, 156–166, 1929. (Cited on page 34)

Aquila, V., Oman, L. D., Stolarski, R., Douglass, A. R., and Newman, P. A.: The Response of Ozone and Nitrogen Dioxide to the Eruption of Mt. Pinatubo at Southern and Northern Midlatitudes, J. Atmos. Sci., 70, 894–900, doi:10.1175/JAS-D-12-0143.1, 2013. (Cited on pages 1 and 16)

Arola, A. and Koskela, T.: On the sources of bias in aerosol optical depth retrieval in the UV range, J. Geophys. Res., 109, 2004. (Cited on pages 2, 27, and 120)

Barton, D. V.: The measurement of NO_2 using Brewer spectrophotometers, Master's thesis, York University, Toronto, Ontario, 2007. (Cited on pages 3, 4, 48, 50, 52, 76, 78, 80, 84, 88, 92, 98, 117, and 124)

Bates, D. R. and Hays, P.: Atmospheric nitrous oxide, Planet. Space Sci., 15, 189–197, 1967. (Cited on pages 1 and 10)

Beirle, S., Platt, U., Wenig, M., and Wagner, T.: Weekly cycle of NO2 by GOME measurements: a signature of anthropogenic sources, Atmos. Chem. Phys., 3, 2225–2232, 2003. (Cited on pages 12, 22, and 151)

Beirle, S., Platt, U., Von Glasow, R., Wenig, M., and Wagner, T.: Estimate of nitrogen oxide emissions from shipping by satellite remote sensing, Geophys. Res. Lett., 31, 2004. (Cited on pages 2 and 12)

Bell, J. N. B. and Treshow, M.: Air pollution and plant life, John Wiley & Sons, 2002. (Cited on pages 2 and 26)

BIPM, IEC, IFCC, ILAC, ISO, and IUPAC: Evaluation of Measurement Data – Supplement 1 to the Guide to the Expression of Uncertainty in Measurement – Propagation of distributions using a Monte Carlo method, Joint Committee for Guides in Metrology, JCGM, 101, 2008. (Cited on page 117)

Bodhaine, B. A., Wood, N. B., Dutton, E. G., and Slusser, J. R.: On Rayleigh optical depth calculations, J. Atmos. Ocean. Tech., 16, 1854–1861, 1999. (Cited on pages 32, 82, 83, and 124)

Boersma, K. F.: Error analysis for tropospheric NO2 retrieval from space, J. Geophys. Res., 109, doi:10.1029/2003JD003962, 2004. (Cited on pages 3, 26, and 39)

Bogumil, K., Orphal, J., Homann, T., Voigt, S., Spietz, P., Fleischmann, O., Vogel, A., Hartmann, M., Kromminga, H., Bovensmann, H., et al.: Measurements of molecular absorption spectra with the SCIAMACHY pre-flight model: Instrument characterization and reference data for atmospheric remote-sensing in the 230–2380 nm region, J. Photoch. Photobio. A, 157, 167–184, 2003. (Cited on pages 82, 83, and 121)

Bouguer, P.: Essai d'optique sur la gradation de la lumière, 1729. (Cited on pages 3 and 30)

Bovensmann, H., Burrows, J., Buchwitz, M., Frerick, J., Noël, S., Rozanov, V., Chance, K., and Goede, A.: SCIAMACHY: Mission objectives and measurement modes, J. Atmos. Sci., 56, 127–150, 1999. (Cited on page 178)

Brewer, A.: A replacement for the Dobson spectrophotometer?, Pure Appl. Geophys., 106, 919–927, 1973. (Cited on page 39)

Brewer, A.: The stratospheric circulation: a personal history, in: Brewer-Dobson Workshop, 13-15 December 1999, Oxford, UK, 1999. (Cited on page 12)

Brewer, A. W. and McElroy, C. T.: Nitrogen dioxide concentrations in the atmosphere, Nature, 246, 129–133, 1973. (Cited on pages 2, 9, 37, 41, and 53)

Brinkmann, R.: Rotational Raman scattering in planetary atmospheres, Astrophys. J., 154, 1087, 1968. (Cited on page 35)

Brühl, C. and Crutzen, P. J.: MPIC two-dimensional model, NASA Ref. Publ, 1292, 103–104, 1993. (Cited on pages 10 and 92)

Brunekreef, B. and Holgate, S. T.: Air pollution and health, Lancet, 360, 1233–1242, 2002. (Cited on pages 2 and 25)

Bucsela, E. J., Krotkov, N. A., Celarier, E. A., Lamsal, L. N., Swartz, W. H., Bhartia, P. K., Boersma, K. F., Veefkind, J. P., Gleason, J. F., and Pickering, K. E.: A new stratospheric and tropospheric NO_2 retrieval algorithm for nadir-viewing satellite instruments: applications to OMI, Atmos. Meas. Tech. Discuss., 6, 1361–1407, 2013. (Cited on page 90)

Burrows, J., Dehn, A., Deters, B., Himmelmann, S., Richter, A., Voigt, S., and Orphal, J.: Atmospheric remote-sensing reference data from GOME-2: part 1. Temperature-dependent absorption cross sections of NO2 in the 231–794 nm range, J. Quant. Spectrosc. Ra., 60, 1025–1031, 1998. (Cited on page 121)

Burrows, J., Richter, A., Dehn, A., Deters, B., Himmelmann, S., Voigt, S., and Orphal, J.: Atmospheric remote-sensing reference data from GOME-2. Temperature-dependent absorption cross sections of O3 in the 231–794 nm range, J. Quant. Spectrosc. Ra., 61, 509–517, 1999. (Cited on pages 120 and 178)

Cappellani, F. and Bielli, A.: Correlation between SO2 and NO2 measured in an atmospheric column by a Brewer Spectrophotometer and at ground-level by photochemical techniques, Environ. Monit. Assess., 35, 77–84, 1995. (Cited on pages 4 and 50)

Cappellani, F. and Kochler, C.: Temperature effects correction in a Brewer MKIV spectrophotometer for solar UV measurements, J. Geophys. Res., 105, 4829–4831, 1999. (Cited on page 46)

Castellanos, P. and Boersma, K. F.: Reductions in nitrogen oxides over Europe driven by environmental policy and economic recession, Scientific reports, 2, 2012. (Cited on pages 2 and 24)

Cede, A., Herman, J., Richter, A., Krotkov, N., and Burrows, J.: Measurements of nitrogen dioxide total column amounts using a Brewer double spectrophotometer in direct Sun mode, J. Geophys. Res., 111, doi:10.1029/2005JD006585, 2006a. (Cited on pages 2, 3, 4, 9, 52, 57, 76, 80, and 120)

Cede, A., Kazadzis, S., Kowalewski, M., Bais, A., Kouremeti, N., Blumthaler, M., and Herman, J.: Correction of direct irradiance measurements of Brewer spectrophotometers due to the effect of internal polarization, Geophys. Res. Lett., 33, 2006b. (Cited on pages 41 and 68)

Cede, A. M., Labow, G., Kowalewski, M. G., Krotkov, N. A., and Dubovik, O.: Deriving aerosol parameters from absolute UV sky radiance measurements using a Brewer double spectrometer, in: Optical Science and Technology, SPIE's 48th Annual Meeting, pp. 323–329, International Society for Optics and Photonics, 2003. (Cited on page 120)

Celarier, E. A., Brinksma, E. J., Gleason, J. F., Veefkind, J. P., Cede, A., Herman, J. R., Ionov, D., Goutail, F., Pommereau, J.-P., Lambert, J.-C., van Roozendael, M., Pinardi, G., Wittrock, F., Sch onhardt, A., Richter, A., Ibrahim, O. W., Wagner, T., Bojkov, B., Mount, G., Spinei, E., Chen, C. M., Pongetti, T. J., Sander, S. P., Bucsela, E. J., Wenig, M. O., Swart, D. P. J., Volten, H., Kroon, M., and Levelt, P. F.: Validation of Ozone Monitoring Instrument nitrogen dioxide columns, J. Geophys. Res., 113, doi:10.1029/2007JD008908, 2008. (Cited on pages 4, 52, and 178)

Chance, K. and Kurucz, R.: An improved high-resolution solar reference spectrum for Earth's atmosphere measurements in the ultraviolet, visible, and near infrared, J. Quant. Spectrosc. Ra., 111, 1289–1295, 2010. (Cited on pages 78 and 83)

Chandrasekhar, S.: Radiative transfer, Courier Dover Publications, 1960. (Cited on page 3)

Chapman, S. Q. J. R.: A theory of upper-atmospheric ozone, Edward Stanford, 1930. (Cited on page 14)

Chartrand, D. J., de Grandpré, J., and McConnell, J. C.: An introduction to stratospheric chemistry: Survey article, Atmos. Ocean, 37, 309–367, 1999. (Cited on pages 1, 15, and 16)

Chen, D., Zhou, B., Beirle, S., Chen, L., and Wagner, T.: Tropospheric NO2 column densities deduced from zenith-sky DOAS measurements in Shanghai, China, and their application to satellite validation, Atmos. Chem. Phys., 9, 3641–3662, 2009. (Cited on page 188)

Chiusolo, M., Cadum, E., Stafoggia, M., Galassi, C., Berti, G., Faustini, A., Bisanti, L., Vigotti, M. A., Dessì, M. P., Cernigliaro, A., Mallone, S., Pacelli, B., Minerba, S., Simonato, L., Forastiere, F., and on behalf of the EpiAir Collaborative Group: Short-Term Effects of Nitrogen Dioxide on Mortality and Susceptibility Factors in 10 Italian Cities: The EpiAir Study, Environ. Health Persp., 119, 1233–1238, doi:10.1289/ehp.1002904, 2011. (Cited on pages 2 and 25)

Cook, P. A. and Roscoe, H. K.: Variability and trends in stratospheric NO2 in Antarctic summer, and implications for stratospheric NOy, Atmos. Chem. Phys., 9, 3601–3612, 2009. (Cited on pages 2 and 24)

Coulson, K. L.: Polarization and Intensity of Light in the Atmosphere, A. Deepak Pub., 1988. (Cited on pages 33 and 130)

Crutzen, P. J.: The influence of nitrogen oxides on the atmospheric ozone content, Q. J. Roy. Meteor. Soc., 96, 320–325, 1970. (Cited on pages 1 and 15)

Daniel, F. Y. and Fessler, J. A.: Mean and variance of single photon counting with deadtime, Phys. Med. Biol., 45, 2043, 2000. (Cited on page 43)

Daniel, J., Solomon, S., Miller, H., Langford, A., Portmann, R., and Eubank, C.: Retrieving cloud information from passive measurements of solar radiation absorbed by molecular oxygen and O2-O2, J. Geophys. Res., 108, 4515, 2003. (Cited on pages 88 and 132)

Diémoz, H.: Characterization of MKIV Brewer #066 for NO2 measurements, in: The 13th Biennial WMO Consultation on Brewer Ozone and UV Spectrophotometer Operation, Beijing (China), 2011) (to be published as a WMO report), 2011. (Cited on page 55)

Diémoz, H., Tarricone, C., Agnesod, G., Siani, A. M., and Casale, P.: Brewer #066: a new location in Italy, Edited by CT McElroy and EW Hare. The Tenth Biennial WMO Consultation on Brewer Ozone and UV Spectrophotometer Operation, Calibration and Data Reporting., Gaw Report, 2007. (Cited on page 139)

Diémoz, H., Siani, A. M., Casale, G. R., di Sarra, A., Serpillo, B., Petkov, B., Scaglione, S., Bonino, A., Facta, S., Fedele, F., Grifoni, D., Verdi, L., and Zipoli, G.: First national intercomparison of solar ultraviolet radiometers in Italy, Atmos. Meas. Tech., 4, 1689–1703, 2011. (Cited on pages 61 and 64)

Diémoz, H., Siani, A. M., and Savastiouk, V.: Capability and limitations in measuring atmospheric nitrogen dioxide column amounts by means of the MKIV Brewer spectrophotometers, Proceedings SPIE, 2013. (Cited on page 73)

Dieudonné, E., Ravetta, F., Pelon, J., Goutail, F., and Pommereau, J.-P.: Linking NO2 surface concentration and integrated content in the urban developed atmospheric boundary layer, Geophys. Res. Lett., 2013. (Cited on pages 3 and 26)

Dirksen, R. J., Boersma, K. F., Eskes, H. J., Ionov, D. V., Bucsela, E. J., Levelt, P. F., and Kelder, H. M.: Evaluation of stratospheric NO2 retrieved from the Ozone Monitoring Instrument: Intercomparison, diurnal cycle, and trending, J. Geophys. Res., 116, doi:10.1029/2010JD014943, 2011. (Cited on pages 2, 11, and 23)

Elokhov, A. S. and Gruzdev, A. N.: Estimation of tropospheric and stratospheric NO2 from spectrometric measurements of column NO2 abundances, in: European Symposium on Optics for Environmental and Public Safety, pp. 444–454, 1995. (Cited on pages 2 and 9)

Environment Canada: Standard operating procedures manual for the Brewer spectrophotometer, version: D.01, 2008. (Cited on page 40)

Evans, W. F. J., Kerr, J. B., Wardle, D. I., McConnell, J. C., Ridley, B. A., and Schiff, H. I.: Intercomparison of NO, NO2 and HNO3 measurements with photochemical theory, Atmosphere, 14, 189–198, 1976. (Cited on page 21)

Eyring, V., Köhler, H. W., Van Aardenne, J., and Lauer, A.: Emissions from international shipping: 1. The last 50 years, J. Geophys. Res., 110, 2005. (Cited on pages 2 and 12)

Fastie, W. G.: A small plane grating monochromator, J. Opt. Soc. Am., 42, 641–647, 1952. (Cited on page 41)

Feng, W., Chipperfield, M. P., Davies, S., Mann, G. W., Carslaw, K. S., Dhomse, S., Harvey, L., Randall, C., and Santee, M. L.: Modelling the effect of denitrification on polar ozone depletion for Arctic winter 2004/2005, Atmos. Chem. Phys., 11, 6559–6573, doi:10.5194/acp-11-6559-2011, 2011. (Cited on pages 1 and 16)

Ferm, M., De Santis, F., and Varotsos, C.: Nitric acid measurements in connection with corrosion studies, Atmos. Environ., 39, 6664–6672, 2005. (Cited on pages 2 and 26)

Finzi, G., Pirovano, G., and Volta, M.: Gestione della qualità dell'aria. Modelli di simulazione e previsione, McGraw-Hill, 2001. (Cited on pages 2 and 25)

Fioletov, V. E., Kerr, J. B., Wardle, D. I., and Wu, E.: Correction of stray light for the Brewer single monochromator, in: Proc. Quadrennial Ozone Symposium, pp. 369–37, 2000. (Cited on page 40)

Fish, D. J., Roscoe, H. K., and Johnston, P. V.: Possible causes of stratospheric NO2 trends observed at Lauder, New Zealand, Geophys. Res. Lett., 27, 3313–3316, 2000. (Cited on pages 3 and 23)

Francesconi, M., Casale, G., Siani, A., and Casadio, S.: Ground-based NO2 measurements at the Italian Brewer stations: a pilot study with Global Ozone Monitoring Experiment (GOME), Nuovo Cimento C Geophysics Space Physics C, 27, 383, 2004. (Cited on pages 3, 4, 51, 153, and 156)

Garcia, R. R. and Solomon, S.: A new numerical model of the middle atmosphere: 2. Ozone and related species, J. Geophys. Res., 99, 12 937–12 951, 1994. (Cited on pages 1 and 14)

Gianelli, S. M.: Aerosol retrievals using rotating shadowband spectroradiometer data, J. Geophys. Res., 110, doi:10.1029/2004JD005329, 2005. (Cited on pages 2 and 27)

Gil, M., Yela, M., Navarro, M., and Cuevas, E.: NO_2 diurnal variability at Izaña Observatory, Tech. rep., 2003. (Cited on page 22)

Gil, M., Yela, M., Gunn, L. N., Richter, A., Alonso, I., Chipperfield, M. P., Cuevas, E., Iglesias, J., Navarro, M., and Puentedura, O.: NO2 climatology in the northern subtropical region: diurnal, seasonal and interannual variability, Atmos. Chem. Phys., 8, 1635–1648, 2008. (Cited on pages 2, 15, 23, 102, 105, and 112)

Goutail, F., Pommereau, J. P., Sarkissian, A., Kyro, E., and Dorokhov, V.: Total nitrogen dioxide at the Arctic polar circle since 1990, Geophys. Res. Lett., 21, 1371–1374, 1994. (Cited on pages 1 and 15)

Grainger, J. and Ring, J.: Anomalous Fraunhofer line profiles, Nature, 193, 762, 1962. (Cited on page 35)

Greenblatt, G. D., Orlando, J. J., Burkholder, J. B., and Ravishankara, A. R.: Absorption measurements of oxygen between 330 and 1140 nm, J. Geophys. Res., 95, 18 577–18 582, 1990. (Cited on pages 52, 82, and 122)

Gröbner, J.: Brewer accuracy, private correspondence, 1998. (Cited on page 120)

Gröbner, J. and Meleti, C.: Aerosol optical depth in the UVB and visible wavelength range from Brewer spectrophotometer direct irradiance measurements: 1991–2002, J. Geophys. Res., 109, D09 202, 2004. (Cited on page 188)

Gröbner, J., Wardle, D. I., McElroy, C. T., and Kerr, J. B.: Investigation of the wavelength accuracy of Brewer spectrophotometers, Appl. Optics, 37, 8352–8360, 1998. (Cited on pages 44, 57, 60, and 83)

Gruzdev, A. and Elokhov, A.: Variability of stratospheric and tropospheric nitrogen dioxide observed by the visible spectrophotometer at Zvenigorod, Russia, Int. J. Remote Sens., 32, 3115–3127, 2011. (Cited on page 106)

Gruzdev, A. N. and Elokhov, A. S.: Validating NO2 measurements in the vertical atmospheric column with the OMI instrument aboard the EOS Aura satellite against ground-based measurements at the Zvenigorod Scientific Station, Izv. Atmos. Ocean. Phys., 45, 444–455, doi:10.1134/S0001433809040057, 2009. (Cited on pages 2, 23, and 188)

Gum, I.: Guide to the expression of uncertainty in measurement, BIPM and IEC and IFCC and ISO and IUPAP and IUPAC and OIML, 1995. (Cited on pages 117 and 118)

Guo, X., Natraj, V., Feldman, D. R., Spurr, R. J., Shia, R.-L., Sander, S. P., and Yung, Y. L.: Retrieval of ozone profile from ground-based measurements with polarization: A synthetic study, J. Quant. Spectrosc. Ra., 103, 175–192, 2007. (Cited on page 188)

Haagen-Smit, A. J.: Chemistry and physiology of Los Angeles smog, Ind. Eng. Chem., 44, 1342–1346, 1952. (Cited on pages 1 and 17)

Harrison, L. and Michalsky, J.: Objective algorithms for the retrieval of optical depths from ground-based measurements, Appl. Optics, 33, 5126–5132, 1994. (Cited on pages 98 and 106)

Hayn, M., Beirle, S., Hamprecht, F. A., Platt, U., Menze, B. H., and Wagner, T.: Analysing spatio-temporal patterns of the global NO2-distribution retrieved from GOME satellite observations using a generalized additive model, Atmos. Chem. Phys., 9, 6459–6477, 2009. (Cited on pages 2, 9, 12, 22, and 24)

Hendrick, F., Mahieu, E., Bodeker, G. E., Boersma, K. F., Chipperfield, M. P., De Mazière, M., De Smedt, I., Demoulin, P., Fayt, C., Hermans, C., Kreher, K., Lejeune, B., Pinardi, G., Servais, C., St ubi, R., van der A, R., Vernier, J.-P., and Van Roozendael, M.: Analysis of stratospheric NO2 trends above Jungfraujoch using ground-based UV-visible, FTIR, and satellite nadir observations, Atmos. Chem. Phys., 12. (Cited on pages 2 and 24)

Herman, J., Cede, A., Spinei, E., Mount, G., Tzortziou, M., and Abuhassan, N.: NO2 column amounts from ground-based Pandora and MFDOAS spectrometers using the direct-sun DOAS technique: Intercomparisons and application to OMI validation, J. Geophys. Res., 114, doi: 10.1029/2009JD011848, 2009. (Cited on pages 5, 10, 26, 137, 138, and 142)

Hermans, C., Vandaele, A., Fally, S., Carleer, M., Colin, R., Coquart, B., Jenouvrier, A., and Merienne, M.-F.: Absorption cross-section of the collision-induced bands of oxygen from the UV to the NIR, in: Weakly interacting molecular pairs: unconventional absorbers of radiation in the atmosphere, pp. 193–202, Springer, 2003. (Cited on pages 82, 83, and 122)

Hilboll, A., Richter, A., and Burrows, J. P.: Long-term changes of tropospheric NO2 over megacities derived from multiple satellite instruments, Atmos. Chem. Phys., 13, 4145–4169, doi:10.5194/acp-13-4145-2013, 2013. (Cited on pages 2, 3, 24, 25, 39, and 179)

Hofmann, D., Bonasoni, P., De Maziere, M., Evangelisti, F., Giovanelli, G., Goldman, A., Goutail, F., Harder, J., Jakoubek, R., Johnston, P., et al.: Intercomparison of UV/visible spectrometers for measurements of stratospheric NO2 for the Network for the Detection of Stratospheric Change, J. Geophys. Res., 100, 16 765–16 791, 1995. (Cited on pages 4 and 50)

Hönninger, G., Von Friedeburg, C., Platt, U., et al.: Multi axis differential optical absorption spectroscopy (MAX-DOAS), Atmos. Chem. Phys., 4, 231–254, 2004. (Cited on pages 2 and 37)

Houghton, J. T., Ding, Y., Griggs, D. J., Noguer, M., van der LINDEN, P. J., Dai, X., Maskell, K., and Johnson, C.: Climate change 2001: the scientific basis, vol. 881, Cambridge University Press Cambridge, 2001. (Cited on pages 2, 12, and 25)

International Ozone Services Inc., .: IOS website, URL `http://www.io3.ca/`, 2013. (Cited on page 57)

Iqbal, M.: An introduction to solar radiation, Academic Press, Orlando, FL, 1983. (Cited on page 34)

Jiang, Y., Yung, Y. L., and Sander, S. P.: Detection of tropospheric ozone by remote sensing from the ground, J. Quant. Spectrosc. Ra., 57, 811–818, 1997. (Cited on page 188)

Jiang, Y., Yung, Y. L., Sander, S. P., and Travis, L. D.: Modeling of atmospheric radiative transfer with polarization and its application to the remote sensing of tropospheric ozone, J. Quant. Spectrosc. Ra., 84, 169–179, 2004. (Cited on page 188)

Johnston, H. S. and Graham, P.: Unpublished absorption coefficients on NO_2 and O_3, dept. of Chem., University of California, Berkeley, 1976. (Cited on pages 4, 47, 51, and 83)

Johnston, J., Kerr, J., McElroy, C., and Wardle, D.: Aberration correction in the Brewer spectrophotometer, Radiat. Prot. Dosim., 91, 133–138, 2000. (Cited on pages 42 and 61)

Kerr, J.: Ground-based measurements of nitrogen dioxide using the Brewer spectrophotometer, in: Ozone in the Atmosphere, vol. 1, p. 340, 1989. (Cited on pages 3, 4, 40, 46, 47, 83, 88, and 124)

Kerr, J.: New methodology for deriving total ozone and other atmospheric variables from Brewer spectrophotometer direct sun spectra, J. Geophys. Res., 107, ACH–22, 2002. (Cited on pages 4, 53, and 80)

Kerr, J., McElroy, C., and Evans, W.: The automated Brewer spectrophotometer for measurement of SO2, O3, and aerosols, in: Proceedings of the WMO/AMS/CMOS Symposium on Meteorological Observations and Instrumentation, pp. 470–472, 1983. (Cited on pages 3 and 39)

Kerr, J., McElroy, C., Wardle, D., Olafson, R., and Evans, W.: The automated Brewer spectrophotometer, in: Atmospheric Ozone, pp. 396–401, Springer, 1985. (Cited on pages 3 and 39)

Kerr, J. B. and Davis, J. M.: New methodology applied to deriving total ozone and other atmospheric variables from global irradiance spectra, J. Geophys. Res., 112, 2007. (Cited on pages 4, 53, and 120)

Kerr, J. B., Evans, W. F. J., and McConnell, J. C.: The effects of NO2 changes at twilight on tangent ray NO2 measurements, Geophys. Res. Lett., 4, 577–579, 1977. (Cited on pages 2, 9, and 15)

Kiedron, P.: Counts normalization and corrections and Poisson noise in and from CI, XL and UV files, Tech. rep., NOAA, 2007. (Cited on page 75)

Kim, S.-W., Heckel, A., McKeen, S. A., Frost, G. J., Hsie, E.-Y., Trainer, M. K., Richter, A., Burrows, J. P., Peckham, S. E., and Grell, G. A.: Satellite-observed US power plant NOx emission reductions and their impact on air quality, Geophys. Res. Lett., 33, 2006. (Cited on pages 2 and 12)

Kipp & Zonen: MKIV Brewer spectrophotometer - Instruction manual, 2007. (Cited on pages 41, 42, and 46)

Kipp & Zonen: Kipp & Zonen e-news February 2012, 2012. (Cited on page 40)

Kokhanovsky, A. A., Budak, V. P., Cornet, C., Duan, M., Emde, C., Katsev, I. L., Klyukov, D. A., Korkin, S. V., et al.: Benchmark results in vector atmospheric radiative transfer, J. Quant. Spectrosc. Ra., 111, 1931–1946, 2010. (Cited on page 92)

Krotkov, N. A., Herman, J. R., Cede, A., and Labow, G.: Partitioning between aerosol and NO2 absorption in the UV spectral region, pp. 588 601–588 601–8, doi:10.1117/12.615285, 2005. (Cited on pages 2 and 27)

Krug, E. C. and Frink, C. R.: Acid rain on acid soil: A new perspective., Science, 217, 520–525, 1983. (Cited on page 2)

Kuester, M. A., Thome, K. J., and Reagan, J. A.: Automated statistical approach to Langley evaluation for a solar radiometer, Appl. optics, 42, 4914–4921, 2003. (Cited on page 98)

Kylling, A., Mayer, B., and Blumthaler, M.: Technical Note: A new discrete ordinate first-order rotational Raman scattering radiative transfer model–implementation and first results, Atmos. Chem. Phys., 11, 10 471–10 485, 2011. (Cited on pages 78 and 92)

Langley, S. P.: The bolometer and radiant energy, in: Proceedings of the American Academy of Arts and Sciences, vol. 16, pp. 342–358, JSTOR, 1880. (Cited on pages 3 and 98)

Latza, U., Gerdes, S., and Baur, X.: Effects of nitrogen dioxide on human health: Systematic review of experimental and epidemiological studies conducted between 2002 and 2006, Int. J. Hyg. Envir. Heal., 212, 271–287, doi:10.1016/j.ijheh.2008.06.003, 2009. (Cited on pages 2 and 25)

Lee, A.: Improvements to the accuracy of measurements of NO2 by zenith-sky visible spectrometers, J. Quant. Spectrosc. Ra., 52, 649–657, 1994. (Cited on pages 1, 105, and 106)

Lee, D. S., Köhler, I., Grobler, E., Rohrer, F., Sausen, R., Gallardo-Klenner, L., Olivier, J. G. J., Dentener, F. J., and Bouwman, A. F.: Estimations of global NO, emissions and their uncertainties, Atmos. Environ., 31, 1735–1749, 1997. (Cited on pages 2 and 10)

Leighton, P. A.: Photochemistry of air pollution, 1961. (Cited on pages 1 and 17)

Leitao, J., Richter, A., Vrekoussis, M., Kokhanovsky, A., Zhang, Q., Beekmann, M., and Burrows, J.: On the improvement of NO2 satellite retrievals-aerosol impact on the airmass factors, Atmos. Meas. Tech., 3, 475–493, 2010. (Cited on pages 3, 26, and 39)

Lelieveld, J., Berresheim, H., Borrmann, S., Crutzen, P. J., Dentener, F. J., Fischer, H., Feichter, J., Flatau, P. J., Heland, J., Holzinger, R., et al.: Global air pollution crossroads over the Mediterranean, Science, 298, 794–799, 2002. (Cited on pages 2 and 14)

Lerdau, M. T.: The NO2 Flux Conundrum, Science, 289, 2291–2293, doi:10.1126/science.289.5488.2291, 2000. (Cited on pages 2, 3, 12, and 26)

Leue, C., Wenig, M., Wagner, T., Klimm, O., Platt, U., and J ahne, B.: Quantitative analysis of NOx emissions from Global Ozone Monitoring Experiment satellite image sequences, J. Geophys. Res., 106, 5493–5505, 2001. (Cited on page 12)

Levelt, P. F., van den Oord, G. H., Dobber, M. R., Malkki, A., Visser, H., de Vries, J., Stammes, P., Lundell, J. O., and Saari, H.: The ozone monitoring instrument, Geoscience and Remote Sensing, IEEE Transactions on, 44, 1093–1101, 2006. (Cited on page 178)

Liley, J. B., Johnston, P. V., McKenzie, R. L., Thomas, A. J., and Boyd, I. S.: Stratospheric NO2 variations from a long time series at Lauder, New Zealand, J. Geophys. Res., 105, 11 633–11 640, doi:10.1029/1999JD901157, 2000. (Cited on pages 2, 3, and 23)

Liu, X., Zhang, Y., Han, W., Tang, A., Shen, J., Cui, Z., Vitousek, P., Erisman, J. W., Goulding, K., Christie, P., et al.: Enhanced nitrogen deposition over China, Nature, 2013. (Cited on pages 2 and 24)

Lövblad, G., Tarrasón, L., Tørseth, K., and Dutchak, S.: EMEP assessment part I European perspective, URL: http://www.emep.int, The Norwegian Meteorological Institute, Oslo, Norway, 2004. (Cited on pages 2 and 24)

Ma, J. Z., Beirle, S., Jin, J. L., Shaiganfar, R., Yan, P., and Wagner, T.: Tropospheric NO_2 vertical column densities over Beijing: results of the first three years of ground-based MAX-DOAS measurements (2008–2011) and satellite validation, Atmos. Chem. Phys., 13, 1547–1567, doi:10.5194/acp-13-1547-2013, 2013. (Cited on pages 2 and 22)

Marenco, F.: On Langley plots in the presence of a systematic diurnal aerosol cycle centered at noon: A comment on recently proposed methodologies, J. Geophys. Res., 112, D06 205, 2007. (Cited on page 98)

Martin, R. V., Parrish, D. D., Ryerson, T. B., Nicks, D. K., Chance, K., Kurosu, T. P., Jacob, D. J., Sturges, E. D., Fried, A., and Wert, B. P.: Evaluation of GOME satellite measurements of tropospheric NO2 and HCHO using regional data from aircraft campaigns in the southeastern United States, J. Geophys. Res., 109, 2004. (Cited on pages 2 and 9)

Martin, R. V., Sioris, C. E., Chance, K., Ryerson, T. B., Bertram, T. H., Wooldridge, P. J., Cohen, R. C., Neuman, J. A., Swanson, A., and Flocke, F. M.: Evaluation of space-based constraints on global nitrogen oxide emissions with regional aircraft measurements over and downwind of eastern North America, J. Geophys. Res., 111, 2006. (Cited on pages 1 and 10)

Mayer, B. and Kylling, A.: Technical note: The libRadtran software package for radiative transfer calculations - description and examples of use, Atmos. Chem. Phys., 5, 1855–1877, 2005. (Cited on page 92)

Mayer, B., Kylling, A., Emde, C., Hamann, U., and Buras, R.: libRadtran user's guide, Tech. rep., 2012. (Cited on pages 3, 31, and 35)

McElroy, C., Elokhov, A., Elansky, N., Frank, H., Johnston, P., and Kerr, J.: Visible light nitrogen dioxide spectrophotometer intercomparison: Mount Kobau, British Columbia, July 28 to August 10, 1991, NASA. Goddard Space Flight Center, Ozone in the Troposphere and Stratosphere, Part 2 p 663-666 (SEE N 95-11006 01-47), 1994. (Cited on pages 4 and 50)

McKenzie, R. and Johnston, P.: Seasonal variations in stratospheric NO2 at 45 S, Geophys. Res. Lett., 9, 1255–1258, 1982. (Cited on pages 2 and 38)

McKenzie, R. L., Johnston, P. V., McElroy, C. T., Kerr, J. B., and Solomon, S.: Altitude distributions of stratospheric constituents from ground-based measurements at twilight, J. Geophys. Res., 96, 15 499–15 511, doi:10.1029/91JD01361, 1991. (Cited on pages 2 and 22)

McLinden, C., McElroy, C., Savastiouk, V., Kerr, J., and Wardle, D.: Absolute Brewer Zenith-sky Radiance and Polarization Measurements with Application to the Retrieval of Aerosol Properties, in: AGU Fall Meeting Abstracts, vol. 1, p. 0073, 2001a. (Cited on page 130)

McLinden, C. A., Olsen, S. C., Prather, M. J., and Liley, J. B.: Understanding trends in stratospheric NOy and NO2, J. Geophys. Res., 106, 27 787–27, 2001b. (Cited on pages 2 and 23)

Meltzer, R., Wilson, A., Kohn, B., and Rives, J.: Temperature dependence of the spectral response for the MKIV Brewers in the UGA/USEPA network, in: 6th Brewer Workshop, Tokyo, Japan, vol. 10, p. 12, 2000. (Cited on pages 46 and 69)

Mendolia, D., D'Souza, R. J. C., Evans, G. J., and Brook, J.: Impact of NO_2 horizontal heterogeneity on tropospheric NO_2 vertical columns retrieved from satellite, multi-axis differential optical absorption spectroscopy, and in situ measurements, Atmos. Meas. Tech. Discuss., 6, 825–866, doi:10.5194/amtd-6-825-2013, 2013. (Cited on pages 1, 3, 10, 18, 22, and 151)

Meyer, C.: Matrix analysis and applied linear algebra, vol. 2, Siam, 2000. (Cited on page 80)

Miyazaki, K., Eskes, H. J., and Sudo, K.: Global NO_x emission estimates derived from an assimilation of OMI tropospheric NO_2 columns, Atmos. Chem. Phys., 12, 2263–2288, doi:10.5194/acp-12-2263-2012, 2012. (Cited on pages 3 and 26)

Monks, P. S.: Gas-phase radical chemistry in the troposphere, Chem. Soc. Rev., 34, 376, doi:10.1039/b307982c, 2005. (Cited on pages 1, 16, 18, 20, and 21)

NASA, U. and USAF, U.: Standard Atmosphere Supplements, US Government Printing Office, Washington, DC, 1976. (Cited on pages 8 and 76)

NDACC: NDACC Protocols, Appendix VII - UV/Vis Instruments, URL `http://www.ndsc.ncep.noaa.gov/organize/protocols/appendix7/`, 2013. (Cited on page 129)

NIST: Atomic Spectra Database Version 5, URL `http://www.nist.gov/pml/data/asd.cfm`. (Cited on page 57)

Noel, S., Bovensmann, H., Burrows, J., Frerick, J., Chance, K., and Goede, A.: Global atmospheric monitoring with SCIAMACHY, Phys. Chem. Earth, 24, 427–434, 1999. (Cited on page 178)

Noxon, J. F.: Nitrogen dioxide in the stratosphere and troposphere measured by ground-based absorption spectroscopy, Science, 189, 547–549, 1975. (Cited on pages 2 and 37)

Noxon, J. F.: Stratospheric NO2: 2. Global behavior, J. Geophys. Res., 84, 5067–5076, doi:10.1029/JC084iC08p05067, 1979. (Cited on pages 2, 10, 11, 20, and 22)

Noxon, J. F., Whipple, E. C., and Hyde, R. S.: Stratospheric NO2: 1. Observational method and behavior at mid-latitude, J. Geophys. Res., 84, 5047–5065, 1979. (Cited on page 12)

Odén, S.: The acidification of air and precipitation and its consequences on the natural environment, State National Science Research Council, 1968. (Cited on page 2)

Olivier, J. G. J., Van Aardenne, J. A., Dentener, F., Ganzeveld, L., Peters, J. A. H. W., et al.: Recent trends in global greenhouse gas emissions: regional trends and spatial distribution of key sources, Non-CO2 Greenhouse Gases (NCGG-4), 90, 043, 2005. (Cited on pages 2 and 12)

Ordónez, C., Richter, A., Steinbacher, M., Zellweger, C., Nüß, H., Burrows, J. P., and Prévôt, A. S. H.: Comparison of 7 years of satellite-borne and ground-based tropospheric NO2 measurements around Milan, Italy, J. Geophys. Res., 111, 2006. (Cited on pages 2, 3, 9, 22, and 26)

Orphal, J.: A critical review of the absorption cross-sections of O3 and NO2 in the ultraviolet and visible, J. Photoch. Photobio. A, 157, 185–209, doi:10.1016/S1010-6030(03)00061-3, 2003. (Cited on pages 51, 57, 120, and 121)

Penndorf, R.: Tables of the refractive index for standard air and the Rayleigh scattering coefficient for the spectral region between 0.2 and 20.0 μm and their application to atmospheric optics, J. Opt. Soc. Am., 47, 176–182, 1957. (Cited on page 32)

Peters, E., Wittrock, F., Großmann, K., Frieß, U., Richter, A., and Burrows, J.: Formaldehyde and nitrogen dioxide over the remote western Pacific Ocean: SCIAMACHY and GOME-2 validation using ship-based MAX-DOAS observations, Atmos. Chem. Phys., 12, 11 179–11 197, 2012. (Cited on page 112)

Petritoli, A., Bonasoni, P., Giovanelli, G., Ravegnani, F., Kostadinov, I., Bortoli, D., Weiss, A., Schaub, D., Richter, A., and Fortezza, F.: First comparison between ground-based and satellite-borne measurements of tropospheric nitrogen dioxide in the Po basin, J. Geophys. Res., 109, 2004. (Cited on pages 2 and 14)

Pinheiro, D. K.: Estudo do comportamento do dióxido de nitrogênio atmosférico com base nos dados do espectrofotômetro Brewer, Ph.D. thesis, São José dos Campos: INPE, INPE-10017-TDI/881, 2003. (Cited on pages 3, 4, 50, and 52)

Piters, A., Boersma, K., Kroon, M., Hains, J., Van Roozendael, M., Wittrock, F., Abuhassan, N., Adams, C., Akrami, M., Allaart, M., et al.: The Cabauw Intercomparison campaign for Nitrogen Dioxide measuring Instruments (CINDI): design, execution, and early results, Atmos. Meas. Tech., 5, 457–485, 2012. (Cited on page 129)

Platt, U. and Stutz, J.: Differential optical absorption spectroscopy, Springer, 2008. (Cited on pages 2, 26, 38, and 82)

Pommereau, J.: Observation of NO2 diurnal variation in the stratosphere, Geophys. Res. Lett., 9, 850–853, 1982. (Cited on page 38)

Pommereau, J. P. and Goutail, F.: O3 and NO2 ground-based measurements by visible spectrometry during Arctic winter and spring 1988, Geophys. Res. Lett., 15, 891–894, 1988. (Cited on pages 2 and 38)

Priestley, J.: Experiments and observations on different kinds of air, vol. 1, J. Johnson, 1775. (Cited on pages 1 and 7)

Rayleigh, J. W. S.: On the transmission of light through an atmosphere containing small particles in suspension, and on the origin of the blue of the sky, The London, Edinburgh, and Dublin Philosophical Magazine and Journal of Science, 47, 375–384, 1899. (Cited on pages 3 and 32)

Redondas, A.: Ozone absolute Langley calibration, Edited by CT McElroy and EW Hare. The Tenth Biennial WMO Consultation on Brewer Ozone and UV Spectrophotometer Operation, Calibration and Data Reporting., Gaw Report, pp. 12–14, 2007. (Cited on page 98)

Redondas, A. and Cede, A.: Brewer algorithm sensitivity analysis, Edited by CT McElroy and EW Hare. The Tenth Biennial WMO Consultation on Brewer Ozone and UV Spectrophotometer Operation, Calibration and Data Reporting., Gaw Report, pp. 12–14, 2007. (Cited on page 121)

Richter, A., Burrows, J. P., N uß, H., Granier, C., and Niemeier, U.: Increase in tropospheric nitrogen dioxide over China observed from space, Nature, 437, 129–132, doi:10.1038/nature04092, 2005. (Cited on pages 2 and 24)

Rinsland, C. P., Weisenstein, D. K., Ko, M. K. W., Scott, C. J., Chiou, L. S., Mahieu, E., Zander, R., and Demoulin, P.: Post-Mount Pinatubo eruption ground-based infrared stratospheric column measurements of HNO3, NO, and NO2 and their comparison with model calculations, J. Geophys. Res., 108, 4437, 2003. (Cited on pages 2 and 23)

Rodgers, C. D.: Inverse methods for atmospheric sounding: Theory and Practice, Series on Atmospheric, Oceanic and Planetary Physics–Vol. 2, World Scientific, 2000. (Cited on page 188)

Roscoe, H., Charlton, A. J., Fish, D. J., and Hill, J. G.: Improvements to the accuracy of measurements of NO2 by zenith-sky visible spectrometers II: errors in zero using a more complete chemical model, J. Quant. Spectrosc. Ra., 68, 337–349, 2001. (Cited on page 105)

Roscoe, H. K., Van Roozendael, M., Fayt, C., du Piesanie, A., Abuhassan, N., Adams, C., Akrami, M., Cede, A., Chong, J., Clémer, K., Friess, U., Gil Ojeda, M., Goutail, F., Graves, R., Griesfeller, A., Grossmann, K., Hemerijckx, G., Hendrick, F., Herman, J., Hermans, C., Irie, H., Johnston, P. V., Kanaya, Y., Kreher, K., Leigh, R., Merlaud, A., Mount, G. H., Navarro, M., Oetjen, H., Pazmino, A., Perez-Camacho, M., Peters, E., Pinardi, G., Puentedura, O., Richter, A., Schönhardt, A., Shaiganfar, R., Spinei, E., Strong, K., Takashima, H., Vlemmix, T., Vrekoussis, M., Wagner, T., Wittrock, F., Yela, M., Yilmaz, S., Boersma, F., Hains, J., Kroon, M., Piters, A., and Kim, Y. J.: Intercomparison of slant column measurements of NO_2 and O_4 by MAX-DOAS and zenith-sky UV and visible spectrometers, Atmos. Meas. Tech., 3, 1629–1646, 2010. (Cited on page 129)

Rothman, L. S., Gordon, I. E., Barbe, A., Benner, D. C., Bernath, P. F., Birk, M., Boudon, V., Brown, L. R., Campargue, A., Champion, J.-P., et al.: The HITRAN 2008 molecular spectroscopic database, J. Quant. Spectrosc. Ra., 110, 533–572, 2009. (Cited on page 82)

Rozanov, V., Rozanov, A., Kokhanovsky, A., and Burrows, J.: Radiative transfer through terrestrial atmosphere and ocean: Software package SCIATRAN, J. Quant. Spectrosc. Ra., 133, 13 – 71, 2014. (Cited on pages 3 and 92)

Russell, A. R., Valin, L. C., and Cohen, R. C.: Trends in OMI NO2 observations over the United States: effects of emission control technology and the economic recession, Atmos. Chem. Phys., 12, 12 197–12 209, doi:10.5194/acp-12-12197-2012, 2012. (Cited on pages 2 and 24)

Samoli, E.: Short-term effects of nitrogen dioxide on mortality: an analysis within the APHEA project, Eur. Respir. J., 27, 1129–1138, doi:10.1183/09031936.06.00143905, 2006. (Cited on pages 2 and 25)

Sanders, R.: Improved analysis of atmospheric absorption spectra by including the temperature dependence of NO2, J. Geophys. Res., 101, 20 945–20, 1996. (Cited on page 78)

Savastiouk, V.: Improvements to the direct-sun ozone observations taken with the Brewer spectrophotometer, Ph.D. thesis, 2005. (Cited on pages 4, 37, 45, 51, 53, 64, and 92)

Schafer, K., Vergeiner, J., Emeis, S., Wittig, J., Hoffmann, M., Obleitner, F., and Suppan, P.: Atmospheric influences and local variability of air pollution close to a motorway in an Alpine valley during winter, Meteorol. Z., 17, 297–309, 2008. (Cited on pages 3 and 26)

Schneider, P. and van der A, R. J.: A global single-sensor analysis of 2002–2011 tropospheric nitrogen dioxide trends observed from space, J. Geophys. Res., 117, doi:10.1029/2012JD017571, 2012. (Cited on pages 2, 24, and 178)

Schofield, R., Connor, B., Kreher, K., Johnston, P., and Rodgers, C.: The retrieval of profile and chemical information from ground-based UV-visible spectroscopic measurements, J. Quant. Spectrosc. Ra., 86, 115–131, 2004. (Cited on pages 2, 37, 105, and 188)

Schreier, F. and García, S. G.: Py4CAtS–Python tools for line-by-line modelling of infrared atmospheric radiative transfer, in: AIP Conference Proceedings, vol. 1531, p. 123, 2013. (Cited on page 82)

Schroeder, R. and Davies, J.: Significance of nitrogen dioxide absorption in estimating aerosol optical depth and size distributions, Atmos. Ocean, 25, 107–114, doi:10.1080/07055900.1987.9649266, 1987. (Cited on pages 2 and 27)

Schumann, U. and Huntrieser, H.: The global lightning-induced nitrogen oxides source, Atmos. Chem. Phys., 7, 3823–3907, 2007. (Cited on pages 2, 10, and 13)

Schuster, A.: Radiation through a foggy atmosphere, Astrophys. J., 21, 1, 1905. (Cited on page 3)

Seinfeld, J. H.: Atmospheric chemistry and physics of air pollution, John Wiley and sons, 1986. (Cited on pages 1 and 15)

Shaw, G. E.: Nitrogen dioxide–Optical absorption in the visible, J. Geophys. Res., 81, 5791–5792, 1976. (Cited on pages 2 and 27)

Slaper, H., Reinen, H., Blumthaler, M., Huber, M., and Kuik, F.: Comparing ground-level spectrally resolved solar UV measurements using various instruments: A technique resolving effects of wavelength shift and slit width, Geophys. Res. Lett., 22, 2721–2724, 1995. (Cited on page 61)

Slusser, J., Gibson, J., Bigelow, D., Kolinski, D., Disterhoft, P., Lantz, K., and Beaubien, A.: Langley method of calibrating UV filter radiometers, J. Geophys. Res., 105, 4841–4849, 2000. (Cited on page 98)

Smith, R. A.: Air and rain: the beginnings of a chemical climatology, Longmans, Green, 1872. (Cited on page 2)

Solomon, S., Schmeltekopf, A. L., and Sanders, R. W.: On the interpretation of zenith sky absorption measurements, J. Geophys. Res., 92, 8311–8319, 1987. (Cited on pages 3, 37, and 38)

Solomon, S., Portmann, R., Sanders, R., Daniel, J., Madsen, W., Bartram, B., and Dutton, E.: On the role of nitrogen dioxide in the absorption of solar radiation, J. Geophys. Res., 104, 12 047–12 058, 1999. (Cited on pages 2 and 25)

Steinbacher, M., Zellweger, C., Schwarzenbach, B., Bugmann, S., Buchmann, B., Ordónez, C., Prevot, A., and Hueglin, C.: Nitrogen oxide measurements at rural sites in Switzerland: Bias of conventional measurement techniques, J. Geophys. Res., 112, 2007. (Cited on pages 3 and 26)

Struthers, H., Kreher, K., Austin, J., Schofield, R., Bodeker, G. E., Johnston, P. V., Shiona, H., and Thomas, A.: Past and future simulations of NO2 from a coupled chemistry-climate model in comparison with observations, Atmos. Chem. Phys., 4, 2227–2239, 2004. (Cited on pages 2 and 23)

Suda, K., Akimoto, H., and Tarasova, O.: WMO/GAW Expert Workshop on Global Long-term Measurements of Nitrogen Oxides and Recommendations for GAW Nitrogen Oxides Network, 2011. (Cited on pages 1, 17, and 19)

Sussmann, R., Stremme, W., Burrows, J. P., Richter, A., Seiler, W., and Rettinger, M.: Stratospheric and tropospheric NO2 variability on the diurnal and annual scale: a combined retrieval from ENVISAT/SCIAMACHY and solar FTIR at the Permanent Ground-Truthing Facility Zugspitze/Garmisch, Atmos. Chem. Phys., 5, 2657–2677, 2005. (Cited on pages 2, 12, and 112)

Sutton, M. A. and Bleeker, A.: Environmental science: The shape of nitrogen to come, Nature, 2013. (Cited on pages 2 and 26)

Tang, W., Cohan, D. S., Lamsal, L. N., Xiao, X., and Zhou, W.: Inverse modeling of Texas NOx emissions using space-based and ground-based NO2 observations, Atmos. Chem. Phys., 13, 11 005–11 018, doi:10.5194/acp-13-11005-2013, 2013. (Cited on page 3)

Terez, E. and Terez, G.: A method to determine atmospheric optical depth using observations of direct solar radiation, J. Geophys. Res., 108, 2003. (Cited on page 105)

Twomey, S., Herman, B., and Rabinoff, R.: An Extension to the Chahine Method of Inverting the Radiative Transfer Equation., J. Atmos. Sci., 34, 1085–1090, 1977. (Cited on page 188)

Valin, L., Russell, A., and Cohen, R.: Chemical feedback effects on the spatial patterns of the NOx weekend effect: a sensitivity analysis, Atmos. Chem. Phys., 14, 1–9, 2014. (Cited on page 153)

van de Hulst, H. C.: Light scattering by small particles, Courier Dover Publications, 1957. (Cited on page 34)

van der A, R. J., Eskes, H. J., Boersma, K. F., van Noije, T. P. C., Van Roozendael, M., De Smedt, I., Peters, D. H. M. U., and Meijer, E. W.: Trends, seasonal variability and dominant NOx source derived from a ten year record of NO2 measured from space, J. Geophys. Res., 113, doi:10.1029/2007JD009021, 2008. (Cited on pages 2, 13, 14, and 24)

Van Roozendael, M. and Hendrick, F.: Recommendiations for NO2 column retrieval from NDACC zenith-sky UV-VIS spectrophotometers, Tech. rep., Network for the Detection of Atmospheric Composition Change (NDACC), 2012. (Cited on pages 82 and 84)

Vandaele, A. C., Hermans, C., Fally, S., Carleer, M., Colin, R., Mérienne, M.-F., Jenouvrier, A., and Coquart, B.: High-resolution Fourier transform measurement of the NO2 visible and near-infrared absorption cross sections: temperature and pressure effects, J. Geophys. Res., 107, 4348, 2002. (Cited on pages 38, 78, 82, 83, 84, and 121)

Vandaele, A. C., Hermans, C., Fally, S., Carleer, M., Merienne, M.-F., Jenouvrier, A., Coquart, B., and Colin, R.: Absorption cross-sections of NO2: simulation of temperature and pressure effects, J. Quant. Spectrosc. Ra., 76, 373–391, 2003. (Cited on page 79)

Vaughan, G., Roscoe, H., Bartlett, L., O'Connor, F., Sarkissian, A., Van Roozendael, M., Lambert, J.-C., Simon, P., Karlsen, K., Høiskar, B., et al.: An intercomparison of ground-based UV-visible sensors of ozone and NO2, J. Geophys. Res., 102, 1411–1422, 1997. (Cited on page 105)

Vaughan, G., Quinn, P. T., Green, A. C., Bean, J., Roscoe, H. K., Van Roozendael, M., and Goutail, F.: SAOZ measurements of NO2 at Aberystwyth, J. Environ. Monitor., 8, 353–361, 2006. (Cited on pages 2, 23, 26, and 50)

Velders, G. J. M., Granier, C., Portmann, R. W., Pfeilsticker, K., Wenig, M., Wagner, T., Platt, U., Richter, A., and Burrows, J. P.: Global tropospheric NO2 column distributions: Comparing three-dimensional model calculations with GOME measurements, J. Geophys. Res., 106, 12 643–12 660, 2001. (Cited on pages 2 and 12)

Vigroux, E.: Absorption de l'ozone dans le spectre visible, Compt. Rend. Acad. Sci. Paris, 235, 149–150, 1952. (Cited on pages 4, 47, and 83)

Visconti, G.: Fondamenti di fisica e chimica dell'atmosfera, Cuen, 2001. (Cited on page 7)

Vlemmix, T., Piters, A., Berkhout, A., Gast, L., Wang, P., and Levelt, P.: Ability of the MAX-DOAS method to derive profile information for NO2: can the boundary layer and free troposphere be separated, Atmos. Meas. Tech., 4, 2659–2684, 2011. (Cited on pages 2 and 37)

Vrekoussis, M., Richter, A., Hilboll, A., Burrows, J., Gerasopoulos, E., Lelieveld, J., Barrie, L., Zerefos, C., and Mihalopoulos, N.: Economic crisis detected from space: Air quality observations over Athens/Greece, Geophys. Res. Lett., 2013. (Cited on pages 167 and 179)

Wagner, T., Chance, K., Frieß, U., Gil, M., Goutail, F., Hönninger, G., Johnston, P., Karlsen-Tørnkvist, K., Kostadinov, I., Leser, H., et al.: Correction of the Ring effect and I0-effect for DOAS observations of scattered sunlight, in: 1st DOAS Workshop, Heidelberg, Germany, pp. 13–14, 2001. (Cited on page 78)

Wagner, T., Von Friedeburg, C., Wenig, M., Otten, C., and Platt, U.: UV-visible observations of atmospheric O4 absorptions using direct moonlight and zenith-scattered sunlight for clear-sky and cloudy sky conditions, J. Geophys. Res., 107, 4424, 2002. (Cited on pages 88 and 132)

Wagner, T., Dix, B. v., Friedeburg, C. v., Frieß, U., Sanghavi, S., Sinreich, R., and Platt, U.: MAX-DOAS O4 measurements: A new technique to derive information on atmospheric aerosols–Principles and information content, J. Geophys. Res., 109, 2004. (Cited on pages 88 and 132)

Wagner, T., Beirle, S., Sihler, H., and Mies, K.: A feasibility study for the retrieval of the total column precipitable water vapour from satellite observations in the blue spectral range, Atmos. Meas. Tech., 6, 2593–2605, 2013. (Cited on pages 80 and 88)

Weatherhead, E., Theisen, D., Stevermer, A., Enagonio, J., Rabinovitch, B., Disterhoft, P., Lantz, K., Meltzer, R., Sabburg, J., DeLuisi, J., et al.: Temperature dependence of the Brewer ultraviolet data, J. Geophys. Res., 106, 34 121–34 129, 2001. (Cited on pages 46 and 69)

Wendisch, M. and Yang, P.: Theory of Atmospheric Radiative Transfer, Wiley-VCH, 2012. (Cited on pages 31, 32, and 33)

Wenig, M., Spichtinger, N., Stohl, A., Held, G., Beirle, S., Wagner, T., Jähne, B., Platt, U., et al.: Intercontinental transport of nitrogen oxide pollution plumes, Atmos. Chem. Phys., 3, 387–393, 2003. (Cited on pages 2 and 12)

Wenig, M., Cede, A., Bucsela, E., Celarier, E., Boersma, K., Veefkind, J., Brinksma, E., Gleason, J., and Herman, J.: Validation of OMI tropospheric NO2 column densities using direct-Sun mode Brewer measurements at NASA Goddard Space Flight Center, J. Geophys. Res., 113, 2008. (Cited on pages 4, 52, and 178)

Werner, R., Valev, D., Atanassov, A., Guineva, V., and Kirillov, A.: Analysis of variations and trends of the NO2 slant column abundance obtained by DOAS measurements at Stara Zagora and at NDACC European mid-latitude stations in comparison with subtropical stations, J. Atmos. Sol.-Terr. Phys., doi:10.1016/j.jastp.2013.01.016, 2013. (Cited on pages 2 and 24)

WHO: Air Quality Guidelines: Global Update 2005: Particulate Matter, Ozone, Nitrogen Dioxide and Sulfur Dioxide, World Health Organization, 2006. (Cited on pages 2 and 25)

Wilks, D.: Statistical methods in atmospheric sciences, International Geophysics Series, 91, 1995. (Cited on page 139)

Wittrock, F., Richter, A., Oetjen, H., Burrows, J. P., Kanakidou, M., Myriokefalitakis, S., Volkamer, R., Beirle, S., Platt, U., and Wagner, T.: Simultaneous global observations of glyoxal and formaldehyde from space, Geophys. Res. Lett., 33, L16 804, 2006. (Cited on page 76)

WMO: Second WMO consultation on ozone measurements by Brewer spectrophotometers, WMO Global Ozone Research and Monitoring Project, 1992. (Cited on page 51)

WMO: Scientific assessment of ozone depletion: 2006, World Meteorological Organisation, Global Ozone Research and Monitoring Project–Report, 50, 572, 2007. (Cited on pages 3 and 23)

WOUDC: URL `http://www.woudc.org/`, 2013. (Cited on pages 40 and 54)

Zhou, Y., Brunner, D., Boersma, K. F., Dirksen, R., and Wang, P.: An improved tropospheric NO2 retrieval for OMI observations in the vicinity of mountainous terrain, Atmos. Meas. Tech., 2, 401–416, doi:10.5194/amt-2-401-2009, URL `http://www.atmos-meas-tech.net/2/401/2009/`, 2009. (Cited on page 178)